MAGNETOM Flash

Issue Number 74 · 3/2019
ISMRM Edition

siemens.com/magnetom-world

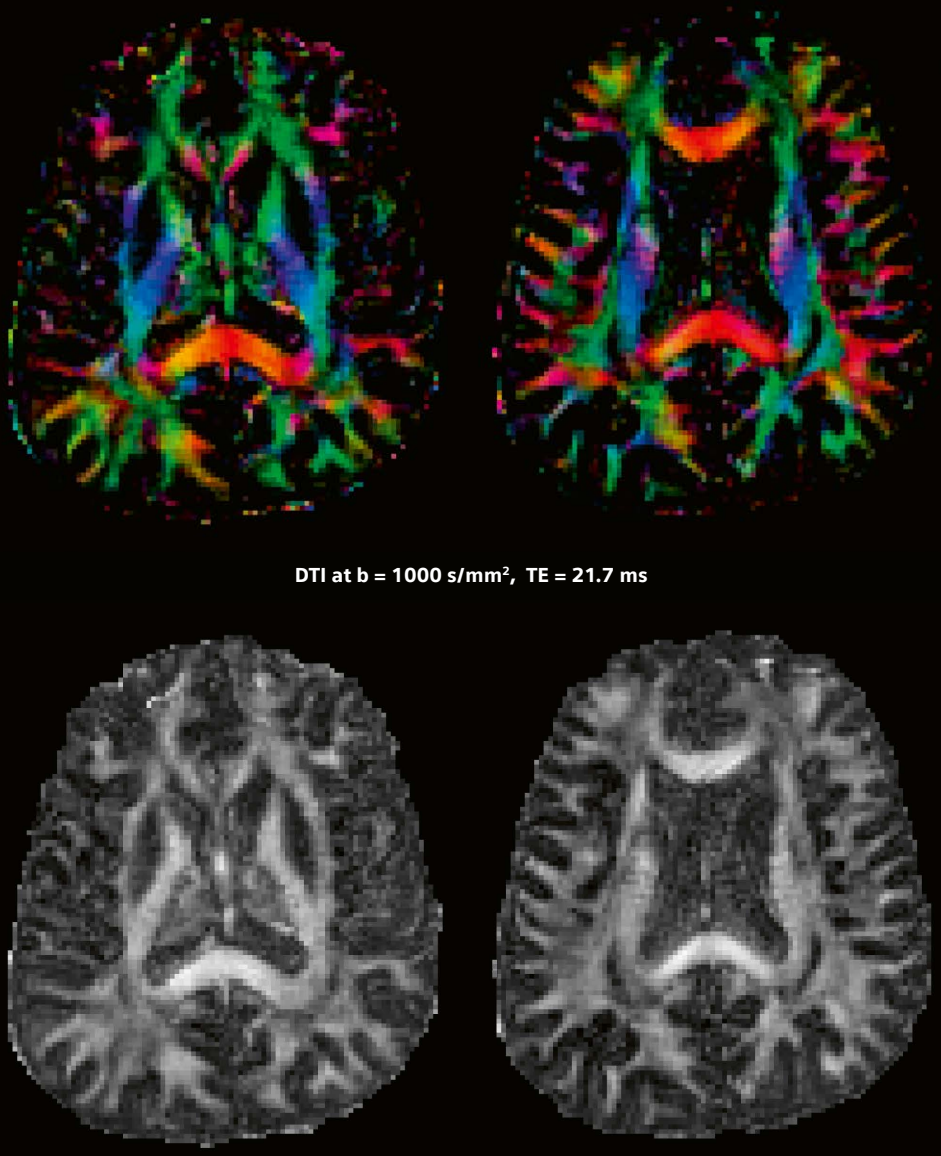

DTI at b = 1000 s/mm², TE = 21.7 ms

SIEMENS Healthineers

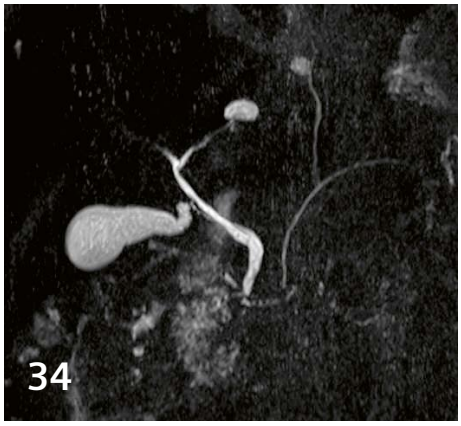

MAGNETOM Sola CAIPI SPACE 3D MRCP acquired in 20 s breath-hold

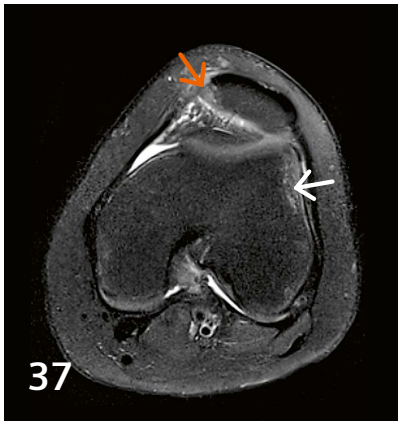

T2w SMS-TSE. MSK and body MRI in children

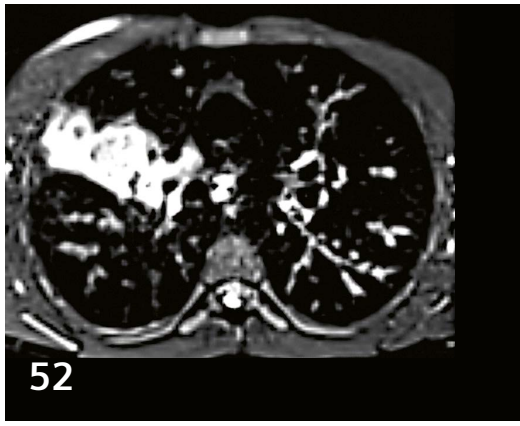

Lung MRI in parenchymal disease

Editorial Comment

Spotlight

Neurology

Body and MSK Imaging

Oncological Imaging

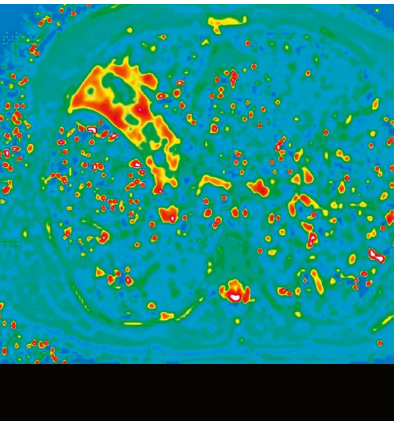

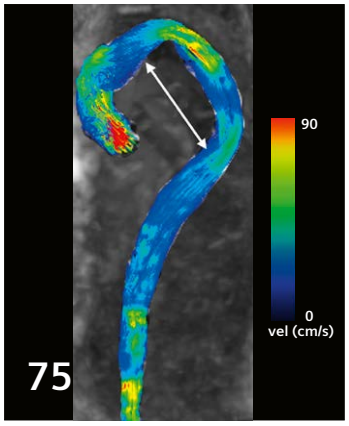

Compressed Sensing 4D Flow[1]

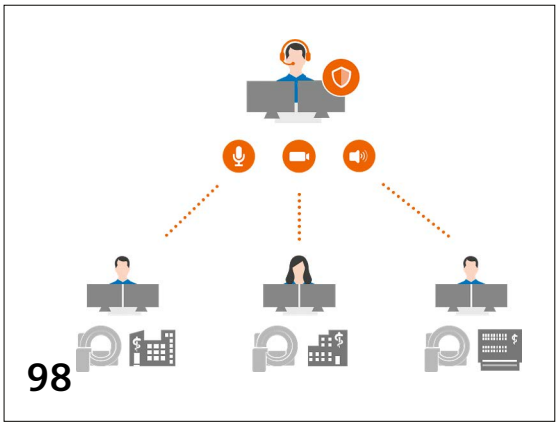

syngo Virtual Cockpit – remote scanning assistance and flexible workforce management

Cardiovascular Imaging

Product News

Meet Siemens Healthineers

Cover courtesy of Lars Mueller, Chantal Tax, and Derek Jones
Cardiff University Brain Research Imaging Centre (CUBRIC), Cardiff, UK

[1]Work in progress: the application is currently under development and is not for sale in the U.S. and in other countries. Its future availability cannot be ensured.
[2]syngo.via Frontier is for research only, not a medical device. syngo.via Frontier MR Total Tumor Load is a released research prototype.
[3]syngo Virtual Cockpit is not commercially available in all countries. For regulatory reasons, its future availability cannot be guaranteed. Precondition: Expert-i enabled

Professor Jürgen Hennig is Co-Chairman and Scientific Director of the Department of Diagnostic and Therapeutic Radiology and Medical Physics at the University Hospital Freiburg, Germany. He is known as the inventor of the RARE sequence, aka Turbo- or Fast Spin-Echo. His research activities are, however, wide-ranging and include methodological developments in MRI and spectroscopy, functional neuroimaging, molecular imaging, MR in oncology, cardiac and cardiovascular MR, and MR in metabolic disease. Professor Hennig's work has been recognized with numerous awards: Among others, the Max Planck Research Award, the Einstein Professorship of the Chinese Academy of Science, the Gold Medal of the Society of Magnetic Resonance, and the Hounsfield Medal of the Imperial College London. Over 480 publications are evidence of his focus on education.

Dear readers and colleagues,

It's that time of the year again and ISMRM is drawing near. A brief look at the program shows, unsurprisingly, that artificial intelligence and deep learning will again dominate the meeting. There is no doubt that AI will, and has already started to, permeate and transform all aspects of our field, from image reconstruction to diagnostic reading and beyond. It is less clear which of the multiple approaches and applications will ultimately take MR to the next level. The development of MR over the roughly 40 years since the first human scanner has never been a straight line. Whenever people thought, now we know everything and the rest will just be improved engineering, a new idea came along and transformed the field. This was the case with the advent of parallel imaging in the late 1990s and compressed sensing about 10 years later, to name just two examples.

Early days

I entered the field in 1984. I was already 33 years old, an age when others were already fairly far along their career path. I was still searching and looking for opportunities. I hadn't exactly been an end-focused student and took my time to complete my studies in Stuttgart (Germany), Imperial College London (UK), Munich, and finally Freiburg (both in Germany). To me, being a student first meant finding out who I am and only second acquiring knowledge and expertise about my chosen subject. At suitable junctures before and after my PhD project as well as before and after my postdoc in Zurich, Switzerland, I took off for typically three months at a time to go backpacking in Nepal, Peru, Indonesia, and Central Africa, the latter with my then fiancée and now wife Annemarie, the first three on my own. Getting into MR was, like many things in my life, rather serendipitous. I really wanted to go into industry and applied for a job with Bruker NMR. They didn't have an opening but Bernhard Knüttel, CEO at that time, told me about a project to install what was to be the 3rd MR scanner in Germany, and Professor Werner Wenz, head of radiology in Freiburg, was looking for a specialist with a PhD to help set up the system. When, after returning from Africa, I started work in Freiburg, I found that preparation of the scanner room had been seriously delayed (some things never change) and that the scanner was still sitting in the factory. So, for the next six months I commuted to Karlsruhe, Germany, to familiarize myself with the equipment and sequence programming. My first project under head of application development Bernhard Ströbel and chief engineer Dieter Ratzel was to implement a radial multiecho sequence for relaxation spectrometry.

Increasing speed

The overriding topic of conversation during coffee breaks and lunches were the long acquisition times of 10 to 15 minutes per scan and possible ways of overcoming them. Sir Peter Mansfield had already shown that this can be done with echo-planar imaging (EPI) and in one of his early publications even mentioned that multi-echo imaging should also be possible with multiple spin echoes. Larry Hall had just published a paper on using a long echo train to acquire all projections for radial reconstruction in a single echo train, but it was clear that this would not work on a clinical scanner since it required exact 180° pulses

We should by all means take a fresh look at 'old' topics in view of everything that we have learned in the meantime, but of course it would be prudent to consider insights already gained rather than wanting to start from scratch.

and only works for very long T2s. At that time, Bruker had decided to switch from radial encoding to Fourier encoding but still use CPMG multi-echo readout to perform relaxometry. Bernhard Stroebel was in charge of developing the 'bread-and-butter' sequence with identical phase encoding in all echoes of the echo train and I thought I'd try using this for echo imaging. We already had experience in adapting the CPMG conditions to the use of switched gradients through previous work on radial imaging, so rewinding the phase-encoding gradient before each refocusing pulse seemed like the natural thing to do and didn't feel very 'inventive'. The first human image we took was of the eye of a volunteer who happened to be scheduled on the day that we completed the first successful phantom experiment. Pulse programming was pretty straightforward in these days, the infamous Z17c process controller allowed only 16 lines of code, so everything had to be compressed into 16 instructions. The array processor used for reconstruction had to be programmed in assembly code, so without the enthusiastic support of chief programmer Arno Nauerth I would not have got very far.

I can't say that RARE (aka TSE or FSE) was an immediate success. On the contrary, for many years I presented the latest developments at the obscure 'Rapid Imaging' sessions at SMRM meetings without much interest shown, alongside Sir Peter Mansfield's equally obscure EPI images. The first attempt at publication was rejected with the remark 'This has been tried before, it doesn't work'. And indeed, there had been previous attempts at spin-echo-based echo imaging, which used different types of phase-cycling schemes to deal with the multiple spurious signals that suddenly appear after multiple refocusing pulses. Luckily, I was unaware of these at the time, otherwise I may well have tried to work along those lines. So sometimes it does pay to not let too much information stand in the way of freethinking ...

Hot topics

My first Society of Magnetic Resonance in Medicine (SMRM) meeting was 1985 in London. It was my first major scientific conference, so I had no idea what to expect. One of my lasting impressions was attending the notorious session when Raymond Damadian used his role as moderator for a lengthy tirade against Paul Lauterbur, which in the end got him expelled from the society.

1 Extract from the table of contents for the 1985 SMRM.

Scientifically, THE hot topic at the time was quantitative MRI (sounds familiar?). A look at the table of contents for one session (Fig. 1) reveals that all the hot topics discussed today were already there, albeit under somewhat different names.

In spite of these similarities, it is quite wrong to say that MR has gone around in a circle. I like to think the path is more like a helix: We have returned to the same point with respect to some coordinates, but have considerably advanced in another dimension. So we should by all means take a fresh look at these 'old' topics in view of everything that we have learned in the meantime, but of course it would be prudent to consider insights already gained rather than wanting to start from scratch.

Relaxometry

Relaxation in tissue is somewhat more complex than the values we get from fitting our data to a basic version of the Bloch equations, irrespective of whether we do that based on 'traditional' exponential fit or more fancy techniques like MR Fingerprinting[1]. Due to tissue heterogeneity, relaxation times are inherently non-monoexponential. As an illustration, Figure 2 shows the T2-spectrum of the human brain acquired from multiexponential analysis of a long echo train with 6 ms echo spacing.

A practical consequence of this is the fact that measured T2s will depend on the actual measurement parameters: Measuring at different TEs will influence the result of a monoexponential fit, a change in TR may lead to different degrees of saturation of different compartments, which will then also show up as a change in the measured T2.

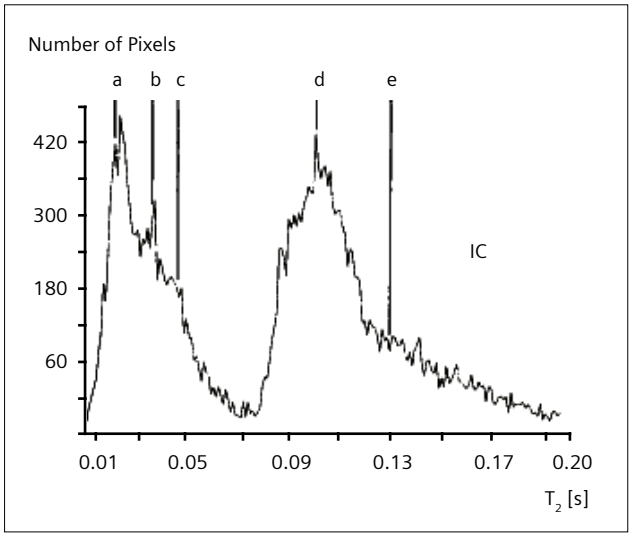

2 T2-spectrum of the brain. *(From K. Gersonde, F Elsberg, Tolxdorff, D. Ratzel, DB. Stroebel. Analysis of Multiple T2 Proton Relaxation Processes in Human Head and Imaging on the Basis of Selective and Assigned T2 Values. Magn Reson Med 1,463–477 (1984)).*

T1 is more innocuous for the simple reason that T1s of most tissues are rather long, which means that spins have had a chance to visit multiple compartments during the T1 decay. Given a typical diffusion constant, the 'averaging radius' over 1 s is about 50 µm, enough to average out most tissue heterogeneity.

On the one hand, the richness of information contained in a full analysis of multiexponential decay offers the possibility of more specific tissue characterization, on the other hand, such relaxometry measurements take time and therefore are not (yet) suitable for practical clinical application. It is, of course, perfectly legitimate to explore whether simplified monoexponential T1s and T2s could be useful as 'biomarkers' for disease. However we should be aware that, especially for T2, the measured values are only approximations, which also depend on the actual measurement sequence used, so the universality implied by the term 'quantitative MRI' is just a fiction. Calibration measurements typically presented to verify the validity of some new method are typically performed on homogeneous solutions and are not really pertinent since they do not reflect tissue heterogeneity.

FLASH

Relaxometry quickly lost general appeal in the late 1980s. This was not so much due to its inherent value but more to the advance in fast imaging, most notably the arrival of fast gradient echo imaging (FLASH). Jens Frahm and Axel Haase had already presented a poster at ISMRM 1985 (p. 980) on fast imaging techniques showing FLASH together with single-shot STEAM imaging. This really took off like a storm the following year. The possibility of acquiring rather interesting looking images in seconds rather than minutes caught the imagination of the community, so already at SMRM 1986 there were multiple abstracts inventing and reinventing FLASH under more or less fanciful new names: I particularly liked GREED for gradient reversal echo, equilibrium driven. Then and thereafter, contrast behavior was investigated and understood, leading to spoiled FLASH, refocused FLASH (FISP), PSIF and ultimately TrueFISP for the fully balanced version – of course, with a full set of unique acronyms for each vendor.

The mixed contrast of gradient echo techniques with variable contributions of T2*, T2, T1, depending on type and parameter selection, limited the use of FLASH to standard imaging, but it has spawned a tremendous growth in new techniques where FLASH is used as a vehicle for new areas of application – MR angiography, Cine Cardiac MR, flow imaging, susceptibility-weighted imaging, MR fluoroscopy – to name but a few. In the following years,

[1] *Work in progress: the application is currently under development and is not for sale in the U.S. and in other countries. Its future availability cannot be ensured.*

SMRM programs were dominated by the development of new sequences and their clinical application. Indeed, nearly all sequences in MR scanners today originate from researchers at academic institutions. There are a few notable exceptions – Gerhard Laub and Chuck Dumoulin come to mind who shared the Gold Medal in 1993 for their work on MR angiography.

Hardware

Hardware development was different in the early years. There always was some RF coil development in academia, but the rest (magnets, gradients) was driven by industry. The advent of shielded gradients in the early 1990s signaled the next transformative step in MR. Liberating MR from the obnoxious eddy currents inherent to the use of unshielded gradients in a superconductive magnet with its many layers of conductive copper and steel led to new degrees of freedom for MR sequences. I was one of the first beneficiaries of that. RARE went for many years largely unnoticed – the challenges for implementation on supercons were the main but not the only reason for this.

Bob Mulkern at Brigham and Women's Hospital, Harvard Medical School, was the first to implement RARE on a 1.5T GE scanner. The first paper on what he originally called FAISE led to an explosive growth, similar to FLASH five years before. Bob could have easily taken the praise and reduced my original work to some insignificant prior art (this has happened in other cases), but he did not. For this, I am forever indebted to him and, in particular, to Ference Jolesz.

Shielded gradients finally brought EPI into clinical application. As early as 1987, Richard Rzedzian and Ian Pykett, both from Peter Mansfield's lab in Nottingham, had introduced the Advanced NMR system, an EPI-only MR system with a resonant gradient system, to the market. Alerted by this unwelcome new competitor, all major vendors intensified their effort to make EPI happen. GE introduced Advanced MR, Siemens followed with the MAGNETOM Vision (regarded by many users as the best MR system ever), which was EPI-ready in 1994.

EPI not only finally facilitated the practical use of diffusion-weighted imaging, its advent also coincided with the introduction of BOLD-based fMRI. Ken Kwong, who was the lucky user of one of the Advanced MR EPI gradients, was the first to perform BOLD-based EPI for fMRI studies.

The introduction of fMRI was not so much a transformational step, it was more like opening the door to a vast new field of application for MR. It also opened up a new and vast area that was not primarily driven by clinical application but by neuroscientific research.

Now, finally, MR seemed to have reached its destination. All the main acquisition modes, FLASH, EPI, and RARE, were working and gave great results, scanners had reached a state of stability and maturity, applications were flourishing. What else was there to do?

The next wave in speed

Then came ISMRM 1997 when Dan Sodickson presented SMASH, a new technique for parallel imaging, which was the start of Parallel MRI, a whole new dimension in accelerated MRI. A few months later, I organized a fast imaging workshop in Asilomar together with David Feinberg. One of the posters was submitted by a young PhD student from Zurich named Klaas Pruessmann on a technique he called 'SENSE'; and although I admit that I didn't get through all the math, I am happy to say that our two-man poster award team recognized this achievement with the poster award (an Asilomar T-shirt, if I remember correctly).

What has happened since then? Not much or a lot depending on how you look at it. It is a sobering thought, but the extremely dynamic and rapid development of all basic technologies with respect to sequences, RF coils, and gradients, which took place between the early 1980s and the mid 1990s, was more or less concluded about 20 years ago. I still operate a 1.5T MAGNETOM Symphony upgraded from a MAGNETOM Sonata bought nearly 20 years ago, and it basically knows most of the tricks of our latest scanners. It is a bit slower, the gradients are not quite as fast and strong, it has a few receive channels less, but basically it is the same machine and perfectly adequate for clinical routine use. Since then, we have, of course, seen the introduction of 3T and more, culminating so far in the 7T MAGNETOM Terra. Translation and adaptation of methods and technologies to higher fields has been an astonishing effort requiring tremendous expertise and skills, but it has been a translation – nothing more. The one fundamental challenge is the fact that the RF wavelength at higher fields approaches the dimension of organs within the body, leading to inhomogeneities of the RF field. As a consequence, image intensity and image contrast may vary across the field. What is worse, the non-negligible E-field contribution in this not-quite-near-field-anymore regime has led to tremendous and still largely unsolved SAR problems. Much creativity and effort has been applied by many groups to these problems, but there is still much more to do.

Free thinking

For me personally, ISMRM 2005 was a real turning point in my scientific work. I had the honor and pleasure of giving the Mansfield lecture in the famous Jackie Gleason theater, home of the famous Jackie Gleason show in the 1950s and 60s. For whatever reason and the first time ever in my career, I went to the theater to test my presentation on stage

rather than just checking it in the preview room (where it worked perfectly). I had a few videos and animations and, what shall I say, not one of them worked. Together with the technician, I spent the whole afternoon reformatting my files and downloading new codecs until everything went smoothly. Other speakers of plenary sessions in the same location were not so lucky and had to spend a lot of their precious presentation time explaining to the audience what they should be seeing, but weren't.

The topic given to me for my lecture was 'Fast Imaging Horizons in Rapid MR Imaging'. In the preparation for the talk, I wanted to end on a cliffhanger to indicate that there is still much to come. So I thought, what's the limiting factor for imaging speed? Gradients, of course. So what about omitting gradients, how can we still get spatial information? By making use of the spatial sensitivity of multicoil arrays. Put like that, imaging speed is only determined by the speed at which one can sample data, which is extremely fast, at megahertz sampling rates, if necessary. In extreme cases, one can allocate each image pixel to a different coil. This led to the term OVOC for 'one voxel one coil imaging' (I later found out that this idea had been published before by Mike Hutchinson in 1988 as a pure thought experiment and I should also like to mention that Fa-Hsuan Lin independently developed a very similar concept with his inverse imaging technique).

Rather than just presenting signal traces corresponding to the time-dependent signal under each coil, one can first acquire a high-resolution image and then use the coil images as a basis for dynamic images generated by the sum-of-squares combination of the reference images with the instantaneous signal. This way one can, in principle, produce images of arbitrary resolution (which is defined by the reference data) at arbitrary speed – spatial resolution appears to be decoupled from temporal resolution. I didn't really expect much when I performed the test experiment, so I was quite pleased and surprised to see that even with the crude 8-channel coil setup that I had, I could clearly see spatially variable ECG- and breathing variations. So this was really the starting point of my still ongoing work on ultrafast fMRI.

Chuck Mistretta generously claims that my talk inspired him to develop what he called the HYPR-technique. He also coined the term 'Hennig limit' for making an image from a single measurement point (or, ultimately, from no data at all, which brings us dangerously close to deep learning and AI).

As another follow-up, I thought that it would actually be neat to sacrifice some of the unnecessary high speed in order to introduce some 'homeopathic' dose of gradient encoding (still not really thinking about producing an image but rather just putting some more spatial discrimination into the multi-sensor readout). For this purpose, it seemed like a smart idea to have each RF coil associated with an individual gradient coil oriented toward the coil coordinates. For multiple coils, these individual gradient fields combine to form a highly non-linear spatial encoding field, which is how PatLoc was born. This led to a further highly fruitful line of research on non-linear spatial encoding fields, which has meanwhile been taken over by Maxim Zaitsev in my group, and several others elsewhere, culminating in his 84-channel gradient matrix coil.

This free thinking to come up with a (however unrealistic) attention-grabber for a lecture has given me the basis for much of my scientific work for more than a decade. This is not the first time that thinking about the fundamentals has led to new ideas – that's why I really enjoy giving introductory lectures or presentations to a more general audience, both of which force one to really think and maybe rethink the basics. (I am still waiting to see what inspiration will come from writing this editorial!)

Looking ahead

The elephant in the room in this account of the technological and methodological development of MR is, of course, the magnet. Current magnets all look the same, big beasts, more or less short, 60–70 cm-wide supercons with 1.5 or 3T field strength. This is a result of the fact that building a superconducting magnet has always been and still is an extremely demanding task defined by very narrow constraints set by materials, currents, and forces. Except for making magnets somewhat shorter and bore sizes somewhat wider, not much seems to have changed since the first supercons were introduced in the mid 1980s. But this is about to change.

Currently, a first step is being taken by the introduction of low-helium magnets, which not only saves on helium costs but reduces the installation effort by avoiding the need for a quench pipe. This is a first step toward making MR more accessible to a wider community. The next step is already on the horizon. Stefan Röll, well-known to many Siemens users, has created his own company Neoscan with the aim of building an MR system based on high-temperature superconductors. The HTS wire is able to sustain unprecedented high current density, which in principle allows the construction of extremely compact magnets. Once this technology has matured, it will be possible to build very slim shielded magnets, where the magnet plus shielding will be only a few tens of centimeters thick (much like current gradient coils.) This will also allow the construction of tailor-made, extremely compact magnets, e.g., for use in areas without much supporting infrastructure. This will take a while to become routinely available. The current wire can be manufactured only with a limited length, too

short to wind a magnet from one strand of wire. Also, the mechanical stability of the wire in strong magnetic fields is still a challenge, to name but two of the difficulties. The 'ISMRM Workshop on Accessible MRI for the World', which is taking place in India as I write this article, shows that new concepts to bring MRI to a larger community is one of the future growth areas for MR.

The one big transformative step that I have not yet addressed is the introduction of compressed sensing presented by Miki Lustig at ISMRM 2006 and published in December 2007. In 2008, it already had 41 citations and 78 in the following year (and nearly 3000 as of today), which demonstrates the immediate huge interest it generated. The promise of acceleration factors way beyond what is achievable with conventional parallel imaging techniques immediately fascinated the community with the promise of finally breaking through the Nyquist limit of 'conventional' imaging (which we also took as the motto for a series of workshops that we held together with UW Madison – watch out for the next installment).

Artificial intelligence

And now AI has arrived to take MR (and not only MR) to the next level of development. Neural networks have been around since the 1980s, so the basic principles have been known for a long time. But new algorithmic approaches like supervised backpropagation as well as the rapid increase in computing power and data storage have now made deep learning feasible for many applications –self-driving cars, language translation, face and speech recognition, to name but a few. In medical imaging and MR, AI got off to a somewhat rocky start, triggered by an ill-informed statement by Geoffrey Hines, one of the pioneers of backpropagation, that AI will make radiologists obsolete within five years. Well, nearly three years have passed since then and radiologists are still around. AI will certainly transform radiology and it will also transform MRI, but in which way is still unclear. It will make some tasks previously performed by humans obsolete, but this will most likely affect the simpler and thus more boring tasks first. Rather than shying away from this new challenge, we should embrace and explore it, and it is good to see that the ISMRM community is doing exactly that. AI has been the hot topic of the last few annual meetings, on which there have already been three workshops, and I think that's exactly the spirit: There is a new opportunity, we should grasp it and explore it even though we still can't see where it will take us. The explosive growth of work on AI has already produced some do's and don'ts:

Using AI for further acceleration seems like one very promising application. Several groups have already shown that a CNN, even when trained on a modest dataset, can produce near-to-perfect images from highly undersampled data. Image segmentation also works extremely well. Even tough tasks like segmentation of hippocampal subregions, which have been tackled by generations of computer scientists with mixed success, seem to work extremely well. (If Geoff Hines had talked about computer scientists working on segmentation he would have been correct.) It has already been shown that AI can be used to generate realistic-looking CT images from MR data (which can be helpful in, e.g., radiation therapy or in MR-PET) or even nice-looking 7T images from 1.5T data (which seems to be less compelling). The possibilities seem unlimited.

I am not so convinced about the use of AI directly on raw data, effectively omitting Fourier transformation. It doesn't seem to make much sense to replace just this part of the reconstruction process by one that has to be trained first. After all, we know exactly how it should be done. I still think that, in problem solving, it is a good strategy to approach the solution in a way that is as close as possible to using everything we know, deploying AI to take the last missing step. This doesn't mean that exploring how FT can be replaced by AI is useless. As we have a 'basic truth' in this area to assess the result, this may actually help to develop some intuition about this mysterious 'black box'.

There is a fundamental difference between innovation brought about by AI and all previous innovations: Previous progress was made by new insights and better understanding. Scientific problems were solved by analyzing and understanding the subject matter, and this understanding could be used to solve new problems. The motor that has driven science over the last few centuries was the fact that solving some problem invariably not only led to an improvement in the issue addressed, but also to new and previously unexpected areas and directions. AI skips the 'understanding' part of the problem-solving process, it produces solutions (and often very good solutions) directly and without generating any understanding. So, without new insights, where will future innovation come from? This is not meant to be a rhetorical question, but only time will tell.

Back to MR. Given the similarity of MR scanners across all vendors, one may think that the technology is mature and, apart from incremental improvements, not much more can be expected in the future. I think that this is wrong and the current situation is more like the calm before the storm. For many years, development in MR followed a path set by GPS (GE – Philips – Siemens). Now companies like SSI, Tesla, ASG, Neoscan have started to develop new magnet concepts, electronics and devices to build MR, from power supplies to spectrometers to RF coils and gradients, become cheaper and better. Last but not least, new and serious competitors from China and

elsewhere are entering the arena. So I am pretty sure that there is a lot of change to come, which may even include a change to the whole business model of MR. I very much agree with the concept Toby Block promoted in his plenary talk last year: It is very appealing to consider a world in which sequence development takes place in a universal, open space, in which any sequence can be executed on any scanner by any vendor (within the hardware constraints of each system, of course). 'Sequence' means not only the pulse program but the whole measurement workflow, including real-time functionality and feedback loops. Having all the bright minds of the scientific community work toward improving MR will accelerate development considerably and will facilitate cross-platform comparisons and multicenter studies as a big step toward standardization as a basis for personalized medicine. Maxim Zaitsev has taken a first step toward such universal programming with his Pulseq platform. There are others, too, and I am very enthusiastic about it for very selfish reason. It would be futile for me to try and master in-depth pulse programming in IDEA, too little time, too long out of touch. But to write a Pulseq sequence in MatLab is doable, even for me. I recently implemented RARE using Pulseq, it took a few hours and 72 lines of code, more than the 16 I originally had, but much less than the implementation on any existing platform.

Is an open and universal sequence development platform a valid business model? Microsoft has shown that it is: It hasn't done badly by providing an open platform with Windows® with the opportunity for anybody to develop their own software while still making a success of its own, very profitable, software business with the Office® package and others. In medical imaging, this is even more straightforward since users can easily develop new sequences, but very few will have the means to go through FDA approval. In this way, the otherwise costly development part will be outsourced, but the business part will still stay with the vendors.

Will that be the future? I don't know. If I have learned one thing over the years, it is that development very rarely takes the most logical and scientifically rational path. The only thing I am pretty sure of is that we can expect many more (radical) developments in MR in years to come.

Jürgen Hennig

We appreciate your comments.
Please contact us at magnetomworld.team@siemens-healthineers.com

Tissue Segmentation and Partial Volume Estimation with Magnetic Resonance Fingerprinting

Dan Ma[1]; Anagha Deshmane[2]; Debra McGivney[1]; Irene Wang[3]; Chaitra Badve[1]; Vikas Gulani[1]; Mark Griswold[1]

[1]Radiology, Case Western Reserve University, Cleveland, OH, USA
[2]Magnetic Resonance Center, Max Planck Institute for Biological Cybernetics, Tuebingen, Germany
[3]Epilepsy Center, Cleveland Clinic, Cleveland, OH, USA

Introduction

Recent demand for precision medicine and personalized diagnostics has led to increased interest in radiomics and robust quantitative imaging with MRI. To this end, recent technical developments have included anatomical volumetry, quantitative relaxometry, and quantification of tissue microstructural and functional properties such as diffusion and perfusion. Specifically, tissue segmentation has become the basis of quantitative volumetric estimation and volume-based post-processing, which have been used to diagnose and characterize several neurological diseases. For example, multiple sclerosis [1], brain plasticity [2, 3], dementia [4], and epilepsy [5, 6] are associated with global and local brain volume and cortical thickness changes. Anatomical segmentation has also been used to target subcortical structures, such as the subthalamic nucleus (STN) [7], for surgical treatments.

The partial volume (PV) effect is a well-known challenge for any imaging modality with limited image resolution, including MRI, and poses a particular challenge for both quantitative mapping and quantitative image analysis. When the image resolution is lower than the dimension of the anatomical structure, e.g. when image voxels span tissue boundaries, some voxels may contain multiple tissue types. The PV effect causes blurring at these interfaces on the MR images because the contrast or signal of the mixed voxel is a weighted average of that from each single tissue component. For quantitative imaging and image post-processing, the assumption that each voxel contains a single and pure tissue type may lead to mis-classification and thus mask some subtle features or tissue changes, especially at tissue boundaries. Assuming that the signal evolution (for example, a relaxation curve) in each image voxel is characterized by a single tissue property (i.e. T1 or/and T2) may cause errors in tissue property quantification in mixed voxels.

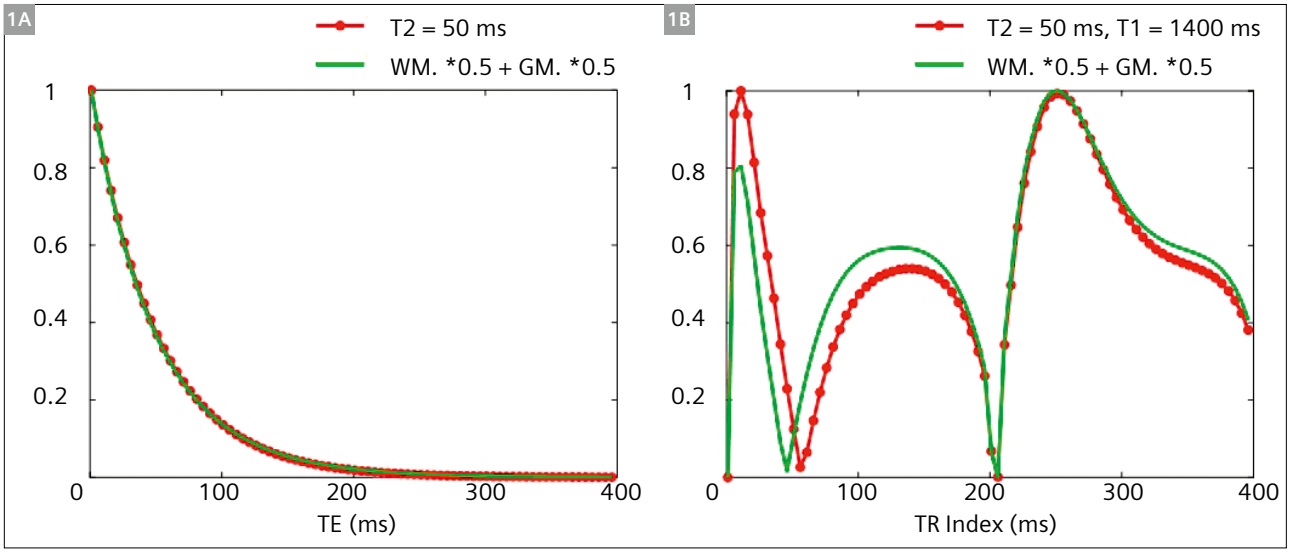

1 Comparison of signal curves from conventional T2 mapping **(1A)** and from MRF **(1B)**. The signal from a PV effect is more distinct from a pure tissue using MRF.

Depending on the desired anatomical scale for analysis of tissue properties within one voxel, certain assumptions about possible voxel compositions can be made. This article concerns multiple tissue components in the slow exchange regime, where no chemical exchange between components is assumed, such that each tissue within a voxel is modeled as a distinct component. Primarily, multi-component models for PV have been used for tissue segmentation, by assuming that each voxel contains mixed signals from pure tissues, such as gray matter (GM), white matter (WM), and CSF for brain tissue segmentation [8–10], or water and fat for fat fraction estimation in the liver [11]. The result of these methods are either hard-threshold tissue classification or soft-threshold tissue fraction maps, which can be further used for tissue volume calculation [6], image feature extraction [12, 13], and disease diagnosis. In addition, multi-component PV models have been used to analyze microstructural features. For example, multiple T2 components have long been considered when analyzing human brain [14], where three components are commonly assumed, including water protons compartmentalized between myelin bilayers, intra- and extracellular water, and free fluid (usually contained in the CSF). The results of the PV analysis consist of a volume fraction of each of the three components in each voxel. The results can be further used to calculate myelin water fraction (MWF), which is estimated as the percentage of the signal with T2 from the fast relaxation components (myelin water) to the total water content. The MWF is an important marker for white matter microstructure, especially myelin generation/degeneration, and thus a change in MWF has been associated with age-related neural tissue changes [15, 16], as well as neurodegenerative diseases such as Multiple Sclerosis [17] and Schizophrenia [18, 19].

In order to resolve multiple tissue components within one voxel, PV estimation methods employ multi-component signal models which are based on either contrast-weighted images or quantitative MRI scans. For the former scenario, weighted images with one or more contrasts are acquired and the PV is estimated based on regularized statistical models of image contrast variations [8, 20, 21]. Using quantitative MR to estimate PV has the benefit of having an additional time domain of the signal change that is characterized by one or more underlying tissue properties, such as T1 and/or T2. The PV effects can then be modeled by assuming that the acquired signal evolution is a mixture of multiple tissue components. For example, MWF estimation is based on multi-exponential T2 relaxation from a multiple spin-echo acquisition [19], and brain tissue segmentation is based on multi-exponential T1 relaxation from an inversion recovery Look-Locker acquisition [22] or based on multi-parametric mapping scans [10, 23]. The tissue fraction of each component is then estimated by interpolating between quantitative results [10], or by solving an inverse problem [22, 23].

MR Fingerprinting (MRF)[1] [24] is a quantitative MR method that provides new opportunities to analyze PV effects and identify multiple tissue components. First, MRF applies pseudorandomized acquisition patterns to generate signal evolutions that never stay at constant steady state and exhibit unique signal variations depending on multiple tissue properties. These two features help to provide more incoherent signals between different tissues, which could improve the ability of tissue separation. As an example, Figure 1 compares signals from a conventional T2 mapping method (left) and from MRF (right). Because signals from the conventional method all follow an exponential pattern, they are typically inseparable in the presence of noise. The mixed signal (green) with equal contributions from gray and white matter 'looks' the same as the signal from another, uniform tissue with a different T2 (red). In MRF, since signals do not follow such a simple evolution due to variable acquisition and multi-parametric sensitivity, the mixed signal is more likely to be distinct from other pure-tissue signals. Second, since the signal model is constructed based on Bloch equations, the effects from multiple tissue properties and confounding factors (B_0, slice profile and B_1 etc. [25-28]) can be accounted for. The PV results could thus be more robust and less dependent on system imperfections. Finally, we will show a few examples that pattern recognition based on a pre-defined dictionary could also make MRF-based PV analysis (PV-MRF) less sensitive to noise than conventional approaches based on inverse methods [23]. In the following sections, the theories and implementations of multiple PV-MRF methods will be introduced, followed by discussions of several emerging neuroimaging applications.

Partial volume signal model and conventional PV analysis

In both conventional quantitative MR and MRF, the acquired signal evolution such as shown in Figure 1B is modeled as a weighted sum of signals from a few known tissue components. Suppose the anatomy of interest contains m component tissues. Let $d_l \in C^{1\times t}$ represent the MRF signal evolution for component tissue $1 \le l \le m$, where t is the number of time points acquired from an MRF scan or other T1 or T2 mapping experiment. We collect these m component signal evolutions in a sub-dictionary $D^{sub} \in C^{t\times m}$. The voxel signal evolution can be modeled as a weighted sum of the component species' signal evolutions:

$$s_i = \Sigma_{l=1}^{m} w_{i,l} d_l = D_{sub} W_i \quad (1)$$

where $w_{i,l}$ is the weight of tissue l in voxel i. For example, in normal brain tissues, we can model $m = 3$ to represent

GM, WM, and CSF. The number of components may be increased in cases of disease or complicated anatomy.

The signal of each component d_l can be simulated and is characterized by their tissue properties, such as T1, T2, and proton density (M_0). The values of these tissue properties can be either gathered from literature, group analysis, or estimated based on quantitative maps acquired from the same subject. The latter approach is more subject-specific and thus takes into account individual physiological variations. For example, multiple histograms of mapped relaxation times can be used to identify characteristic relaxation properties of the modeled tissues [22, 24]. Alternatively, *k*-means clustering can be used with MRF to identify voxels with similar relaxation properties based on T1 and T2 maps acquired from an MRF scan, yielding *k* clusters whose centroids represent characteristic {T1, T2} properties. The properties corresponding to those tissue clusters can then be selected as components in the PV model [23]. Note that the number of histograms or tissue clusters will affect T1 and T2 values of component tissues and thus affect the accuracy of the PV analysis.

After the representative tissue properties are determined and the signals from D_{sub} are simulated (by Bloch equations, for example), the partial volume, or tissue fraction, of each component within a voxel is estimated by solving this linear model. The Moore-Penrose pseudoinverse is commonly applied to compute the signal weights:

$$W_i = (D^H_{sub} D_{sub})^{-1} D^H_{sub} s_i \quad (2)$$

where the superscript *H* represents the Hermitian adjoint or complex transpose operator. The weights are then normalized such that the sum of the weights has unit magnitude, and the result can be interpreted as a tissue fraction.

Tissue segmentation and partial volume quantification with PV-MRF

Solving the above inverse problem requires high SNR, which is typically not acquired in MRF due to highly accelerated *k*-space sampling and thus severe aliasing artifacts. The results are further prone to errors when more tissue components are assumed. Since dictionary matching has been shown to have relatively high error tolerance, a new dictionary-based PV-MRF has been proposed and has been shown to reduce the effect of over-fitting errors [23]. PV-MRF therefore adopts the concept of MRF, by converting a least-squares fitting problem into a pattern matching problem, where the weights are identified by exhaustive search of a new dictionary that contains all possible combinations of component tissues. To this end, a weight table $\tilde{W} \in R^{m \times h}$ that lists all possible weight combinations is first constructed, where *h* is the number of weight combinations. Next, a separate PV dictionary is constructed,

$$D_{pv} = D_{sub} \tilde{W} \in C^{t \times h} \quad (3)$$

where each column of D_{pv} contains a mixed tissue signal evolution calculated from the weighted sum of the *m* modeled component tissues with a certain weight combination. Finally, tissue fractions are estimated by matching the acquired signal to all signals from the PV dictionary. The weight combination corresponding to the highest inner product are selected and converted into multiple tissue fraction maps.

Figure 2 compares tissue fraction maps estimated from MRF signals using the pseudoinverse (2A) and dictionary based (2B) PV-MRF methods. GM, WM, and CSF maps from five 2D slices for one subject scanned on a 3T MAGNETOM Prisma are shown. Sequence parameters for each of the 2D MRF scans are: field of view = 300 x 300 mm^2, voxel resolution = 1.2 x 1.2 x 5 mm^3, TA = 31 seconds [29].

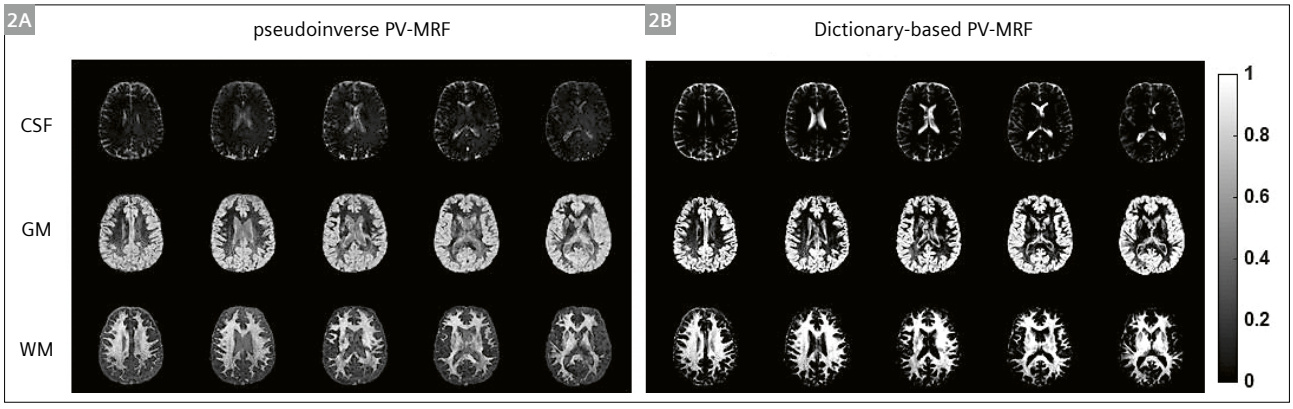

2 Comparison of partial volume estimation with MRF using conventional analysis by partial volume model inversion **(2A)** and dictionary-based PV-MRF **(2B)**. Dictionary matching is more robust to noise-like artifacts in MRF signals than the pseudoinverse calculation, allowing for better descrimination of tissues and more accurate estimation of tissue fractions [23].

PV-MRF can segment pure tissues, as well as visualize mixtures of GM and WM in deep gray matter structures. However, the PV fraction maps computed by pseudoinverse show residual CSF contributions in the GM and WM maps. The dictionary based PV-MRF maps exhibit better discrimination of pure tissues.

Figure 3 shows an example of all six 3D quantitative maps[1], including T1, T2, proton density, as well as GM, WM, and CSF fraction maps computed with a partial volume dictionary, acquired from a healthy volunteer scanned on a 3T MAGNETOM Prisma system. All maps are inherently co-registered because they are obtained from the same dataset. Sequence parameters for the 3D MRF scan are: field of view = 300 x 300 x 144 mm^3, voxel resolution = 1.2 x 1.2 x 1.2 mm^3 isotropic, TA = 12 minutes [30].
To compute tissue fraction maps using dictionary based PV-MRF, three tissue components, GM, WM, and CSF are assumed. *K*-means clustering of mapped T1 and T2 values with $k = 7$ is used to analyze tissue compositions based on the quantitative maps. Three clusters are then manually selected to identify the characteristic relaxation times of the modeled tissue components, which are subsequently used to construct D_{sub} and D_{pv}.

Bayesian model based PV-MRF

Most segmentation methods assume that the brain consists of only three tissue components (GM, WM, and CSF) and use this assumption to represent every voxel as a weighted sum of these three tissues. A limitation in this approach may be evident in cases of pathology, where a diseased or unhealthy tissue may not be composed of these three tissues, but may contain a different component not represented in the PV model. In this case, forcing a fixed model on the voxel signals will result in erroneous tissue fraction calculations and diseased tissue will not be properly characterized. To account for variations in both diseased and healthy tissues and relax the constraints of a fixed tissue model, a model was recently proposed using the Bayesian framework in which signal evolutions are fit to a larger dictionary with no prior assumption about how many or which tissue types may comprise the voxel signal [31]. In this method, the signal evolution is still modeled as a weighted sum of dictionary elements as in equation (1), however, a larger subset of tissue types is used with the assumption that many of the weights W_i should be zero, or in other words, that W_i should be a sparse vector,

$$s_i = DW_i \quad (4)$$

where D is the full MRF dictionary of simulated signal evolutions, and is of size t x n, where $n >> t$. This is, however, an underdetermined problem, and solving using linear least-squares will result in a weight vector W_i which is not sparse. To achieve the desired result, a sparsity-promoting prior is placed on W_i, guiding the algorithm to fit the signal evolution to the dictionary using only a few significant entries to represent the signal. The result of applying this model to a voxel signal evolution is a distribution of dictionary entries and corresponding weights that best describe the characteristics of the signal, and a voxel result is a matrix containing the T1, T2 pairs and corresponding weight values of the most significantly contributing dictionary entries.

An example of this method applied to a 3D MRF acquisition in an epilepsy patient is shown in Figure 4. The scatter plot shows Bayesian MRF results from four pixels indicated from a T1 map, one containing pure white matter (red), one containing pure gray matter (blue), one containing a mixture of white matter and gray matter (green) and one containing an epileptic lesion (black). The key advantage of using this Bayesian method is that the lesion cluster is not forced to fit to a fixed tissue model,

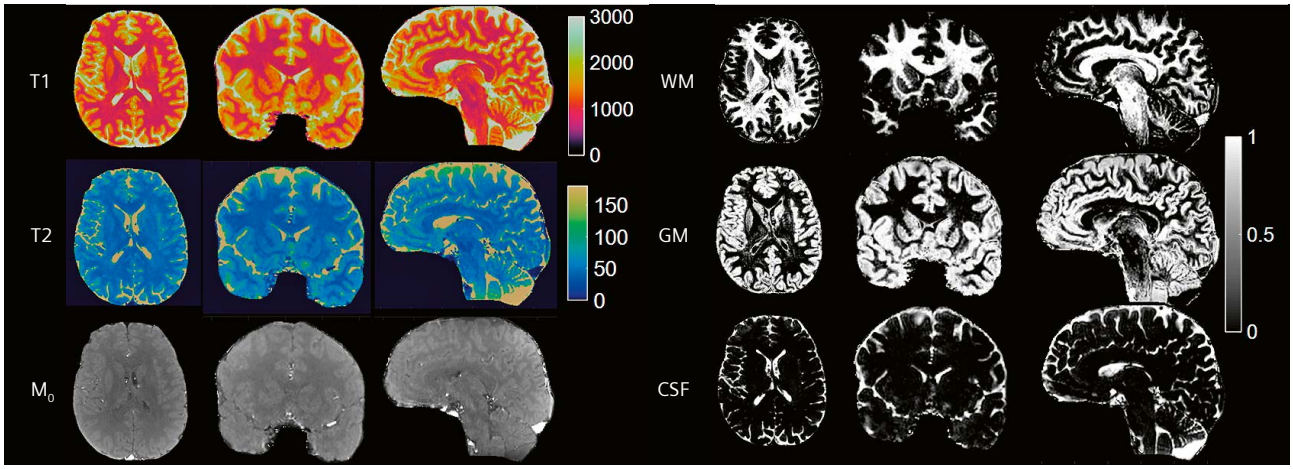

3 Six quantitative maps acquired from a single 3D MRF scan, providing co-registered 3D isotropic T1, T2, M_0 maps and GM, WM, CSF tissue fraction maps [30].

which may not include the relaxation properties of the lesion. The lesion is shown as a single cluster, which is different from those of two pure tissues (red and blue), while the PV pixel is identified by two separate green clusters, which are overlapped with the clusters from two pure tissues. This approach gives us a completely new tool to detect and characterize lesions.

The key feature of the Bayesian MRF method is that signal evolutions are not forced to fit a fixed model with predefined relaxation properties. However, this freedom results in distributions across voxels that may vary slightly, even within similar tissue structures. Summarizing the results is done most effectively by segmentation, using tissue fraction maps calculated from the Bayesian MRF results. To this end, voxel-wise results from the Bayesian method are combined across the full image or 3D volume and grouped using a Gaussian mixture model applied to the conglomerate T1, T2, and weight matrices. As there is no fixed tissue model in the Bayesian analysis, choosing a large enough number *K* of Gaussian distributions to represent the full range of possible tissue distributions is desirable. In a normal volunteer, one can assume fewer Gaussian distributions than in the case of disease. The mixture model allows for a probability to be associated to each point in T1, T2 space for each of the *K* Gaussian distributions. By using the Gaussian probability densities as a mask, tissue fraction maps can be calculated by multiplying the calculated weighted by the corresponding probabilities. These maps are normalized so that for each voxel, the fraction across each of the *k* classes is equal to one.

Potential clinical applications for neuroimaging

Epilepsy

Conventional MRI can be limited in its ability to recognize the existence and extent of subtle lesions, particularly focal cortical dysplasia (FCD). Up to 50% of potential epilepsy surgery candidates had a diagnosis

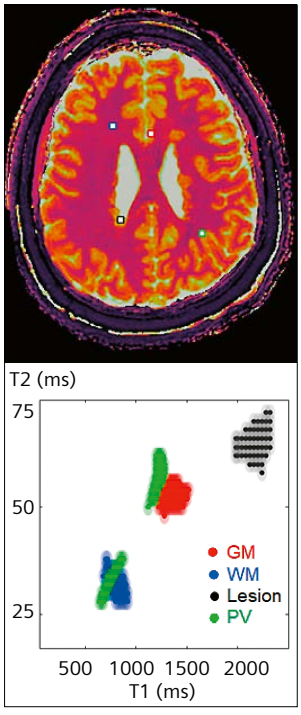

4 Example of Bayesian MRF results from a patient with right temporal-parietal epilepsy. Tissue compositions from four pixels located at healthy tissues (GM and WM), PV tissue at GM and WM boundary and epileptic nodule were analyzed. The results were able to separate lesion from healthy tissues, as well as PV effects.

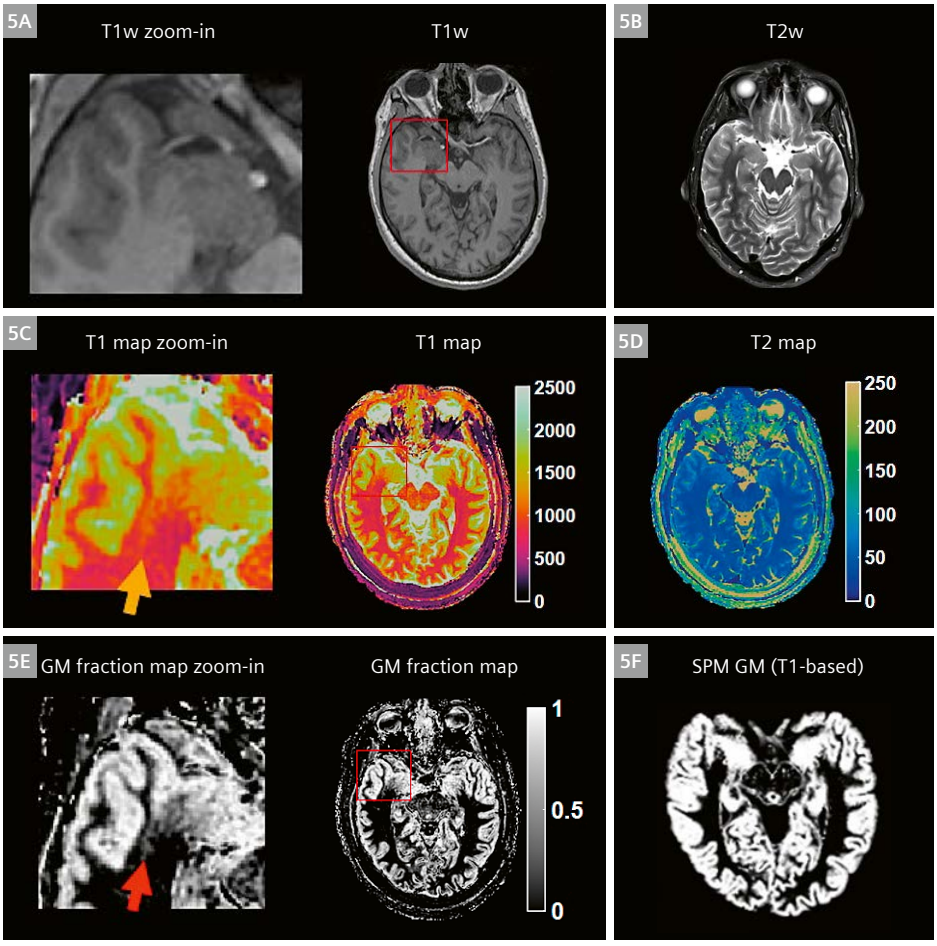

5 Patient with right temporal lobe epilepsy. **(5A, B)** T1w and T2w images from the clinical scans; **(5C, D)** T1 and T2 maps from the 3D MRF scan; **(5E, F)** GM fraction map from PV-MRF and T1w-based SPM segmentation. The potential epilepsy pathology (zoomed-in) identified from the MRF were not seen from the conventional MR scans [30].

of 'negative MRI', as there is no identifiable lesion to guide surgery. Our group recently demonstrated that 3D whole brain MRF and PV-MRF techniques can aid detection and characterization of lesions in epilepsy patients [30]. First, a fast and whole brain 3D MRF scan was applied to simultaneously quantify T1, T2, and proton density maps with 1.2 mm isotropic image resolution. The isotropic 3D maps allowed identification of lesions from multiple orientations and multiple tissue properties. Second, dictionary based PV-MRF [23] was applied to the same data to generate gray matter, white matter, and CSF maps. These maps could resolve multiple tissue components from a single voxel and additionally provide new contrasts along tissue boundaries. All available maps from a single scan are shown in Figure 3.

Figure 5 shows the MRF findings from a patient with right temporal lobe epilepsy. The clinical MRI showed that the right amygdala was enlarged with hyperintense FLAIR signal, with the right temporal lobe otherwise unremarkable by visual inspection (Figs. 5A, B). As shown in Figure 5C–E, MRF maps revealed a previously unseen signal abnormality 'tail' in addition to the amygdala hyperintensity. A subtle increase in the T1 value was seen on the T1 map (Fig. 5C) and increased gray matter fraction on the GM fraction map of the right superior temporal region (Fig. 5E), indicating potential abnormality. Figure 5E and 5F compare the GM fraction maps from MRF and from SPM segmentation of T1-weighted images. The GM map estimated from MRF not only identified the subtle tissue abnormality, but also showed wider variations of the gray matter fractions across the brain, which is believed to correspond to underlying cytostructure differences among different cortical regions. While this abnormality had no significant conspicuity on conventional MRI, the location of the abnormality was highly concordant with interictal and ictal EEG localization. Histopathology of the surgical specimen showed mild malformation of cortical development.

Figure 6 shows MRF and PV-MRF results from another patient with right temporo-parietal epilepsy, who had known bilateral periventricular heterotopias. As shown in Figure 6A and 6B, the nodules showed uniform signal intensity on clinical MRI scans as well as post-processing analysis using SPM segmentation of T1-weighted images. From Figure 6C and 6D, both the MRF T1 map and PV-MRF GM fraction maps showed increased values in the nodules at the right occipital horn. This distinct signal abnormality was not appreciable on the conventional MRI scans. The patient underwent invasive evaluation with stereotactic EEG (SEEG) targeting multiple brain regions. The nodules with abnormal signals shown by MRF and PV-MRF were consistent with the interictal SEEG findings and ictal onset of a typical seizure. Electrical stimulation of the electrodes at the right occipital horn produced habitual auras.

Brain development in early childhood

Chen et al. have recently applied MRF and dictionary based PV-MRF to characterize early brain developmental changes for healthy children from birth to five years old, who were enrolled in the UNC/UMN Baby Connectome Project [16]. In addition to T1 and T2 maps estimated from MRF scans, myelin water fraction (MWF) maps were estimated using dictionary based PV-MRF, by estimating tissue fractions from a three-compartment model including myelin water, intracellular/extracellular water, and free water. Representative T1, T2, and MWF maps from five subjects at different

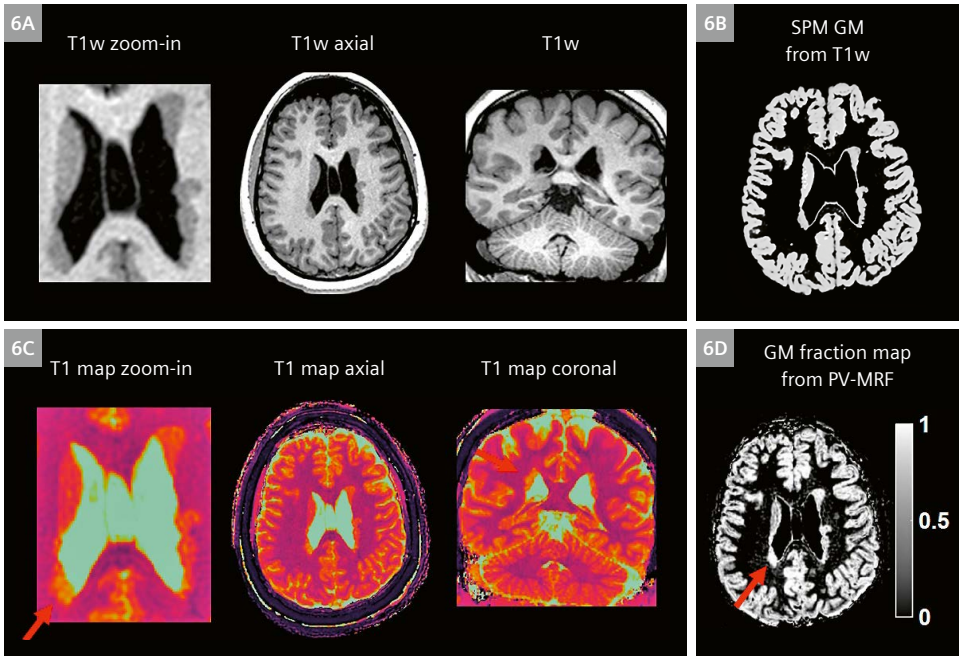

6 Patient with right temporo-parietal epilepsy. MRF was able to differentiate the active/epileptogenic heterotopic nodules from the non-active/non-epileptogenic ones **(6A)** Axial and coronal T1w image from the clinical scan. **(6B)** Corresponding T1 map from MRF. **(6C)** GM fraction map from T1w-based SPM segmentation. **(6D)** GM fraction map from PV-MRF [30].

ages are shown in Figure 7. Both T1 and T2 values decrease while MWF increases with age. Based on the results from 28 children, R1 (1/T1) and R2 (1/T2) showed a marked increase until approximately 20 months of age, followed by a slower increase for all WM regions. The MWF remained at a negligible level until about 6 months of age and gradually increased afterwards. In addition, significant differences in R1 and MWF trajectories were observed across different white matter region, and the spatial pattern for myelination during early brain development matches well to the previous findings obtained from post-mortem brain tissues [32].

Brain tumors

Depending on the stage, cancers originating or metastasized in the brain can be heterogeneous, containing regions of solid cellular neoplasms, edema, inflammation, cysts, and necrosis. However, conventional approaches using pseudoinverse calculations to invert partial volume models result in less accurate tissue fraction estimations as the PV model complexity increases. Moreover, these complex PV models can be difficult to establish, since unlike normal tissue segmentation or microstructure evaluation, the relaxation properties of heterogeneous tissue compartments cannot be easily determined for each subject or obtained from the literature. PV analysis in tumors therefore requires careful construction of a comprehensive partial volume model, which encompasses multiple types of diseased tissue.

In heterogeneous tissues such as the region in and around the brain tumor, pure tissues may not occupy enough voxels for *k*-means clustering of mapped T1 and T2 values to identify unique tissues. Bayesian MRF analysis provides particular value in these scenarios. Figure 8 shows the results from three different slices of a patient diagnosed with a glioblastoma brain tumor (GBM). The patient gave written consent and was scanned with 3D-MRF FISP acquisition with image resolution of 1.2 x 1.2 x 3 mm^3. A Gaussian mixture model was applied to the Bayesian results, with $K = 14$ Gaussian distributions found. Shown in Figure 8 are the weight maps from 8 of these distributions, corresponding to (from left to right) white matter, two gray matter classes, CSF, and two clusters related to the tumor pathology. Remaining maps from the other eight tissue distributions correspond to other tissues, such as fat and bone surrounding the brain, or may have very small weights in comparison to the six shown.

Bayesian MRF and dictionary-based PV-MRF work hand-in-hand. In place of or in addition to using *k*-means clustering of T1 and T2 times, Bayesian MRF can help establish the relaxation times of healthy and diseased tissues in and around the brain tumor. This information can

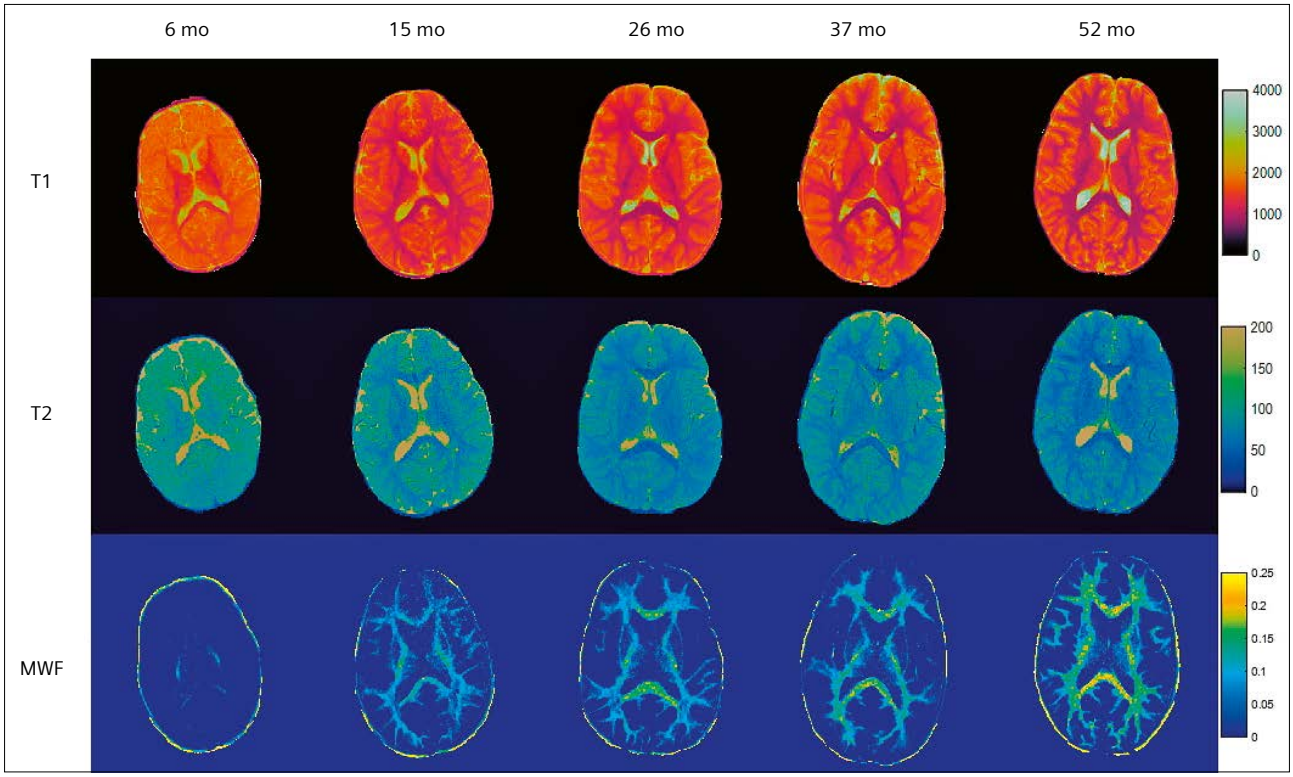

7 Representative T1, T2 and MWF maps from five subjects at different ages. Similar slice location that covers the genu and splenium of the corpus callosum was selected. Both T1 and T2 decrease while MWF increases with age [16].

then be used to construct D_{sub} and D_{pv} for dictionary-based PV-MRF for segmentation and estimation of diseased tissue fractions. Figure 9 shows an example of tissue segmentation and partial volume estimation using dictionary-based PV-MRF [23] in a patient with a small-cell lung cancer metastasis in the brain, scanned with 3D MRF on a 3T MAGNETOM Prisma system. Clinically-acquired FLAIR and contrast-enhanced T1-weighted images show an enhancing tumor with cystic and necrotic components, and surrounding edema. MRF provides 3D maps of T1, T2, and M_0, from which distinct relaxation times for normal appearing brain tissues (fat, GM, WM, CSF) and diseased tissues could be identified by *k*-means clustering and confirmed by Bayesian MRF analysis in these regions. An expanded partial volume dictionary containing all possible combinations of six tissue components allows for segmentation and volume fraction estimation of normal as well as tumor tissues, including solid enhancing components, cystic components, and the surrounding edema. Note that dictionary-based PV-MRF provides quantitative maps of tissue volume

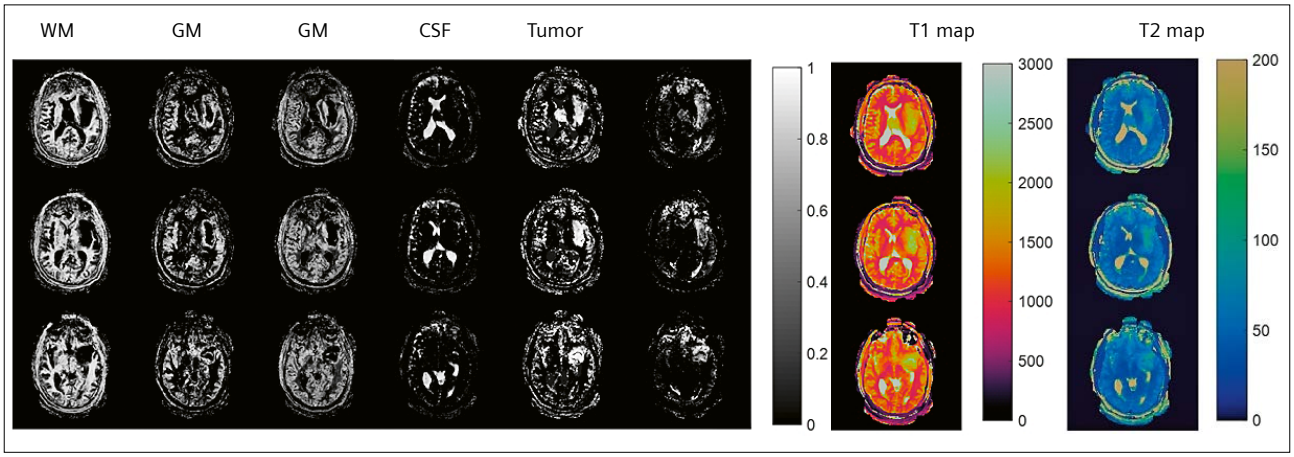

8 Six partial volume maps are displayed on the left for three different slices in a patient with glioblastoma. Since the method makes no assumptions about which type of tissues are present, the resulting cluster labels are assigned as a final step. From left to right are weight maps for white matter, gray matter, a mix of gray matter and wm/gm partial volume, csf, solid tumor, and some peritumoral white matter. Note there are two lesions. On the far right are the corresponding T1 and T2 maps for each slice [33].

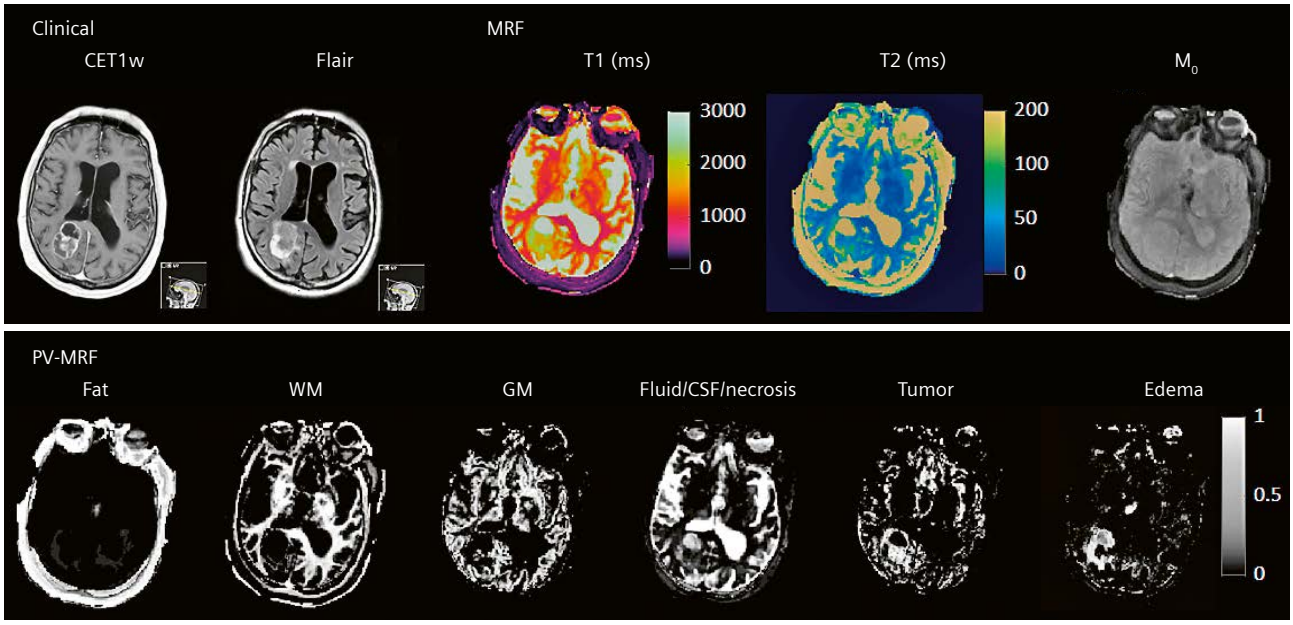

9 Segmentation of a small-cell lung cancer metastasis in the brain using dictionary-based PV-MRF and 3D MRF acquisition. Dictionary matching enables the use of expanded multi-component models and segmentation of more tissue types compared to conventional partial volume analysis [23].

fractions, as shown in Figure 9 [23], whereas the Bayesian MRF visualization illustrated in Figure 8 visualizes weighted probabilities that each voxel corresponds to the particular tissue class.

Improved synthetic imaging

It is sometimes the case that certain contrast weightings are unavailable for diagnosis, due to poor patient compliance or scan time limitations. Quantitative mapping of underlying tissue MR properties with methods like MRF opens the possibility for synthetic MRI. Rather than scanning the patient again to acquire new images with the desired contrast, these images can be synthesized or calculated off-line by applying known equations to the underlying tissue properties T1, T2, and M_0, mapped with quantitative MRI. With this approach, image contrast can be optimized for discrimination of lesions without the associated lengthy scan time. Synthetic imaging can also be a useful aid in the transition between interpreting multiple weighted-contrast images, which is currently standard clinical practice, and quantitative maps.

While typical T1- and T2-weighted images are straightforward to calculate, synthetic MRI of widely used sophisticated contrast weightings such as fluid attenuated inversion recovery (FLAIR) still pose a challenge due to partial volume effects. This challenge is illustrated in Figure 10. In a FLAIR sequence, the image is acquired when the magnetization of the fluid is nulled and does not contribute to the voxel signal. However, in voxels containing partial volumes mapped T1 and T2 values will be influenced by the long relaxation times associated with fluids. A synthetic FLAIR image calculated from mapped MRF relaxation times therefore will have poor contrast in the sulci, where partial volumes of fluid contaminate the mapped relaxation times.

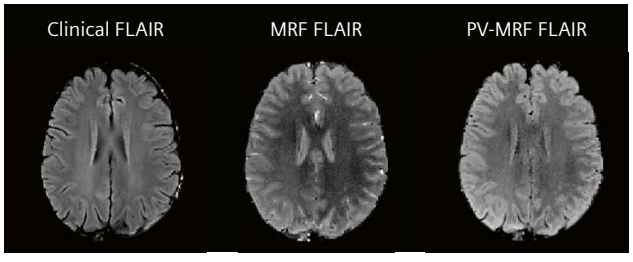

10 Improved synthetic MRI with PV-MRF. In a fluid attenuated inversion recovery (FLAIR) sequence, the magnetization of fluid is nulled and does not contribute signal in the acquired image (left). Synthetic FLAIR images calculated from MRF parameter maps exhibit distorted contrast in regions containing partial volumes of CSF such as the sulci, since the relaxation times in these voxels reflect contributions from fluid. Estimation of fluid fractions by PV-MRF and removal of the fractional fluid contribution to the voxel signal evolution allows for more accurate estimation of relaxation times in these partial volume voxels, enabling improved contrast in the synthetic FLAIR images [34].

Here again the uniqueness of MRF signal evolutions provides an advantage: not only can fluid partial volumes in each voxel be quantified with PV-MRF, the corresponding contribution of fluid signals can also be subtracted from the measured voxel signal. The remaining voxel signal, reflecting the signal evolutions of the remaining non-fluid tissues, can be matched to the MRF dictionary again and the resulting T1 and T2 maps can be used to calculate the synthetic FLAIR image. This approach improves the contrast of the synthetic FLAIR by effectively "nulling" the partial volume contribution of fluid in each voxel in post-processing [34].

Conclusion

MRF allows for fast, robust, simultaneous quantification of multiple tissue properties. Moreover, the unique signal shapes generated by the pseudorandom MRF sequence allow for additional insight into the multi-component contributions to the voxel signal evolution. Using dictionary-based PV-MRF, partial volumes of healthy and diseased tissues and microstructures can be robustly segmented and estimated. Properties of component tissues, including diseased tissues in tumors, can be determined without prior knowledge by *k*-means clustering of quantitative MRF results or through sophisticated Bayesian analysis of sub-voxel compositions. In combination, MRF, Bayesian MRF, and PV-MRF can provide new, clinically-relevant information about subtle tissue changes which may not be apparent on conventional weighted MR images.

[1] *Work in progress: the application is currently under development and is not for sale in the U.S. and in other countries. Its future availability cannot be ensured.*

References

1 Warfield, S. K. et al. Automated segmentation of multiple sclerosis lesion subtypes with multichannel MRI. Neuroimage 32, 1205–1215 (2006).
2 Pundik, S., Scoco, A., Skelly, M., McCabe, J. P. & Daly, J. J. Greater Cortical Thickness Is Associated With Enhanced Sensory Function After Arm Rehabilitation in Chronic Stroke. Neurorehabil. Neural Repair (2018).
3 Busch, V., Gaser, C. & Busch, V. Changes in grey matter induced by training Newly honed juggling skills show up as a transient feature on a brain-imaging scan. Nature 427, 311–312 (2004).
4 Barnes, J., Ourselin, S. & Fox, N. C. Clinical application of measurement of hippocampal atrophy in degenerative dementias. Hippocampus 19, 510–516 (2009).
5 Adler, S. et al. Towards in vivo focal cortical dysplasia phenotyping using quantitative MRI. NeuroImage Clin. 15, 95–105 (2017).
6 Hong, S. J., Bernhardt, B. C., Schrader, D. S., Bernasconi, N. & Bernasconi, A. Whole-brain MRI phenotyping in dysplasia-related frontal lobe epilepsy. Neurology 86, 643–650 (2016).

7 Li, N. et al. Optimization and comparative evaluation of nonlinear deformation algorithms for atlas-based segmentation of DBS target nuclei. Neuroimage 184, 586–598 (2018).
8 Choi, H. S., Haynor, D. R. & Kim, Y. Partial volume tissue classification of multichannel magnetic resonance images-a mixel model. IEEE Trans. Med. Imaging 10, 395–407 (1991).
9 Alfano, B. et al. Unsupervised, automated segmentation of the normal brain using a multispectral relaxometric magnetic resonance approach. Magn. Reson. Med. 37, 84–93 (1997).
10 West, J., Warntjes, J. B. M. & Lundberg, P. Novel whole brain segmentation and volume estimation using quantitative MRI. Eur. Radiol. 22, 998–1007 (2012).
11 Reeder, S. B., Cruite, I., Hamilton, G. & Sirlin, C. B. Quantitative Assessment of Liver Fat with Magnetic Resonance Imaging and Spectroscopy. J. Magn. Reson. Imaging (2011).
12 Huppertz, H. J. et al. Voxel-based 3D MRI analysis helps to detect subtle forms of subcortical band heterotopia. Epilepsia 49, 772–785 (2008).
13 Wang, I. & Alexopoulos, A. MRI postprocessing in presurgical evaluation. Curr. Opin. Neurol. 29, 168–174 (2016).
14 Whittall, K. P. et al. In Vivo Measurement of T2 Distributions and Water Contents in Normal Human Brain. Magn. Reson. Med. 37, 34–43 (1997).
15 Guttmann, C. R. G. et al. White matter changes with normal aging. Neurology 42, 5–5 (1998).
16 Chen, Y. et al. MR Fingerprinting enables quantitative measures of brain tissue relaxation times and myelin water fraction in early brain development. Neuroimage 186, 782–793 (2019). 186, 782-793 (2019).
17 Monohan, E. et al. Measuring longitudinal myelin water fraction in new multiple sclerosis lesions. NeuroImage Clin. 9, 369–375 (2015).
18 Flynn, S. W. et al. Abnormalities of myelination in schizophrenia detected in vivo with MRI and post-mortem with analysis of oligodendrocyte proteins. Mol. Psychiatry 8, 811–820 (2003).
19 Honer, W. G. et al. 48 echo T2 myelin imaging of white matter in first-episode schizophrenia: Evidence for aberrant myelination. NeuroImage Clin. 6, 408–414 (2014).
20 Shattuck, D. W., Sandor-Leahy, S. R., Schaper, K. A., Rottenberg, D. A. & Leahy, R. M. Magnetic Resonance Image Tissue Classification Using a Partial Volume Model. Neuroimage 13, 856–876 (2001).
21 Bonar, D. C., Schaper, K. A., Anderson, J. R., Rottenberg, D. A. & Strother, S. C. Graphical analysis of MR feature space for measurement of CSF, gray-matter, and white-matter volumes. J. Comput. Assist. Tomogr. 17, 461–70
22 Shin, W. et al. Automated brain tissue segmentation based on fractional signal mapping from inversion recovery Look-Locker acquisition. Neuroimage 52, 1347–1354 (2010).
23 Deshmane, A. et al. Partial volume mapping using magnetic resonance fingerprinting. NMR Biomed. (2019). doi:10.1002/nbm.4082
24 Liao, C. et al. Detection of Lesions in Mesial Temporal Lobe Epilepsy by Using MR Fingerprinting. Radiology 288, 804–812 (2018).
25 Ma, D. et al. Slice profile and B1 corrections in 2D magnetic resonance fingerprinting. Magn. Reson. Med. 78, 1781–1789 (2017).
26 Buonincontri, G. & Sawiak, S. J. MR fingerprinting with simultaneous B1 estimation. Magn. Reson. Med. 76, 1127–1135 (2016).
27 Cloos, M. A. et al. Multiparametric imaging with heterogeneous radiofrequency field: Additional material. Nat. Commun. 7, (2016).
28 Körzdörfer, G. et al. Magnetic resonance field fingerprinting. Magn. Reson. Med. 81, 2347–2359 (2019).
29 Jiang, Y., Ma, D., Seiberlich, N., Gulani, V. & Griswold, M. a. MR fingerprinting using fast imaging with steady state precession (FISP) with spiral readout. Magn. Reson. Med. (2014).
30 Ma, D. et al. Development of high-resolution 3D MR fingerprinting for detection and characterization of epileptic lesions. J. Magn. Reson. Imaging 1–14 (2018). doi:10.1002/jmri.26319
31 McGivney, D. et al. Bayesian estimation of multicomponent relaxation parameters in magnetic resonance fingerprinting. Magn. Reson. Med. 80, 159-170 (2018).
32 Hertz-Pannier, L. et al. The early development of brain white matter: A review of imaging studies in fetuses, newborns, and infants. Neuroscience 276, 48–71 (2014).
33 McGivney D., Jiang Y, Ma D, Badve C., Gulani V., Griswold M. Segmentation of brain tissues using a Bayesian estimation of multicomponent relaxation values in magnetic resonance fingerprinting. Proc. Intl. Soc. Mag. Reson. Med. 26 (2018) No. 1022.
34 Deshmane, A. et al. Accurate Synthetic FLAIR Images Using Partial Volume Corrected MR Fingerprinting. in Proc.Intl.Soc.Mag.Reson.Med (2016).

Contact

Dan Ma
Department of Radiology
Case Western Reserve University,
School of Medicine
11100 Euclid Ave
Cleveland, OH 44106
USA
Tel.: +1 216-844-3916
dxm302@case.edu

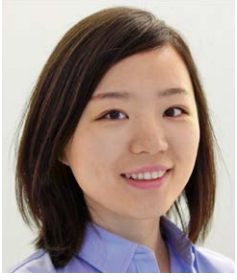

Unprecedented Echo Times for Diffusion MRI Using Connectom Gradients, Spiral Readouts and Field Monitoring

Lars Mueller; Chantal MW Tax; Derek K Jones

Cardiff University Brain Research Imaging Centre (CUBRIC), Cardiff, UK

Summary

- Using a unique combination of the ultra-strong (300 mT/m) magnetic field gradients provided on the MAGNETOM Connectom[1] scanner, a diffusion-weighted MRI sequence with spiral EPI read-out, and a field camera to monitor and correct for deviations from prescribed *k*-space trajectories, we present high quality images with unprecedented short echo times for diffusion MRI in the living human brain
- For b = 1000 s/mm^2, the echo time is 21.7 ms
- These short echo times confer two advantages:
  - Enhanced signal to noise ratio (SNR) due to reduced T2-weighted signal loss (which makes measurement of tissue with short T2, e.g., muscle, more robust)
  - Sensitivity to species previously 'invisible' in diffusion MRI, e.g., the myelin water, opening up the possibility of measuring their diffusion properties for the first time.
- In summary, this unique combination of hardware, sequence, field monitoring and reconstruction opens up a new window into tissue microstructural properties in the living human brain.

[1] *MAGNETOM Connectom is ongoing research. All data shown are acquired using a non-commercial system under institutional review board permission. Siemens does not intend to commercialize the system.*

The challenge of diffusion MRI

The introduction of diffusion-weighted imaging [3] into the armoury of quantitative MRI techniques, has revolutionised our understanding of tissue properties *in vivo* across a wide range of organs. Characterizing the *anisotropic* diffusion of water in tissue, allows properties such as density, shape, size, and orientation of different tissue compartments to be inferred [e.g., 1, 2, 6, 9].

A successful diffusion MRI sequence has two key components:

1. The application of sufficient diffusion-weighting (through the application of magnetic field gradients for a finite duration) that makes the sequence sensitive to **microscopic** displacements.
2. A very rapid read-out of the image, to effectively 'freeze' the physiological motion (**macroscopic** displacements) that would otherwise corrupt the diffusion-weighted image.

Regarding the first point, the field of diffusion MRI has been a key driver in the development of gradient technologies, providing higher and higher gradient amplitudes [10, 19]. The amount of diffusion weighting depends on the **product** of the amplitude and duration of the gradient pulses, and thus the stronger the gradient, the less time it needs to be applied to achieve the same diffusion-weighting. Regarding the second point, by far the most prevalent read-out is echo planar imaging (EPI), introduced into diffusion MRI by Turner et al. [21] (Fig. 1).

Thus, both stronger gradients and echo-planar readouts have improved the robustness and utility of diffusion

MRI since its initial inception. However, both of these pulse components take time to play out. In the most commonly-used pulse sequence, the diffusion-weighted **spin echo**, during these times the signal is constantly being lost due to an additional mechanism, i.e., transverse (T2) relaxation. Not only does this reduce the signal to noise ratio (SNR), but it also means that the signal from species with shorter T2 will contribute much less than species with longer T2.

The motivation for myelin

In the brain, the white matter fibres form the 'motorways' that transport packets of information between different brain regions. The white matter derives its name from the color of the myelin, a fatty layer that wraps around the axons, serving multiple functions (including speeding conduction velocity and reducing the energy requirements for signal transmission). The myelin is a key component of the white matter, and deficits in myelin have been implicated in a wide range of neurological, psychiatric, and developmental disorders, and it has thus been the focus of investigation and key-driver of a number of methodological advances in MRI, including multi-component relaxometry (looking at the water trapped between the layers of myelin, i.e. the 'myelin water' [13, 14, 22]), magnetization transfer imaging (looking at the macromolecules in the myelin *per se* [24], and quantitative susceptibility imaging [7]. However, myelin is rarely considered in diffusion MRI experiments [8]. The ultra-short T2 of the macromolecules themselves is too short (80 ms) to contribute to the spin echo signal, but also the myelin water (T2 ≤ 20 ms) for the echo times **typically** used in a diffusion-weighted spin echo sequence (TE ~80 ms), contributes around 2% of the signal (Fig. 2). Therefore, the contribution of myelin to the diffusion MRI signal in most human MRI experiments is effectively negligible.

If, however, we were able to **shorten** the echo times of the diffusion-weighted experiment to the point that the contribution from the myelin-water becomes non-negligible, the ability to quantify microstructural properties of the myelin space could offer new windows into the pathophysiology of a number of neurological and psychiatric diseases, provide earlier, differential diagnoses, and provide earlier access to treatment.

This article explores how we can achieve those shorter echo times in diffusion MRI, through manipulation of the two key components:

1. the gradient amplitude; and
2. the imaging read-out strategy.

We consider the challenges in implementation of this new approach, and the solutions we have developed to ameliorate them.

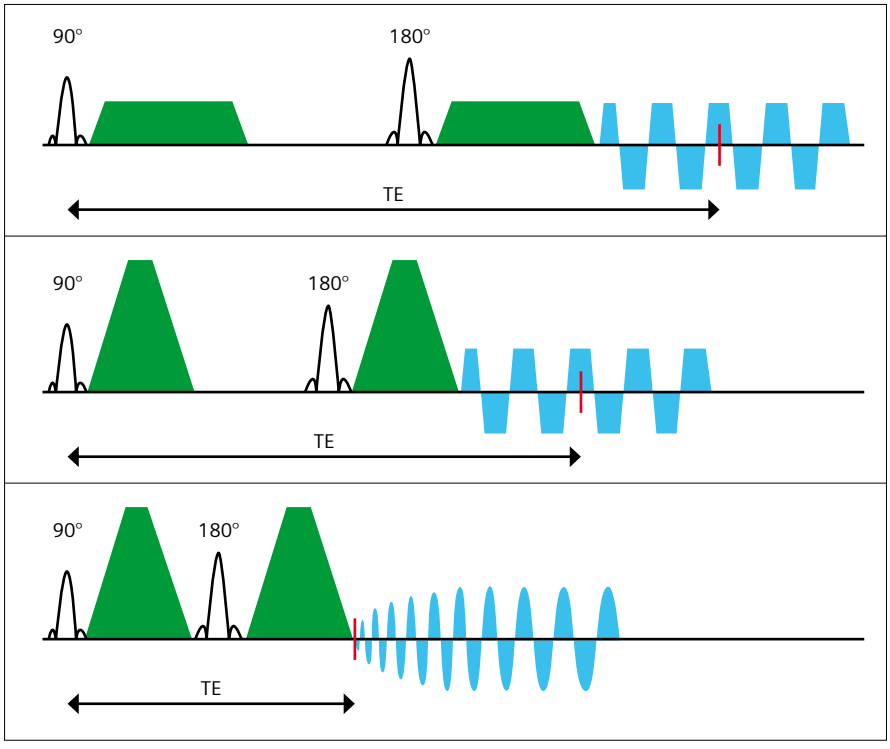

1 Sequence diagrams for different diffusion sequences. The diffusion encoding gradients are shown in green, the readout gradients are blue and the time of the spin echo is marked in red. Ultra-strong gradients and spiral readout are both needed to achieve the shortest possible echo times (TE). Top: Diffusion weighted spin echo (DWSE) sequence with echoplanar imaging (EPI) readout with normal gradient amplitude. Middle: DWSE-EPI with ultra-strong gradients. Bottom: DWSE sequence with ultra-strong gradients and spiral readout.

1. Stronger gradients to reduce the time for diffusion-encoding

The key component that reduces the diffusion-encoding time is an ultra-strong gradient system that enables stronger diffusion weightings per unit time compared to conventional gradient systems. In a typical Stejskal-Tanner experiment (Fig. 1), the amount of diffusion-weighting is determined by two factors: First, the gradient strength and duration of the diffusion-pulse (which can be expressed by q, where $q = \gamma G\delta$); and second, the duration between the diffusion-pulses during which molecular displacements take place (or the diffusion time, which can be expressed by τ, where $\tau = (\Delta - \delta/3)$). The amount of diffusion-weighting in an experiment can then be summarised by the b-value $b = q^2\tau = \gamma^2 G^2\delta^2(\Delta - \delta/3)$ [15]. From this equation, it becomes apparent that increasing the gradient-strength allows a much wider range of experiments, in that:

1. for a given b-value, a higher gradient strength allows to reduce the pulse-duration δ and the time between pulses Δ, overall shortening the time needed for diffusion-encoding. The reduction of the shortest possible TE is a direct consequence of this, and thus a wider range of TEs can be achieved;
2. for a given pulse-duration δ, a higher gradient strength provides higher q-values, and thus a wider range of q-values can be sampled;
3. for a given diffusion time, a wider range of b-values can be maintained.

While this clearly outlines the advantages of ultra-strong gradients for the usage for diffusion MRI, there are also challenges; image artifacts can become amplified or

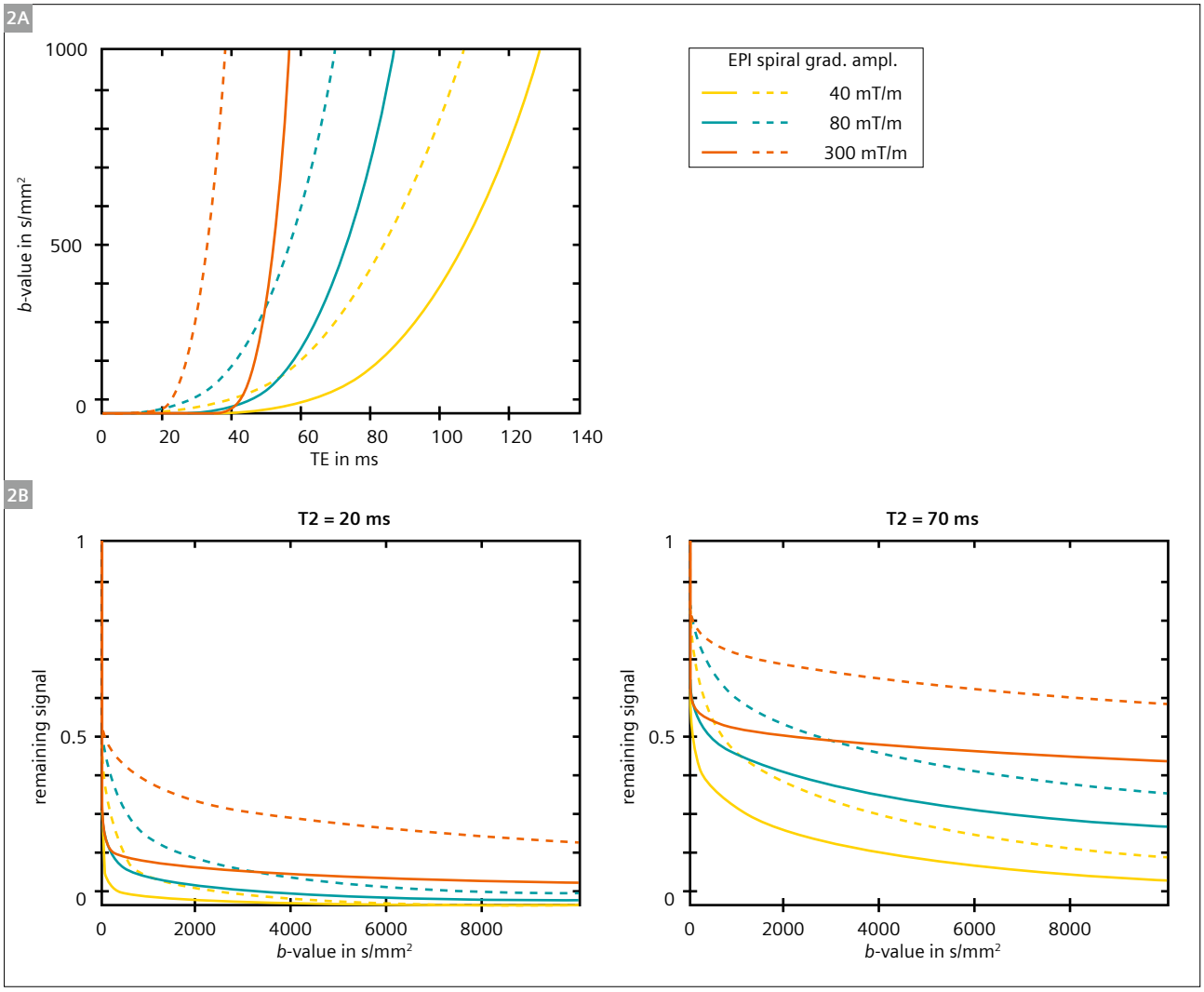

2 Relationships between b-value, echo time (TE), and T2-decay for spiral and EPI with different gradient amplitudes. For the EPI Grappa factor 2, partial fourier 6/8 and bandwidth per pixel of 2004 Hz (1536 Hz for 40 mT/m) were assumed at a resolution of 1.5 mm and FOV of 230 mm. **(2A)** Achievable b-value in given TE. **(2B)** Remaining normalized signal due to T2-decay at the shortest TE for the b-value.

additional artifacts can be observed compared to moderate gradient strengths [10, 19]. The stronger the gradient, the higher the amplitude of the long-time constant eddy currents. This will interfere with the readout gradients, which will lead to a deviation of the prescribed gradients for image readout and thus to image distortions. Achieving ultra-high gradient amplitudes furthermore comes at the cost of reducing the region over which the gradient system behaves linearly [10, 19]. In regions where the gradients exhibit nonlinearity, additional image distortions are to be expected [4, 11]. Geometrical distortions resulting from eddy currents and gradient nonlinearities are commonly corrected during post-processing; while eddy current-distortions can be ameliorated by registering the diffusion images non-rigidly, distortions from gradient nonlinearities require knowledge on the nonuniformities so that the images can be unwarped. It should be noted that eddy currents and gradient-nonlinearities distort the images in concert with B_0 inhomogeneity, and disentangling these effects is challenging.

Gradient nonlinearities additionally mean that the *b*-matrix as imposed by the diffusion gradients is spatially varying depending on the degree of nonlinearity. This means that, even when designed as such, *b*-vectors can become non-uniformly distributed over the hemisphere and *b*-values can deviate from the 'shell'. This can significantly impact diffusion measures when such deviations are not appropriately taken into account [4]. By estimating diffusion models or representations where the *b*-matrix associated with each DWI is adjusted voxel-wise, the adverse effects can be minimized at the cost of longer computation times. The situation is further exacerbated if the participant moves during the scan, as the *b*-value at a given position (after motion correction), is effectively changing over time, requiring *spatiotemporal tracking* of the *b*-matrix [17].

2. Reducing the time between diffusion encoding and *k*-space centre readout

In standard diffusion MRI, the image is read out with EPI, which traverses the *k*-space from one end to the other in parallel lines. Since the centre of *k*-space mostly determines the signal level in the final image, it is acquired at the time of the spin echo. Therefore, part of the *k*-space needs to be acquired beforehand, prolonging TE. Changing

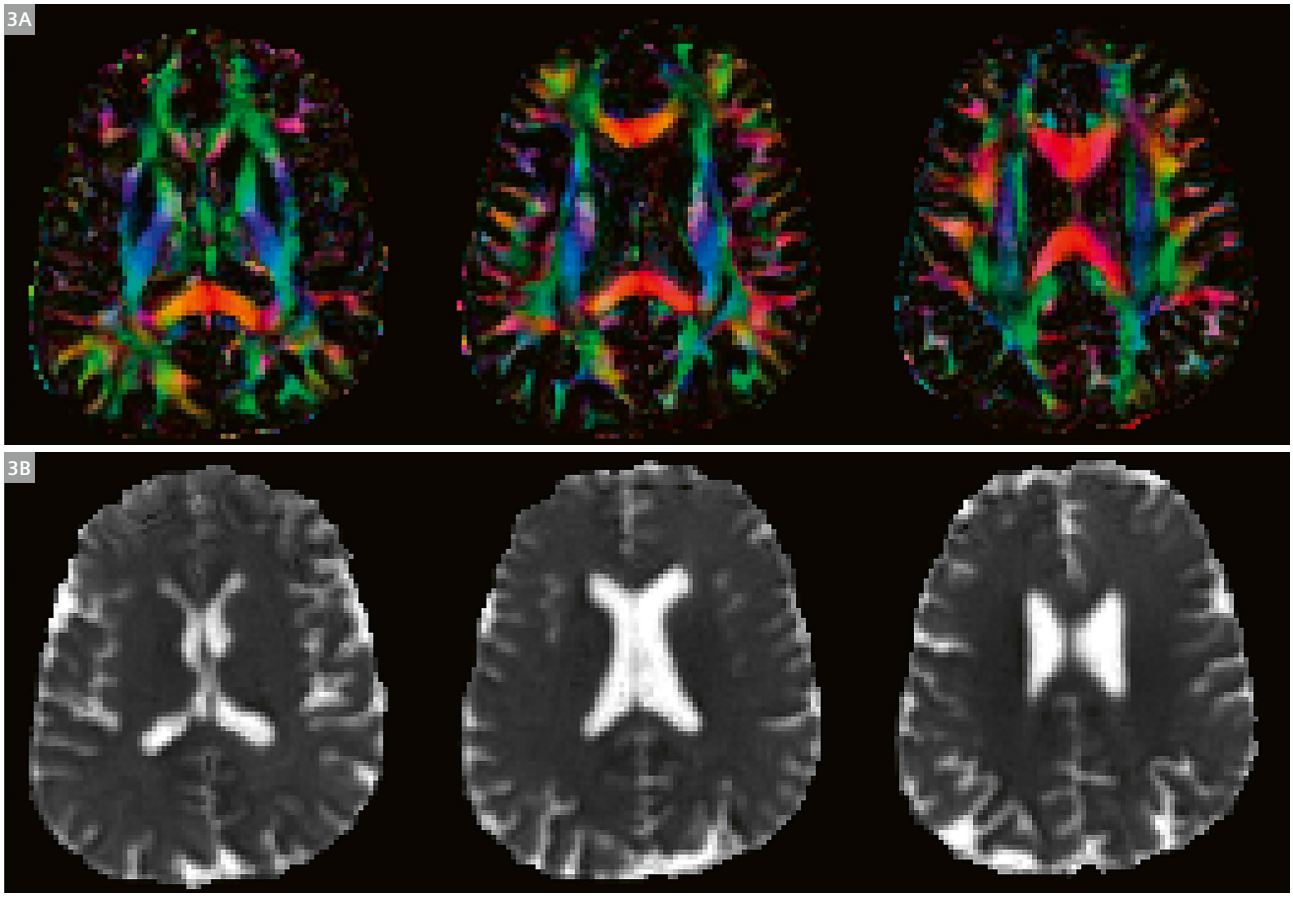

3 Direction-encoded fractional anisotropy **(3A)** and mean diffusivity **(3B)** calculated from diffusion data acquired with TE = 21 ms and b = 1000 s/mm².

the readout trajectory to a spiral starting at the centre negates this necessity of data acquisition before the spin echo. The use of a spiral readout allows shorter TE, compared to EPI, but introduces new difficulties in the imaging process. While the typical artefacts for an EPI readout (e.g., distortions due to eddy currents or B_0 inhomogeneities, ghosting due to gradient imperfections) can be handled in image processing, the artefacts with spiral readouts are often corrected during the image reconstruction. The main sources for artefacts in spiral imaging are:

1. B_0-inhomogeneities
2. T2* decay during the readout
3. Eddy currents and other gradient imperfections leading to a mismatch between prescribed and actual gradients.
4. Gradient nonlinearities (similar to EPI)

To measure the B_0 inhomogeneities, a B_0-map can be estimated by using a multi echo gradient echo sequence. This requires a few minutes additional acquisition time but is essential to reduce blurring. If an additional image with the same timing is acquired with the body coil, they can be combined to estimate the coil sensitivities necessary for a SENSE-type reconstruction. SENSE enables the undersampling of the spiral data and thus shorter readout times leading to less T2* blurring.

The gradients during the readout were measured with a spatio-temporal field monitoring approach [5] with a commercially available field camera. Knowledge of the B_0-map and the real *k*-space trajectory were combined with the knowledge of gradient nonlinearities in a single reconstruction pipeline [16], expanding on a previously introduced approach [23].

Unprecedented echo times and opportunites they present

Bringing together the ultra strong-gradients of the Connectom and a spiral readout with a proper reconstruction pipeline enables diffusion-weighted imaging at unprecedented TE *in vivo*. For b = 1000 s/mm^2, TE = 21.7 ms (see Fig. 3). This opens up new and exciting possibilities in diffusion imaging. Obviously, by reducing the (unwanted) T2-related signal decay during the diffusion encoding, the SNR is enhanced. This can be particularly important for species where diffusion MRI is challenging, e.g., in muscle, because the T2 is short.

Beyond the enhanced SNR, such a reduction in TE opens up new opportunities for exploration of brain microstructure and physiology. For example, with this short TE it might become feasible to measure the diffusion of myelin water [20]. Another promising new avenue is to explore the new contrast mechanism of diffusion-weighted fMRI, by looking into the TE dependence [18] or acquiring gradient echo and diffusion-weighted spin echo at the same TR with only tens of milliseconds between [18]. At present, we have only explored single shot spiral-EPI readouts. Future work will explore the combined use of multi-shot, navigated interleaved acquisitions [12], and external field monitoring to provide enhanced spatial resolution, while maintaining short echo times for diffusion MRI.

Overall objective	Shorten the echo time	
	Encoding	**Readout**
Objective	Shorten diffusion-encoding time	Shorten the time between diffusion encoding and the image readout of the center of *k*-space
Method	Increase the gradient strength	Spiral readout
Challenges	• Gradient nonlinearities and eddy currents cause geometrical distortions • Gradient nonlinearities cause spatiotemporally varying *b*-matrices	Interactions of readout gradients with • gradient nonlinearities and eddy-current induced fields cause geometrical distortions • mechanical vibrations cause signal loss and geometrical distortions
Solution	Image registration to correct for geometrical distortions. Compute spatiotemporally varying *b*-matrices from gradient nonlinearity information	Use field camera measurements to derive the actual readout trajectories

Table 1: Summary of key objectives, the methods, challenges, and solutions.

References

1 Assaf Y, Basser PJ. Composite hindered and restricted model of diffusion (CHARMED) MR imaging of the human brain. Neuroimage. 2005 Aug 1;27(1):48-58.
2 Assaf Y, Blumenfeld-Katzir T, Yovel Y, Basser PJ. AxCaliber: a method for measuring axon diameter distribution from diffusion MRI. Magn Reson Med. 2008 Jun;59(6):1347-54.
3 Le Bihan D, Breton E. Imagerie de diffusion in vivo par résonance magnétique nucléaire CR Acad. Sci. Paris T. 1985, 301 (Série II) (1985), pp. 1109-1112.
4 Bammer R, Markl M, Barnett A, Acar B, Alley MT, Pelc NJ, Glover GH, Moseley ME. Analysis and generalized correction of the effect of spatial gradient field distortions in diffusion-weighted imaging. Magn Reson Med. 2003 Sep;50(3):560-9.
5 Barmet C, De Zanche N, Pruessmann KP. Spatiotemporal magnetic field monitoring for MR. Magn Reson Med. 2008 Jul;60(1):187-97.
6 Basser PJ, Mattiello J, Le Bihan D. MR diffusion tensor spectroscopy and imaging. Biophys J. 1994 Jan;66(1):259-67.
7 Duyn JH, Schenck J. Contributions to magnetic susceptibility of brain tissue. NMR Biomed. 2017 Apr;30(4).
8 Harkins KD, Does MD. Simulations on the influence of myelin water in diffusion-weighted imaging. Phys Med Biol. 2016 Jul 7;61(13):4729-45.
9 Jespersen SN, Lundell H, Sønderby CK, Dyrby TB. Orientationally invariant metrics of apparent compartment eccentricity from double pulsed field gradient diffusion experiments. NMR Biomed. 2013 Dec;26(12):1647-62.
10 Jones DK, Alexander DC, Bowtell R, Cercignani M, Dell'Acqua F, McHugh DJ, Miller KL, Palombo M, Parker GJM, Rudrapatna US, Tax CMW. Microstructural imaging of the human brain with a 'super-scanner': 10 key advantages of ultra-strong gradients for diffusion MRI. Neuroimage. 2018 Nov 15;182:8-38.
11 Jovicich J, Czanner S, Greve D, Haley E, van der Kouwe A, Gollub R, Kennedy D, Schmitt F, Brown G, Macfall J, Fischl B, Dale A. Reliability in multi-site structural MRI studies: effects of gradient non-linearity correction on phantom and human data. Neuroimage. 2006 Apr 1;30(2):436-43.
12 Liu C, Bammer R, Kim DH, Moseley ME. Self-navigated interleaved spiral (SNAILS): application to high-resolution diffusion tensor imaging. Magn Reson Med. 2004 Dec;52(6):1388-96.
13 MacKay A, Whittall K, Adler J, Li D, Paty D, Graeb D. In vivo visualization of myelin water in brain by magnetic resonance. Magn Reson Med. 1994 Jun;31(6):673-7.
14 MacKay A, Laule C, Vavasour I, Bjarnason T, Kolind S, Mädler B. Insights into brain microstructure from the T2 distribution. Magn Reson Imaging. 2006 May;24(4):515-25.
15 Mattiello J, Basser PJ, Le Bihan D. The b matrix in diffusion tensor echo-planar imaging. Magn Reson Med. 1997 Feb;37(2):292-300.
16 Mueller L, Rudrapatna SU, Tax CMW, Wise RG, Jones DK. Diffusion MRI with b = 1000 s/mm² at TE < 22 ms using single-shot spiral readout and ultra-strong gradients: Implications for microstructure imaging. International Society for Magnetic Resonance in Medicine, Montreal, 2019.
17 Rudrapatna SU, Parker G, Roberts J, Jones DK. Strategies for correcting gradient-nonlinearity effects in ultra-high gradient Diffusion MRI experiments. International Society for Magnetic Resonance in Medicine, Paris, 2018.
18 Rudrapatna SU, Mueller L, Wright ME, Jones DK, Wise RG. A GRANDIOSE sequence to time-lock BOLD and diffusion-weighted fMRI contrasts in humans using ultra-strong gradients and spirals. International Society for Magnetic Resonance in Medicine, Montreal, 2019.
19 Setsompop K, Kimmlingen R, Eberlein E, Witzel T, Cohen-Adad J, McNab JA, Keil B, Tisdall MD, Hoecht P, Dietz P, Cauley SF, Tountcheva V, Matschl V, Lenz VH, Heberlein K, Potthast A, Thein H, Van Horn J, Toga A, Schmitt F, Lehne D, Rosen BR, Wedeen V, Wald LL. Pushing the limits of in vivo diffusion MRI for the Human Connectome Project. Neuroimage. 2013 Oct 15;80:220-33.
20 Tax CMW, Rudrapatna SU, Mueller L, Jones DK. Characterizing diffusion of myelin water in the living human brain using ultra-strong gradients and spiral readout. International Society for Magnetic Resonance in Medicine, Montreal, 2019.
21 Turner R, Le Bihan D, Maier J, Vavrek R, Hedges LK, Pekar J. Echo-planar imaging of intravoxel incoherent motion. Radiology. 1990 Nov;177(2):407-14.
22 Whittall KP, MacKay AL, Graeb DA, Nugent RA, Li DK, Paty DW. In vivo measurement of T2 distributions and water contents in normal human brain. Magn Reson Med. 1997 Jan;37(1):34-43.
23 Wilm BJ, Barmet C, Gross S, Kasper L, Vannesjo SJ, Haeberlin M, Dietrich BE, Brunner DO, Schmid T, Pruessmann KP. Single-shot spiral imaging enabled by an expanded encoding model: Demonstration in diffusion MRI. Magn Reson Med. 2017 Jan;77(1):83-91.
24 Wolff SD, Balaban RS. Magnetization transfer contrast (MTC) and tissue water proton relaxation in vivo. Magn Reson Med. 1989 Apr;10(1):135-44.


Lars Mueller


Chantal Tax


Derek Jones

Contact

Professor Derek Jones, BSc, MSc, PhD
Director of CUBRIC
Cardiff University Brain Research Imaging Centre
Outram Road, Block 2, Level 1
Maindy Road
Cardiff, CF24 4HQ
UK
Tel.: +44(0)29 2087 9412
jonesd27@cardiff.ac.uk

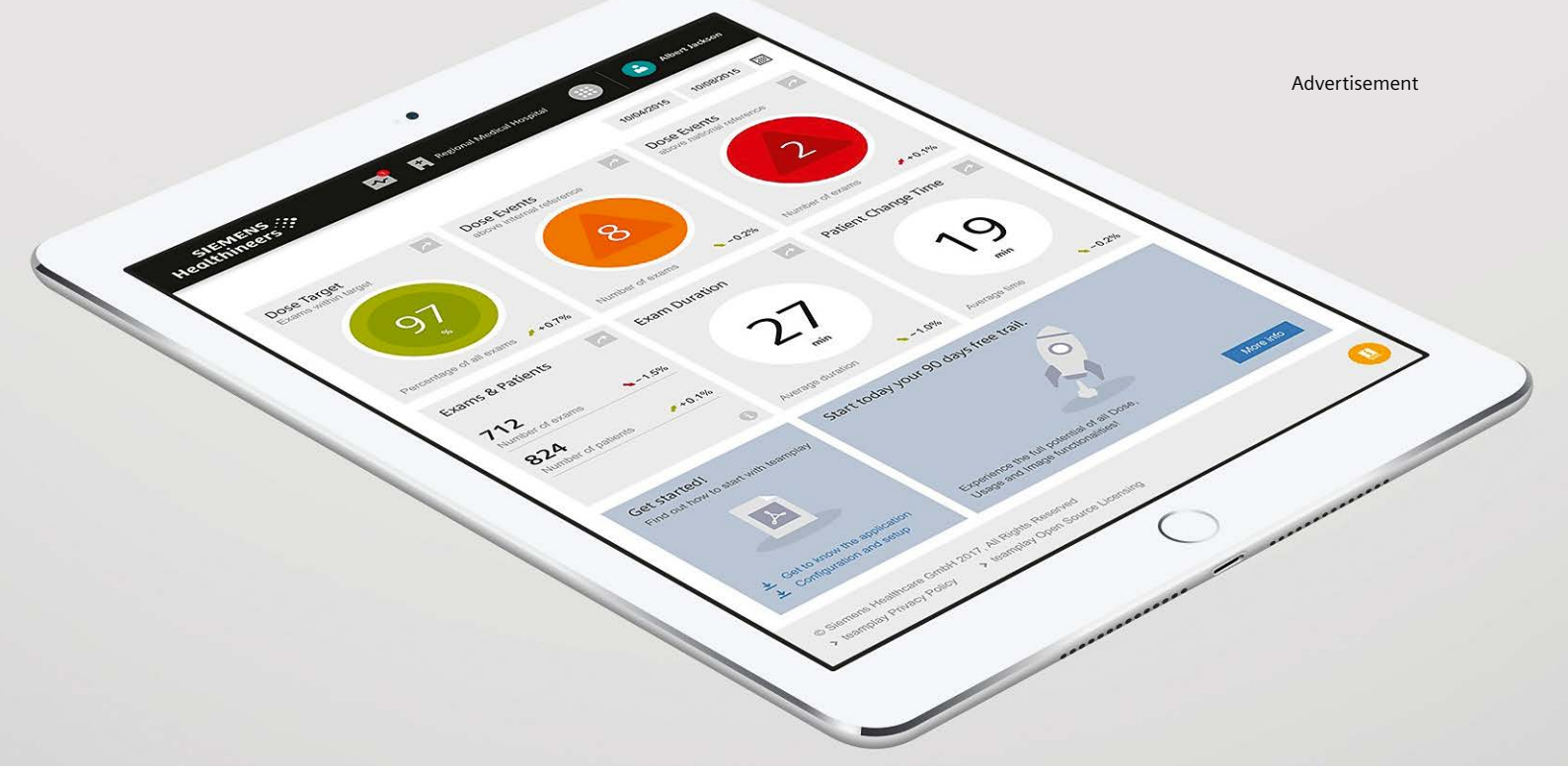

teamplay – Get the most out of your data in radiology and cardiology

healthcare.siemens.de/healthineers-digital-ecosystem/teamplay

To advance digitalization in healthcare, teamplay[1] is a departmental performance management solution that brings together healthcare professionals in a team effort. By connecting medical institutions and their imaging devices, teamplay apps aspire to create the biggest radiology and cardiology team in the world and provide its members with tools to tackle big data and the challenges of increasing cost pressure.

The cloud-based solution teamplay with its apps will help you make prompt and well-informed decisions by offering an intelligible overview of your performance data.

It monitors quantities such as imaging throughput or dose levels, utilization of staff, rooms and resources of your whole department down to every device and procedure, simplifying your reporting and showing you where workflows need adjustments. It links you to other users of teamplay and their data to offer comparable benchmarks[2] and an effortless exchange of images and reports with other healthcare providers.

[1] *Please check if teamplay is available in your country.*
[2] *Availability of Benchmarking option depends on a minimum number of considered subscribers to guarantee customer anonymity and data protection.*

SIEMENS Healthineers

Perfusion Imaging in Pediatric Brain Tumors: Pseudo-continuous Arterial Spin Labeling at Work

Giovanna Stefania Colafati[1]; Chiara Carducci[1]; Ioan Paul Voicu[1,2]; Antonio Napolitano[3]

[1]Department of Imaging, Neuroradiology Unit, Bambino Gesù Children's Hospital, Rome, Italy
[2]Department of Hematology/Oncology and Stem Cell Transplantation, Bambino Gesù Children's Hospital, IRCCS, Rome, Italy
[3]Medical Physics Unit, Risk Management Enterprise, Bambino Gesù Children's Hospital, Rome, Italy

Patient history

A 2-year-old male patient[1] with a history of gait and balance problems, associated with nausea, was admitted to our Emergency Department. A brain CT scan revealed a posterior fossa mass.

Patient underwent brain and spine MRI with MAGNETOM Skyra 3T (Siemens Healthcare, Erlangen, Germany) to characterize the lesion. The protocol in use in our institution includes conventional 2D and 3D sequences as well as advanced sequences acquired before and after endovenous injection of contrast medium, including the Pseudo-Continuous Arterial Spin Labeling (PCASL) sequence[2] (Fig. 1).

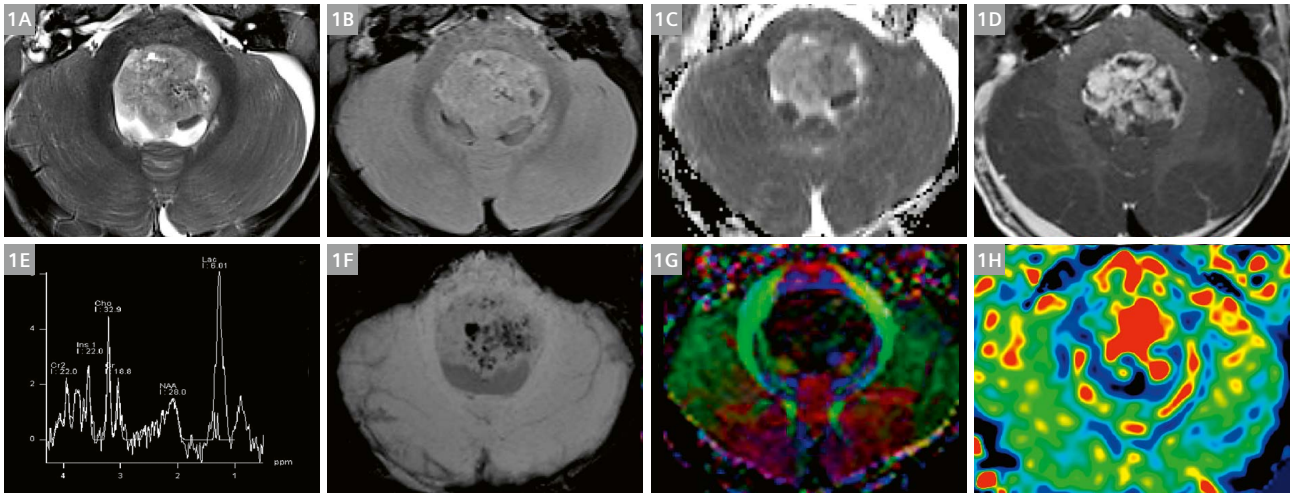

1 Multiparametric MR imaging of the lesion (**1A** axial T2-weighted; **1B** axial FLAIR; **1C** ADC map; **1D** axial high-resolution 3D T1-weighted Gradient Echo Sequence (MPRAGE) reconstruction; **1E** Spectroscopy; **1F** axial Susceptibility-Weighted Imaging (SWI); **1G** Fractional Anisotropy color map from Diffusion Tensor Imaging (DTI); **1H** Pseudo-continuous Arterial Spin Labeling (PCASL)[2] with a 3D background-suppressed Gradient and Spin-Echo (GRASE)). An intraventricular posterior fossa mass is seen (1A–D, 1F–H). The lesion presents a heterogeneous appearance due to solid-enhancing components (1A, B, D), necrotic portions (1D), regions with restricted diffusivity (1C) and low-signal foci consistent with calcifications (1F). Spectroscopy reveals increase of Choline, decrease in N-acetylaspartate, and a peak of lactate and lipids (1E). Low FA values are seen within the lesion (1G). PCASL cerebral blood flow (CBF) color maps (1H) show high CBF values within the lesion.

[1]MR scanning has not been established as safe for imaging fetuses and infants less than two years of age. The responsible physician must evaluate the benefits of the MR examination compared to those of other imaging procedures. Note: This disclaimer does not represent the opinion of the authors.
[2]WIP, the product is currently under development and is not for sale in the US and in other countries. Its future availability cannot be ensured.

PCASL sequence details

Pseudo-continuous labeling was performed with a prototype sequence[2] using a labeling period of 1500 ms, followed by a 1500-ms post-label delay (inversion time 3000 ms). Whole-brain images were obtained with a 3D background-suppressed Gradient and Spin-Echo (GRASE) sequence, with a TR of 4.6 s, turbo factor = 14 and EPI factor = 21. The sequence required a 6-minute acquisition time, including M0 used for Cerebral Blood Flow (CBF) quantification. Other ASL parameters were TE 15.6 ms; FOV 192 x 192 mm; matrix 64 x 64; measurements 6, and segments 6. For CBF quantification T1 blood and T1 tissue of 1650 ms and 1330 ms respectively was used. Circular 2D regions of interest (ROIs) with a mean area of 50 mm^2 were manually positioned in the most perfused area of the lesion. In addition to CBF, an rCBF was computed normalizing it with the mean value within another ROI in the normal-appearing gray matter of a cerebellar hemisphere.

Quantitative analysis revealed CBF and rCBF values of 58 mL/min/100 g and 1.9 respectively. The child underwent surgical resection of the lesion. Histology revealed an ependymoma grade 2, according to the 2016 World Health Organization classification.

Conclusion

MRI has a key role in examining pediatric brain tumors noninvasively. Both conventional and advanced sequences allow to obtain useful information at diagnosis for surgical planning, after surgery, for monitoring treatment response, and at further follow-up. In the pediatric population, among Perfusion-Weighted Imaging (PWI) techniques, a growing interest is currently emerging in arterial spin labeling (ASL) [1–3], a completely noninvasive and repeatable perfusion technique, that generates an image by magnetically "labeling" water molecules in arterial blood as an endogenous tracer. ASL can be generated using three main techniques of proton labeling: continuous labeling (CASL), pulsed labeling (PASL) and pseudo-continuous labeling (PCASL) [4]. A consensus paper from the ISMRM Perfusion Study Group and the European Consortium for ASL in Dementia recommends pseudo-continuous labeling, background suppression, a segmented three-dimensional readout without vascular crushing gradients, and calculation and presentation of both label/control difference images and cerebral blood flow in absolute units using a simplified model [5].

The evaluation of brain tumor perfusion with ASL may have a different impact in children compared to the adult population, due to their distinct clinical characteristics. Specifically, because of the advantage of higher CBF signal with a better signal-to-noise ratio in children compared to adults, it is possible to obtain robust quantitative perfusion data in this population without endovenous gadolinium administration. This could potentially avoid recently emerging concerns regarding gadolinium tissue accumulation [3]. Another potential advantage of ASL is that the sequence can be repeated in cases of failed sedation or patient motion [1].

Quantitative ASL-derived CBF and rCBF values have been proven useful in pediatric tumor evaluation and grading and quantitative CBF values have shown similar diagnostic accuracy to the most commonly used contrast-based cerebral blood volume, in differentiating between tumoral subtypes [3]. It has also been reported that ASL CBF values correlate significantly with micro-vascular density [1]. The quantitative CBF values we obtained in our patient are in line with literature.

ASL imaging is proving to be a useful tool from diagnosis to follow-up. It should be considered for implementation in the routine workup of pediatric patients with brain tumors.

References

1 Yeom KW, Mitchell LA, Lober RM et al. Arterial spin-labeled perfusion of pediatric brain tumors. AJNR Am J Neuroradiol 2014;35(2):395-401. doi: 10.3174/ajnr.A3670.

2 Dangouloff-Ros V, Deroulers C, Foissac F, et al. Arterial Spin Labeling to predict brain tumor grading in children: correlations between histopathologic vascular density and perfusion MR imaging. Radiology.2016 Nov;281(2):553-566. Epub 2016 Jun 3.

3 Morana G, Tortora D, Staglianò S et al. Pediatric astrocytic tumor grading: comparison between arterial spin labeling and dynamic susceptibility contrast MRI perfusion. Neuroradiology. 2018 Apr;60(4):437-446. doi: 10.1007/s00234-018-1992-6. Epub 2018 Feb 16.J.-C.

4 Ferré, E. Bannier, H. Raoult et al. Arterial spin labeling (ASL) perfusion: techniques and clinical use. Diagn Interv Imaging. 2013 Dec;94(12):1211-23. doi: 10.1016/j.diii.2013.06.010. Epub 2013 Jul 11.

5 Alsop DC, Detre JA, Golay X et al. Recommended implementation of arterial spin-labeled perfusion MRI for clinical applications: A consensus of the ISMRM perfusion study group and the European consortium for ASL in dementia. MagnReson Med. 2015 Jan;73(1):102-16. doi: 10.1002/mrm.25197. Epub 2014 Apr 8.

Contact

Dr. Giovanna Stefania Colafati
Bambino Gesù Children's Hospital
Department of Imaging
Neuroradiology Unit
Largo S. Onofrio 4
Rome, Italy (00165)
gstefania.colafati@opbg.net

3D ASL Perfusion: Biomarker of Activity in Japanese Encephalitis

Babu Peter Sathyanathan, M.D., D.N.B

Barnard Institute of Radiology, Madras Medical College, Chennai, India

Introduction

Japanese encephalitis (JE) is mosquito-borne flaviviral endemic encephalitis that is still a major health problem in some countries of the Far East and Southeast Asia. Most patients with JE present with flu-like symptoms, anorexia, nausea, vomiting, neck rigidity, hemiparesis, convulsions, and/or altered mentality. Children under 15 years of age are principally affected in endemic areas. The most consistent and characteristic MR imaging findings in JE are bilateral symmetric T2 hyperintensities in both thalami, with or without hemorrhage.

Case report

A 62-year-old male patient who had previously been healthy was admitted to the emergency department at Rajiv Gandhi Government General Hospital, Madras Medical College, Chennai, India. He was in a disoriented state and had been suffering from recurrent new onset seizures and fever for one day. On examination, the patient was initially restless but then became drowsy and stopped responding to oral commands. After admission, he suffered no seizures or fever episodes.

The patient was referred to the 3T MRI Centre at the Barnard Institute of Radiology for MRI of the brain. MR imaging was performed on a 3T MAGNETOM Skyra (Siemens Healthcare, Erlangen, Germany) on the second day of hospital admission. A standard institutional brain protocol (T1w sagittal, T2w axial, FLAIR coronal, DWI, MR angiogram) was performed, along with a contrast study and 3D ASL perfusion using PASL with a FAIR Q2TIPS method.

Radiological differential diagnosis for unilateral gyral edema with diffusion restriction and increased perfusion in ASL includes:

1. Encephalitis
2. Infarct

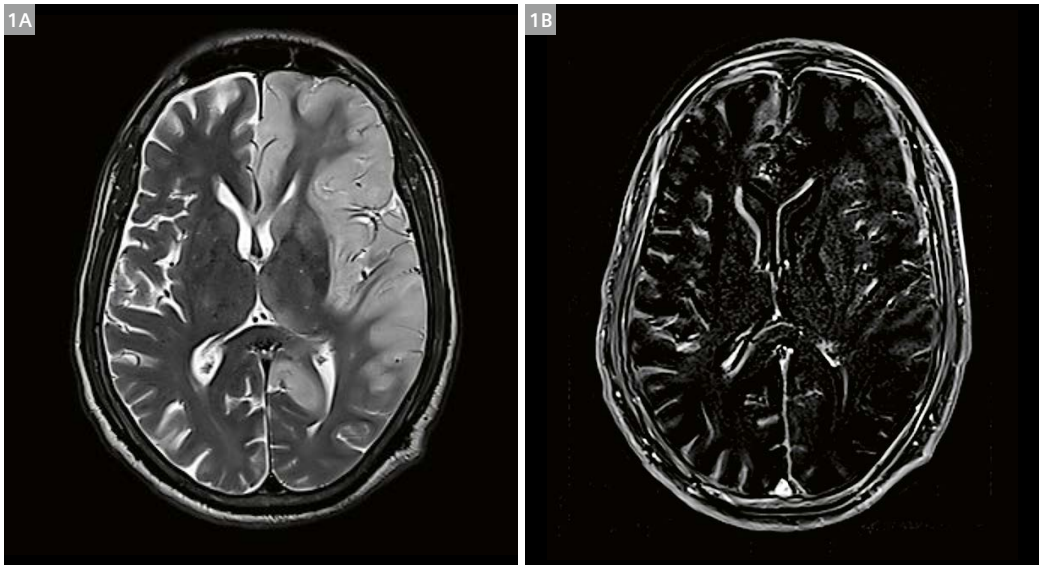

1 **(1A)** T2w shows significant gyral edema in the left frontoparieto-temporal region and hyperintensity in the left caudate, putamen, and thalamus.
(1B) T1 contrast subtracted image shows no abnormal enhancing areas in the brain parenchyma.

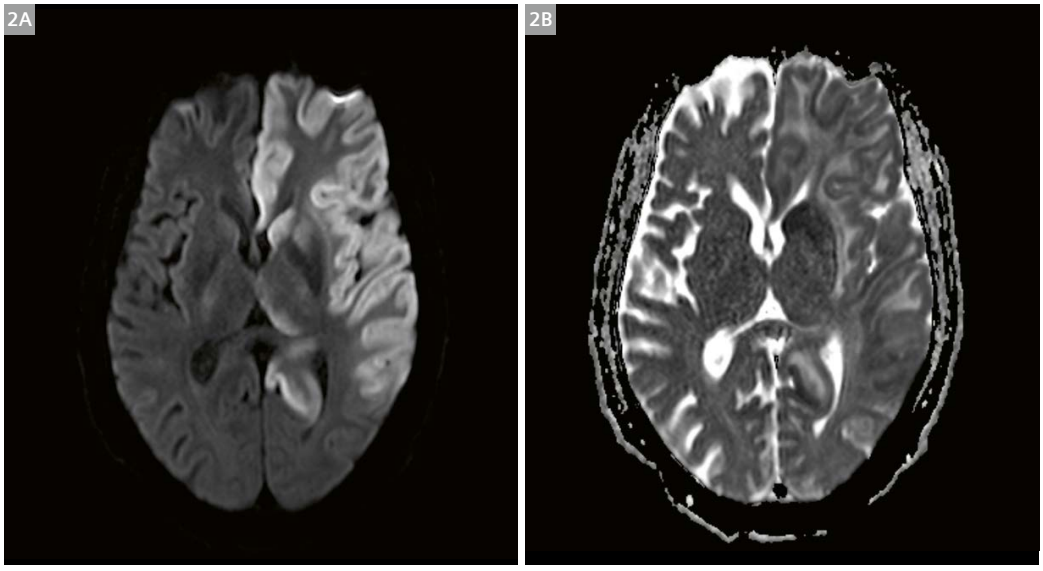

2 **(2A)** DWI; **(2B)** ADC shows diffusion restriction in the left fronto-parietotemporal region and left deep grey matter.

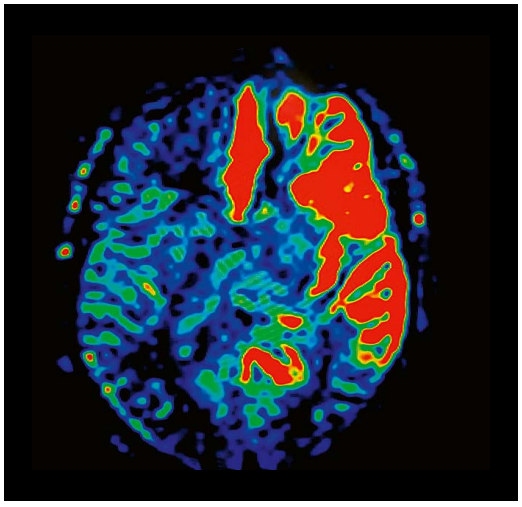

3 ASL image shows increased cerebral blood flow in the left frontoparietotemporal region

Age	Sex	No.	Hospital	Sample	Receiving date	Investigation	Result
62	Male	MS-5787	RGGGH	Blood & CSF	29.12.2016	HSV	negative
						CMV	negative
						VZV	equivocal
						HBSAg	negative
						EBV	negative
						JE serum	positive
						JE CSF	positive

Table 1: Serology report

Follow-up MRI

After treatment with empirical antibiotics, anticonvulsants, and anti-edema measures, the patient clinically improved and became conscious, oriented, and ambulant. Follow-up MRI was performed after three weeks.

Discussion

Although the present case concerns a 62-year-old man, JE is mostly found in children and young adults. Patients with JE are often asymptomatic in the beginning. After a few days, they typically present with non-specific febrile illness, coryza, diarrhea, and rigors. If patients progress to

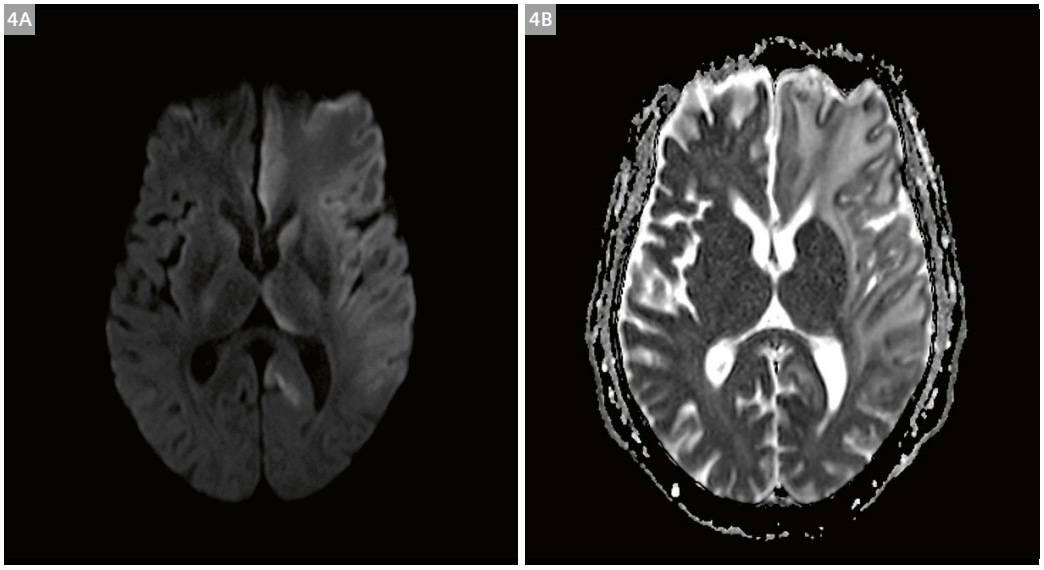

4 **(4A)** DWI; **(4B)** ADC shows normalization of ADC values with facilitated diffusion in the left fronto-parietotemporal region and deep grey matter.

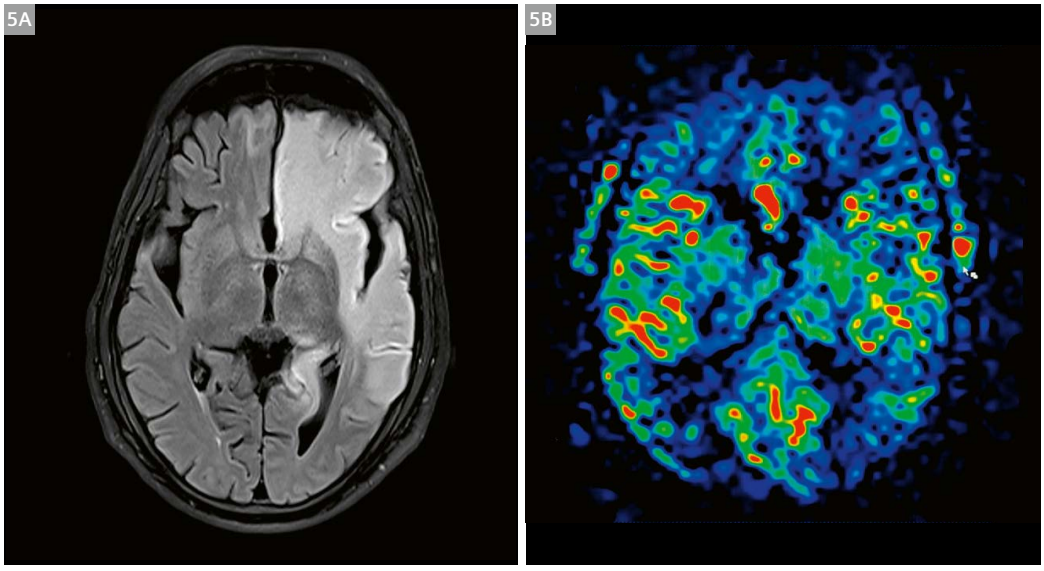

5 **(5A)** Axial FLAIR image shows persistent gyral edema. **(5B)** ASL image shows normalization of perfusion with decreased cerebral blood flow in the left fronto-parietotemporal region and deep grey matter.

meningoencephalitis, symptoms such as neck rigidity, cachexia, and convulsions occur. If they survive, there is gradual recovery with or without persistent symptoms of neurologic injuries.

The diagnosis of JE is based on essential and supportive criteria [1]. According to the essential criteria, patients must present with acute encephalitic syndrome, which is defined as a person of any age, at any time of year, having acute onset of fever and a change in mental status and/or new onset of seizures. Supportive criteria include the following:

1. Patient comes from a known JE-endemic area
2. JE-virus-specific IgM are detected in serum and cerebrospinal fluid using MAC ELISA
3. Thalamic lesions appear on CT or MRI scans with an appropriate clinical and epidemiological background

For confirmation of the disease, patients must fulfill the essential criteria and any two of the three supportive criteria [1].

Pathologic changes in the brains of acute JE patients are characterized by glial nodules and circumscribed necrolytic foci mainly in the bilateral thalami, substantia nigra, basal ganglia, brain stem, cerebellum, cerebral cortex, and white matter [2]. The MR imaging findings reflect the pathologic changes in those areas [3, 4]. The characteristic finding most consistently present in JE is the bilateral involvement of both thalamic lesions with or without hemorrhage on MR imaging [4]. Reports of unilateral lesion in JE are extremely rare [2, 5].

Our case displays unilateral involvement of the left frontoparietotemporal gyrus and the left deep grey matter (caudate nucleus, putamen, and thalamus) showing T2 hyperintensity with diffusion restriction and increased perfusion in ASL.

In terms of whether this could be an infarct: Despite such massive hemispherical involvement with diffusion restriction, no neurological deficit is present. In addition, an infarct usually involves decreased perfusion. Our case has increased perfusion with no neurological deficit, so it is less likely to be an infarct.

Follow-up imaging revealed persistent signal changes in T2w and FLAIR sequences. However, decreased cerebral blood flow with ASL perfusion as well as facilitated diffusion was observed.

Temporal lobe involvement is much more common in herpes simplex encephalitis (HSE) than in JE. This may cause problems in differentiating JE from HSE. A typical MR imaging finding in HSE is bilateral asymmetric T2 hyperintensity in the limbic systems, such as the medial temporal lobes, insular cortices, and inferolateral frontal lobes, regardless of hemorrhage and contrast enhancement. Unilateral temporal lobe involvement is not uncommon in HSE, but it typically spares deep gray matter such as the thalamus, basal ganglia, and substantia nigra. Therefore, the concurrent involvement of the temporal lobe, thalamus, substantia nigra, and basal ganglia in our case indicate that this is more likely to be JE than HSE.

Conclusion

We reported a rare case of JE with unilateral involvement of the thalamus, caudate nucleus, putamen, and frontoparietotemporal lobe. ASL perfusion can be a useful biomarker to assess disease activity in these patients. To our knowledge, no reports of using ASL perfusion to follow up on Japanese encephalitis patients exist.

Acknowledgment

The author wishes to acknowledge the support of Dr Kanmani Kiruba, M.D.

References

1 1 Basumatary LJ, Raja D, Bhuyan D, et al. Clinical and radiological spectrum of Japanese encephalitis. J Neurol Sci. 2013;325(1-2):15-21.
2 Handique SK, Das RR, Barman K, et al. Temporal lobe involvement in Japanese encephalitis: problems in differential diagnosis. AJNR Am J Neuroradiol. 2006;27(5):1027-31.
3 Kalita J, Misra UK. Comparison of CT scan and MRI findings in the diagnosis of Japanese encephalitis. J Neurol Sci. 2000;174(1):3-8.
4 Kumar S, Misra UK, Kalita J, et al. MRI in Japanese encephalitis. Neuroradiology. 1997;39(3):180-4.
5 Yakushiji Y, Kurohara K, Tanaka A, et al. A case of Japanese encephalitis presenting with unilateral lesions in diffusion-weighted MRI. Rinsho Shinkeigaku. 2001;41(9):602-5.

Contact

Babu Peter Sathyanathan, M.D., D.N.B
Professor of Radiology
Barnard Institute of Radiology
Madras Medical College
Rajiv Gandhi General Hospital
Opposite to Chennai Central Railway Station
Chennai, Tamilnadu, India
drbabupeter@gmail.com

First Impression and Experience on the MAGNETOM Sola – New Zealand

Sandra Winsor, MMRT, DCR(R)

Pacific Radiology, Nelson, New Zealand

The first MAGNETOM Sola 1.5T with BioMatrix technology to be installed in New Zealand (NZ), arrived at Pacific Radiology Nelson in December 2018.

Pacific Radiology provides MRI services to the Nelson and Tasman region covering a geographical area of 10,000 km^2 and a population of 104,000.

Located at the top of the South Island, Nelson is renowned for having the most sunshine hours per year across NZ, and is home to many who enjoy an outdoors lifestyle. The favorite pastime of Nelsonians is mountain biking, hence the MAGNETOM Sola is kept busy by those unfortunate enough to suffer a 'mountain bike' injury. Consequently, the primary workload is musculoskeletal, but has a portion of neuro, abdominal, pelvic, and vascular cases to create variety over the course of our daily schedule.

The configuration of the Nelson MAGNETOM Sola features the 70 cm bore and the large 50 cm FOV in the z-direction. The 48-channel system was selected to ensure availability of high density 20-channel head neck, body 18 and spine 32 coils. XJ gradients with an amplitude 33 mT and a slew rate 125 T/m/s ensures adequate performance for the needs of private practice imaging.

Additional options purchased include the 18-channel Large UltraFlex Coil and Simultaneous Multi Slice (SMS) TSE.

First impression

The MAGNETOM Sola presents itself in a gorgeous, smoothly curvaceous, glossy white finish, declaring a myriad of new design features waiting to be discovered.

The iPad like touch screen BioMatrix Interfaces on each side of the scanner, allow one touch positioning without the need for laser light localization. This is a great feature for improving turn around times between patients. Simpler controls on the BioMatrix Interface allow easy volume, lighting and air adjustments, which are replicated at a handy location within the new *syngo* XA11 software environment.

In the control room it is exciting to see the much longed for, large screen monitor which houses the new *syngo* XA11 software. The new interface has a completely fresh appearance, and while it initially presents as an unknown, it exudes a familiarity to beckon you in. Once

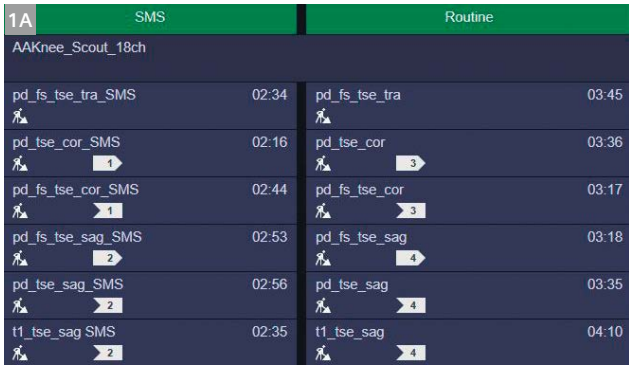

1A Comparison of SMS vs. routine sequences while maintaining the same image quality.

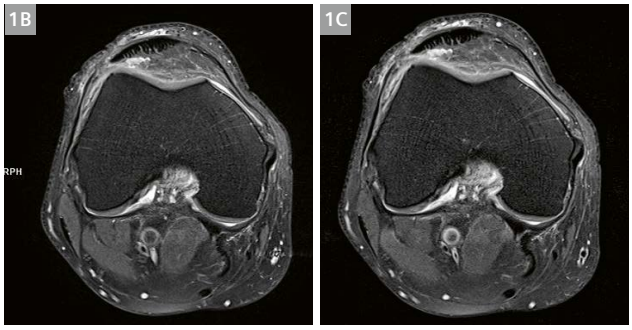

1B, C Transverse PD fat sat:
SMS **(1B)** 2.34 minutes vs. Routine **(1C)** 3.45 minutes vs.

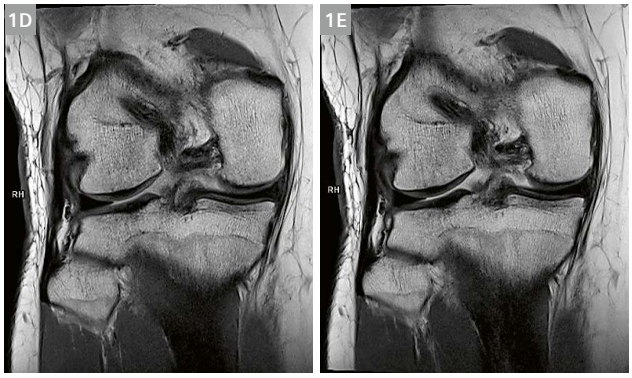

1D, E Coronal PD:
SMS **(1D)** 2.16 minutes vs. Routine **(1E)** 3.36 minutes vs.

introduced to some of the new features of *syngo* XA11, you find yourself automatically reverting to some old traits, which have reassuringly been ported across to the new interface. Functions such as series +/- and image +/- on the keyboard remain the same.

There are three components to the latest software, Exam, View&Go, and the Dot Cockpit. Users of previous versions of *syngo* will most likely have come across the Dot Cockpit before now. Much has stayed the same in the Cockpit, although a practical new feature is the 'replace sequence' option. Depending on where a new sequence is dragged and released into a protocol, there is the option to replace an existing obsolete sequence, or add it to the protocol.

View&Go is quite a different kettle of fish compared to the Viewing and Post Processing tabs in the VE software. Those who have had *syngo*.via experience will find it an easy transition to master View&Go.

This leaves the Exam and Browser interface to be conquered. Again, previous experience with *syngo*.via assists in the transition, and over time and experimentation, some superb new elements emerge.

A redesigned intercom guarantees quality com-mu-nication with the patient, where a new feature allows you to hear patient responses before releasing the speak button. Previously patient responses were missed if the speak button was not released quickly enough.

The official handover of the system was the beginning of January 2019, where the brief was to develop standard protocols with the best image quality in a reasonable time frame. As the radiologists were familiar with images from another vendors system, it was important that they were comfortable with the look of the new Siemens images. Now that this has been established, the next step is to embark on acceleration techniques, starting with SMS in the knee. Small steps lead to robust protocols and to date we have made significant time changes in the knee protocol with SMS (Fig. 1).

While the scan times of these SMS protocols are not ground breaking, it is important to observe the possibilities of acceleration between a routine sequence and SMS. When six minutes or more can be shaved from a single study, the possibility of scanning one extra patient per day is feasible.

As we further explore this technique, more time savings in the knee protocol are envisaged.

For the current ankle protocol, it is anticipated that eight minutes will be shaved form the standard protocol. What is really exciting, is that there is the potential to achieve scan times on the 1.5T MAGNETOM Sola, that are more in line with 3T systems.

Radiologists impressions

The radiologists are equally impressed with the MAGNETOM Sola, and are observing improved image quality. SMS is seeing a lot of excitement, as time savings will translate to higher throughput.

Indeed, there are a multitude of new attributes on the Sola that are exciting and begging to be explored, so in summary, here is a selection of favorites so far from Nelson.

Favorite feature

Start Timer

The Start Timer is a clear winner, as the system is programmed to switch on at 7.45 am Monday to Friday. This means that when walking through the door just prior to 8.00 am, the large screen monitor presents with a big green tick indicating the system is up and running and ready to go. At a glance, the green tick reassures that the helium and cooling are in specification, leaving a quick QA on a coil of choice to complete the morning QA process. Auto positioning is not new, but has been enhanced to a superior version where the Select&GO at the BioMatrix Interface, allows selecting the body region to be scanned,

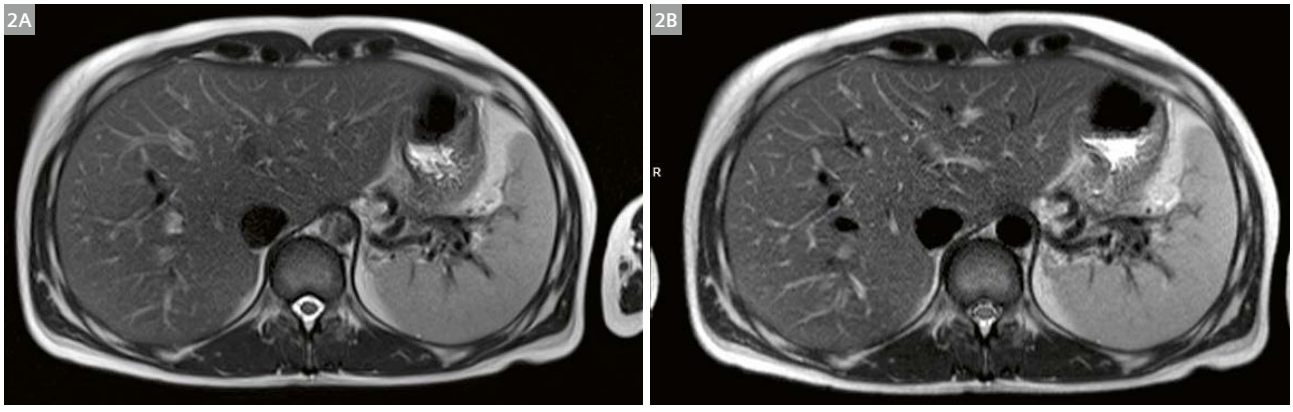

2 Transverse HASTE breath-hold **(2A)** BioMatrix triggered **(2B)**, with the advantage of slices being consistently ordered from the dome of the liver to the apex with the triggering technique.

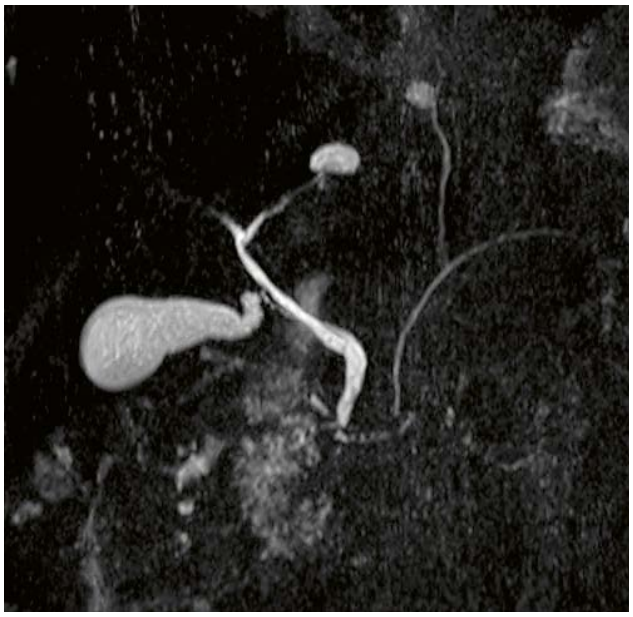

3 CAIPI SPACE 3D MRCP acquired in 20 s breath-hold.

and the patient is transported to isocenter. No longer does a specific protocol with associated body region need to be in the Exam Queue ready to go.

Favorite acceleration technique

SMS TSE or CAIPIRINHA SPACE
SMS TSE is the most exciting new acceleration technique to emerge, as it can be used in so many MSK protocols. Entire protocols can be adapted to reach scan times previously seen only at 3T, while maintaining beautiful image quality (Fig. 1A–E).

CAIPIRINHA SPACE provides some incredible examples with great time savings, for example whole brain 3D T1 SPACE can be achieved in 2.30 mins. As 3D SPACE is not a work horse sequence, SMS takes the number one spot.

Favorite hardware

Large monitor vs. BioMatrix Sensors
The large monitor is a sight for sore eyes and really transports the whole system into a modern era. Double mouse clicks enlarge images from the GSP for easier planning, and right mouse push/pull scrolls through images quickly.
Keyboard shortcuts are plentiful and crucial to swift navigation of tools and commands. To name a few:

Control G: Couples or uncouples graphics
H: Turns reference lines on/off
Esc: Deselects any tool selected
O: Allows images to be rotated in postprocessing
P: Activates the punch tool in 3D MIP

BioMatrix Sensors for respiratory navigation, what a revolution. The respiratory cycle and breathing pattern can be seen throughout any examination, and abdominal sequence strategies can be planned ahead at a glance. Respiratory triggered sequences are quickly and easily set up with robust results (Fig. 2).

First equal placing for these two in the hardware category.

Favorite coil

Tiltable head coil vs. Ultra Flex Large 18
How uncomfortable is it for a kyphotic patient to endure a brain MRI? The patient ends up with pillows under their buttocks to tip them back so that they fit into a standard head coil, but still the head can be teetering in the breeze and the anterior coil does not fit. Now we have a fabulous solution, the head coil can be tilted 9°–18°, the anterior coil fits and the patient is comfortable for the duration of the scan.

The Ultra Flex Large 18 has so many areas of application, shoulders, elbows, brachial plexus, prostate, but the favorite area is single hip imaging. The coil is more flexible, slimmer and has more coil elements than any predecessor.
It reaches across the hip anteriorly and posteriorly in most patients and the image quality is noticeably improved.

Tiltable head coil is the favorite in this category.

Favorite sequence

The champion of sequences on the *syngo* XA11 software is CAIPI SPACE MRCP 3D.

3D MRCP SPACE sequences can be a laborious sequence where scan times varied from around 4 minutes to an incredible 8 minutes in a certain type of patient. Often after the long wait, the outcome was less than agreeable and single breath-hold sequences were required at different degrees of angulation.

The CAIPI SPACE MRCP 3D is a revolution as it is acquired in a 20 second breath-hold with a resolution of 0.6 x 0.6 x 1.1 mm covering the entire biliary tree (Fig. 3).

The DICOM files are available for download at

www.siemens.com/magnetom-world
> Clinical Corner > Protocols > DICOM Images

Contact

Sandra Winsor MMRT, DCR(R)
Charge MRI Technologist
Pacific Radiology
Nelson
New Zealand
sandra.winsor@pacificradiology.com

Musculoskeletal and Body MRI in Children

Sarah D. Bixby, M.D.; Reid C. Nichols, RT (R) MR; Ali Gholipour, Ph.D.

Department of Radiology, Boston Children's Hospital, Boston, MA, USA

MRI imaging in pediatric patients is as much about the process as it is about the result. While high-quality images are the ultimate goal, for children an imaging study is a success if diagnostic images are obtained while minimizing the risk to the patient, which includes reducing the risk of anesthesia [1–2]. There are many ways to improve spatial resolution and gain signal-to-noise ratio (SNR) in MRI, though most strategies cost time. In clinical practice there are limitations on patient cooperation and magnet utilization that require a practical approach to imaging. While working with children is enormously satisfying, there are also challenges that come with pediatric imaging which require minimizing exam times, eliminating labor-intensive breath-holding instructions, and imaging through motion (respiratory and gross motion). Motion is a major obstacle when it comes to imaging young children. In many instances, the difference between a non-diagnostic exam and a successful exam may simply require reducing sequence time by half. While this used to require unacceptable compromise in image quality, this is no longer true. With increased field strength magnets (i.e. 3T), appropriate selection of multichannel phased array coils, and parallel imaging techniques, scan times have decreased considerably from where they started. With a few additional strategies it is not only possible, but more than likely that a complete exam can be performed in a young child[1] without sedation.

Advanced protocol planning, sequence prioritization, real-time exam monitoring, and skilled patient handling are also critical elements of a successful MRI examination in a young child.

A fundamental principle in imaging pediatric patients is to limit sequences to only those that are necessary, acquiring the most high yield sequences first. Patient cooperation is limited and young patients often have tolerance for two or three sequences. Radiologists should assume the most critical diagnostic information must be obtained in the first ten minutes of an exam. If those first sequences are diagnostic, the patient will be spared a follow-up exam under anesthesia. MRI is increasingly being used to screen patients with certain symptoms for presence or absence of disease, such as fracture detection in limping toddlers, evaluation for infection in children with fever of unknown origin, or appendicitis screening in patients with right lower quadrant pain. MRI may be the best means of detecting fractures in certain locations when the bones have not yet ossified (Fig. 1), and for localizing disease when patients are unable to verbalize symptoms.

[1] *MR scanning has not been established as safe for imaging fetuses and infants less than two years of age. The responsible physician must evaluate the benefits of the MR examination compared to those of other imaging procedures. Note: This disclaimer does not represent the opinion of the authors.*

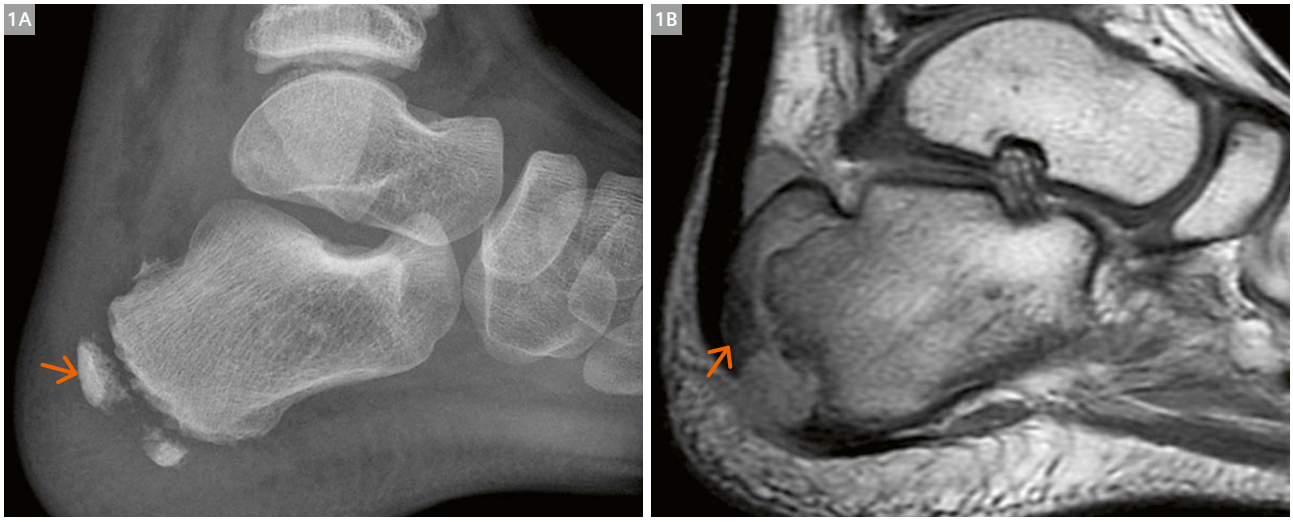

1 6-year-old female with calcaneal apophyseal fracture **(1A)** Lateral radiograph of the ankle reveals a normal-appearing apophysis (orange arrow). **(1B)** Sagittal PD-weighted TSE sequence reveals avulsion of the calcaneal apophysis, not appreciated on radiographs secondary to the lack of ossification.

It is more important to acquire images quickly to allow actionable diagnosis, rather than spending additional time enhancing imaging quality at the expense of patient cooperation.

Monitoring MRI examinations in real-time allows for adjustment of imaging parameters as the study unfolds [3]. As toddlers are often unable to articulate the location and nature of their symptoms, imaging requires looking far and wide initially and focusing down on an abnormality once identified. Setting up an MRI in a toddler with an unexplained limp, for example, often requires using one or more body matrix coils (depending on the child) to perform initial sequences with a large field of view (FOV) from the pelvis to the feet (Fig. 2). These sequences can be performed quickly, with need for additional sequences determined by the presence or absence of abnormal findings. Without real-time radiologist supervision, these protocol modifications would not be possible and the examination may need to be repeated.

While vigilant exam monitoring, careful protocoling, and adept patient handling are critical to successful imaging of children, these efforts may still fall short of the goal without additional sequence advancements. Accelerated acquisitions and motion robust sequences are, therefore, particularly valuable in pediatric imaging. Acceleration techniques allow for substantial reductions in imaging times so that they may be tolerated by young patients; in our experience this generally means shorter than two minutes per sequence. In pediatric musculoskeletal imaging, MRI protocols rely heavily on turbo spin-echo (TSE) sequences which include proton density (PD), intermediate weighted (IW), and T2-weighted images. Accelerated TSE acquisitions can be obtained through *k*-space undersampling in parallel imaging [4]; however a reduction or acceleration factor of R comes with a reduction of $1/\sqrt{R}$ in (SNR). In addition, SNR is also reduced by the noise amplification factor, or the *g*-factor (geometry factor) penalty that varies by the location in an image depending on the number of aliased replicates per voxel based on coil sensitivities [5]. The *g*-factor penalty depends on the receive coil design and coverage, and the geometry of imaging and can vary between 1 and 2 across the image. Simultaneous multi-slice (SMS) is another technique to accelerate imaging that excites multiple spatially distributed slices simultaneously by using a multi-band radiofrequency pulse and techniques to control aliasing and reduce the *g*-factor penalty [5–11]. Data obtained from receive coils from simultaneously excited slices are separated to reconstruct images. When parallel imaging and SMS are both applied, imaging times can be reduced 4- to 8-fold over traditional methods. In our routine knee MRI protocol we compared an accelerated T2-weighted TSE sequence using a parallel imaging iPAT factor of 2 with an SMS factor of 2 to achieve 4-fold acceleration against our traditional sequence without the SMS acceleration (Figs. 3, 4). We found both the SMS TSE and the TSE were equivalent in identifying pertinent imaging findings [12]. Compared to the traditional sequence, the SMS accelerated sequence is nearly twice as fast (Table 1). Further reduction in imaging time can be gained by increasing the SMS factor, with incremental cost to SNR. In our patient population we found that 4-fold acceleration is sufficient for most patients, and additional acceleration can be reserved for patients who are extremely nervous or fidgety, given the modest reduction in SNR.

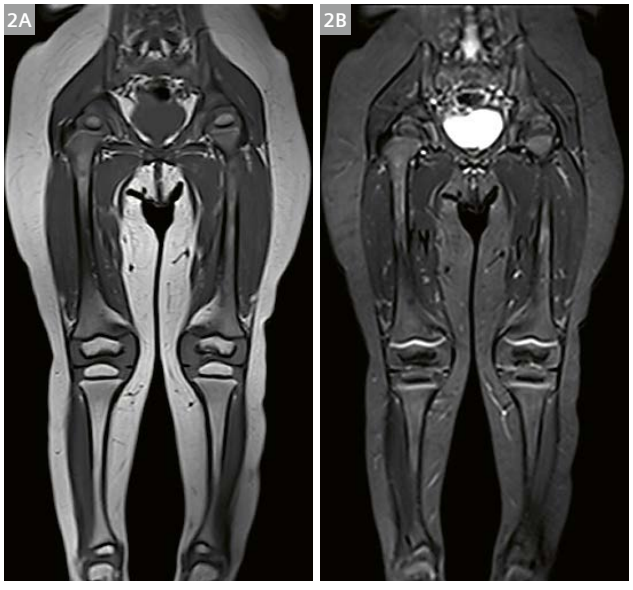

2 2-year-old female with limp. Coronal T1 **(2A)** and STIR **(2B)** sequences through the entire pelvis and lower extremities were performed using a body matrix coil as an initial screen to identify areas of pathology. No abnormality was identified.

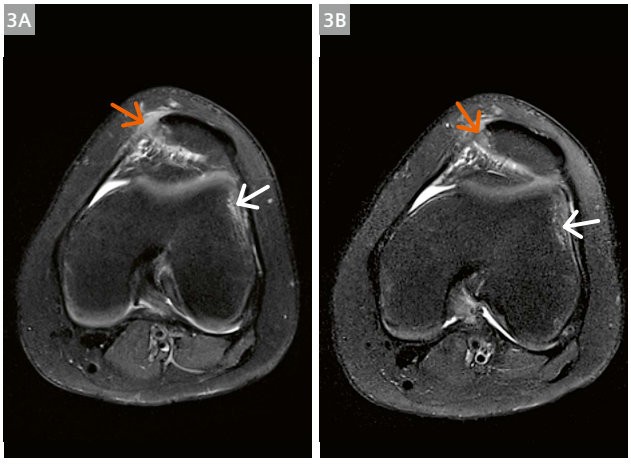

3 11-year-old female with patellar dislocation. **(3A)** Axial T2-weighted TSE image with fat suppression and **(3B)** corresponding axial T2-weighted SMS TSE image demonstrates a tear of the medial retinaculum (orange arrow) and a bone contusion at the lateral femoral condyle (white arrow).

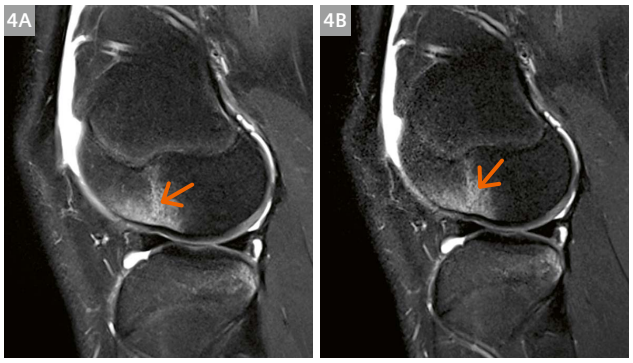

4 14-year-old boy with lateral femoral contusion (orange arrow) undergoing MRI. **(4A)** Sagittal T2-weighted TSE sequence and **(4B)** corresponding sagittal T2-weighted SMS TSE sequence for comparison.

The 3D TSE volumetric SPACE (Sampling Perfection with Application optimized Contrasts using different flip angle Evolution) acquisition is integral for imaging of large joints (knee and ankle) in children [13–18]. The three-dimensional, high-spatial resolution, isotropic images can be reconstructed into any imaging plane from a single volumetric data set, making it helpful for identifying subtle cartilage defects or ligamentous injuries. The imaging time, however, is relatively long which makes it particularly vulnerable to motion. The standard PD-weighted SPACE sequence in the knee protocol at our institution is 7 minutes and 40 seconds. Parallel imaging techniques can be applied to the acquisition but may cause aliasing artifacts and increase noise. CAIPIRINHA "Controlled Aliasing in Parallel Imaging Results in Higher Acceleration" [19] is a parallel imaging strategy that uses *k*-space sampling patterns designed to reduce aliasing and overlap on reconstructed images. While aliasing artifacts are still present, they are shifted to the corners of the image space.

Parameters	T2-weighted TSE	T2-weighted SMS TSE
Plane	Sagittal	Sagittal
Acquistion time (min:sec)	2:45	1:50
TR (ms)	4500	3000
TE (ms)	53	53
Echo train length	34	33
Matrix	384	384
Parallel imaging acceleration factor and reconstruction	2 (GRAPPA)	2 (GRAPPA)
FOV (mm)	140	140
Voxel dimension (mm)	0.4 x 0.4 x 3.0	0.4 x 0.4 x 3.0

Table 1: MRI parameters for T2-weighted TSE sequence versus T2-weighted SMS TSE sequence in the knee.

Parameters	PD-weighted 3D SPACE	PD-weighted 3D CAIPIRINHA SPACE
Plane	Sagittal	Sagittal
Acquistion time (min:sec)	7:40	4.00
TR (ms)	1000	1000
TE (ms)	49	49
Echo train length	41	41
Flip angle (°)	120	120 (variable)
Matrix	320 x 320 x 240	320 x 320 x 240t
Parallel imaging acceleration factor and reconstruction	2 (GRAPPA)	2 (GRAPPA)
FOV (mm)	162 x 249	162 x 249
Voxel dimension (mm)	0.54 x 0.54 x 1	0.54 x 0.54 x 1

Table 2: MRI parameters for Proton Density (PD)-weighted 3D SPACE sequence versus PD-weighted 3D CAIPIRINHA SPACE sequence in the knee.

Combined CAIPIRINHA and SPACE allows for 4-fold acceleration through undersampling in both the phase and partition encoding directions [14]. We compared the standard PD-weighted SPACE sequence in the knee with the CAIPIRINHA PD-weighed SPACE sequence (Table 2). Applying CAIPIRINHA to SPACE reduced our scan time from 7:40 minutes to 4:00 minutes without compromise in image quality (Figs. 5, 6). We reserve this sequence for slightly older patients (above the age of 8) who are able to cooperate for the 4 minute long acquisitions. In the younger patients, 2D sequences are still generally preferred. Anticipated pathologies in our youngest patients do not typically require such fine spatial resolution, and these patients reap greatest benefit from short acquisitions that require periodic opportunities for breaks.

Motion robust imaging alternatives are highly valuable in pediatric patients, particularly for abdominal and pelvic imaging [20]. Examinations that require breath-held sequences often require the child to be anesthetized and intubated to allow for periods of suspended respiration. With the aim of reducing need for anesthesia and/or the depth of anesthesia, free-breathing imaging capabilities are imperative. In the abdomen, 3D volumetric interpolated breath-hold examination (VIBE) imaging offers the most robust approach to acquiring T1-weighted imaging. VIBE allows for high spatial resolution with relatively fast imaging acquisitions of the entire abdomen [21, 22]. Depending on parameter selection, it is possible to acquire images through the entire field of view in approximately 20 seconds in a cooperative patient. Even adult patients may have difficulty breath-holding for a 20 second sequence [23], and children are even less likely to manage this. Cartesian VIBE obtained during free-breathing produces motion artifact within the image (Fig. 7) which limits the diagnostic quality of the sequence [24, 25]. T1-weighted images can be acquired with respiratory navigation, though this is less developed than navigated T2-weighted sequences, and image quality is inferior to the conventional breath-hold sequences [26–28]. Additionally, navigated T1-weighted imaging is not possible with fat suppression, which limits its utility for post-contrast imaging. A modified version of the VIBE sequence is a radial VIBE sequence that uses rectilinear sampling in the *z*-direction and radial sampling in the *xy* plane [24]. This sequence can be performed during free-breathing, and the radial sampling of *k*-space mitigates the effect of respiratory motion such that image quality is superior to the traditional breath-hold Cartesian VIBE [24]. The product version of this sequence is called StarVIBE, which is our standard for T1-weighted imaging in pediatric patients. Although the acquisition time is longer than a traditional VIBE sequence, the respiratory motion is distributed throughout the image such that there is little perception of the motion within the image. This technique is especially helpful for post-gadolinium enhanced imaging in the liver, kidneys, and bowel (Fig. 8). The ability to obtain high spatial-resolution, motionless imaging in patients who are freely breathing has dramatically altered our approach to sedating patients. We utilize the StarVIBE sequence in any child undergoing abdominopelvic imaging, for both pre and post-contrast fat-suppressed imaging.

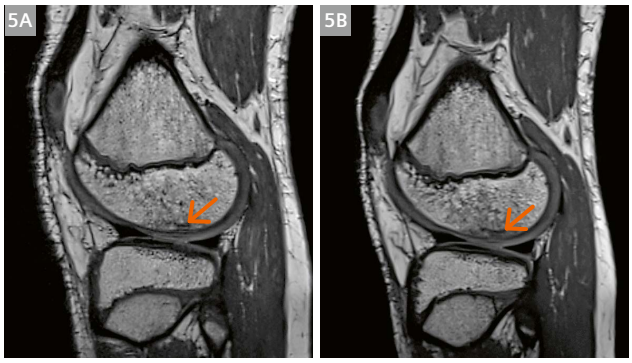

5 11-year-old female with lateral femoral condylar impaction fracture (orange arrow) seen on both **(5A)** sagittal PD-weighted SPACE sequence, and **(5B)** corresponding sagittal PD-weighted CAIPIRINHA SPACE sequence for comparison.

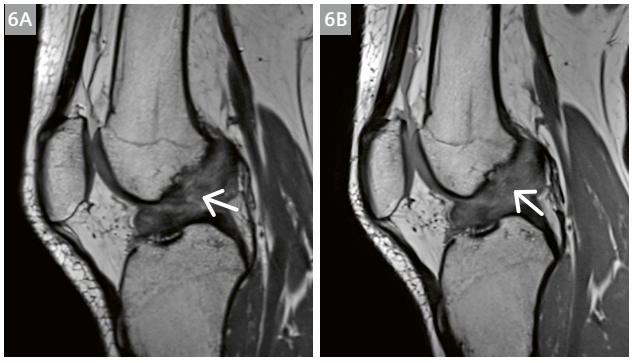

6 15-year-old female with ACL tear (white arrow). **(6A)** Sagittal PD-weighted SPACE sequence and **(6B)** corresponding sagittal PD-weighted CAIPIRINHA SPACE sequence through the ruptured ACL for comparison.

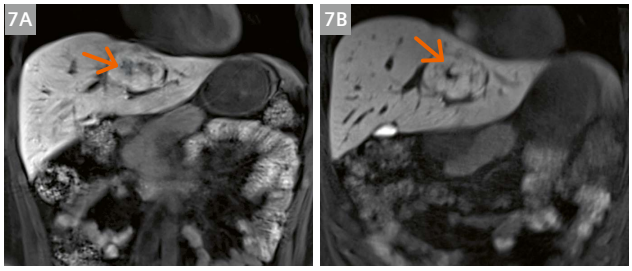

7 20-year-old female with FNH-like liver lesion. **(7A)** Coronal T1 VIBE with breath-holding after administration of Eovist contrast media reveals delayed uptake in a liver lesion (orange arrows), though images are degraded by motion. **(7B)** Sequence repeated with StarVIBE sequence with free-breathing demonstrates reduced motion artifact with better depiction of the lesion.

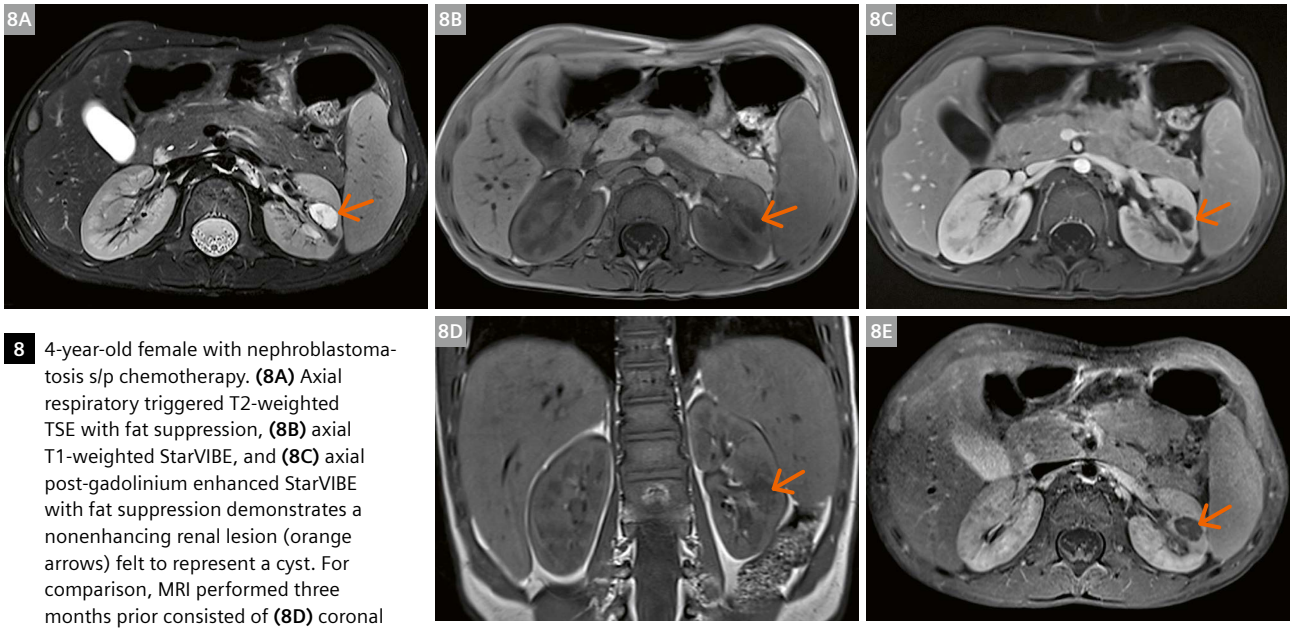

8 4-year-old female with nephroblastomatosis s/p chemotherapy. **(8A)** Axial respiratory triggered T2-weighted TSE with fat suppression, **(8B)** axial T1-weighted StarVIBE, and **(8C)** axial post-gadolinium enhanced StarVIBE with fat suppression demonstrates a nonenhancing renal lesion (orange arrows) felt to represent a cyst. For comparison, MRI performed three months prior consisted of **(8D)** coronal respiratory triggered T1-weighted TSE, **(8E)** axial post-gadolinium enhanced T1 TSE with fat suppression. Motion artifact is noted in the image from respiration.

The lack of breath-holding as a requirement for imaging obviates the requirement for endotracheal intubation, unless there are other reasons for which it would be required. A dynamic StarVIBE sequence is also available which allows for both high temporal resolution in addition to high spatial resolution images during dynamic contrast injection [29, 30], using compressed sensing techniques as a means to vastly undersample the data and reduce imaging times [20]. We are currently investigating this technique in the pediatric population, particularly with regard to renal, hepatic and bowel wall imaging.

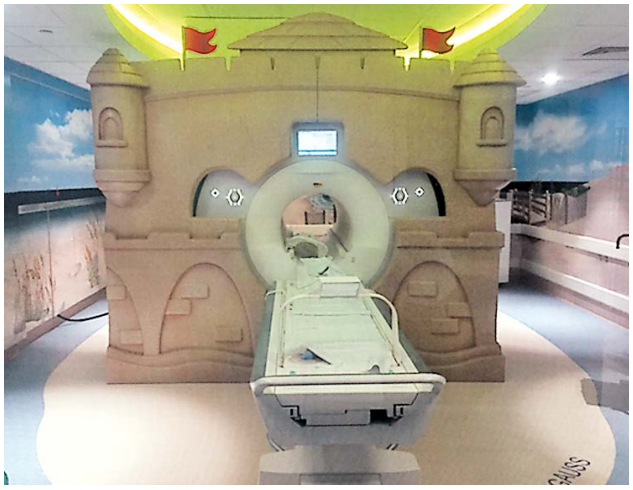

9 3T MAGNETOM Prisma MR scanner embedded in a sandcastle design. The room is decorated with decals in the theme of an ocean scene.

MR imaging in pediatric patients requires a team approach and collective efforts toward reducing our dependency upon sedation as a mechanism to acquire diagnostic, motion-free images. These include tailored protocoling, real-time monitoring, and utilization of accelerated or motion robust sequences. With the use of SMS TSE and CAIPIRINHA SPACE, MSK imaging examinations in children can be dramatically shortened without compromising image quality. StarVIBE imaging in the abdomen allows for high-resolution, free-breathing, T1-weighted imaging thereby eliminating requirement for endotracheal intubation for abdominal MRI in sedated patients. Reducing the anxiety and apprehension around the scanner and the scan room is also important in achieving patient cooperation. This can be achieved through embedding the scanner in a structure, such as a sandcastle, train, or boat (Fig. 9), decorating the room with colorful designs, distracting the patient with a movie during the scan, or preparing prior to the scan at a mock scanner or simulating the experience with virtual reality headsets. All of these strategies are currently employed at our hospital, oftentimes in combination. Further developments in prospective motion correction using motion cameras embedded in the magnet and sensors on the patient are currently being developed through collaborations with KinetiCor (Honolulu, HI, USA), with broad applications in the pediatric population. Our hope is that through these collective efforts we will drastically reduce the number of children requiring sedation for MRI, and improve the patient experience by reducing exam lengths and delays.

References

1 Callahan MJ, MacDougall RD, Bixby SD, Voss SD , Robertson RL, Cravero JP. Ionizing radiation from computed tomography versus anesthesia for magnetic resonance imaging in infants and children: patient safety considerations. Pediatr Radiol 2018; 48(1):21-30.
2 Paterson N, Waterhouse P. Risk in pediatric anesthesia. Paediatr Anaesth 2011; 21:848-857.
3 Robertson RL, Silk S, Ecklund K, Bixby SD, Voss SD, Robson CD. Imaging optimization in children. J Am Coll Radiol 2018; 15(3 Pt A):440-443.
4 Griswold MA, Jakob PM, Heidemann RM, Nittka M, Jellus V, Wang J, Kiefer B, Haase A. Generalized autocalibrating partially parallel acquisitions (GRAPPA). Magn Reson Medicine 2002 Jun; 47(6):1202-1210.
5 Breuer FA, Kannengiesser SA, Blaimer M, Seiberlich N, Jakob PM, Griswold MA. General formulation for quantitative G-factor calculation in GRAPPA reconstructions. Magn Reson Med 2009 Sep; 62(3):739-746.
6 Setsompop K, Gagoski BA, Polimeni JR, Witzel T, Wedeen VJ, Wald LL. Blipped-controlled aliasing in parallel imaging for simultaneous multislice echo planar imaging with reduced g-factor penalty. Magn Reson Med 2012 May 1; 67(5):1210-1224.
7 Barth M, Breuer F, Koopmans PJ, Norris DG, Poser BA. Simultaneous multislice (SMS) imaging techniques. Magn Reson Med 2016 Jan; 75(1):63-81.
8 Feinberg DA, Setsompop K. Ultra-fast MRI of the human brain with simultaneous multi-slice imaging. J Magn Reson 2013; 229:90-100.
9 Fritz J, Fritz B, Zhang J, Thawait GK, Joshi DH, Pan L, Wang D. Simultaneous multislice accelerated Turbo Spin Echo magnetic resonance imaging comparison and combination with in-plane parallel imaging acceleration for high-resolution magnetic resonance imaging of the knee. Invest Radiol 2017; 52:529-537.
10 Poser BA, Anderson RJ, Guerin B, Setsompop K, Deng W, Mareyam A, Serano P, Wald LL, Stenger VA. Simultaneous multislice excitation by parallel transmission. Magn Reson Med 2014; 71:1416-1427.
11 Gagoski BA, Bilgic B, Eichner C, Bhat H, Grant PE, Wald LL, Setsompop K. RARE/Turbo Spin Echo imaging with simultaneous multislice wave-CAIPI. Magn Reson Med 2015; 73:929–938.
12 Benali S, Johnston PR, Gholipour A, Dugan ME, Heberlein K, Bhat H, Bixby SD. Simultaneous multi-slice accelerated turbo spin echo of the knee in pediatric patients. Skeletal Radiol 2018 Jun; 47 (6):821-831.
13 Fritz J, Fritz B, Thawait GG, Meyer H, Gilson WD, Raithel E. Three-Dimensional CAIPIRINHA SPACE TSE for 5-Minute High-Resolution MRI of the Knee. Invest Radiol 2016; 51:609-617.
14 Fritz J, Ahlawat S, Fritz B, Thawait GK, Stern SE, Raithel E, Klyce W, Lee RJ. 10-min 3D Turbo Spin Echo MRI of the knee in children: arthroscopy-validated accuracy for the diagnosis of internal derangement. J Magn Reson Imaging 2018; doi: 10.1002/jmri.26241. epub ahead of print.

Contact

Sarah D. Bixby, M.D.
Associate Professor of Radiology
Department of Radiology
Boston Children's Hospital
300 Longwood Avenue,
Main Building, 2nd Floor
Boston, MA 02115
USA
Tel.: +1 857 218 4006
sarah.bixby@childrens.harvard.edu

15 Fritz J, Raithel E, Thawait GK, Gilson W, Papp DF. Six-fold acceleration of high-spatial resolution 3D SPACE MRI of the knee through incoherent k-space undersampling and iterative reconstruction – first experience. Invest Radiol 2016; 51:400–409.
16 Fritz J, Ahlawat S, Thawait GK, Raithel E, Gilson W, Lee RJ. 3D MRI of knee in pediatric patients with CAIPIRINHA SPACE: diagnostic performance assessment with arthroscopic correlation. Proc Intl Soc Mag Reson Med 2017; 25:1151.
17 Kalia V, Fritz B, Johnson R, Gilson WD, Raithel E, Fritz J. CAIPIRINHA accelerated SPACE enables 10-min isotropic 3D TSE MRI of the ankle for optimized visualization of curved and oblique ligaments and tendons. Eur Radiol 2017; 27:3652–3661.
18 Del Grande F, Delcogliano M, Guglielmi R, Raithel E, Stern SE, Papp DF, Candrian C, Fritz J. Fully automated 10-minute 3D CAIPIRINHA SPACE TSE MRI of the knee in adults. A multicenter, multireader, multifield-strength validation study. Invest Radiol 2018; 53:689-697.
19 Breuer FA, Blaimer M, Heidemann RM, Mueller MF, Griswold MA, Jakob PM. Controlled aliasing in parallel imaging results in higher acceleration (CAIPIRINHA) for multi-slice imaging. Magn Reson Med 2005 Mar 1; 53(3):684-691.
20 Jaimes C, Kirsch KE, Gee MS. Fast, free-breathing and motion-minimized techniques for pediatric body magnetic resonance imaging. Pediatr Radiol 2018; 48:1197-1208.
21 Rofsky NM, Lee VS, Laub G, Pollack MA, Krinsky GA, Thomasson D, Ambrosino MM, Weinreb JC. Abdominal MR imaging with a volumetric interpolated breath-hold examination. Radiology 1999; 212:876-884.
22 Lee VS, Lavelle MT, Krinsky GA, Rofsky NM. Volumetric MR imaging of the liver and applications. Magn Reson Imaging Clin N Am 2001; 9(4):697-716.
23 Krinsky GA, Lee VS, Theise ND, Weinreb JC, Rofsky NM, Diflo T, Teperman LW. Hepatocellular carcinoma and dysplastic nodules in patinets with cirrhosis: prospective diagnosis with MR imaging and explanation correlation. Radiology 2001; 219(2):445-54.
24 Chandarana H, Block TK, Rosenkrantz AB, Lim RP, Kim D, Mossa DJ, Babb JS, Kiefer B, Lee VS. Free-breathing radial 3D fat-suppressed T1-weighted gradient echo sequence. A viable alternative for contrast-enhanced liver imaging in patients unable to suspend respiration. Invest Radiol 2011; 46:648-653.
25 Chandarana H, Block KT, Winfeld MJ, Lala SV, Mazori D, Giuffrida E, Babb JS, Milla SS. Free-breathing contrast-enhanced T1-weighted gradient-echo imaging with radial k-space sampling for paediatric abdominopelvic MRI. Eur Radiol 2014; 24:320-326.
26 Vasanawala SS, Iwadate Y, Church DG, Herfkens RJ, Brau AC. Navigated abdominal T1-W MRI permits free-breathing image acquisition with less motion artifact. Pediatr Radiol 2010; 40:340-344.
27 Young PM, Brau AC, Iwadate Y, Vasanawala S, Daniel BL, Tamrazi A, Herfkens RJ. Respiratory navigated free breathing 3D spoiled gradient-recalled echo sequence for contrast-enhanced examination of the liver: diagnostic utility and comparison with free breathing and breath-hold conventional examinations. Am J Roentgenol AJR 2010; 195:687-691.
28 Azevedo RM, Campos ROP, Ramalho M, Heredia V, Dale BM, Semelka RC. Free-breathing 3D T1-weighted gradient echo sequence with radial data sampling in abdominal MRI: preliminary observations AJR Am J Roentgenol 2011; 197:650-657.
29 Kim KW, Lee JM, Jeon YS, Kang SE, Baek JH, Han JK, Choi BI, Bang Y-J, Kiefer B, Block KT, Ji H, Bauer S, Chin K. Free-breathing dynamic contrast-enhanced MRI of the abdomen and chest using a radial gradient echo sequence with K-space weighted image contrast (KWIC). Eur Radiol 2013; 23:1352–1360.
30 Kaltenbach B, Roman A, Polkowski C, Gruber-Rouh T, Bauer RW, Hammerstingl R, Vogl TJ, Zangos S. Free-breathing dynamic liver examination using a radial 3D T1-weighted gradient echo sequence with moderate undersampling for patients with limited breath-holding capacity. Eur J Radiol 2017; 86:26-32.

Fat-suppressed Magnetic Resonance Imaging – How to do it Perfectly

Weiling Lee[1]; Soo Lee Lim[1]; Jamie Xiu Mei Ho[2]; Helmut Rumpel

[1] Department of Diagnostic Radiology, Singapore General Hospital, Singapore
[2] Radiology Department, Sengkang General Hospital, Singapore

New fat suppression features have been added to the *syngo* MR E11 software upgrade that have relevance in clinical applications. This article will first highlight fatsuppression in the 'joint mode' for small fields of view (FOV) and spectral attenuated inversion recovery (SPAIR) in the 'thorax' or 'abdomen/pelvis' modes for large FOV. These modes have been chosen because their improved frequency profiles and offsets better compensate for non-uniform water-fat patterns. Then, we present examples of the two-point TSE-Dixon method linked with a seed-growing analysis.

As is commonly known, fat suppression has always been a challenge in MRI. The subject of the pitfalls and artifacts due to body fat affecting the diagnostic quality of images has been described in many review articles [1] and is constantly being refined by researchers and practitioners.

Background

As protons of fat have short T1 and long T2 relaxation times, they appear bright in an MR image diluting the dynamic range of the image, thus reducing the contrast between the tissues of interest. The fat signal may also be spatially misregistered and interfere with the water signal destructively, giving rise to dark bands at the fat-water interface. This so-called chemical shift artifact may affect the depiction of anatomic details in the images. Fat suppression is, therefore, desirable in order to improve image quality.

In MR imaging, fat suppression is not one single method. Rather, it consists of several different techniques each meant to address specific needs of various imaging scenarios, such as: small FOV imaging (e.g., joints), large FOV imaging (e.g., abdomen), off-centre imaging (e.g., shoulder), and elimination of dark bands from images. The challenge to fat suppression is to find the optimal and robust technique for particular application, taking into consideration its impact on image signal-to-noise ratio (SNR) and its sensitivity to B_0 inhomogeneities.

Table 1 lists the different fat-suppression methods commonly available on a clinical scanner. As the table shows, the methods can be classified into three techniques according to the different MR properties of fat and water that these methods are based on frequency differences,

Techniques	Preparation	Evolution	Detection	Characteristics
Fat-saturation	**Chemical shift selective**	**(Spoiler gradient pulse)**	Fat-suppressed image	sensitive to frequency errors in B_0 inhomogeneity
Selective water excitation	**Chemical shift selective**		Fat-void image	
Phase encoding the chemical shift	Non-selective	**Phase shift** non-centred refocussing pulse	Chemical shift images	sensitive to phase errors in B_0 inhomogeneity
Dixon	Non-selective	**Opposite phase** for water and fat	Water-fat images	
TSE-Dixon	Non-selective	**Multiple short TE-echoes** within one scan	Water-fat images	
STIR	Non-selective inversion	**T1-recovery for fat-nulling**	Fat-void image	altered contrast
SPAIR	**Chemical shift selective**	**T1-recovery for fat-nulling**	Fat-void image	unchanged contrast but sensitive to B_0 inhomogeneity

Table 1: Available fat-suppression or fat-void techniques subdivided into modules of preparation – evolution – detection. The first expresses the preparation for fat-water separation, the second the mechanism to obtain fat-water separation, and the third outlines the results.

phase shifts or T1 differences. As with fast imaging techniques, which can be expressed through a sequence of ordered events as preparation – evolution – detection [2], the various fat suppression methods follow a similar principle: the preparation – evolution periods condition the proton spins for subsequent fat suppressed image acquisition after the two events.

In the following three types of fat suppression techniques, the relevant MR properties of fat will first be described followed by the way such properties are exploited for fat suppression. While there is no singular technique that would provide perfect fat suppression under all circumstances, a good understanding of the principles behind these different techniques can help the user choose the appropriate fat suppression techniques in specific clinical applications.

Spectral fat saturation: 'Frequency-related' technique

Fat (or triglyceride), a sub-type of lipid, consists of three fatty acids bound to a molecule of glycerol. The fatty acid has several protons peaks [10]: Olefinic protons peak at 5.3 ppm; allylic protons and protons adjacent to the carboxyl group peak at 2.0 ppm; and the terminal methyl group peak at 0.9 ppm. The main peak is, however, the aliphatic methylene groups located at 1.3 ppm. Given that the water proton resonance frequency is 4.7 ppm with reference to silicon, the fat peak and the water peak are, therefore, separated by 3.4 ppm. This translates to 210 Hz at 1.5T and 420 at 3T.

A magnetic resonance spectrum of vertebral bone marrow from a healthy volunteer undergoing MR imaging (of water protons) is shown in Figure 1. As the word 'frequency-selective' implies, the technique applies a saturation pulse, tuned to the fat frequency (aliphatic methylene groups in the fat), to the imaging volume. Water protons are then imaged without contribution from the saturated fat methylene/methyl protons. The technique therefore affects only one peak at a time. Given the small separation of the water and fat spectra, the robustness of this technique depends on spectral line broadening.

Spectral line width and how it is broadened

For a tissue with a specific T2 value, the intrinsic full width at half maximum (FWHM) of its spectral signal is 1/(πT2) (Fig. 2A). This theoretical value cannot be achieved practically: Magnetic field inhomogeneities and susceptibility effects (e.g., at air-to-bone interfaces) would both reduce T2 to T2*, broadening the FWHM of the spectral signal to 1/(πT2*) (Fig. 2B). The T2* effect can, however, be minimized by 'shimming' and can be done as described in the following section.

How is shimming done?

A 3D-DESS sequence can be used to generate a field map (spatial distribution of the magnetic field inhomogeneities) over a defined volume (the 'shim box'). The field map is calculated from the phase evolution between the two echoes acquired per TR [4]. Shim currents derived from the map drive the shim coils to correct for field inhomogeneities. In applications such as cardiac MRI, where motion is an issue, a 2D multi-echo sequence can be used instead to create the field map. A good shim can reduce the T2* effect, but cannot eliminate it completely.

Contraindications for shimming

Water protons in MR images come from two sources: Free water and bound water. Protons from free water have a spectrally sharp peak while protons from bound water are held tightly to proteins and muscles and have a broad range of resonant frequencies (i.e., very short T2). In living tissues, the bound water protons would undergo slow exchange with free water protons through a process known as 'magnetization transfer'. The net effect is that the spectrum of free water is broadened slightly. This spectral broadening cannot be changed by shimming. Figure 2C demonstrates the condition we usually have in practice when we have achieved 'the best shim'. A further example is shown in Figure 3.

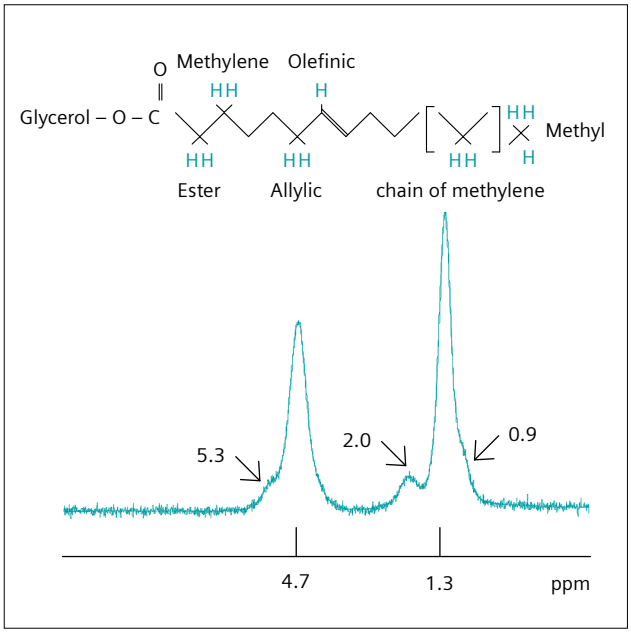

1 Vertebral magnetic resonance spectroscopy (TR/TE/NEX 3000/30/4) shows water peak at 4.7 ppm. The assignment of the peaks of a fatty acid of a triglyceride is as follows: Olefinic protons at 5.3 ppm, allylic protons, and protons adjacent to the carboxyl group at 2.0 ppm, aliphatic methylene groups (main peak) at 1.3 ppm, and terminal methyl groups at 0.9 ppm.

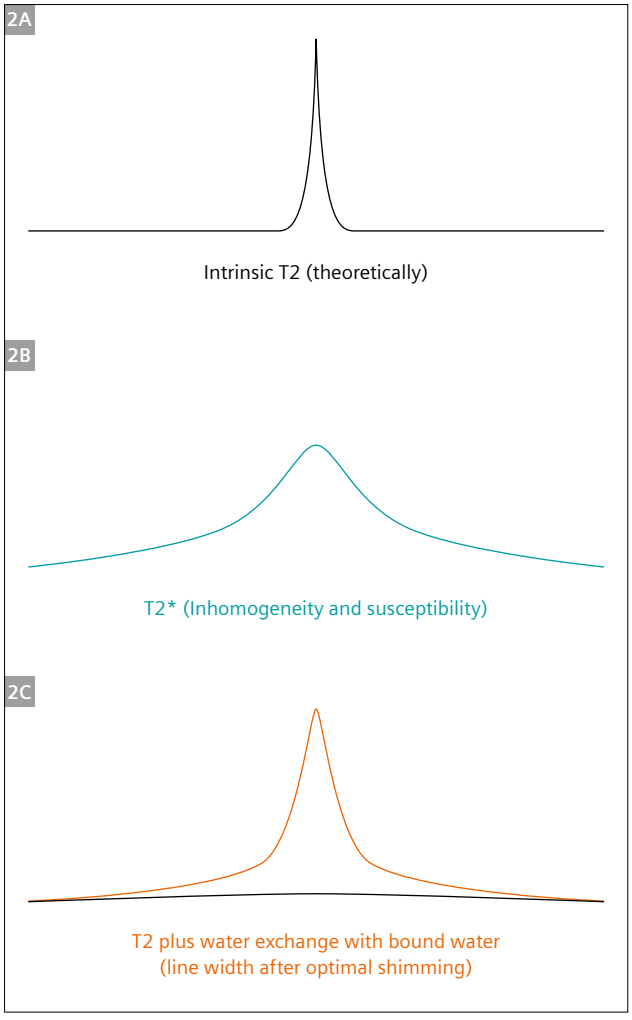

2 The figure depicts the linewidth to which the water signal is shimmed – **(2A)** theoretical FWHM that equals 1/(πT2), **(2B)** significantly broadened linewidth with inhomogeneities and susceptibility effect with a patient inside the magnet, **(2C)** Result after shimming. Two water signals (free water and bond water) are shown in slow exchange. They are chemically indistinguishable but with different rotational and translational energies, and thus different T2.

In small FOV imaging (such as of small joints of hand, wrist, or foot), field inhomogeneities and susceptibility variation in the imaging volume is smaller. Sinc pulses with sharper frequency profiles are available for excitation in this case (Fig. 4A). Broadened saturation pulses suppressing residual fat signal can also be off-set to lower frequencies to avoid partial water suppression (Fig. 4B).

This technique is less robust in large FOV imaging (e.g., thorax, abdomen or breast) where large variation of field inhomogeneities and susceptibility effects leads to spectral line broadening for both fat and water over the imaging volume. The spectrally selective technique for fat suppression or water excitation is, therefore, less effective.

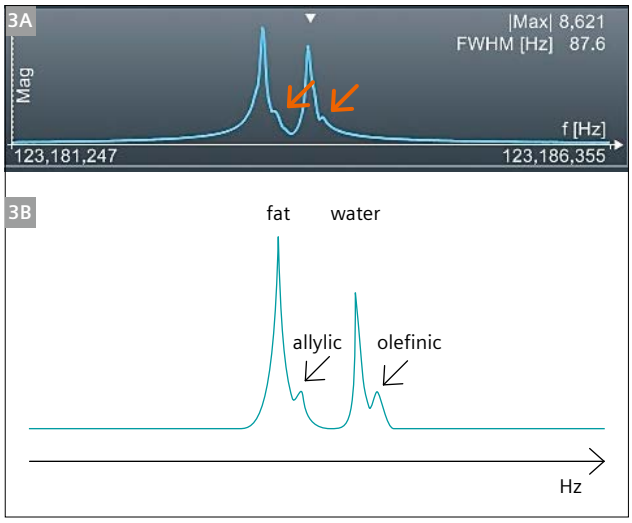

3 Ideal shim when signals for olefinic and allylic protons are resolved. Note that the scale in 'adjust frequency confirm' is from 0 Hz to 5000 Hz. Water resonates at a higher frequency; thus, the spectrum appears mirrored to the ppm scale. Signals from olefinic and allylic protons are approximately 5% of the main methylene peak.

Dixon method: 'Phase-related techniques'

When spins are tipped onto the transverse plane, their phase (angular position in the transverse plane) evolved over time, TE (the 'evolution-period'), is given by the product of their corresponding resonance frequency and TE. Note that frequency shifts due to B_0 inhomogeneities also affect phase shift.

Phase-related water-fat separation

TE in a sequence can be used to encode chemical shift information. At a given TE, species with different resonance frequencies (or chemical shifts) will have different phases in the transverse plane. By collecting echoes at multiple TE values, the phases of these echoes can be used to resolve the different species in the imaging volume. This is the principle of chemical shift imaging [5]. For this method to work, the number of echoes must be equal to or greater than the number of chemical species to be separated.

Dixon [6] first proposed collecting two echoes at two different TE values to separate water and fat. The two TE values were chosen such that water and fat will have the same phase (in-phase) in one TE and opposite phase (out-of-phase, i.e., 180°) in the other TE (the so-called 'two-point Dixon'). The in-phase and out-of-phase images are then added or subtracted to produce fat-only and water-only images. At 1.5T where water and fat spectra are separated by ~210 Hz, it would take ~2.2 ms to develop a 180° phase difference between water and fat in the two echoes. Echoes will be out-of-phase again at

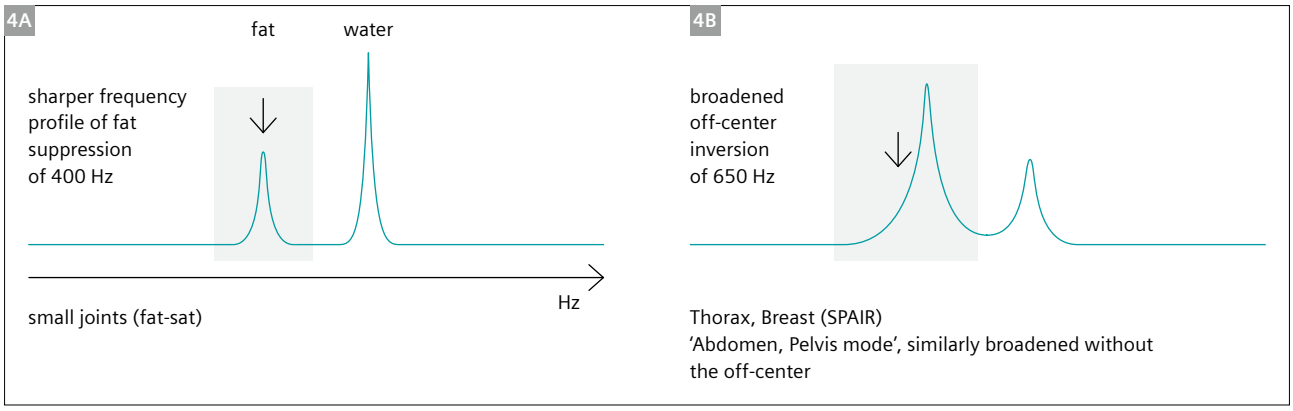

4 Bandwidth of **(4A)** fat-saturation, **(4B)** adiabatic inversion (SPAIR).

TE = 6.6 ms, 11 ms, etc. These are the differences the two TE values need to observe in the Dixon method and are magnetic field dependent. The two echoes can be collected in two separate acquisitions or as dual echo in one acquisition.

In practice, B_0 inhomogeneity changes the resonance frequencies of the chemical species and introduces phase errors in the echoes in this method. Taking this into account, Glover [7] later proposed to collect one more echo ('three-point Dixon'). Information from the three echoes is then used to derive the water image, fat image, and B_0 inhomogeneities.

TSE-Dixon: An alternative approach

The Dixon method requires specific TE values to achieve in-phase and out-of-phase images. However, in TSE-Dixon, TE and inter-echo spacing are chosen based on contrast and readout bandwidth among other considerations. The constraints imposed on the choice of TE values by the Dixon method severely limit the possible TE values allowed in TSE. Moreover, these TE values are magnetic field strength dependent.

In this alternative approach, fat-water images with variable contrasts (or TE values) are reconstructed from the multiple echoes in TSE without requiring water and fat to be in-phase or out-of-phase [8]. A signal model is then used (in *syngo* MR E11 software) to identify the water and fat components. The information is used to reconstruct the water and fat images in a two-point Dixon manner at non-180° phase shifts in conjunction with a seed-growing algorithm [9]. This greatly increases the flexibility on the choice of TE in TSE-Dixon. Protocols are no longer dependent on the magnetic field and gradient strengths. Inter-echo times as short as about 2 ms and up to 12.5 ms are now possible for T2-Dixon. There is also an averaging effect when multiple echoes of a pulse train are used in the model fitting. BLADE acquisition mode in TSE-Dixon further reduces motion artefacts.

STIR/SPAIR: 'T1-related technique'

As the T1 of fat is very short, so is the inversion time needed to null it (i.e., short TI). The STIR (short tau inversion recovery) and SPAIR (spectral attenuated inversion recovery) methods both use an inversion pulse followed by a short TI (appropriately selected to null fat) for recovery before image acquisition. Note that T1 and hence TI depends on B_0 (1.5T versus 3T) but not on B_0 inhomogeneities. Thus, it is the method of choice for large FOV imaging, such as in breast, abdomen, pelvis, thorax and neck, especially in coronal view.

The difference between STIR and SPAIR

A golden rule in MRI is that an advantage comes with a disadvantage. The inversion-recovery technique STIR is insensitive to main field inhomogeneity. However, it is also chemically *non-selective*. Since the inversion pulse affects both fat and water protons, image contrast and SNR are also both altered. Unlike STIR, SPAIR is chemically selective [10]. It is targeted to the frequency of fat, leaving the contrast of water protons untouched. It is therefore the method of choice when B_0 homogeneities are acceptable.

The difference between selective fat inversion and spectral fat saturation

A larger FOV covers a wider range of B_0 inhomogeneities and thus results in broader lines as shown in Figure 4B. This may result in partially overlapping water and fat signals. As an additional parameter, the frequency of the adiabatic fat inversion pulse can be shifted to lower frequencies, avoiding water contamination, especially for thorax and breast imaging. The frequency shift is a trade-off to suppress any residual fat and not affect the water signal.

Pictorial essay

In Figures 5 to 11, we show how to use the spectrum in 'Confirm Frequency Adjustment' after shimming to guide the choice of optimal protocol and give a side-by-side pictorial essay of these spectra and the corresponding fat-sat, TSE-Dixon or SPAIR images. This is demonstrated on a MAGNETOM Skyra 3T with *syngo* MR E11 software.

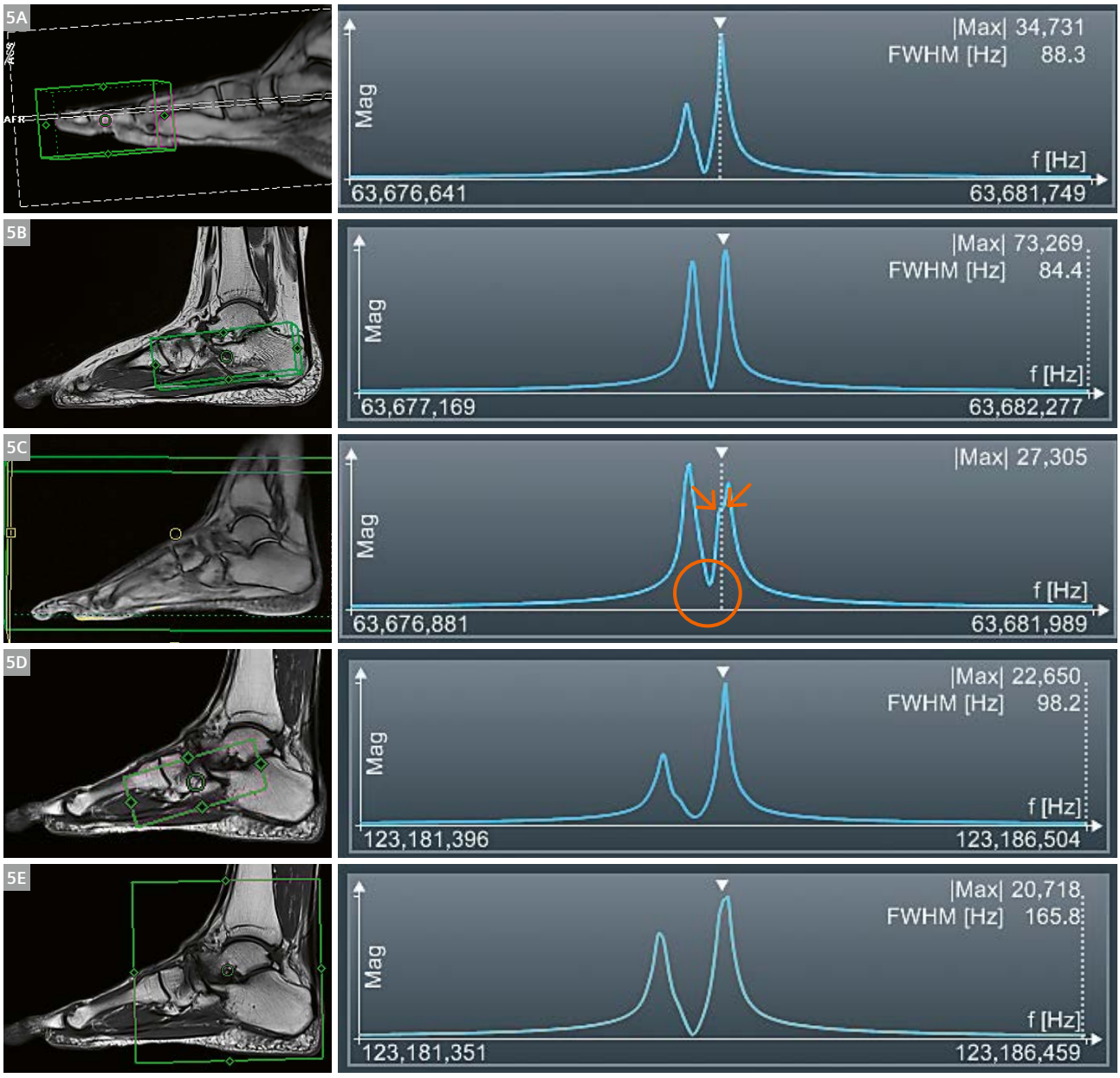

5 Shim box of different volumes for the foot
In shim box planning, there is a trade-off between its size and air/tissue. **(5A–C)** at 1.5T (MAGNETOM Area, MAGNETOM Avanto^{fit}). Small volumes avoiding air within the shim box result in good shim quality for fat saturation or SPAIR **(5A, B)**. Volume of entire foot **(5C)** has a different air-fat-water composition. Different water frequencies are now superimposed due to B_0 inhomogeneities (arrows). As fat and water signals partially overlap (circle), off-center SPAIR or TSE-Dixon with a seed-growing algorithm are the preferred sequences. Similar results at 3T **(5D, E)**. Signals for olefinic and allylic protons are partially resolved in **(5D)**, whilst in **(5E)** the signals are broadened by susceptibility effects of inhomogeneous tissue composition of air, subcutaneous fat, bone marrow, tendons, and muscles.

Conclusion

Should adjustments be hidden in the background or should they guide the operators planning the scans? Both can be correct in different cases. With technological advancements in MRI, the 'push button' technology is adequate for most routine scans.

Shimming results could indicate how to proceed with techniques that rely on the linewidth of the signal. This is especially true for MR spectroscopy of areas with hemorrhage or other susceptibility effects in close proximity. This applies in a similar way to the fat-water separation. Pathologies may cause stronger susceptibility effects which broaden the signals. As shown in the pictorial essay, the shape of the water-fat signals has been affected in variably by the patient's susceptibility, but their separations are satisfactory for scanning accurately fat-suppressed images. If fat and water signals overlap or multiple fat-water patterns are visible due to strong B_0 inhomogeneities, shimming should be repeated for a different volume or orientation and the scan protocol adapted to integrate the variety of new options in the fat-sat, TSE-Dixon, and SPAIR protocols in *syngo* MR E11 software.

References

1 Bley TA, Wieben O, François CJ, Brittain JH, Reeder. Fat and Water Magnetic Resonance Imaging. JMRI, 2009; 31:4–18.
2 Ho JXM, Chan LL, Rumpel H. How Modules of Imaging Sequences Fit Together: An Overview of Recent Advances in MR Imaging. MAGNETOM Flash, 2014; 60:82-87.
3 Schwartz AV. Marrow Fat and Bone: Review of Clinical Findings. Frontiers in Endocrinology. 2015;6:40. doi:10.3389/fendo.2015.00040.
4 Juchem C. Shimming: Fields, Coils and Control. Proc Intl Soc Mag Reson Med 21, 2013.
5 Rumpel H, Pope JM. Chemical Shift Imaging in Nuclear Magnetic Resonance: A Comparison of Methods. Concepts in MagnReson 1993; 5:43-55.
6 Dixon WT. Simple proton spectroscopic imaging. Radiology 1984; 153:189-194.
7 Glover GH, Schneider E. Three point Dixon technique for true water fat decomposition with B_0 inhomogeneity correction. Magn Reson Med, 1991; 18:371-383.
8 Ma J. Dixon Techniques for Water and Fat Imaging. JMRI, 2008; 28:543–558.
9 Yu H, Reeder SB, Shimakawa A, Brittain JH, Norbert J. Pelc NJ. Field Map Estimation with a Region Growing Scheme for Iterative 3-Point Water-Fat Decomposition. MRM 2005; 54:1032-1039.
10 Lee YS, Low CK, Rumpel H. STIR versus SPAIR in Breast Imaging: A Case-Based Discussion. MAGNETOM Flash, 2011; 46:54-55.

Abbreviations

TIRM:	short tau inversion recovery
SPAIR:	SPectral Attenuated Inversion Recovery
DESS:	Dual Echo Steady State
FWHM:	Full Width at Half Maximum

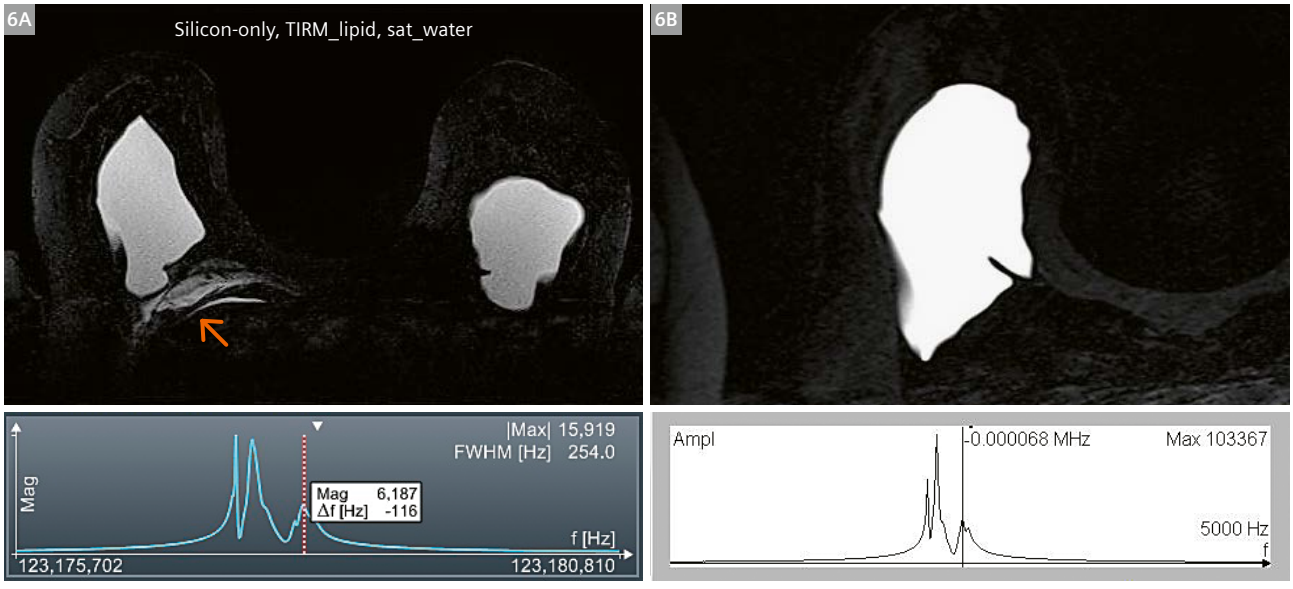

6 Readjustment of shim volume
Seatbelt injuries of the breast after an accident. Differentials are silicon leakage or hematoma/edema. 'Silicone-only' image with TIRM for fat-void and water-selective suppression a) with global shim, b) unilateral shim revealed better silicon-fat-water separation, and thus completes selective water suppression. (Silicon signal on the left followed by fat signal and water signal on the right.)

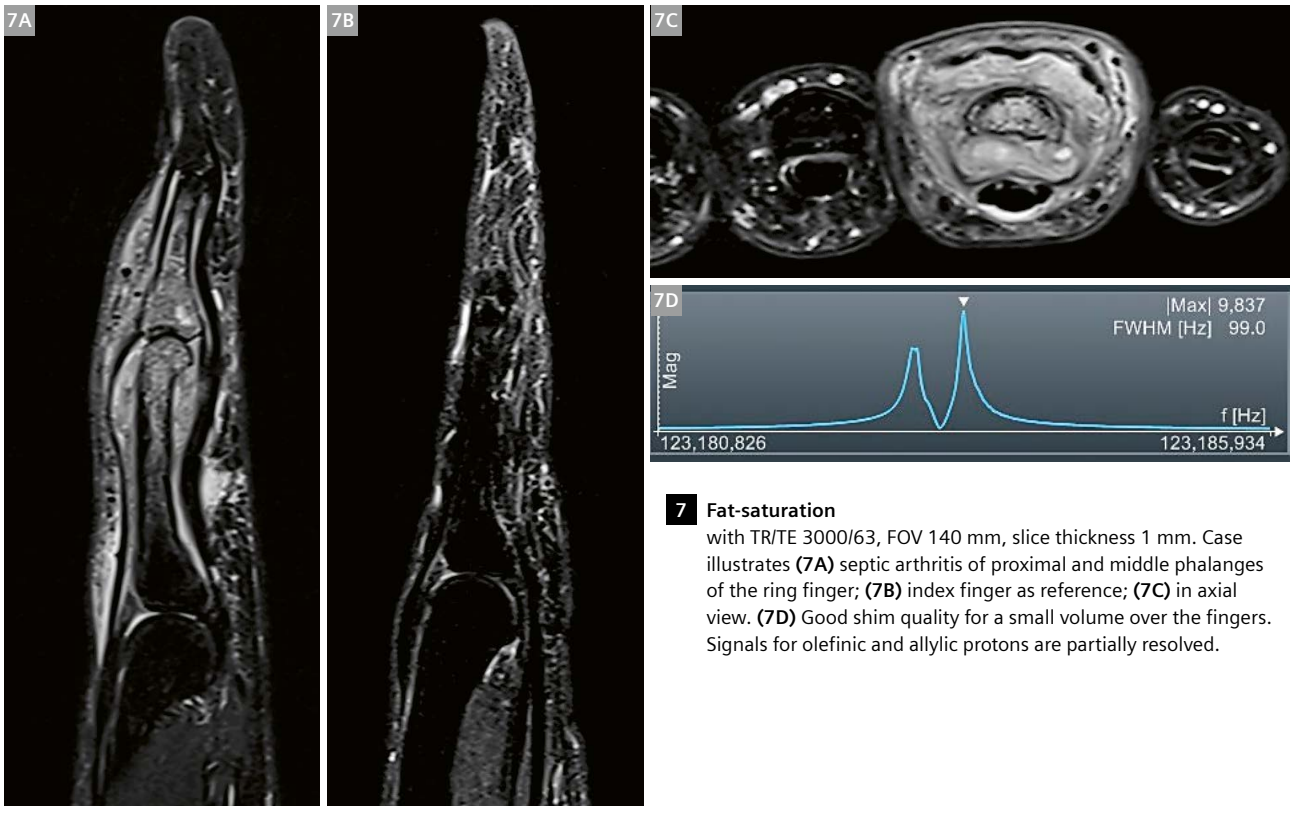

7 Fat-saturation
with TR/TE 3000/63, FOV 140 mm, slice thickness 1 mm. Case illustrates **(7A)** septic arthritis of proximal and middle phalanges of the ring finger; **(7B)** index finger as reference; **(7C)** in axial view. **(7D)** Good shim quality for a small volume over the fingers. Signals for olefinic and allylic protons are partially resolved.

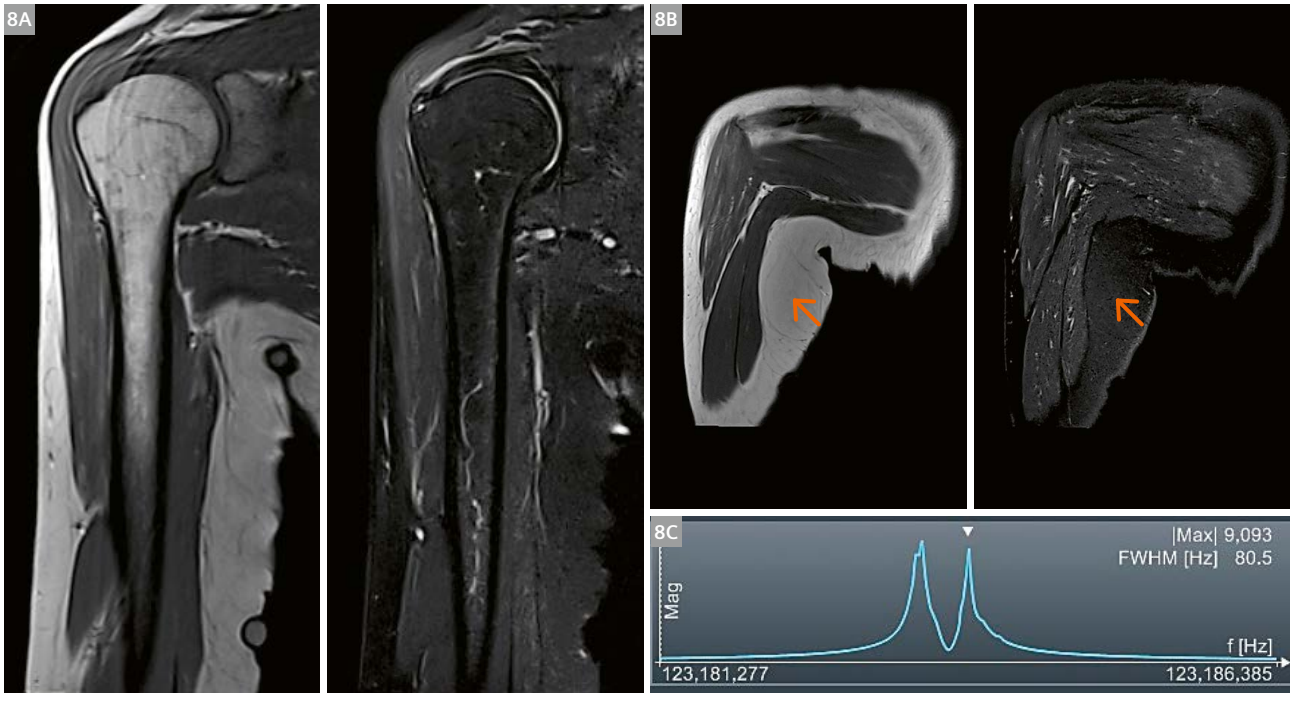

8 Fat-saturation
with TR/TE 3500/66, FOV 240 mm, slice thickness 3 mm. Case illustrates a lipomatous lesion. **(8A)** T1-weighted image and T2-weighted image with fat-saturation of long bone; **(8B)** lipoma demonstrated with arrow; **(8C)** good shim quality for a large volume over the shoulder and upper arm. Signals for olefinic and allylic protons are partially resolved.

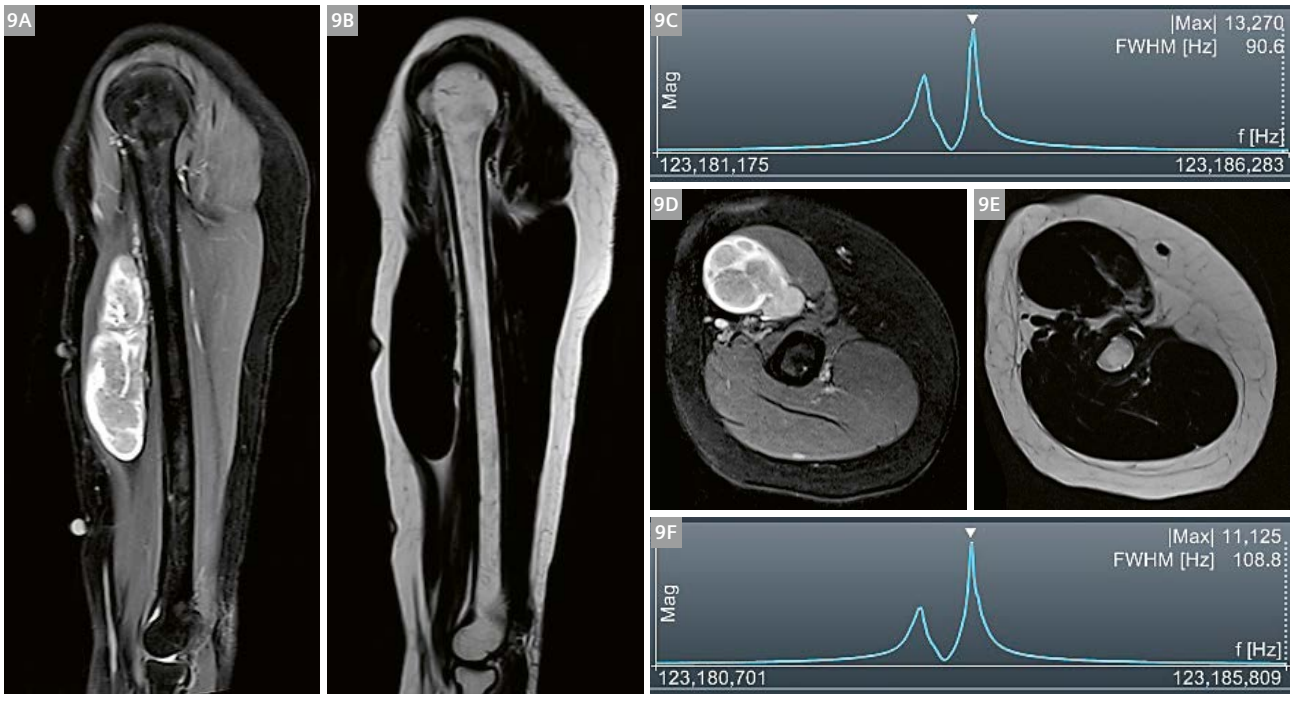

water-only fat-only

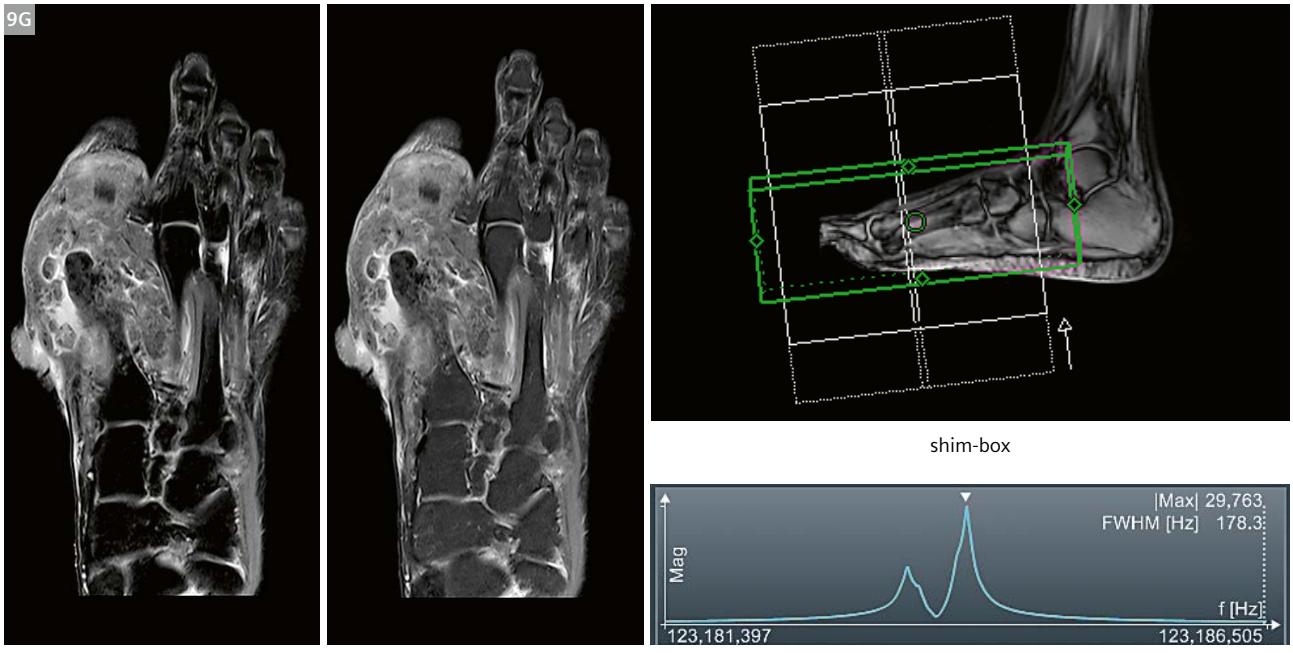

shim-box

water-only weak overlay of fat

9 TSE-Dixon
with TR/TE 5200/TE56, inter-echo spacing 9.3 ms, turbo factor 13, applied to regions of good shim quality: **(9A–F)** Case illustrates neurofibroma, demonstrated in sagittal and axial orientation of the upper arm, **(9G)** Case illustrates gout arthritis and infection of the foot. Dixon water-only image and with weak fat-suppression option are shown.

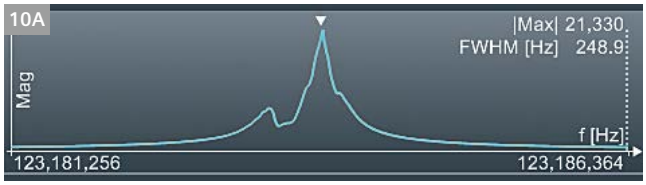

10 TSE-Dixon
with TR/TE 4400/82, inter-echo spacing 10.2 ms, turbo factor 11. **(10A)** Fat-water pattern shows intentionally 'poor' shim with partially overlapping peaks; **(10B)** fat-only and water-only images based on two-point Dixon and region growing algorithm with excellent fat-water delineation.

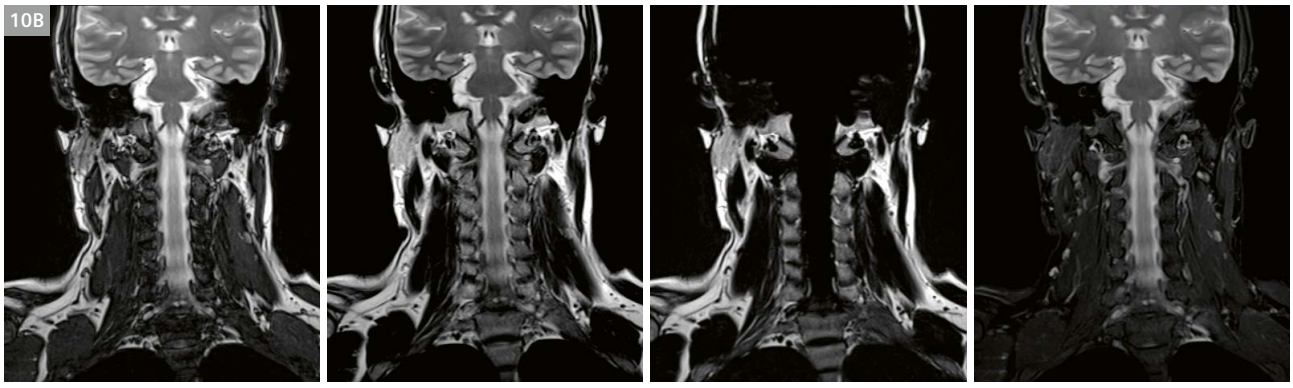

phase-in | phase-out | fat-only | water-only

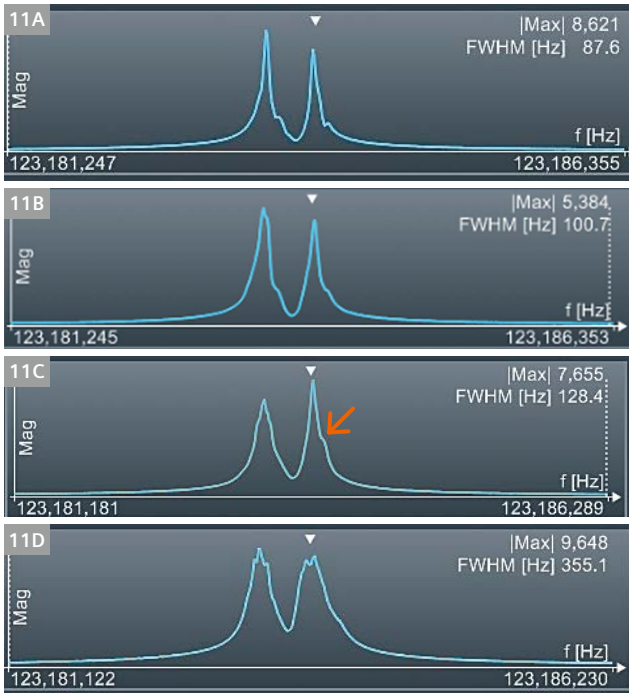

11 Abdomen protocol (T2-SPAIR)
Four clinical scenarios are shown according to shim quality: **(11A)** Ideal shim: Case illustrates kidney nodules. **(11B)** Good shim: Case illustrates liver for hepatocellular carcinoma. **(11C)** Acceptable shim: Slightly different water frequencies are superimposed due to B_0 inhomogeneities rather than a partially resolved signal of olefinic protons (arrow) based on signal intensities. Broadening of the signals is observed.

(11D) Suboptimal shim: Surgical clip within the region of interest broadens the water signal more than 4-fold. Improved shim may be obtained with 'thorax mode' for off-center fat inversion or TSE-Dixon.

Soo Lee Lim | Jamie Xiu Mei Ho | Weiling Lee

Contact

Weiling Lee, MMagResonTech
Department of Diagnostic Radiology
Singapore General Hospital
Outram Road, Block 2, Level 1
Singapore 169608

Lung MRI in Parenchymal Disease

Gaël Dournes, M.D., Ph.D.[1,2,3]

[1] Université de Bordeaux, Centre de Recherche Cardio-Thoracique de Bordeaux, France
[2] Inserm, Centre de Recherche Cardio-Thoracique de Bordeaux, France
[3] CHU de Bordeaux, Service d'Imagerie Thoracique et Cardiovasculaire, Service des Maladies Respiratoires, Service d'Exploration Fonctionnelle Respiratoire, Pessac, France

Introduction

Lung MRI has long been considered beyond the scope of MR examinations due to specific technological challenges. These include very low lung proton content, susceptibility artifacts at alveolar and parenchymal interfaces, and cardio-respiratory motions. However, recent technological solutions have emerged that could improve the clinical application of lung MRI. MRI is a radiation-free imaging modality that offers the possibility of combining both morphological and functional information, including tissue contrast characterization. This is important in an era where novel therapies have revolutionized the management of patients, which can lead to an increased need for repeat imaging to assess response to a certain treatment. In addition, artificial intelligence could allow advanced combination of data to better phenotype patients and/or predict disease outcome, since it goes beyond just morphological information. Thus, lung MRI may eventually prove a powerful tool to determine the full complexity of lung diseases that are still by no means well understood. In the following article, we summarize the most recent advances in lung MRI and give examples from our own clinical experience, with a particular focus on the potential benefit of lung MRI for routine clinical use. Images have been acquired using a 1.5T MAGNETOM Aera MRI scanner.

1. Morphological MRI

1.1 Lung MRI with ultrashort echo time

The most prominent development in morphological MRI is the advent of 3-dimensional (3D) sequences using Ultrashort Echo Time (UTE)[1] [1, 2] or even Zero Echo Time (ZTE)[1]. These sequence techniques overcome the technical difficulty of lung MRI due to the very fast decay of the lung signal, caused by the short T2* of the lung parenchyma, by shortening the TE down to a few microseconds. Conventional MR sequences use echo times in the order of magnitude of the millisecond. Imaging quality similar to that of a CT scan has been demonstrated using 3D UTE MRI in airway [3], interstitial lung disease [2] or lung nodules [4]. To date, two main sequence acquisition schemes have been developed to capture the *k*-space either with spheres or stacks of spirals. Recent evaluation has shown that a spherical mode of acquisition provides clearer detail and a higher signal than stacks of spirals. However, the 3D UTE Spiral VIBE prototype sequence[1] comprises a fully automated respiratory synchronization was possible using the stack-of-spirals sequence. This was found to be more robust to motion and therefore potentially suitable for routine applications [2].

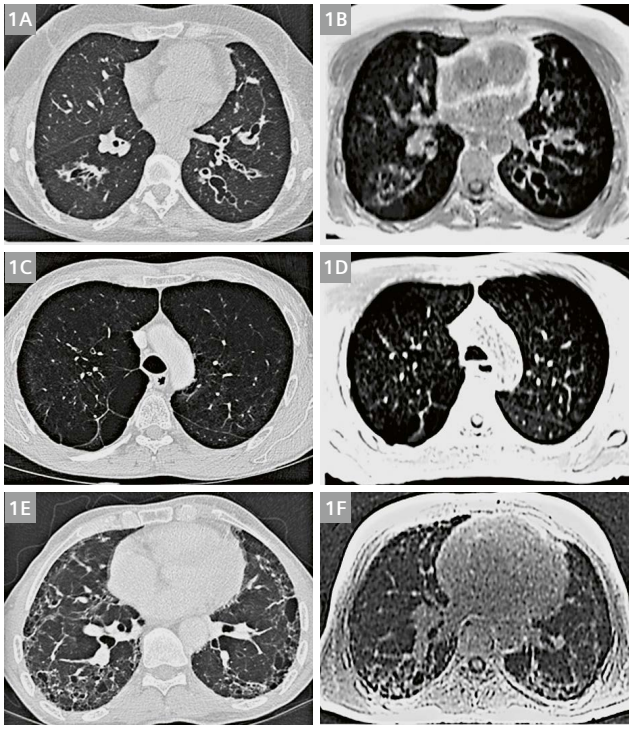

1 **Morphological MRI**
CT **(1A, C, E)** and 3D UTE spiral VIBE sequence[1] **(1B, D, F)** acquired in a patient with cystic fibrosis (1A, B); chronic obstructive pulmonary disease (1C, D); and idiopathic fibrosis (1E, F). Images 1A and B show indications of proximal airway alteration, such as bronchiectasis, wall thickening, and mucus plugs. Images 1C and D show destruction of the lung parenchyma. This can be seen as hypoattenuating areas using CT imaging (1C) or hyposignal intensity on MRI (1D). Images 1E and F show interstitial modifications such as honeycombing, reticulation, and traction bronchiectasis. Note the good visual agreement between CT and 3D UTE MRI to depict structural alterations at high resolution.

[1] *WIP, the product is currently under development and is not for sale in the U.S. and in other countries. Its future availability cannot be ensured.*

1.2 Qualitative and quantitative imaging of airways

Imaging of airways is one the most challenging areas of lung MRI. Indeed, imaging of the central bronchi requires high spatial resolution to achieve clear distinction between the airway wall and airway lumen. Conversely, small airway disease requires high contrast resolution to allow identification of parenchymal intensities lower than that of the normal lung, as a surrogate of small airway disease alterations. Radiation-free evaluation of patients with chronic airway diseases such as cystic fibrosis or asthma, has been used to create an MR scores of disease severity.

3D UTE could be used not only to visualize structural abnormalities qualitatively (Fig. 1) but also to quantify the extent of disease (Fig. 2). In this context, quantification of central airway remodeling has recently been reported in 3D [5], as well as volumetric quantification of emphysema in patients with COPD [6]. These quantitative measurements may be beneficial to improve the reproducibility and the reliability of structural evaluation, as compared with visual analysis.

1.3 Interstitial lung disease

3D UTE allows visualization of visual parenchymal alterations such as honeycombing, reticulation, traction bronchiectasis, cysts or ground glass opacities, with similar reproducibility to that of gold standard CT imaging (Fig. 2). Imaging plays a pivotal role in the management of patients with interstitial lung disease (ILD), and MRI may also play a role in improved phenotyping of patients.

1.4 Evolution of respiratory synchronization.

Image acquisition with 3D UTE with high isotropic resolution still takes several minutes and therefore respiratory motion compensation is needed. Early respiratory synchronization has been proposed using external devices such as a belt. These devices were shown to be inefficient at suppressing motion adequately in certain cases such as obese patients or patients with irregular breathing [2]. More recently, respiratory synchronization using fully automated sequences makes this potentially suitable for routine applications [7]. Novel applications using 4D MRI with dynamic lung MR imaging have also been reported [8]. A further recent approach has shown that MRI could be applied *in vivo* using pulsatile flow ventilation with breath-hold for 10 minutes or longer [9].

2. Contrast MRI

2.1 T1- and T2-weighted MR sequences

The true benefit of MRI is the ability to add tissue contrast characterization to purely morphological information. Critical phenomena related to inflammation or remodeling processes can be seen, which can allow clinicians to adapt or follow-up treatment.

At our institution, we use the T1 VIBE sequence, which is a gradient echo sequence using low flip angle and rapid repetition time. A spoiler removes transverse magnetization and offers strong T1 weighting. The main advantage of T1 VIBE is the rapid acquisition, enabling T1 information to be obtained within an apnea of less than 15 seconds.

To obtain T2 contrast information, the T2 BLADE sequence is one of the most commonly used sequence for lung imaging. The blade-like trajectory through *k*-space offers some unique advantages. The center of *k*-space, which contains the highest signal amplitude and contributes most to image contrast, is oversampled, meaning that the signal-to-noise and contrast-to-noise ratios are high. Over-sampling in this region also leads to redundant information, meaning that the data for new each blade can be compared to the data from previous blades for consistency. If the patient moves between blades, the data for the second blade can be corrected (or even completely discarded) based on how anomalous its key information appears. Owing to the need for long TE and TR, the sequence is

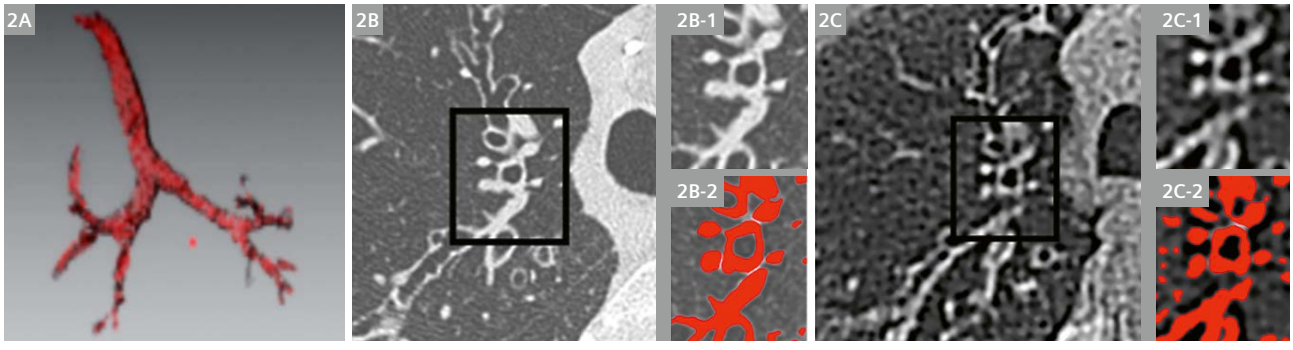

2 **Morphological MRI**
Quantitative measurement of central airways using 3D UTE MRI. Owing to the 3D isotropic resolution of the 3D UTE sequence and the contrast difference between bronchial air and the lung parenchyma, a 3D extraction of the bronchial tree from MRI was possible **(2A)**. Images 2B and 2C represent the right superior lobe of a cystic fibrosis patient using CT imaging **(2B)** and 3D UTE MRI **(2C)**. The black rectangle indicates the area of magnification of the right apical segmental bronchus as shown on 2B-1 (CT imaging) and 2C-1 (MRI), respectively. The high spatial resolution of MRI makes automated quantification of the bronchial wall and lumen areas feasible (shown here in red on 2B-2 and 2C-2).

T2-weighted. Moreover, respiratory synchronization using a navigator positioned on the diaphragm also allows the removal of respiratory motion artifacts.

2.2 Characterization of airway inflammation

Acute inflammation of the airways causes increased water and cellular content within the airway wall and/or lumen, which results in increased signal in a T2-weighted acquisition [10, 11]. A T2 BLADE sequence enables a more sensitive detection of airway inflammation (Fig. 3). Combining T1 and T2 sequences has also been demonstrated as efficient in increasing the specificity of evaluation. In a study conducted in 110 patients with cystic fibrosis, mucus impaction with the so-called IMIS sign (Inverted Mucoid Impaction Signal) was found to be 100% specific for the diagnosis of allergic broncho-pulmonary aspergillosis (ABPA) (Fig. 4). This is particularly important in CF patients, since ABPA requires the use of corticosteroids instead of antibiotics [12]. A quantitative measurement of T1 or T2 mapping is also possible using novel sequences, combining both morphological T2 and T2 quantification [13] (Fig. 5).

2.3 Detection of inflammation in ILD

ILD may also benefit from the use of contrast characterization. Lung inflammation can be visualized accurately using T2 contrast.

Specific evaluation can also be found in some disease conditions, where an increase in iron can modify the signal from the lung parenchyma.

Characterization and quantification of T1 and T2 are also possible using novel MR sequences and mapping of the lung signal [13, 14]. These quantifications may open up the possibility of quantitative evaluations in ILD to assess disease extent or severity, especially in patients undergoing specific treatment (Fig. 6).

2.4. Diffusion MRI

Diffusion MRI can be used to differentiate between those areas of inflammation associated with increased cellular content and those related to increased vasogenic edema, i.e. free water content (Fig. 7). Combining the extent of T2-weighted diffusion MRI visually has been shown to discriminate CF patients with respiratory exacerbation

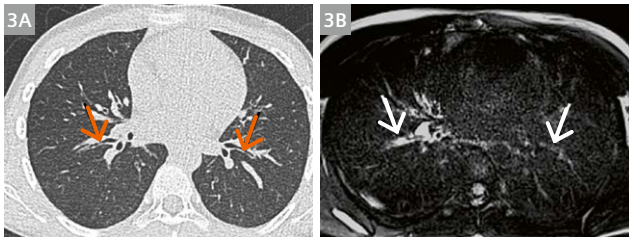

3 **Contrast MRI**
CT scan **(3A)** and T2 BLADE MRI **(3B)** of a 9-year-old female with cystic fibrosis during respiratory exacerbation. On the CT image, orange arrows indicate segmental bronchi that do not appear morphologically different. On the MR image, there is a marked hyperintense T2 signal from the right-sided bronchi compared with the left bronchi (white arrows) indicating an acute inflammatory state of the right lung.

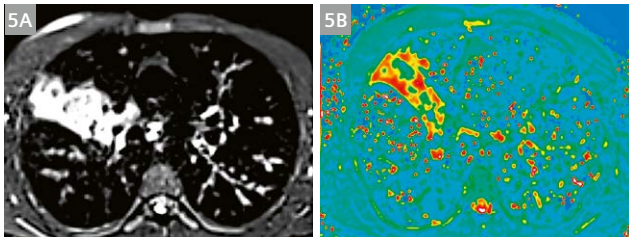

5 T2 radial TSE **(5A)** and corresponding T2 mapping reconstruction **(5B)** in a male with cystic fibrosis and respiratory exacerbation. Both morphological information (5A) and signal intensity information (5B) are available to assess the disease severity and follow-up treatment, both qualitatively (5A) and quantitatively (5B).

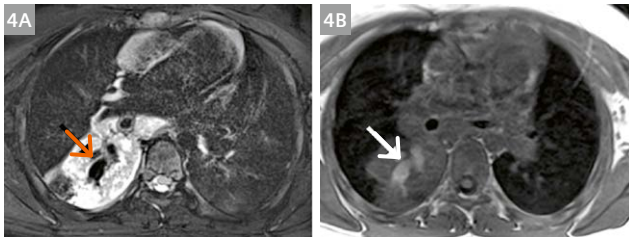

4 T2-weighted **(4A)** and T1-weighted **(4B)** MRI of a young female with cystic fibrosis. There is acute lung consolidation of the right lower lobe shown by hyper T2 and hypo T1 contrasts. Conversely, there is a large bronchocele within the lung infiltrate with complete reversal of contrast. This is indicated by the hypo T2 (orange arrow) and hyper T1 (white arrow) contrasts. The inverted mucus impaction signal (IMIS) is specific to the diagnosis of allergic bronchopulmonary aspergillosis, which requires corticosteroid treatment.

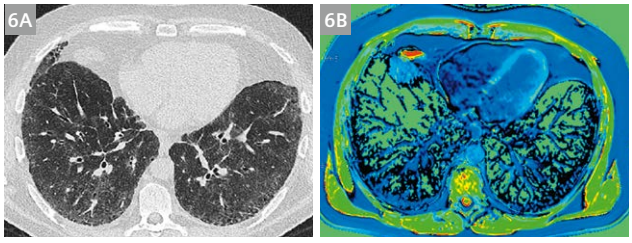

6 CT scan **(6A)** and postcontrast-enhaned T1 mapping **(6B)** in a young male with severe sarcoidosis. There is diffuse ground glass opacity on image 6A. On image 6B, the postcontrast reduction of T1 values is predominantly located within the peribronchovascular and subpleural regions. This indicates the lymphatic dominance of lesions, which is in agreement with the physiopathology of the disease. Note that the degree of T1 reduction can be quantified on image 6B.

[15]. However, the spatial resolution of Diffusion MRI does not allow the assessment of fine structures such as bronchial wall and mucus plugs, whereas the signal visible on Diffusion MRI relates to both a T2-shinethrough effect and a diffusion effect [16].

3. Functional MRI

3.1 Contrast-enhanced MRI of perfusion

One of the most widely documented applications of functional MRI is MRI perfusion in chronic airway disease. In cystic fibrosis, it has been proposed that this evaluation technique could be part of the disease scoring of severity. Variations in treatment and applicability to children as young as 2 or 3 years old have been consistently demonstrated [17, 18]. Nevertheless, developing non-contrast-enhanced MR would increase the clinical applicability [16].

3.2 Contrast-enhanced MRI of ventilation

MRI of ventilation using noble gases has been a major breakthrough in the study of small airway disease impairment providing an exquisite level of details [20, 21]. Fusion between ventilation maps and morphological UTE volumes has been proposed to assess disease severity [22]. However, specialist MR scans are needed and the examination is cost-intensive.

Ventilation MRI using oxygen has also shown potential in cases of lung allograft rejection [23] or cystic fibrosis [24]. However, oxygen is non-specific between ventilation and perfusion.

3.3 Non contrast-enhanced MRI of ventilation and perfusion

A promising development in functional MRI is the Fourier decomposition MRI [25]. This technique has been shown to generate ventilation-weighted and perfusion-weighted maps, without any contrast product injection or ventilation (Fig. 8). The technique has been validated against hyperpolarized ^{3}He and dynamic contrast-enhanced MRI [26]. Another variant is SENCEFUL MRI [27]. However, this technique is 2D only and may require a very long acquisition time to cover an entire lung. Evaluation in patients with lung disease could be helpful by adding deeper insights into small airway disease in patients with asthma, COPD, or cystic fibrosis.

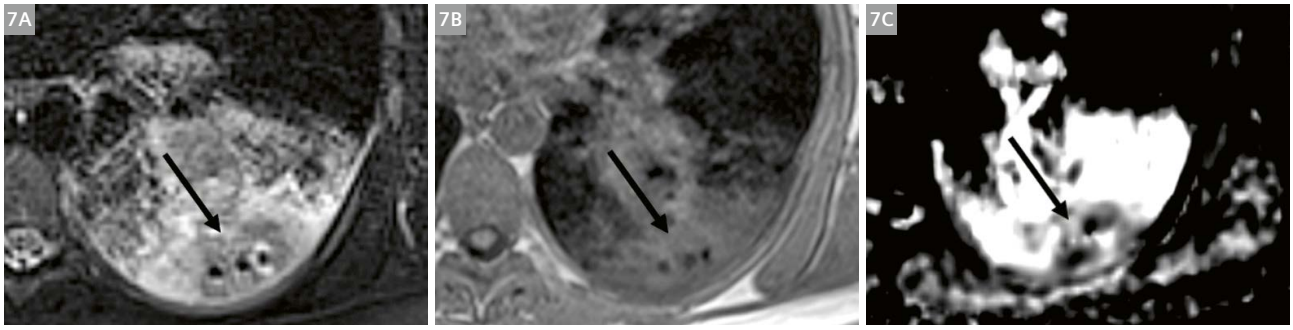

7 **Contrast MRI**
T2 BLADE **(7A)**, T1 VIBE **(7B)** and Diffusion **(7C)** MR sequences in a female with cystic fibrosis and respiratory exacerbation. There is an area of intra-parenchymal air within a lung consolidation of the left lower lobe (black arrow). The diffusion coefficient map in C confirms a restricted area within a water-filled consolidation. This is compatible with an abscess that requires intensive antibiotic therapy.

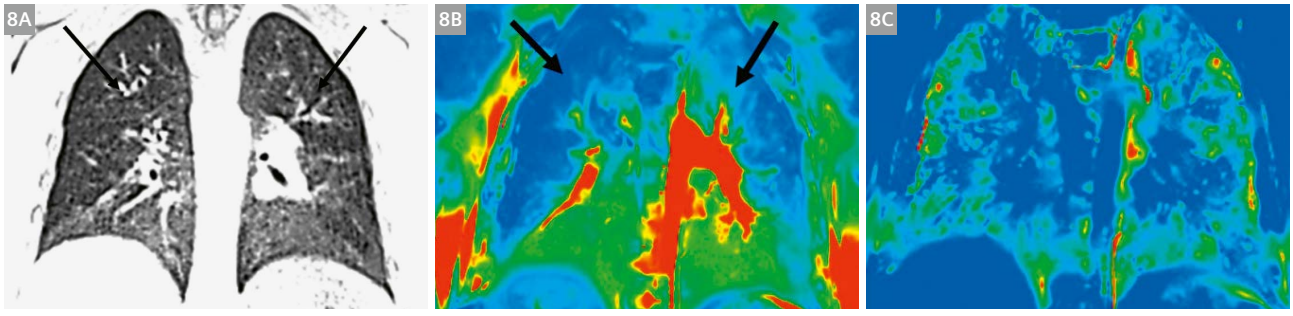

8 **Functional MRI**
3D UTE **(8A)** and Fourier transform reconstruction of lung perfusion **(8B)** and ventilation **(8C)** in a young female with cystic fibrosis and respiratory exacerbation in a coronal view. Black arrows show areas of reduced perfusion on image B, with a regional distribution resembling the areas of hypointensities on image 8A. However, there are multiple ventilation defects on image 8C that do not perfectly match the perfusion defects, reflecting the two different types of information.

3.4. Contrast-enhanced MRI in ILD

A few reports exist on the use of contrast agents in ILD in humans. However, better characterization of tissue components related to fibrosis (Fig. 9), inflammation or vascular disease could be expected from MRI [28].

4. Proposed lung MR protocol

Physicians can, of course, always adapt their protocol according to the clinical context. For routine application, the main constraints are imaging quality, acquisition time, and the tolerability of the patient, especially those with breathing difficulties.

Therefore, the prototype 3D UTE Spiral VIBE[1] pulse sequence has a strong argument for consideration as the core of any MR protocol dedicated to lung imaging. Indeed, 3D UTE delivers morphological information similar to that from a CT scan. Isotropic voxel dimension enables 3D reformations in all directions, preventing the need for repeated 2D acquisitions. The lack of repetition of MR sequences leads to a dramatic reduction in acquisition time. This makes the procedure more tolerable for the patient, especially when repetition of 2D sequences may require repeated breath-holding maneuvers. In addition to the information provided on central airways, UTE MRI also visualizes variations in the signal of the lung parenchyma as a surrogate for distal airway remodeling.

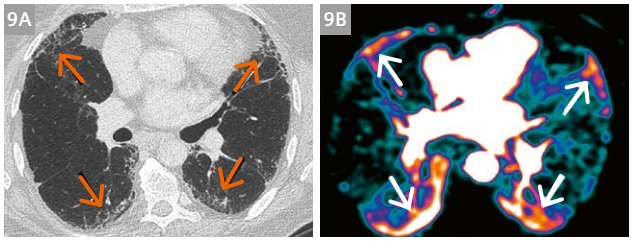

9 CT image **(9A)** and first-pass perfusion MRI **(9B)** in an older male with idiopathic pulmonary fibrosis. Orange arrows on the CT image indicate areas of honeycombing. There is marked increased velocity in first-pass perfusion in the areas of honeycombing on image 9B (white arrows).

Moreover, simple tissue contrast characterization is possible using MR sequences such as T1 VIBE and T2 BLADE. The former lasts 15 seconds within a single breath-hold and the latter usually 3 to 4 minutes in free breathing.

Vascular assessment is often beneficial for follow-up of patients with chronic lung disease, owing to the need for catheter placement that may potentially lead to complications due to thrombus. A quick overview of the vascular trunks and bed can be provided, for example using the TrueFISP sequence.

Finally, functional MRI with or without contrast product injection or inhalation may be used either in a specific disease condition or to answer research questions.

Table 1 summarizes the proposed standardized lung MR protocol including 3D UTE MRI, T1 VIBE, T2 BLADE, and TrueFISP sequences as a core, in 8 to 10 minutes, and without contrast media exposure, and then with additional functional sequences adapted to the clinical context.

Conclusion

Lung MRI is a powerful tool to assess and follow-up lung diseases without the use of ionizing radiation. Recent technological innovations allow the robust evaluation of both morphological and functional information with direct implications for clinical routine use.

Core protocol	Sequence	Acquisition time	Expected information	Typical clinical use
Morphology	3D UTE Spiral VIBE[1]	6 minutes	Isotropic high resolution with 3D reformations	Any
Contrast	T1 VIBE	15 seconds	T1 contrast	Any
	T2 BLADE	2–4 minutes	T2 contrast	Any
	TrueFISP	20 seconds	Vascular contrast	Any
Clinically oriented sequences				
Perfusion	Contrast-enhanced or noncontrast-enhanced sequence			Airway diseases
Ventilation	Contrast-enhanced or noncontrast-enhanced sequence			Airway diseases
Diffusion	DWI-MRI			Inflammation, cancer

Table 1: Proposed standardized lung MRI protocol for routine use

References

1 Dournes G, Grodzki D, Macey J, Girodet P-O, Fayon M, Chateil J-F, et al. Quiet Submillimeter MR Imaging of the Lung Is Feasible with a PETRA Sequence at 1.5 T. Radiology 2015 Jul;276(1):258–65.
2 Dournes G, Yazbek J, Benhassen W, Benlala I, Blanchard E, Truchetet M-E, et al. 3D ultrashort echo time MRI of the lung using stack-of-spirals and spherical k -Space coverages: Evaluation in healthy volunteers and parenchymal diseases. J Magn Reson Imaging 2018;48(6):1489-1497.
3 Dournes G, Menut F, Macey J, Fayon M, Chateil J-F, Salel M, et al. Lung morphology assessment of cystic fibrosis using MRI with ultra-short echo time at submillimeter spatial resolution. Eur Radiol 2016 Nov;26(11):3811–20.
4 Kumar S, Rai R, Stemmer A, Josan S, Holloway L, Vinod S, et al. Feasibility of free breathing Lung MRI for Radiotherapy using non-Cartesian k-space acquisition schemes. Br J Radiol 2017 Dec;90(1080):20170037.
5 Baldacci F, Laurent F, Berger P, Dournes G. 3D human airway segmentation from high hesolution MR imaging. Eleventh International Conference on Machine Vision (ICMV 2018); 1-3 November, 2018; Munich, Germany.
6 Roach DJ, Crémillieux Y, Serai SD, Thomen RP, Wang H, Zou Y, et al. Morphological and quantitative evaluation of emphysema in chronic obstructive pulmonary disease patients: A comparative study of MRI with CT. J Magn Reson Imaging 2016 Dec;44(6):1656–63.
7 John P. Mugler, III, Samuel W. Fielden, Craig H. Meyer, et al. Breath-hold UTE Lung Imaging using a Stack-of-Spirals Acquisition. Proc. Intl. Soc. Mag. Reson. Med. 23 (2015); # 1476.
8 Feng L, Delacoste J, Smith D, Weissbrot J, Flagg E, Moore WH, et al. Simultaneous Evaluation of Lung Anatomy and Ventilation Using 4D Respiratory-Motion-Resolved Ultrashort Echo Time Sparse MRI. J Magn Reson Imaging 2019;49(2):411-422. [Epub 2018 Sep 25].
9 Beigelman-Aubry C, Peguret N, Stuber M, Delacoste J, Belmondo B, Lovis A, et al. Chest-MRI under pulsatile flow ventilation: A new promising technique. PLoS One 2017;12(6):e0178807.
10 Wielpütz MO, Eichinger M, Biederer J, Wege S, Stahl M, Sommerburg O, et al. Imaging of Cystic Fibrosis Lung Disease and Clinical Interpretation. Rofo 2016 Sep;188(9):834–45.
11 Renz DM, Scholz O, Böttcher J, Maurer MH, Denecke T, Schwarz C, et al. Comparison between magnetic resonance imaging and computed tomography of the lung in patients with cystic fibrosis with regard to clinical, laboratory, and pulmonary functional parameters. Invest Radiol 2015 Oct;50(10):733–42.
12 Dournes G, Berger P, Refait J, Macey J, Bui S, Delhaes L, et al. Allergic Bronchopulmonary Aspergillosis in Cystic Fibrosis: MR Imaging of Airway Mucus Contrasts as a Tool for Diagnosis. Radiology 2017 Oct;285(1):261–9.
13 Natsuaki, Yutaka, Mahesh Bharath Keerthisavan, Ali Bilgin, Bradley D. Bolster, Kevin J. Johnson, Xiaoming Bi, Gerhard Laub, Maria I. Altbach. Flexible and Efficient 2D Radial TSE T2 Mapping with Tiered Echo Sharing and with "Pseudo" Golden Angle Ratio Reordering. Proceedings of the 25th ISMRM annual meeting, Honolulu, HI, May 2017.
14 R. Deichmann, A. Haase. Quantification of T1 Values by SNAP-SHOT-FLASH NMR Imaging. Journal of Magnetic Resonance 96, 608-612 (1992).
15 Ciet P, Serra G, Andrinopoulou ER, Bertolo S, Ros M, Catalano C, et al. Diffusion weighted imaging in cystic fibrosis disease: beyond morphological imaging. Eur Radiol 2016 Nov;26(11):3830–9.
16 Dournes G, Laurent F. Restricted magnetic resonance diffusion of lung consolidation is not specific for respiratory exacerbation. Eur Respir J 2017 Nov;50(5): doi: 10.1183/13993003.01621-2017.
17 Wielpütz MO, Puderbach M, Kopp-Schneider A, Stahl M, Fritzsching E, Sommerburg O, et al. Magnetic resonance imaging detects changes in structure and perfusion, and response to therapy in early cystic fibrosis lung disease. Am J Respir Crit Care Med 2014 Apr 15;189(8):956–65.
18 Wielpütz MO, Eichinger M, Wege S, Eberhardt R, Mall MA, Kauczor H-U, et al. Mid-Term Reproducibility of Chest MRI in Adults with Clinically Stable Cystic Fibrosis and Chronic Obstructive Pulmonary Disease. Am J Respir Crit Care Med 2019; doi: 10.1164/rccm.201812-2356LE.
19 Mall MA, Stahl M, Graeber SY, Sommerburg O, Kauczor H-U, Wielpütz MO. Early detection and sensitive monitoring of CF lung disease: Prospects of improved and safer imaging. Pediatr Pulmonol 2016 Oct;51(S44):S49–60.
20 Aliverti A, Pennati F, Salito C, Woods JC. Regional lung function and heterogeneity of specific gas volume in healthy and emphysematous subjects. Eur Respir J 2013 May;41(5):1179–88.
21 Thomen RP, Sheshadri A, Quirk JD, Kozlowski J, Ellison HD, Szczesniak RD, et al. Regional ventilation changes in severe asthma after bronchial thermoplasty with (3)He MR imaging and CT. Radiology 2015 Jan;274(1):250–9.
22 Woods JC, Conradi MS. 3He diffusion MRI in human lungs. J Magn Reson 2018 Jul;292:90–8.
23 Renne J, Lauermann P, Hinrichs JB, Schönfeld C, Sorrentino S, Gutberlet M, et al. Chronic Lung Allograft Dysfunction: Oxygen-enhanced T1-Mapping MR Imaging of the Lung. Radiology 2015 Jul;276(1):266–73.
24 Zha W, Nagle SK, Cadman RV, Schiebler ML, Fain SB. Three-dimensional Isotropic Functional Imaging of Cystic Fibrosis Using Oxygen-enhanced MRI: Comparison with Hyperpolarized 3He MRI. Radiology 2019 Jan;290(1):229–37.
25 Bauman G, Puderbach M, Deimling M, Jellus V, Chefd'hotel C, Dinkel J, et al. Non-contrast-enhanced perfusion and ventilation assessment of the human lung by means of fourier decomposition in proton MRI. Magn Reson Med 2009 Sep;62(3):656–64.
26 Bauman G, Puderbach M, Heimann T, Kopp-Schneider A, Fritzsching E, Mall MA, et al. Validation of Fourier decomposition MRI with dynamic contrast-enhanced MRI using visual and automated scoring of pulmonary perfusion in young cystic fibrosis patients. Eur J Radiol 2013 Dec;82(12):2371–7.
27 Veldhoen S, Weng AM, Knapp J, Kunz AS, Stäb D, Wirth C, et al. Self-gated Non-Contrast-enhanced Functional Lung MR Imaging for Quantitative Ventilation Assessment in Patients with Cystic Fibrosis. Radiology 2017;283(1):242–51.
28 Romei C, Turturici L, Tavanti L, Miedema J, Fiorini S, Marletta M, et al. The use of chest magnetic resonance imaging in interstitial lung disease: a systematic review. Eur Respir Rev 2018 Dec 31; 27(150): doi: 10.1183/16000617.0062-2018.

Contact

Dr. Gaël Dournes, M.D., Ph.D.
Centre de Recherche Cardio-thoracique de Bordeaux
INSERM U1045
Université Bordeaux Segalen
146 rue Léo Saignat
33076 Bordeaux Cedex
France
Tel: +33 5 57 57 46 02
Fax: +33 5 57 57 16 95
gael.dournes@chu-bordeaux.fr

The Importance of Collaboration between Clinical Radiology and Radiation Oncology in the Era of Precision Radiation Therapy

Amish Lakhani, MBBS MA (Cantab) FRCR[1]; Yat Man Tsang, BSc MSc PhD[2]; Roberto Alonzi, BSc MBBS MRCP FRCR MD[3]; Anwar R. Padhani, MBBS FRCP FRCR[1]

[1]Consultant Radiologist, Paul Strickland Scanner Centre, Mount Vernon Hospital, Northwood, Middlesex, UK
[2]Consultant Radiographer – Specialised Service Delivery, Mount Vernon Hospital, Northwood, Middlesex, UK
[3]Consultant Clinical Oncologist, Mount Vernon Hospital, Northwood, Middlesex, UK

Introduction

Radiation therapy is an essential component in the management of many cancer patients. It can be used for primary treatment, local control, and palliation in over 50% of cancer patients [1]. Radiation therapy has been shown to be an integral part of the treatment regime in 40% of patients who are cured of cancer, therefore making this treatment modality extremely cost-effective [2].

Key to the success of radiation therapy is the ability of the radiation oncologist to accurately delineate the tumor to maximize delivery of the radiation dose to the cancer whilst minimizing dose toxicity to the adjacent normal tissues. This has become increasingly possible with technological advances in highly conformal radiation therapy delivery methods such as intensity-modulated radiotherapy (IMRT) and stereotactic body radiation therapy (SBRT). Paralleling the advances in radiotherapy delivery methods are the technological advances in imaging with the development of next-generation techniques such as magnetic resonance imaging (MRI) with quantitative functional biomarkers, and positron emission tomography/computed tomography (PET/CT) with novel tracers. These advances in imaging have improved the sensitivity and specificity of identifying tumor location and extent [3]. In this article we highlight examples of these advancements and demonstrate how collaboration between the clinical radiology and radiation oncology departments enhances treatment effectiveness.

Imaging in the cancer patient's pathway

Imaging is an integral component in almost every step of the cancer patient's pathway from detection and localization of cancer all the way to monitoring for recurrence once treatment is completed (Fig. 1). Using prostate cancer as an example, we will demonstrate how technological advancements in imaging are able to image the tumor microenvironment and normal tissues, and how we can use this to aid accurate and successful radiation treatments.

Multiparametric MRI (mpMRI) of the prostate is now routinely used in patients with suspected prostate cancer [4]. With mpMRI we can utilize multiple MRI sequences to depict different biological properties: Morphological T1 and

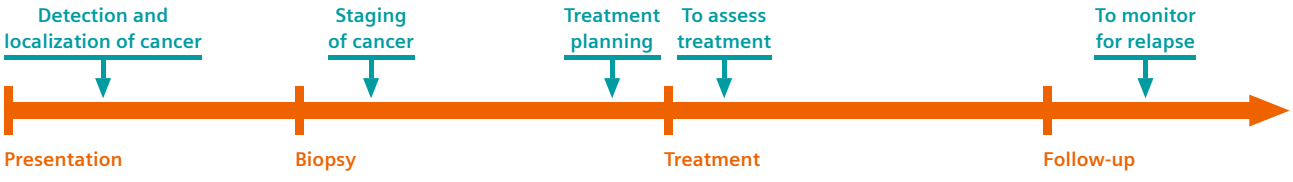

1 Imaging (green arrows) is integral throughout the cancer patient's pathway (orange arrow).

T2-weighted sequences give us information on anatomy; diffusion-weighted imaging (DWI) informs us of cellular density and necrosis; spectroscopy identifies cell proliferation and replacement of normal glandular tissues; and dynamic contrast enhancement (DCE) gives us information on perfusion and vascular permeability. Utilizing these properties it is possible to accurately detect, localize, and locally stage prostate cancer. mpMRI is also important to guide and/or direct biopsy via fusion techniques, and MRI may also be used to perform an in-bore biopsy if required.

If a patient is diagnosed with prostate cancer localized to the pelvis, pelvic radiotherapy may be a suitable treatment option even in the presence of oligometastases. Even though mpMRI has been shown to yield high detection rates of clinically significant prostate cancer (csPC) [5], multiple studies have shown it can underestimate the volume and extent of intra-prostatic disease in patients with known prostate cancer [6]. This is why it is important to include the entire prostate gland in the gross tumor volume (GTV) when planning radiotherapy. However, we can also utilize the confidence of mpMRI in identifying the more aggressive index lesions which can be given a focal boost of radiation treatment (Fig. 2). In this example, the mpMRI clearly shows the dominant right-sided index lesion on the anatomical and DWI, allowing this patient to undergo biologically optimized radiotherapy; the planning computer optimization software was programmed to maximize the radiation dose to the dominant index lesion with a focal boost, and to limit the dose to the rest of the gland to a defined ceiling.

In another case example (Fig. 3), following a multi-disciplinary team (MDT) discussion, it was decided that a patient with organ-confined prostate cancer would be treated with highly conformal SBRT. At the MDT, the reporting radiologist described the prostate volume, index lesion location, and confirmed that the tumor was organ-confined. The radiation oncologist chose the optimal treatment plan. It is important for the radiologist to carefully assess the risk of gross extra-prostatic extension of tumor. Whilst the tumor may seem organ-confined, if there is increased tumor-capsule contact length, there is an increasing risk of microscopic extra-prostatic extension [7]. In fact, 20–50% of clinically organ-confined tumors ultimately have extra-prostatic extension (usually microscopic) at prostatectomy [8]. If this is a concern and the radiation oncologist is made aware, treatment margins at the site of the tumor can be extended and treatment margins elsewhere around the gland can be tighter, thereby helping to minimize potential side effects of including adjacent normal tissues in the radiotherapy field. An interventional radiologist inserted fiducial markers to aid with dynamic target tracking. Imaging with MRI was again subsequently employed to visualize the fiducial markers and prostate outline after insertion for radiotherapy planning purposes.

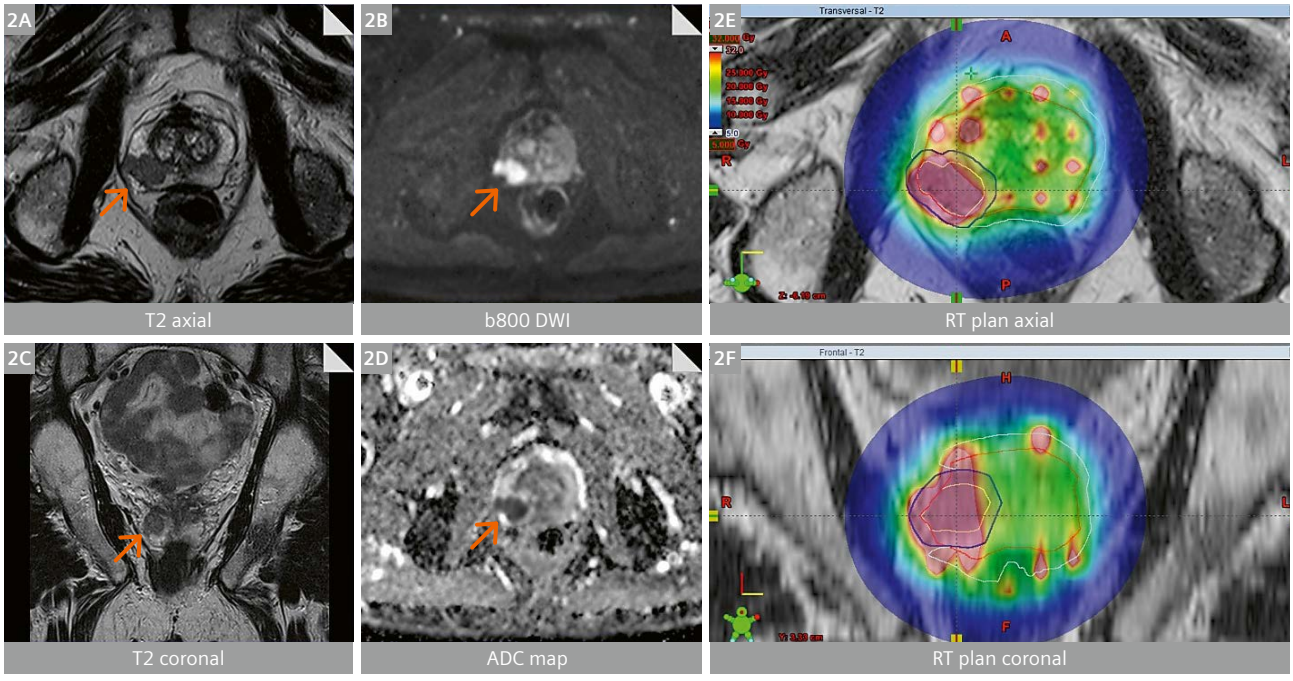

2 A 75-year-old man with raised PSA (18 ng/mL). Imaging with mpMRI **(2A-D)** and bone scan found a suspicious prostatic lesion in the right peripheral zone (arrows) with staging of T3a N0 M0 (extra-prostatic extension but no involved lymph nodes or distant sites of metastatic disease). The patient underwent an MR-directed and systematic biopsy which showed 5/12 positive biopsies (all right-sided) with a maximum Gleason score of 4+3. Brachytherapy catheters were inserted under general anesthetic and the patient received high-dose brachytherapy to the entire gland with a focal boost to the dominant right-sided index lesion **(2E, F)**.

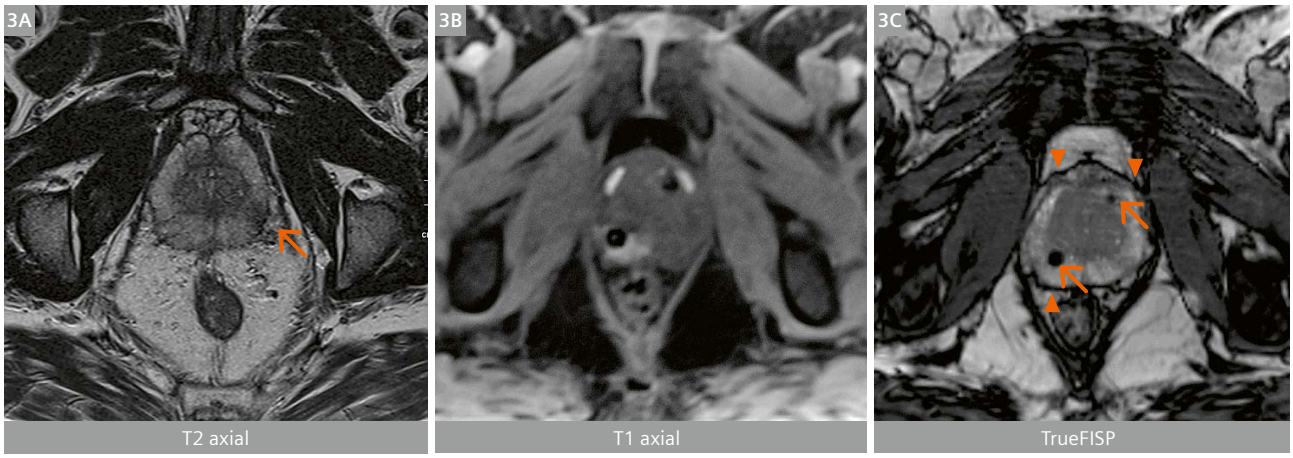

3 A 62-year-old man with raised PSA (9 ng/mL) underwent an mpMRI which demonstrated organ-confined index lesion (arrow) in the left peripheral zone **(3A)**. The patient was discussed at the MDT, and SBRT was decided. Fiducial markers were inserted by an interventional radiologist, and a radiotherapy planning MRI was performed. T1-weighted axial imaging **(3B)** showed hemorrhage post fiducial marker insertion, and a TrueFISP sequence **(3C)** clearly delineates the prostatic outline (arrowheads) and the location of the fiducial markers (arrows) to aid with radiation treatment planning.

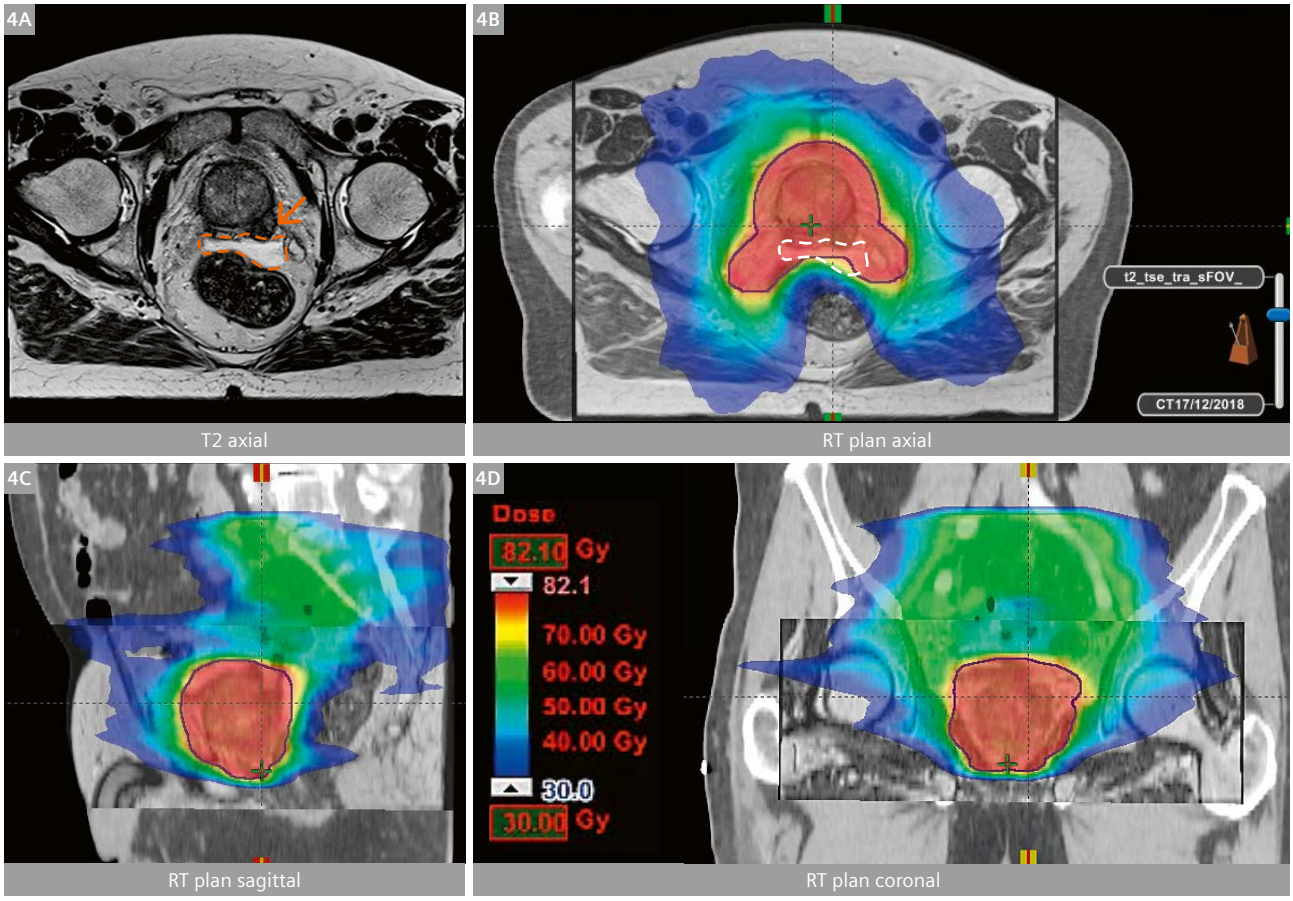

4 A 73-year-old man diagnosed with prostate cancer with iliac nodal involvement was referred for external beam radiotherapy (EBRT). **(4A)** The T2-weighted axial sequence demonstrates an index lesion in the left posterior peripheral zone (arrow), which was initially abutting the rectum. A rectal spacer (dashed outline) was inserted between the prostate gland and rectum, and the patient underwent radiation therapy planning scans **(4B-D)**. These show how the rectal spacer allows for minimal dose to the rectum without compromising the dose intensity to the prostate gland.

With collaboration between radiation oncology and clinical radiology, reporting radiologists can tailor reports to give pertinent positive and negative findings that would be relevant for a patient undergoing radiation therapy. Figure 4 shows a case where the clinical radiologist noted that the posterior prostatic lesion was abutting the rectum and therefore the patient would be at higher risk of rectal toxicity if external beam radiation therapy was selected. This was flagged in the report and at the MDT, and the patient subsequently had a biodegradable balloon spacer inserted between the prostate and the rectum to allow the radiation oncologist to accurately treat the posterior prostatic tumor while reducing the risk of rectal toxicity. This patient was successfully treated with radiotherapy without developing rectal toxicity. Three years after treatment, the patient developed biochemical recurrence and pain in the bony pelvis, so he underwent a pelvic MRI with morphological sequences only (Figs. 5A, B), which demonstrated a suspicious lesion within the S1 vertebral body extending to both sacral alar. Radiation therapy was considered and a CT-based radiotherapy treatment plan was performed. However, the MDT agreed that next-generation imaging with whole-body (WB) MRI using WB-DWI should be performed prior to radiation treatment (Figs. 5D, E) to exclude other sites of metastatic disease. Although no other sites of metastatic disease were identified, the DWI sequences demonstrated that the signal abnormality previously depicted in the posterior part of the vertebral body represented active hypercellular disease, whereas the signal change in both sacral alar was due to bilateral sacral insufficiency fractures, which are a well-recognized side effect of hormonal therapy, which the

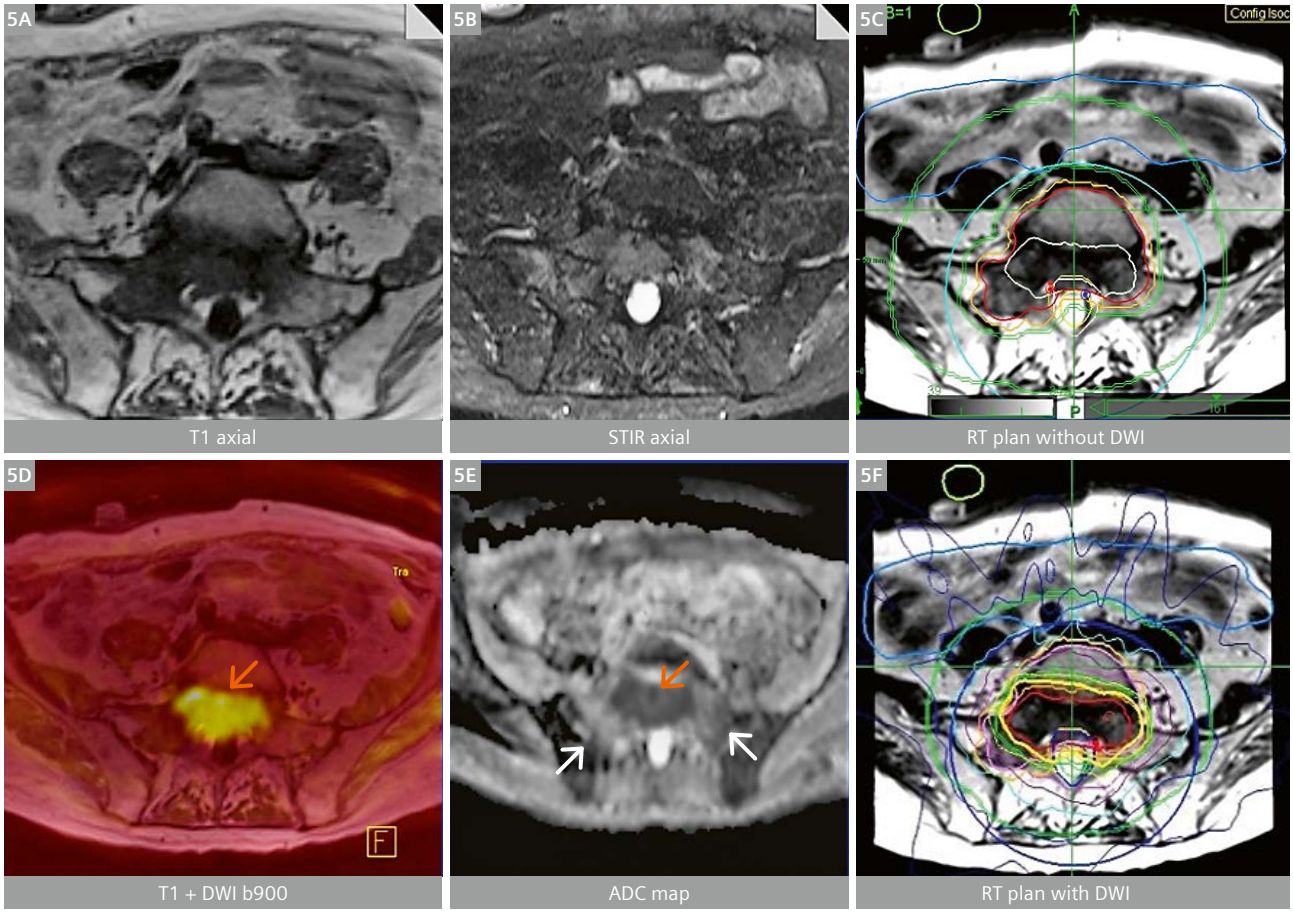

5 The patient in Figure 4 presented three years later with increasing pelvic pain. An MRI of the pelvis with morphological T1W **(5A)** and STIR **(5B)** sequences was performed. This demonstrated a suspicious lesion in the posterior part of the S1 vertebral body extending to both sacral alar. A radiotherapy plan was created **(5C)** using the information from this standard pelvic MRI. After MDT discussion, it was decided that the patient should undergo a WB-MRI with DWI to rule out other sites of metastatic disease. Other metastatic sites were excluded, but the functional data gleaned from this advanced study demonstrated active disease posteriorly in the S1 vertebral body as high signal on the b900 DWI sequence **(5D)** and low signal on the corresponding ADC map **(5E)**, indicating active hypercellular disease (orange arrows). However, the signal changes in both sacral alar demonstrated high signal (white arrows) on the ADC map **(5E)**, indicating T2-shine-through due to edema from bilateral sacral insufficiency fractures, presumably secondary to previous hormonal therapy administered three years prior. The inclusion of the functional data from the WB-MRI led to a significant alteration of the radiotherapy plan **(5F)** and minimized dose to non-metastatic regions.

patient had previously received. This significantly altered the CT-based radiation therapy field and inappropriate dose administration to non-malignant tissues was avoided due to valuable information gleaned from advanced imaging techniques.

In our final example, we discuss a case of how highly conformal SBRT was successfully used repeatedly in a prostate cancer patient with oligorecurrent disease to postpone the use of androgen deprivation therapy (ADT) (Figs. 6, 7). The patient had previously undergone a radical prostatectomy followed by pelvic radiotherapy because of pathological extra-prostatic disease on post-operative histology. The patient presented one-year post pelvic EBRT with biochemical recurrence. Knowledge of previous radiation therapy and potential side effects is crucial for the clinical radiologist as the pelvic MRI demonstrated a suspicious lymph node just above the previous radiation therapy field visible as bone marrow atrophy (Fig. 6). Next-generation imaging with WB-MRI which includes WB-DWI confirmed no other sites of distant metastatic disease and, following the MDT, the patient was selected for SBRT. A follow-up WB-MRI with DWI and drop in PSA confirmed successful treatment. Figure 7 demonstrates how the patient was followed with next-generation imaging techniques and PSA surveillance, and developed further oligometastatic disease which was treated with ablative radiation therapy techniques on three occasions over the subsequent years. Thus, the close collaboration between clinical radiology and radiation oncology colleagues with understanding and use of the technological advances in each other's fields successfully allowed the postponement of ADT use and therefore avoided the onset of potential side effects such as osteoporosis and metabolic syndrome [9].

Alternative radiation therapy techniques

Next-generation imaging techniques such as WB-MRI with DWI can also be extremely valuable in assessing a patient's suitability for different radiotherapy treatments. Radium-223 (^{223}Ra) is a calcium-mimetic alpha-particle

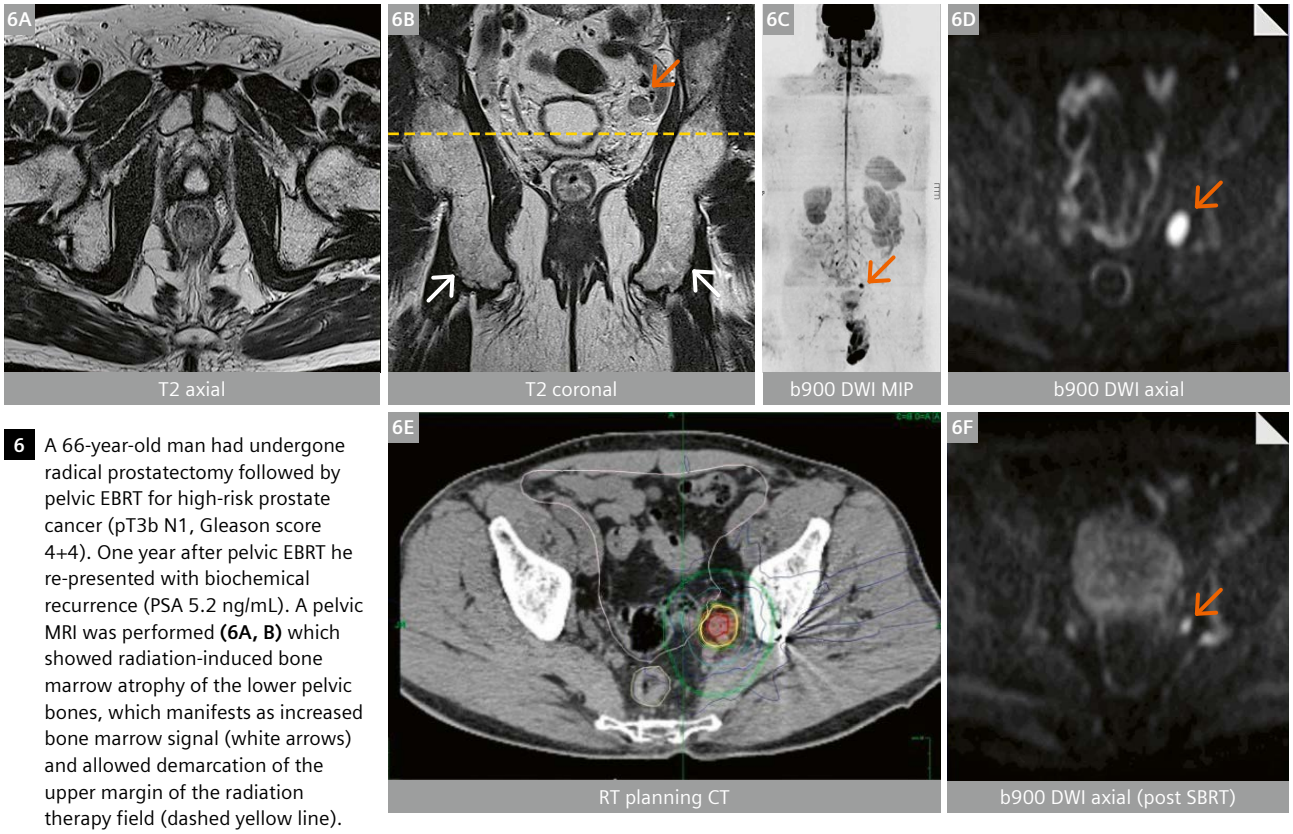

6 A 66-year-old man had undergone radical prostatectomy followed by pelvic EBRT for high-risk prostate cancer (pT3b N1, Gleason score 4+4). One year after pelvic EBRT he re-presented with biochemical recurrence (PSA 5.2 ng/mL). A pelvic MRI was performed **(6A, B)** which showed radiation-induced bone marrow atrophy of the lower pelvic bones, which manifests as increased bone marrow signal (white arrows) and allowed demarcation of the upper margin of the radiation therapy field (dashed yellow line). There was no suggestion of local recurrence at the prostatectomy bed. However just above the previous radiotherapy field there was a rounded left internal iliac lymph node (orange arrow) highly suspicious for a site of disease.

A WB-MRI with DWI was performed (**6C**: b900 DWI MIP, **6D**: b900 DWI axial) which confirmed that this was the only site of active disease (arrow) and therefore, the patient underwent SBRT following fiducial marker insertion (**6E**: planning CT). A follow-up WB-MRI three months post treatment (**6F**: b900 DWI axial) demonstrated successful ablative treatment with SBRT, which was in concordance with a reduction in PSA.

emitter which is taken up preferentially in areas of high bone turnover, particularly at sites of active bone metastases [10]. Thus, ^{223}Ra is a suitable treatment option in prostate cancer patients with bone metastatic disease and no soft tissue deposits >3 cm. WB-MRI with DWI and PET/CT with novel tracers such as gallium- and fluoride-labelled prostate-specific membrane antigen (PSMA) have been shown to have higher specificity and sensitivity to detect bone and soft tissue metastatic disease compared to conventional imaging techniques such as CT and bone scans [12, 13]. Therefore, these more advanced imaging techniques can be vital in accurate patient selection for these alternative radiation therapy techniques.

Conclusions and future directions

As advanced radiation therapy and imaging techniques are becoming more widely adopted, clinical radiologists and radiation oncologists should be aware of novel imaging and treatment developments in each other's specialties. To deliver the promise of precision radiation therapy for improved patient outcomes and decreased side effects, increased precision of imaging is needed. This is enabled with multiparametric functional imaging methods where quantitative imaging biomarkers can be mapped onto radiation planning imaging to show tumor probability maps and areas of heterogeneity. Imaging is also used to assess the effectiveness of radiation therapies and their potential side-effects.

The use of next-generation imaging techniques will be key to facilitate the use of novel treatment developments such as theranostics, which combines specific targeted pharmacotherapies based on specific targeted diagnostic tests such as ^{177}Lutetium-PSMA treatment [13]. Close collaboration between clinical radiology and radiation oncology departments will assist in these high-precision treatment advancements to allow personalized medicine for cancer patients.

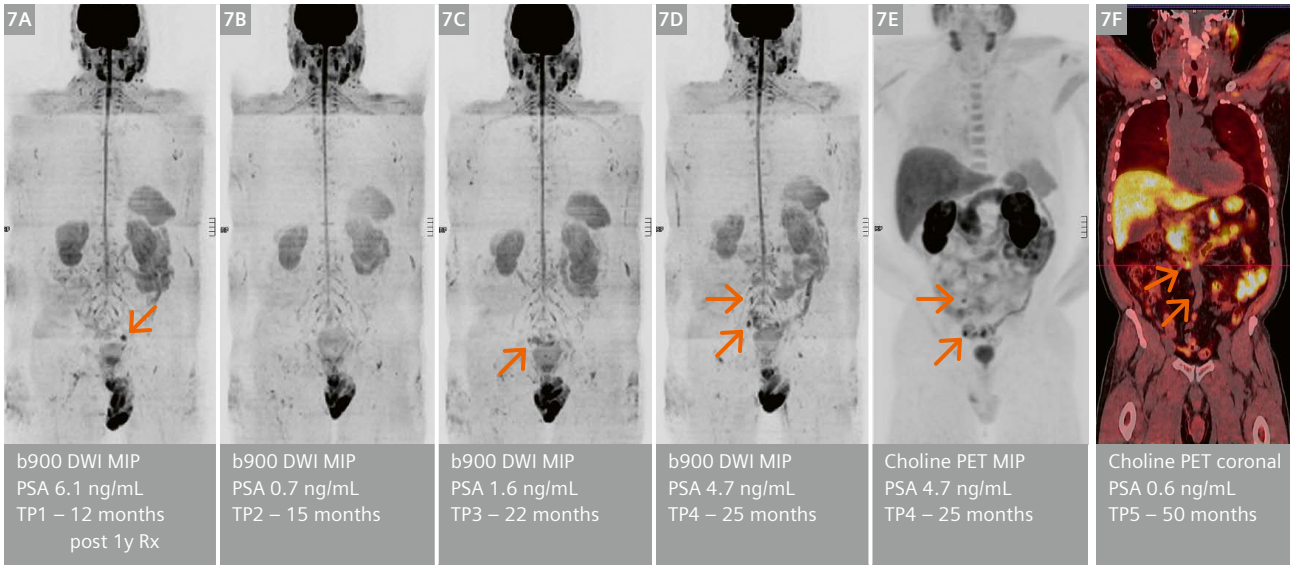

7 This series of images demonstrates how next-generation imaging techniques were used to enable advanced radiation therapy techniques for the patient from Figure 6 to postpone the use of ADT.

(7A) The WB-DW MRI MIP 12 months after prostatectomy and pelvic EBRT demonstrated a solitary left internal iliac lymph node (arrow) above the radiotherapy field which was treated with SBRT.

(7B) WB-MRI three months after SBRT shows successful treatment of the left internal iliac lymph node with a corresponding reduction in PSA.

(7C) WB-MRI performed seven months later due to a rise in PSA demonstrated a subtle focus in the right internal iliac region (arrow), which was reported as indeterminate but warranted close surveillance.

(7D) WB-MRI follow-up performed three months later showed an increase in size of the previous indeterminate right internal iliac lymph node and a new right common iliac lymph node in keeping with two nodal metastases (arrows).

(7E) A concurrent choline-PET/CT study confirmed these findings (arrows), which also correlated with the PSA rise. Two further SBRT treatments were performed and subsequent WB-MRI and choline-PET/CT studies showed no sites of active disease, and the PSA dropped to 0.02 ng/mL.

(7F) Two years after the previous SBRT treatments, the patient's PSA rose to 0.6 ng/mL and a choline-PET/CT study detected two new avid retroperitoneal lymph nodes (arrows), which were also treated with SBRT.

One year following the third SBRT treatments, there was new biochemical failure and imaging did not reveal any unequivocal sites of disease. After discussion with the patient, treatment with ADT was finally commenced after being postponed by over four years due to these advancements in imaging and radiation therapy techniques.

References

1 R. Atun, D. A. Jaffray, M. B. Barton, F. Bray, M. Baumann, B. Vikram, T. P. Hanna, F. M. Knaul, Y. Lievens, T. Y. M. Lui, M. Milosevic, B. O'Sullivan, D. L. Rodin, E. Rosenblatt, J. Van Dyk, M. L. Yap, E. Zubizarreta, and M. Gospodarowicz, "Expanding global access to radiotherapy," Lancet Oncol. 2015; 16(10):1153-86.
2 R. Baskar, K. A. Lee, R. Yeo, and K. W. Yeoh, "Cancer and radiation therapy: Current advances and future directions," Int. J. Med. Sci. 2012;9(3):193-9.
3 A. R. Padhani, F. E. Lecouvet, N. Tunariu, D. M. Koh, F. De Keyzer, D. J. Collins, E. Sala, S. Fanti, H. A. Vargas, G. Petralia, H. P. Schlemmer, B. Tombal, and J. de Bono, "Rationale for Modernising Imaging in Advanced Prostate Cancer," Eur. Urol. Focus. 2017;3(2-3):223-239.
4 H. U. Ahmed, A. El-Shater Bosaily, L. C. Brown, R. Gabe, R. Kaplan, M. K. Parmar, Y. Collaco-Moraes, K. Ward, R. G. Hindley, A. Freeman, A. P. Kirkham, R. Oldroyd, C. Parker, and M. Emberton, "Diagnostic accuracy of multi-parametric MRI and TRUS biopsy in prostate cancer (PROMIS): a paired validating confirmatory study," Lancet. 2017;389(10071):815-822.
5 N. L. Hansen, T. Barrett, C. Kesch, L. Pepdjonovic, D. Bonekamp, R. O'Sullivan, F. Distler, A. Warren, C. Samel, B. Hadaschik, J. Grummet, and C. Kastner, "Multicentre evaluation of magnetic resonance imaging supported transperineal prostate biopsy in biopsy-naïve men with suspicion of prostate cancer," BJU Int. 2018,122(1):40-49.
6 S. Borofsky, A. K. George, S. Gaur, M. Bernardo, M. D. Greer, F. V. Mertan, M. Taffel, V. Moreno, M. J. Merino, B. J. Wood, P. A. Pinto, P. L. Choyke, B. Turkbey, "What Are We Missing? False-negative Cancers at Multiparametric MR Imaging of the Prostate," Radiology. 2018,286(14):186-195.
7 E. Baco, E. Rud, L. Vlatkovic, A. Svindland, H. B. Eggesbø, A. J. Hung, T. Matsugasumi, J.-C. Bernhard, I. S. Gill, and O. Ukimura, "Predictive Value of Magnetic Resonance Imaging Determined Tumor Contact Length for Extracapsular Extension of Prostate Cancer," J Urol. 2015 Feb;193(2):466-72.
8 A. Gallina, F. K. Chun, N. Suardi, J. A. Eastham, P. Perrotte, M. Graefen, G. Hutterer, H. Huland, E. A. Klein, A. Reuther, F. Montorsi, A. Briganti, S. F. Shariat, C. G. Roehrborn, A. De Taille, L. Salomon, and P. I. Karakiewicz, "Comparison of stage migration patterns between Europe and the USA: an analysis of 11 350 men treated with radical prostatectomy for prostate cancer," BJU Int. 2008 Jun;101(12):1513-8.
9 P. Sountoulides and T. Rountos, "Adverse Effects of Androgen Deprivation Therapy for Prostate Cancer: Prevention and Management," ISRN Urol. 2013 Jul 25;2013:240108. doi: 10.1155/2013/240108.
10 S. Dadhania, R. Alonzi, S. Douglas, A. Gogbashian, R. O. B. Hughes, D. Dalili, N. Vasdev, J. I. M. Adshead, and T. I. M. Lane, "Single-centre Experience of Use of Radium 223 with Clinical Outcomes Based on Number of Cycles and Bone Marrow Toxicity," Anticancer Res. 2018 Sep;38(9):5423-5427.
11 G. Shen, H. Deng, S. Hu, and Z. Jia, "Comparison of choline-PET / CT, MRI, SPECT, and bone scintigraphy in the diagnosis of bone metastases in patients with prostate cancer: a meta-analysis," Skeletal Radiol. 2014 Nov;43(11):1503-13.
12 M. Eiber, T. Maurer, M. Souvatzoglou, A. J. Beer, A. Ruffani, B. Haller, F. Graner, K. Hubert, U. Haberhorn, M. Eisenhut, H. Wester, J. E. Gschwend, and M. Schwaiger, "Evaluation of Hybrid 68 Ga-PSMA Ligand PET/CT in 248 Patients with Biochemical Recurrence After Radical Prostatectomy," J Nucl Med. 2015 May;56(5):668-74.
13 L. Emmett, K. Willowson, J. Violet, J. Shin, A. Blanksby, and J. Lee, "Lutetium 177 PSMA radionuclide therapy for men with prostate cancer: a review of the current literature and discussion of practical aspects of therapy," J Med Radiat Sci. 2017 Mar;64(1):52-60.

Contact

Amish Lakhani, MBBS MA (Cantab) FRCR
Paul Strickland Scanner Centre
Mount Vernon Hospital
Northwood
Middlesex HA6 2RN
UK
amish.lakhani@stricklandscanner.org.uk

We are looking forward to hearing from you

Founded in 1993 the MAGNETOM Flash magazine has been around almost as long as MAGNETOM MRI scanners.

In times of online media and digitalization we would value your feedback to ensure that the magazine continues to fit your interests and professional needs.

Please take a moment to complete a brief reader survey at
www.siemens.com/magnetom-world

MR Total Tumor Load – First Clinical Experience in Pediatric Oncology Patients

Ilias Tsiflikas, M.D.[1]; Robert Grimm, Ph.D.[2]; Jürgen F. Schäfer, M.D.[1]

[1]Pediatric Radiology, Department of Diagnostic and Interventional Radiology, University Hospital of Tübingen, Tübingen, Germany
[2]Siemens Healthineers, Erlangen, Germany

Abstract

The *syngo*.via Frontier MR Total Tumor Load application[1] comes with benefits in pediatric oncology evaluation not only in cases of metastatic bone disease but also in solid tumors, and could further help to establish DWI as a prognostic factor in the assessment of tumor therapy.

Introduction

In recent years, advancements in MR techniques have shortened examination times. This has led to whole-body (WB) MRI becoming essential in staging and managing pediatric oncology patients, where a curative approach is much more common [1]. As a result, an S1 guideline entitled "Whole-body MRI in children" was recently published in Germany [2]. Besides the benefits of radiation-free examinations and excellent tissue characterization, MRI offers the possibility of combining anatomical and functional imaging using techniques such as diffusion-weighted imaging (DWI) for local staging and precise assessments of metastatic spread and total tumor burden at diagnosis as an important factor in planning treatment and predicting outcomes. Several recent studies have compared the diagnostic accuracy of whole-body DWI (WB-DWI) in pediatric lymphomas with conventional methods such as computed tomography (CT), scintigraphic methods, and positron emission tomography (PET). The results are promising [3, 4]. In neuroblastic tumors, DWI has also proved valuable for differentiating malignant and benign tumors based on differences in the apparent diffusion coefficient (ADC), finding higher ADC values in benign tumors like ganglioneuroma than in malignant neuroblastoma [5–7]. Two recent papers further evaluated the role of, respectively, DWI and ADC values as a complementary prognostic marker in neuroblastoma. The findings showed that, under therapy, increasing ADC values were an indicator of good response and prognosis [8, 9]. A limitation of quantitative ADC measurement is the lack of tools to perform efficient evaluation for multifocal disease. The recently introduced *syngo*.via Frontier MR Total Tumor Load prototype application[1] provides a solution that uses threshold-based segmentation on diffusion-weighted images to identify regions of disease and to analyze the overall tumor volume and histogram metrics of the corresponding ADC maps [10]. A pilot study demonstrated excellent inter- and intra-observer agreement using this application in metastatic bone disease [11].

In this report, we will show the diagnostic options for the *syngo*.via Frontier MR Total Tumor Load application in pediatric oncology based on three case studies on Hodgkin lymphoma and stage 4 neuroblastoma respectively.

Case study 1

A 14-year-old girl presented with a supraclavicular swelling first noticed a week previously. Sonography revealed pathological lymph node enlargement suspicious for lymphoma. Biopsy of the lymph node established the diagnosis of classical Hodgkin lymphoma. A WB-PET-MRI using a standardized protocol including WB-DWI on a 3T PET/MR imaging system (Biograph mMR; Siemens Healthcare, Erlangen, Germany) [12] was performed for initial staging and early response after two months.

In the initial staging, cervical, mediastinal, and left axillary lymph node involvement without extranodal manifestations was demonstrated, resulting in a stage 2 classification. The early response study after two cycles of chemotherapy shows a complete metabolic response with only a small residual morphological tumor on the left supraclavicular region (Fig. 1).

The diffusion-weighted images of both examinations were analyzed using a *syngo*.via Frontier MR Total Tumor Load threshold-based segmentation. The pretreatment ADC histogram shows an unimodal distribution of ADC values with high excess kurtosis (Fig. 2). The follow-up study after two months shows significant reduction in volume and a greater spread in the lower ADC range, which is related to partial response.

[1]*syngo.via Frontier is for research only, not a medical device. syngo.via Frontier MR Total Tumor Load is a released research prototype.*

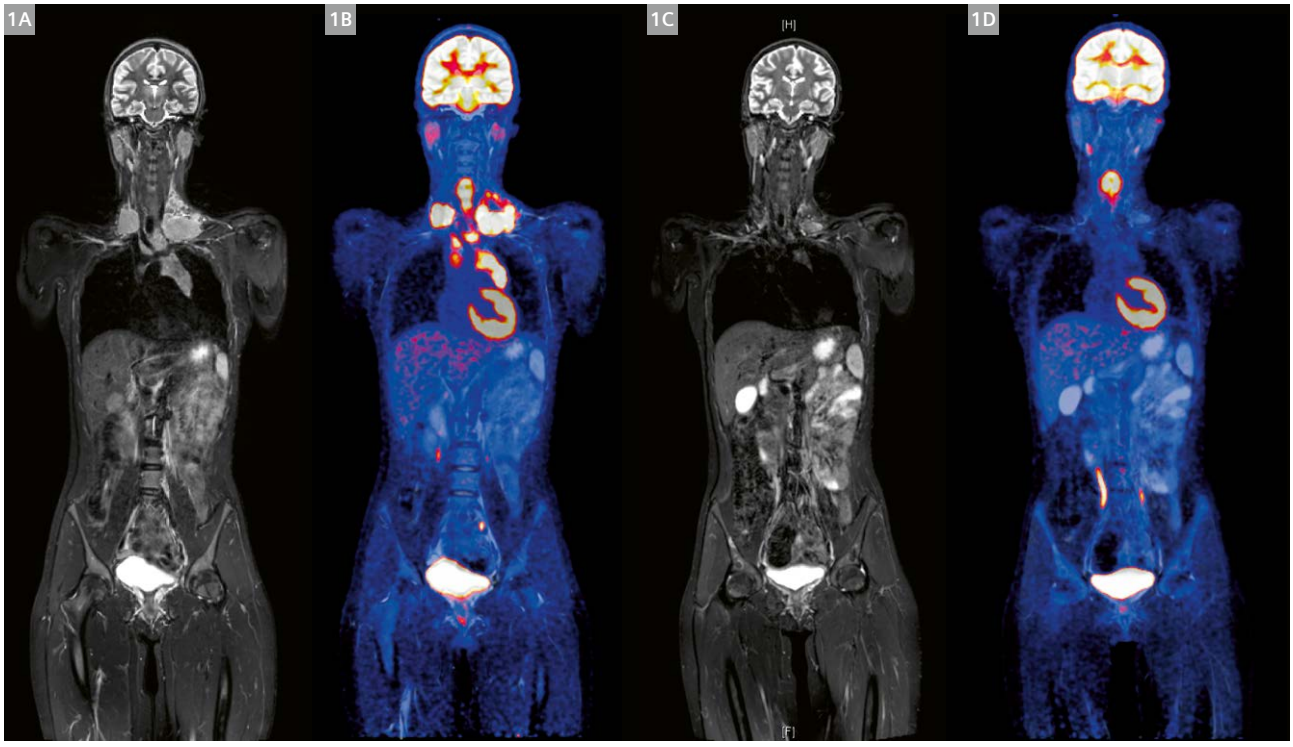

1 **Morphological and functional images of baseline and follow-up PET/MRI**
Baseline examination **(1A, 1B)** shows cervical and mediastinal lymph node involvement in a coronal short tau inversion recovery whole-body sequence (1A) and fused ^{18}F FDG-PET and short tau inversion recovery sequence. In the follow-up examination **(1C, 1D)**, only morphological residuals in the left supraclavicular regions remain.

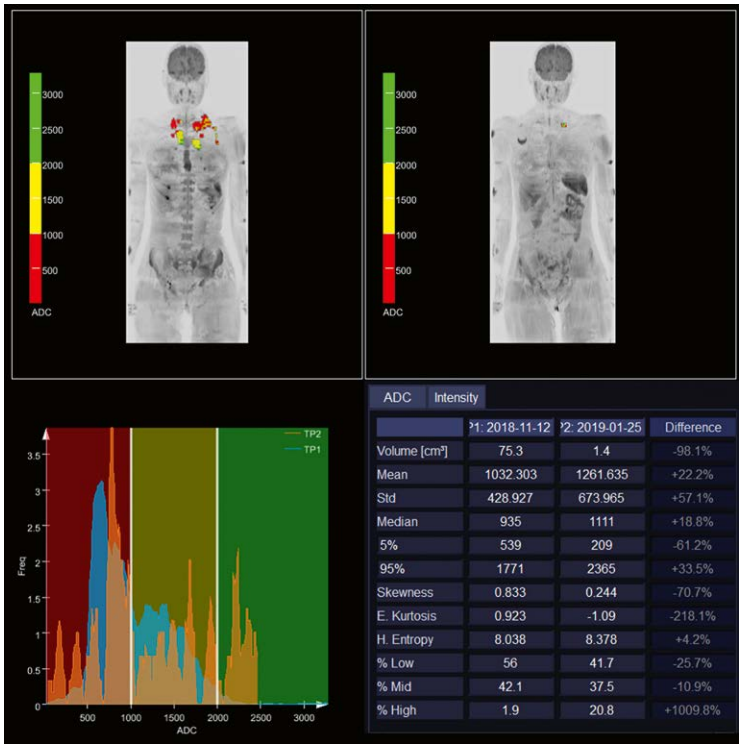

	1: 2018-11-12	2: 2019-01-25	Difference
Volume [cm³]	75.3	1.4	-98.1%
Mean	1032.303	1261.635	+22.2%
Std	428.927	673.965	+57.1%
Median	935	1111	+18.8%
5%	539	209	-61.2%
95%	1771	2365	+33.5%
Skewness	0.833	0.244	-70.7%
E. Kurtosis	0.923	-1.09	-218.1%
H. Entropy	8.038	8.378	+4.2%
% Low	56	41.7	-25.7%
% Mid	42.1	37.5	-10.9%
% High	1.9	20.8	+1009.8%

2 **ADC histogram changes over time**
WB tumor load segmentations were undertaken using the *syngo*.via Frontier MR Total Tumor Load software[1]. Besides the reduction in tumor volume, a shift in ADC value distribution between baseline and follow-up examination indicate a partial response.

Case study 2

A 10-month-old[2] boy presented with ptosis that had been noted for four weeks. In addition, a palpable abdominal mass was detected. WB-MRI was performed using our institution's standard protocol as previously published [13] on a 1.5T MR imaging system (MAGNETOM Avanto; Siemens Healthcare, Erlangen, Germany). The examination demonstrated a suprarenal mass on the right side with suspicious mesenteric nodes and hepatic metastases as well as osseous lesions in the left orbit, both proximal humerus and femora, the lumbar vertebra, and the pelvis. Chemotherapy was initiated. In the follow-up study after three months, the osseous lesions show almost complete regression and the suprarenal mass also shows a significant reduction (Fig. 3). Evaluation with *syngo*.via Frontier MR Total Tumor Load shows an unimodal distribution of ADC values with high excess kurtosis (Fig. 4) in both examinations without significant change in the mean ADC value. After surgical resection, the histopathological evaluation of the suprarenal mass revealed that it still contained 90% vital tumor cells.

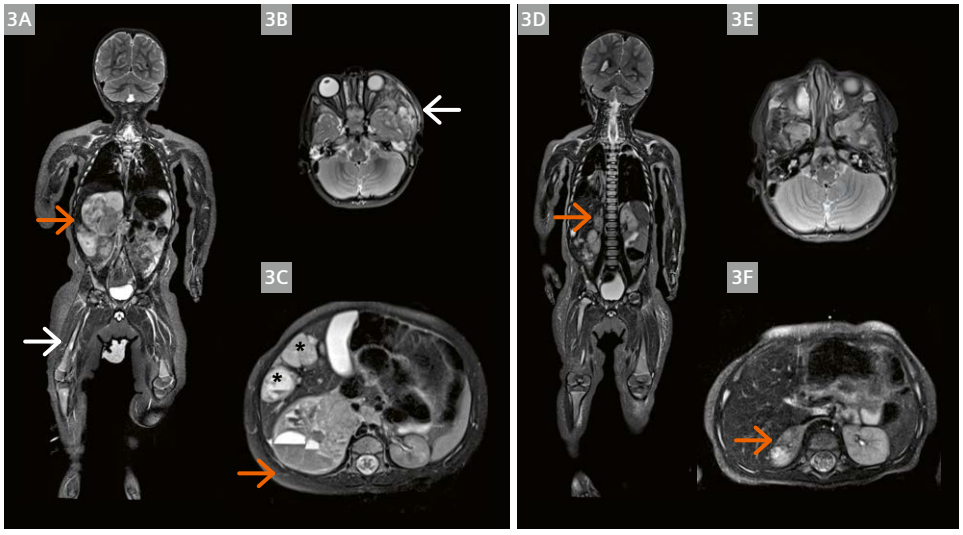

3 Morphological images of baseline and follow-up WB-MRI
The baseline examination **(3A–C)** shows a suprarenal mass in a coronal short tau inversion recovery whole-body sequence **(3A)** and a transversal T2-weighted fat-suppressed sequence (**3C**, orange arrow) with signs of tumor bleeding and necrosis. Osseous metastases are also visible in the right femur (**3A**, white arrow) and left orbit (**3B**, white arrow). The follow-up examination **(3D–F)** shows only residual suprarenal tumor on the right side (**3F**, right-hand arrow).

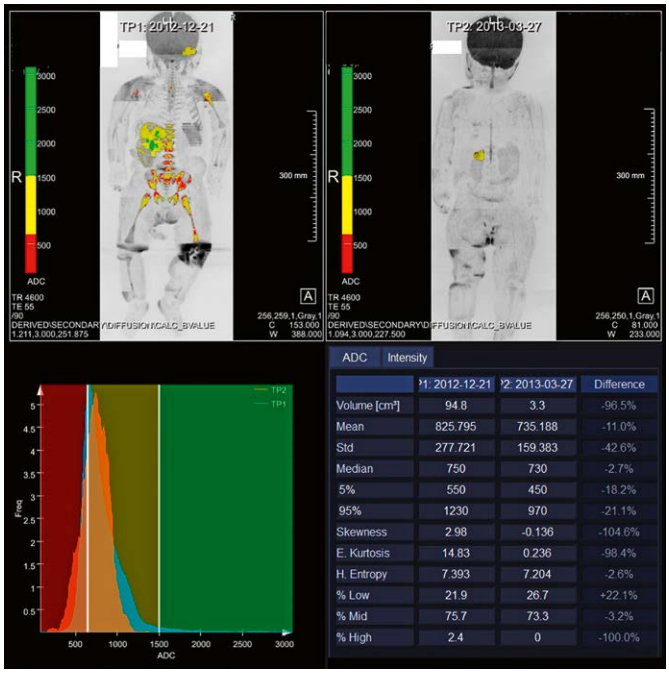

4 ADC histogram changes over time
WB tumor load segmentations indicate a clear reduction in tumor volume is visible, but the distribution of ADC values of tumor mass has not changed significantly between baseline and follow-up examination. This is interpreted as a sign of tumor vitality.

[2] *MR scanning has not been established as safe for imaging fetuses and infants less than two years of age. The responsible physician must evaluate the benefits of the MR examination compared to those of other imaging procedures. Note: This disclaimer does not represent the opinion of the authors.*

Case study 3

A 10-year-old girl presented with a histopathologically proven ganglioneuroma after surgical biopsy at a different hospital. The MRI shows a heterogenous suprarenal tumor on the left side with heterogenous ADC values suspicious for a mixed tumor in the form of a ganglioneuroblastoma (Fig. 5A). Evaluation with *syngo*.via Frontier MR Total Tumor Load shows the heterogeneity of the tumor with a three-modal distribution of ADC values that were measured in the complete tumor (Fig. 5B).

Discussion

The *syngo*.via Frontier MR Total Tumor Load application has been developed for ADC histogram analysis. The main advantage is the possibility to analyze the ADC histogram of the complete tumor volume, rather than just a region of interest (ROI) or volume of interest (VOI). Several case reports show the opportunities for using the application in cases of metastatic bone disease in particular [14–16]. Further, a pilot study demonstrated that the application achieved excellent inter- and intra-observer agreement in metastatic bone disease [11].

MRI plays an important role in pediatric radiology, and this is not only due to its ability to perform radiation-free examinations. A variety of pediatric oncologic diseases have a better prognosis than oncologic diseases in adults, but precise staging and follow-up are crucial for the outcome. In addition to providing morphological information, MRI offers the opportunity to combine functional imaging using DWI. So far, DWI has been analyzed visually or by measuring the ADC values in an ROI. The possibility of evaluating ADC histograms of the total tumor volume opens up new approaches for assessing treatment response or even generating a complementary prognostic factor.

In the first case study, we demonstrated that, as well as a reduction in tumor volume, a shift in the distribution of ADC values is observed with a good therapy response in Hodgkin lymphoma.

The second case study shows that, in neuroblastoma, a lack of change in ADC value distribution under therapy is a sign of persistent tumor vitality despite a significant reduction in tumor volume.

In the third case study, we saw that *syngo*.via Frontier MR Total Tumor Load can visualize tumor heterogeneity in neuroblastic tumors using ADC color projections, histograms, and descriptive histogram statistics.

We have demonstrated that the *syngo*.via Frontier MR Total Tumor Load application has benefits for evaluating pediatric oncology in both metastatic bone disease and solid tumors, and could further help to establish DWI as a prognostic factor in assessments of tumor therapy. However, proving this hypothesis will require large-scale, multicenter studies.

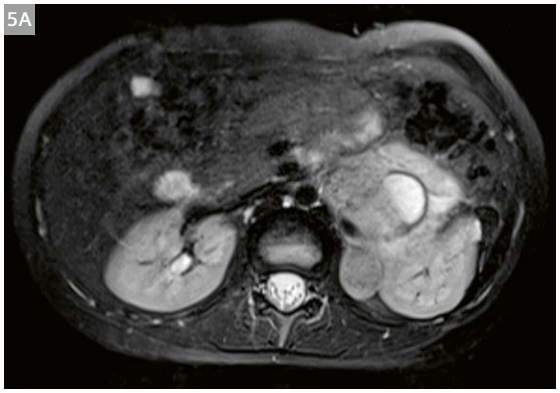

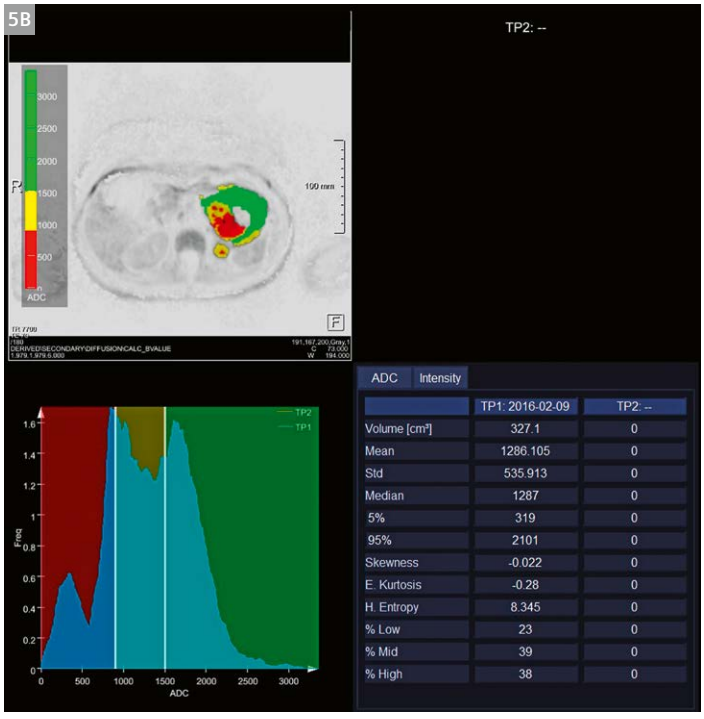

5 **Morphological images and ADC histogram**
In the transversal T2-weighted fat-suppressed sequence **(5A)** the heterogeneous suprarenal tumor of the left side is well demonstrated. Correlating the ADC histogram **(5B)** in the MR Total Tumor Load software[1] shows the heterogeneity in the color projection and also in the three-modal distribution of the ADC values. The lowest ADC peak corresponds to active tumor core and is visualized in red, the second peak at an ADC of approximately 900–1300 µm²/s represents surrounding tissue with increased cellularity and is overlaid in yellow. ADC values of 1500 µm²/s and above are considered fluid components and are back-mapped in green.

References

1 Atkin KL, Ditchfield MR. The role of whole-body MRI in pediatric oncology. J Pediatr Hematol Oncol. 2014;36(5):342-52.
2 Mentzel H-J, Schäfer JF, et al. Whole-Body MRI in Children [Ganzkörpermagnetresonanztomografie im Kindes- und Jugendalter]. 2018; AWMF Registernummer: 064/018. Klasse: S1. Available from: https://www.awmf.org/leitlinien/detail/ll/064-018.html.
3 Baranska D, Matera K, Podgorski M, et al. Feasibility of diffusion-weighted imaging with DWIBS in staging Hodgkin lymphoma in pediatric patients: comparison with PET/CT. MAGMA. 2018; doi: 10.1007/s10334-018-0726-4. [Epub ahead of print].
4 Regacini R, Puchnick A, Luisi FAV, et al. Can diffusion-weighted whole-body MRI replace contrast-enhanced CT for initial staging of Hodgkin lymphoma in children and adolescents? Pediatr Radiol. 2018;48(5):638-47.
5. Gahr N, Darge K, Hahn G, et al. Diffusion-weighted MRI for differentiation of neuroblastoma and ganglioneuroblastoma/ganglioneuroma. Eur J Radiol. 2011;79(3):443-6.
6 Neubauer H, Li M, Muller VR, et al. Diagnostic Value of Diffusion-Weighted MRI for Tumor Characterization, Differentiation and Monitoring in Pediatric Patients with Neuroblastic Tumors. Fortschr Röntgenstr. 2017;189(7):640-50.
7 Uhl M, Altehoefer C, Kontny U, et al. MRI-diffusion imaging of neuroblastomas: first results and correlation to histology. Eur Radiol. 2002;12(9):2335-8.
8 Demir S, Altinkaya N, Kocer NE, et al. Variations in apparent diffusion coefficient values following chemotherapy in pediatric neuroblastoma. Diagn Interv Radiol. 2015;21(2):184-8.
9 Peschmann AL, Beer M, Ammann B, et al. Quantitative DWI predicts event-free survival in children with neuroblastic tumours: preliminary findings from a retrospective cohort study. Eur Radiol Exp. 2019;3(1):6.
10 Grimm R, Padhani AR. Whole-body Diffusion-weighted MR Image Analysis with *syngo*.via Frontier MR Total Tumor Load. MAGNETOM Flash. 2017;68(2):73-5.
11 Blackledge MD, Tunariu N, Orton MR, et al. Inter- and Intra-Observer Repeatability of Quantitative Whole-Body, Diffusion-Weighted Imaging (WBDWI) in Metastatic Bone Disease. PLoS One. 2016;11(4):e0153840.
12 Schafer JF, Gatidis S, Schmidt H, et al. Simultaneous whole-body PET/MR imaging in comparison to PET/CT in pediatric oncology: initial results. Radiology. 2014;273(1):220-31.
13 Schaefer JF, Tsiflikas I. Whole body MRI in children [Ganzkörper-MRT bei Kindern]. Radiologie up2date. 2014;14(3):259-78.
14 Dalili D, Padhani AR, Grimm R. Quantitative WB-MRI with ADC Histogram Analysis for Response Assessment in Diffuse Bone Disease. Magnetom Flash. 2017;69(3):32-7.
15 Dalili D, Padhani AR, Grimm R. Quantitative WB-MRI with ADC Histogram Analysis for Complex Response of Bone Marrow Metastatic Disease. MAGNETOM Flash. 2017;69(3):38-42.
16 Dalili D, Joshi PV, Padhani AR, Grimm R. Evolution of the Malignant Bone Marrow with Successful Therapy – Quantitative Analysis with Whole-body Diffusion-weighted MRI. MAGNETOM Flash. 2017;69(3):43-8.

Ilias Tsiflikas

Jürgen Schäfer

Contact

Ilias Tsiflikas, M.D.
Pediatric Radiology
Department of Diagnostic and Interventional Radiology
University Hospital of Tübingen
Hoppe-Seyler-Str. 3
72072 Tübingen
Germany
ilias.tsiflikas@med.uni-tuebingen.de

Cardiotoxicity in Cancer Therapy – the Role of Cardiovascular Magnetic Resonance

Christian P. Houbois[1,2]; Paaladinesh Thavendiranathan, MD SM[1,3,4]; Bernd J. Wintersperger, MD EBCR FAHA[1,2]

[1] Department of Medical Imaging, Peter Munk Cardiac Centre, University Health Network, Toronto, Canada
[2] Department of Medical Imaging, University of Toronto, Toronto, Canada
[3] Division of Cardiology, Peter Munk Cardiac Centre, University Health Network, Toronto, Canada
[4] Department of Medicine, University of Toronto, Toronto, Canada

Introduction

Cardiovascular magnetic resonance (CMR) imaging has become a mainstay in the assessment of various cardiac pathologies including ischemic and non-ischemic cardiomyopathies. Beyond the sole aspect of functional deterioration, CMR has convincingly demonstrated to provide further information on the underlying cause contributing sufficient information to narrow the differential diagnosis. Furthermore, insight into the myocardial composition may shed light into the risk prediction of certain diseases and may also allow monitoring of therapeutic interventions and their effects on the heart.

In recent years, the link between tumor therapies and cardiac disease has gained substantial attention and is currently focus of multiple ongoing large-scale studies. With the continuous improvement of survival rates of patients with various malignancies, potential detrimental effects on cardiac function and outcome including increased morbidity and mortality has become the center of such investigations. Outside study settings, major centers with large oncology and cardiac programs have started to establish Cardio-Oncology clinics, in order to help guide oncologists in their treatment planning in patients with pre-existing cardiac disease as well as taking care of patients with potential tumor therapy regimen related cardiovascular effects and potential development of heart failure (HF).

Tumor therapy and heart failure

Todays' therapy regimens in patients with malignant neoplasms may be based on surgical approaches, local or extended radiation therapy (RT) as well as systemic tumor therapies or a combination thereof. While surgical approaches and RT generally affect structures within the application field, systemic therapies may not only result in anti-tumor effects but may also affect otherwise normal body tissue, including the heart. Such negative effects of tumor-related therapy on the heart are generically referred to as cardiotoxicity. The known impact of anthracycline (AC) related tumor therapy possibly resulting in HF may often also be referred to as anthracycline induced heart failure (AIHF).

While modern personalized medicine approaches result in the continuous development of new anti-tumor drugs amongst different drug classes, AC still remain a mainstay of modern tumor therapy regimens. They are commonly used in treatment of breast malignancies, sarcomas and also hematologic malignancies. It is estimated that up to 60% of childhood cancer survivors have been exposed to AC therapy regimens and/or chest radiation [1; 2].

Up to ~20% of patients undergoing AC based tumor therapy (with or without combination therapy) may experience AC related cardiotoxicity with the development of HF. The incidence generally increases with increasing cumulative AC dosing. Specifically designed studies employing short interval imaging (echocardiography) based monitoring of the ventricular function, the vast majority (up to 98%)

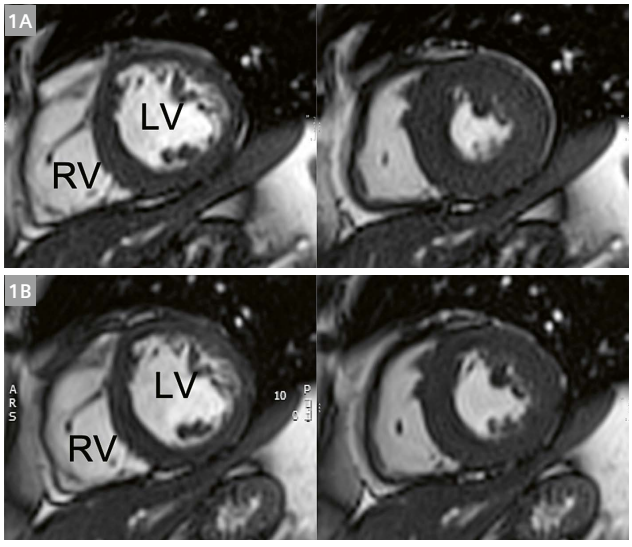

1 Standard cine imaging in a patient with breast cancer **(1A)** prior to chemotherapy and **(1B)** one year after the end of anthracycline/trastuzumab combination therapy. Images demonstrate almost identical slice positioning (Cardiac Dot Engine) in diastole (left), but already visually a clear reduction in global ejection fraction is seen in systolie (right). The ejection fraction had dropped by ≥ 10% to < 50%.

LV = left ventricle; RV = right ventricle

of cardiotoxicity related HF developed either during the systemic cancer therapy or within one year after the end of therapy [3] (Fig. 1). Among patients experiencing such detrimental effects, the vast majority of patients will not entirely recover their cardiac function despite initiation of HF therapy [3]. The risk of cardiac events in this population is significantly increased and in case of confirmed AIHF, mortality may exceed 50% within two years.

Anthracyclines (e.g. doxorubicin, epirubicin) have been known from early use to potentially cause HF and still remain the drug class most commonly related to HF. However, also other drug classes may result in negative cardiovascular effects or may increase the risk of HF in combination with AC based therapy schemes. These classes include monoclonal anti-bodies (MAB) such as trastuzumab, tyrosine kinase inhibitors (TKI) as well as immune checkpoint inhibitors (ICI).

Meanwhile, guidelines have been developed helping to identify patient populations who are specifically at risk for cardiotoxicity related HF [4]. In general, the risk is specifically depending on the dosage of AC therapy, but also the amount of potentially applied additional radiation, potential cardiovascular risk factors as well as the combination of certain drug classes (e.g. anthracycline-trastuzumab combination therapy) [4].

Of specific interest is also the class of aforementioned ICI's, a group of agents that has generally demonstrated lower rates of cardiotoxicity, but that may specifically cause autoimmune myocarditis in rare instances resulting in high complication rates [5].

Cardiovascular magnetic resonance and cardiotoxicity

The breadth of techniques available in CMR for assessment of cardiac function, myocardial deformation and myocardial tissue characterization makes it a potentially ideal tool for assessment and monitoring of patients with increased risk of developing cancer therapy related cardiotoxicity.

Functional cardiac imaging

Today's definitions of cardiotoxicity are almost exclusively based on the assessment of the left ventricular (LV) ejection fraction (EF). As such, the known high accuracy and precision of CMR in the assessment of cardiac volume and function is perfectly suited to guide clinicians according to current definitions of cardiotoxicity [6]. With little variation, published criteria of cardiotoxicity follow a change in LVEF with main cut-offs at a drop of ≥ 10% to under 50% or 55%/53% respectively (Fig. 1) [7–9]. More subtle changes in LVEF (≥ 5%) should be considered as possibly related to cardiotoxicity in patients with symptoms of heart failure (HF) [8]. However, it is important to keep in mind that such thresholds are generally based on echocardiography or multigated acquisition (MUGA) radionuclide ventriculography, modalities that generally suffer from a higher inter-scan and inter-observer variability. Although there is no separate cut-off criterion based on CMR, recent study data suggests that MUGA results may potentially result in misclassification of patients [10].

In any of the above LVEF based definitions of cardiotoxicity, proper baseline assessment and follow scans are required; single time assessment of the cardiac function would not allow adequate judgement. In addition to standard imaging approaches, CMR may play an increasingly important role in the monitoring of such patients. Various clinical experiences report cases where echocardiography based functional assessment would have missed a significant drop in LVEF.

However, from decades of imaging experience it is known that LVEF changes may only occur as a delayed relation to local changes. Therefore, assessment of myocardial deformation may provide a more sensitive and earlier insight into myocardial changes. In the field of echocardiography, the application of speckle tracking echocardiography (STE) has pushed the use of strain imaging towards clinical use including assessment of cardiotoxicity. CMR offers various techniques for myocardial deformation imaging including myocardial tagging, sensitivity encoding (SENC) and displacement encoding with stimulated echoes (DENSE). However, such techniques have never been established on a larger scale in clinical routine CMR.

Most recently, developments of techniques that allow assessment of myocardial strain in routinely acquired cine balanced steady state free precession (bSSFP) data sets have opened a whole new avenue of myocardial deformation assessment. The different available techniques rely either on feature tracking algorithms or employ motion correction techniques for calculation of deformation in cine bSSFP [11–15]. Especially, prototype deformation map-based techniques such as TrufiStrain[1] (Siemens Medical Imaging Technologies, Princeton, US) demonstrated promising and highly reproducible results compared to accepted standard of reference such as myocardial tagging (Figures 2–4) [12; 14]. In the application of cardiotoxicity evaluation, CMR based strain has also demonstrated great promise aiming at early detection of changes.

Tissue characterization

Qualitative tissue characterization techniques such as T2-weighted imaging or Late Gadolinium Enhancement (LGE) imaging have long played a role in the assessment of various cardiomyopathies and inflammatory changes such as myocarditis [16, 17]. However, the use of LGE imaging in assessment of cardiotoxicity appears limited. As an

[1] *WIP, the product is currently under development and is not for sale in the U.S. and in other countries. Its future availability cannot be ensured.*

exception, LGE may play a role in assessment of possible autoimmune myocarditis/pericarditis which may occur during ICI therapy and is considered a bad prognostic marker (Fig. 5).

As a potential new marker of cardiotoxicity related tissue level changes, cardiac relaxometry techniques such as T1 mapping, T2 mapping as well as derived markers such as extracellular volume fraction (ECV) have been proposed and evaluated in various experimental and clinical studies predominately focused on the effects of anthracycline therapy.

In animal studies, the repeated application of anthracycline doses lead to a continuous increase in native T1 values over the course of 12–14 weeks while other studies have demonstrated that T2 values are increased in the early phase (~4–6 weeks) suggesting myocardial edema [18, 19]. However, the later study also demonstrated that despite elevated T2 values in early stages, ECV was not elevated until later stages. A possible explanation of elevated T2 and normal ECV might be the occurrence of intracellular edema.

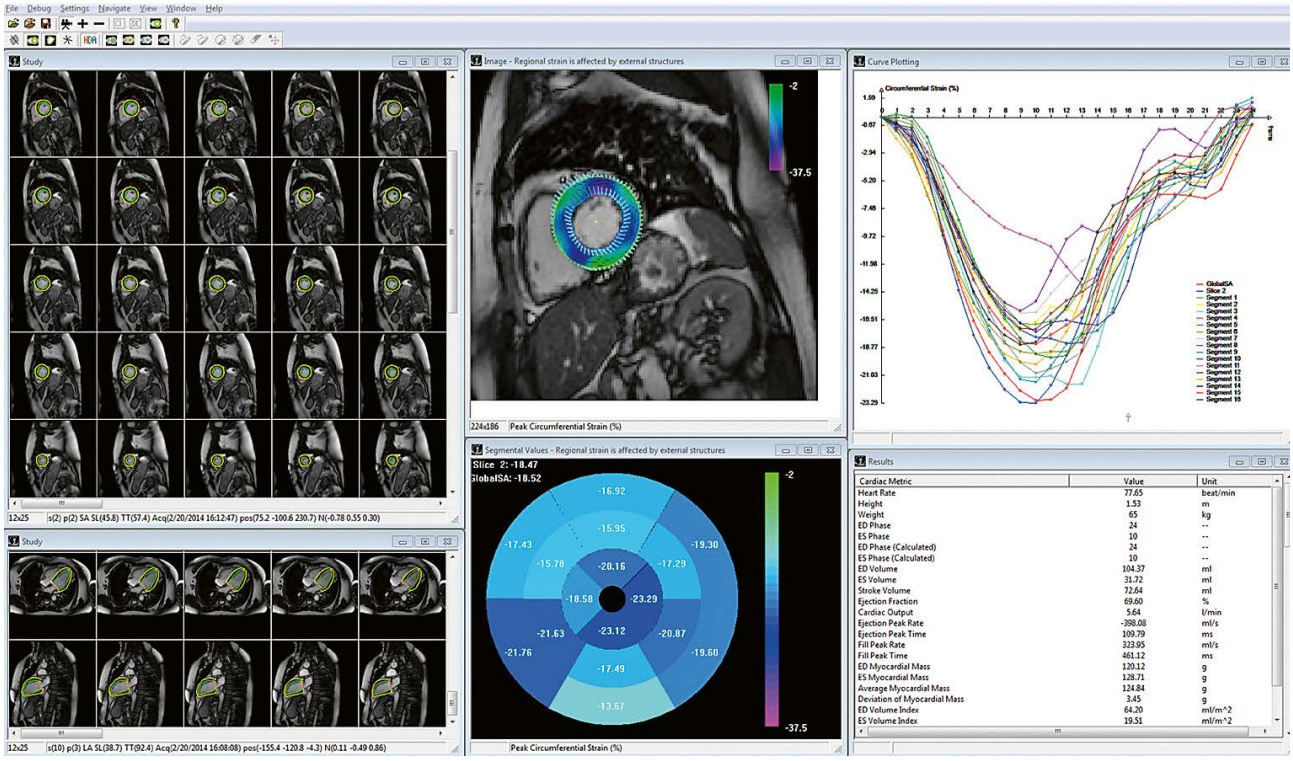

2 Standard screen overview of TrufiStrain[1], a prototype software for cine derived strain analysis. The left part of the layout demonstrates the fully automated (short axis) and semiautomated (long axis) segmentation of the endo- and epicardial contours. The center part highlights a visual overlay of strain data onto cine data as well as a bullseye plot of AHA segment strain results. On the right, a visual display of the strain curves (circumferential in this case) for all 16 AHA segments as well as the entire slice with additional results of automated functional analysis at the bottom.

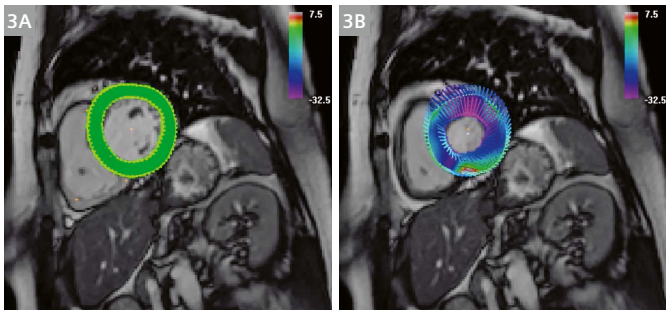

3 Single short axis slice in a healthy volunteer in **(3A)** diastole and **(3B)** systole with time point related strain result overlay; the colored lines on the systolic display visualize the direction and magnitude of endo- as well as epicardial motion from diastole to systole.

Changes in myocardial T1 as well as ECV values have also been demonstrated in patient studies. As in many other cardiomyopathies, pre-contrast T1 values as well as ECV increase after chemotherapy, likely related to development of interstitial fibrosis [20]. However, hyperacute reactions within the myocardium may result in an initial T1 value decrease possible indicating worse outcome [21]. Currently, there is still limited data from prospective longitudinal studies available to clearly describe potential differences in quantitative cardiac relaxometry in patients with and without development of functional deterioration after chemotherapy. Similar to functional analysis, likely sequential longitudinal imaging, including pre-therapy assessment of T1 and T2 data, is required to identify and differentiate true tissue changes from imaging related variability. A possibly even more promising use of cardiac relaxometry techniques may again relate to patients under ICI therapy with possible autoimmune myocarditis changes (Fig. 5). Similar to recent recommendations regarding the diagnosis of myocarditis in general, changes in quantitative tissue markers may help earlier and more accurate diagnosis [22].

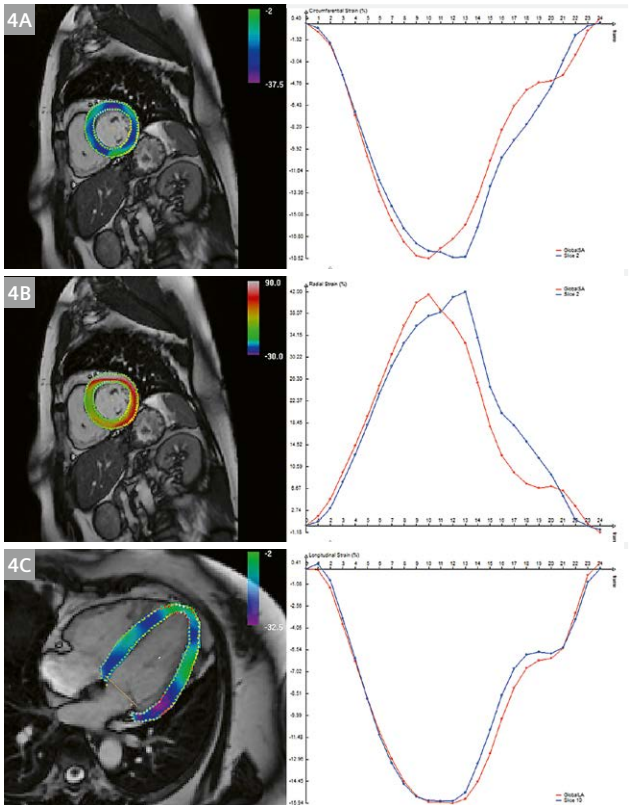

4 Demonstration of three major directions/orientations of myocar dial strains typically evaluated; **(4A)** circumferential strain, **(4B)** radial strain and **(4C)** longitudinal strain. As strain is a measure of length changes in relation to an applied force, the typical shortening in evaluation on circumferential and longitudinal strain result in negative strain values while the thickening during systole results in positive values for radial strain.

Conclusion

While the playing field of potentially cardiotoxic tumor therapy generally hasn't substantially changed, decades of study results have helped to better understand risk factors and relationships between tumor therapy and cardiac failure. Furthermore, there is a much-increased awareness of the potential interaction between tumor therapy and heart failure resulting in the new subspecialty of 'Cardio-Oncology'. While imaging has long played a role in cancer patients undergoing chemotherapy, CMR is rapidly entering the field and is more frequently being employed. The accuracy and precision of CMR functional assessment proves beneficial in early identification of functional deterioration. Added information might be gathered from cine CMR based strain analysis and quantitative myocardial tissue markers (T1/T2/ECV mapping). However, the timing and specific application of CMR during the course of cancer therapy, especially in

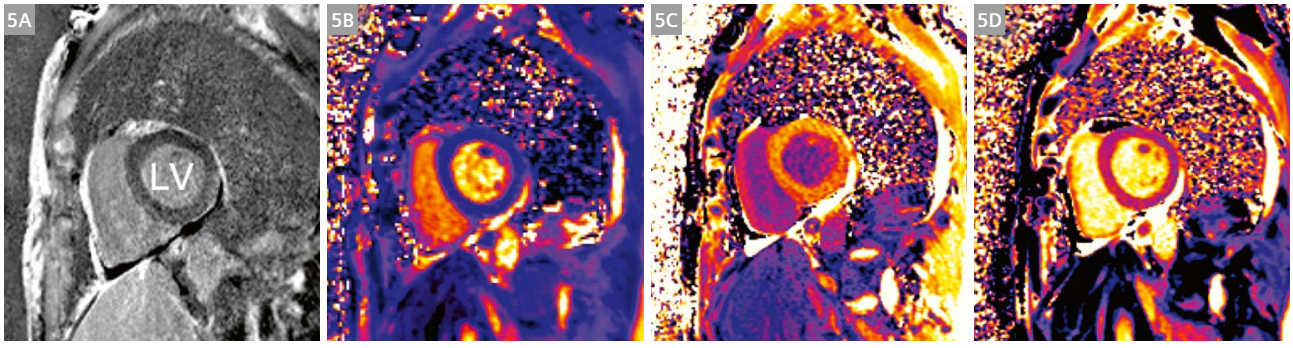

5 Patient undergoing immune checkpoint inhibitor (ICI) cancer therapy with troponin elevation and suspicion of immune myocarditis. While **(5A)** LGE imaging possible demonstrates very faint diffuse enhancement, cardiac relaxometry with T1 and T2-mapping (1.5T) provides further information. **(5B)** T2 mapping reveals a T2 time of 55 ms while **(5C)** pre-contrast T1 values were 1184 ms and **(5D)** post-contrast T1 values 519 ms (0.15 mmol/kg Gadobutrol). Based on the patient's hematocrit the ECV is calculated to 38%.

patients at risk, has yet to be determined. For a better understanding of that role, additional data on the general test-retest variability of such quantitative markers is still required. Furthermore, society guidelines and definitions of cardiotoxicity would need to further extend beyond the sole criteria of cardiac function.

References:

1 Smith LA, Cornelius VR, Plummer CJ et al. (2010) Cardiotoxicity of anthracycline agents for the treatment of cancer: systematic review and meta-analysis of randomised controlled trials. BMC Cancer 10:337.
2 Armenian SH, Hudson MM, Mulder RL et al. (2015) Recommendations for cardiomyopathy surveillance for survivors of childhood cancer: a report from the International Late Effects of Childhood Cancer Guideline Harmonization Group. Lancet Oncol 16:e123-136.
3 Cardinale D, Colombo A, Bacchiani G et al. (2015) Early detection of anthracycline cardiotoxicity and improvement with heart failure therapy. Circulation 131:1981-1988
4 Armenian SH, Lacchetti C, Barac A et al (2017) Prevention and Monitoring of Cardiac Dysfunction in Survivors of Adult Cancers: American Society of Clinical Oncology Clinical Practice Guideline. J Clin Oncol 35:893-911.
5 Escudier M, Cautela J, Malissen N et al. (2017) Clinical Features, Management, and Outcomes of Immune Checkpoint Inhibitor-Related Cardiotoxicity. Circulation 136:2085-2087.
6 Grothues F, Smith GC, Moon JC et al. (2002) Comparison of interstudy reproducibility of cardiovascular magnetic resonance with two-dimensional echocardiography in normal subjects and in patients with heart failure or left ventricular hypertrophy. Am J Cardiol 90:29-34.
7 Schwartz RG, McKenzie WB, Alexander J et al. (1987) Congestive heart failure and left ventricular dysfunction complicating doxorubicin therapy. Seven-year experience using serial radionuclide angiocardiography. Am J Med 82:1109-1118.
8 Seidman A, Hudis C, Pierri MK et al. (2002) Cardiac dysfunction in the trastuzumab clinical trials experience. J Clin Oncol 20:1215-1221.
9 Plana JC, Galderisi M, Barac A et al. (2014) Expert consensus for multimodality imaging evaluation of adult patients during and after cancer therapy: a report from the American Society of Echocardiography and the European Association of Cardiovascular Imaging. J Am Soc Echocardiogr 27:911-939.
10 Huang H, Nijjar PS, Misialek JR et al. (2017) Accuracy of left ventricular ejection fraction by contemporary multiple gated acquisition scanning in patients with cancer: comparison with cardiovascular magnetic resonance. J Cardiovasc Magn Reson 19:34.
11 Lamacie MM, Thavendiranathan P, Hanneman K et al. (2017) Quantification of global myocardial function by cine MRI deformable registration-based analysis: Comparison with MR feature tracking and speckle-tracking echocardiography. Eur Radiol 27:1404-1415.
12 Lamacie MM, Houbois CP, Greiser A, Jolly MP, Thavendiranathan P, Wintersperger BJ (2019) Quantification of myocardial deformation by deformable registration-based analysis of cine MRI: Validation with tagged CMR. Eur Radiol. DOI: 10.1007/s00330-019-06019-9.
13 Keller EJ, Fang S, Lin K et al (2017) The consistency of myocardial strain derived from heart deformation analysis. Int J Cardiovasc Imaging 33:1169-1177
14 Jolly MP, Jordan JH, Melendez GC, McNeal GR, D'Agostino RB, Jr., Hundley WG (2017) Automated assessments of circumferential strain from cine CMR correlate with LVEF declines in cancer patients early after receipt of cardio-toxic chemotherapy. J Cardiovasc Magn Reson 19:59.
15 Barreiro-Perez M, Curione D, Symons R, Claus P, Voigt JU, Bogaert J (2018) Left ventricular global myocardial strain assessment comparing the reproducibility of four commercially available CMR-feature tracking algorithms. Eur Radiol. 10.1007/s00330-018-5538-4.
16 Cummings KW, Bhalla S, Javidan-Nejad C, Bierhals AJ, Gutierrez FR, Woodard PK (2009) A pattern-based approach to assessment of delayed enhancement in nonischemic cardiomyopathy at MR imaging. Radiographics 29:89-103.
17 Friedrich MG, Sechtem U, Schulz-Menger J et al. (2009) Cardiovascular magnetic resonance in myocarditis: A JACC White Paper. J Am Coll Cardiol 53:1475-1487.
18 Hong YJ, Park HS, Park JK et al. (2017) Early Detection and Serial Monitoring of Anthracycline-Induced Cardiotoxicity Using T1-mapping Cardiac Magnetic Resonance Imaging: An Animal Study. Sci Rep 7:2663.
19 Farhad H, Staziaki PV, Addison D et al. (2016) Characterization of the Changes in Cardiac Structure and Function in Mice Treated With Anthracyclines Using Serial Cardiac Magnetic Resonance Imaging. Circulation Cardiovascular imaging 9:e003584.
20 Jordan JH, Vasu S, Morgan TM et al. (2016) Anthracycline-Associated T1 Mapping Characteristics Are Elevated Independent of the Presence of Cardiovascular Comorbidities in Cancer Survivors. Circulation Cardiovascular imaging 9
21 Muehlberg F, Funk S, Zange L et al. (2018) Native myocardial T1 time can predict development of subsequent anthracycline-induced cardiomyopathy. ESC Heart Fail. 10.1002/ehf2.12277.
22 Ferreira VM, Schulz-Menger J, Holmvang G et al. (2018) Cardiovascular Magnetic Resonance in Nonischemic Myocardial Inflammation: Expert Recommendations. J Am Coll Cardiol 72:3158-3176.

Christian Houbois

P. Thavendiranathan

Bernd Wintersperger

Contact

Bernd J. Wintersperger, MD EBCR FAHA
Department of Medical Imaging
Toronto General Hospital, 1 PMB-273
585 University Avenue
Toronto, Ontario, M5G 2N2
Canada
Tel.: 416-340-4800 ex. 8593
Bernd.Wintersperger@uhn.ca

Highly Accelerated 4D Flow Imaging using Compressed Sensing – a Comparison with Conventional 4D Flow in Healthy Volunteers and Patients with Aortic Diseases

Tilman Emrich, M.D.[1]; Daniel-Sebastian Dohle, M.D.[2]; Ning Jin, Ph.D.[3]

[1]Department of Diagnostic and Interventional Radiology, University Medical Center Mainz, Germany
[2]Department of Cardiothoracic Surgery, University Medical Center Mainz, Germany
[3]Cardiovascular MR R&D, Siemens Medical Solutions, Chicago, USA

Introduction

3D cine phase-contrast (PC) imaging with three-dimensional velocity encoding (4D Flow) is an emerging imaging tool in cardiovascular diseases. 4D Flow allows the visualization of flow in all directions and spatial regions within the volume imaged and can be used to analyze complex hemodynamic properties without the need for invasive procedures and ionizing radiation. Compared with conventional 2D PC imaging, 4D Flow enables investigation of the internal data consistency (i.e. Qp/Qs measurement within the same dataset) and provides the flexibility to retrospectively place the analysis plane at any location within the imaging volume [1]. Furthermore, novel imaging biomarkers, such as wall shear stress (WSS) or loss of kinetic energy, can be estimated from 4D Flow datasets.

Nevertheless, clinical applications with 4D Flow are limited by their long acquisition time and the need for offline reconstruction, which takes several hours. Recently, a highly accelerated 4D Flow sequence[1] has been developed using Compressed Sensing (CS) acceleration with image reconstruction implemented on the scanner, which allows 4D Flow imaging of the aorta in less than two minutes, whole heart and the aorta in under seven minutes, and online image reconstruction under five minutes. This article describes our initial experience of CS 4D Flow[1] sequences in healthy volunteers and aortic diseased patients.

[1]*WIP, the product is currently under development and is not for sale in the U.S. and in other countries. Its future availability cannot be ensured.*

Table 1: Average volunteer stroke volume and peak velocity.

	Ascending Aorta	Aortic Arch	Descending Aorta	Mean
4D net flow (ml/cycle)	85.25	59.87	67.43	70.85
Δ% net flow	-5.34	-7.33	-11.55	-8.07
4D mean peak velocity (cm/s)	61.10	46.97	58.06	55.38
Δ% mean peak velocity	-6.09	-7.51	-6.20	-6.60

Δ%: Mean difference in percent between conventional and CS accelerated 4D Flow acquisition. Negative values in Δ% net flow show underestimation by CS 4D Flow.

Technical background

4D Flow MRI sequence was implemented using retrospective ECG gating and symmetric 4-point velocity encoding. Images were acquired during free-breathing with navigator gating and Respiratory Controlled Adaptive *k*-space Reordering (ReCAR) to acquire central *k*-space during end expiration and peripheral *k*-space during inspiration to reduce motion artifacts [2]. CS acceleration was achieved using a variable-density phyllotaxis pattern for subsampling with sampling patterns rotated between successive cardiac time frames to form a fully sampled center for coil sensitivity estimation and spatial-temporal L1 regularization for image reconstruction (Fig. 1).

Methods

4D Flow imaging was performed on a MAGNETOM Prisma 3 Tesla MRI scanner (Siemens Healthcare, Erlangen, Germany). The study population was recruited from two prospective cohort studies at the University Medical Center Mainz, Germany.

All 4D Flow acquisitions were performed in sagittal orientation to cover the whole heart and the thoracic aorta during free-breathing with navigator gating. CS 4D Flow was acquired with an acceleration rate of 7.7, and the conventional 4D Flow was acquired with a GRAPPA acceleration rate of 3. Imaging protocols include the following parameters: TE/TR for conventional and CS 4D Flow: 38.64 / 2.28 ms and 40.48 / 2.36 ms; FOV: 380 and 360 mm, Matrix: 160 x 80 and 160 x 102, FA: 8° and 7°. All image processing was performed using the cvi[42] 4D Flow plugin (Circle Cardiovascular Imaging, Calgary, Canada).

Clinical applications

We want to demonstrate the clinical applications of this prototype in three case-based steps:

1. Validation in healthy volunteers
For validation, CS and the conventional 4D Flow were acquired on 20 volunteers from the Mainz Cohort MR (MaiCo-MR) study before contrast injection. Both 4D Flow datasets were successfully acquired in all subjects.

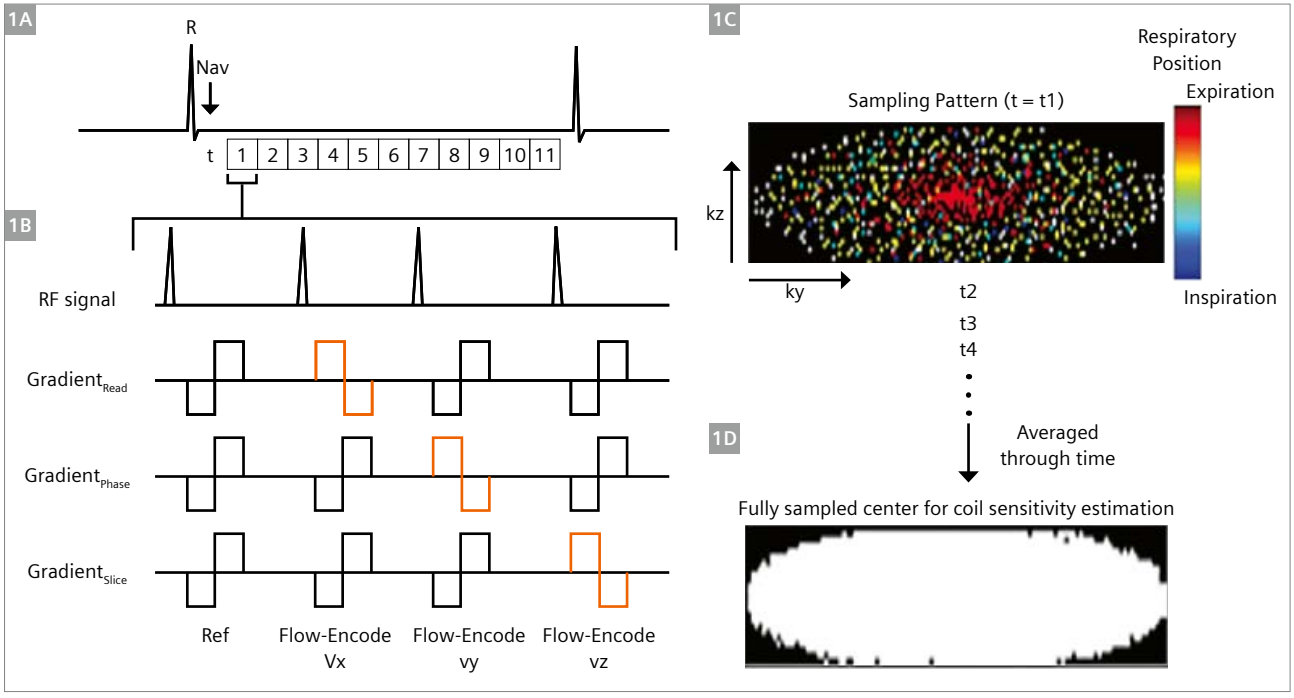

1 CS acquisition and reconstruction. **(1A, 1B)** Retrospectively-gated flow acquisition using symmetric 4-point encoding gated to the cardiac cycle. Only bipolar flow gradients are depicted. Imaging gradients are not included for simplicity. Navigator echoes (Nav) were played out after R-wave detection in the ECG tracing. Numbers (1–11) represent succesive cardiac time frames t_n, n = 1, 2 ... 11). In each cardiac phase a segment of *k*-space (views per segment = 2) is acquired. **(1C)** ReCAR with combined with spiral phyllotaxis subsampling pattern in the kz/ky dimensions of a single time frame that is subsequently rotated for each frame (t_n). Central *k*-space is acquired during expiration (red) and outer *k*-space is acquired during inspiration (blue) to mitigate respiratory motion artifacts. When all cardiac time frames are combined they form a fully sampled center of *k*-space, **(1D)**, for coil sensitivity estimation.
Adapted with permission from [2].

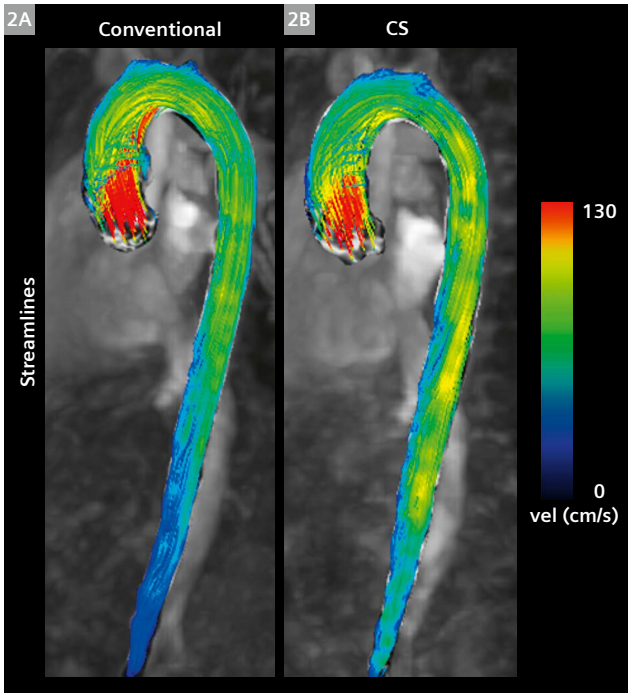

2 Peak systolic 3D streamlines of the thoracic aorta reconstructed from **(2A)** conventional 4D Flow (GRAPPA R3) and **(2B)** CS 4D Flow (R7.7) acquisitions.

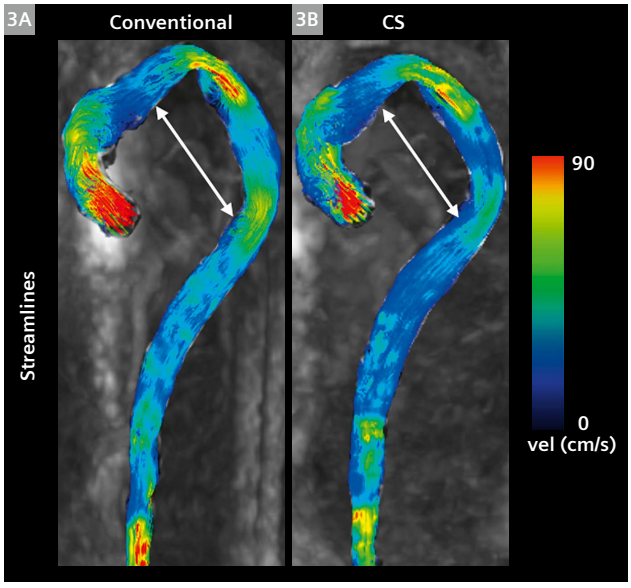

3 Peak systolic 3D streamline visualization of the aortic arch with "frozen elephant trunk", reconstructed from conventional 4D Flow (**3A** left) and CS 4D Flow images (**3B** right). The arrows show the beginning and the end of the stent-graft.

Compared with conventional 4D Flow, CS 4D Flow significantly reduced scan time, whilst image quality was subjectively equal for both techniques (Fig. 2). The mean total acquisition time was 6:51 min for CS 4D Flow as opposed to 10:56 min for the conventional 4D Flow, which equates to a 37% reduction in time. Flow quantification was performed at three locations along the aorta: ascending aorta, the aortic arch and the descending aorta.

A mild underestimation of stroke and velocity was found in the comparison of CS-based measurements compared with conventional acquisitions (mean underestimation net flow: -8.07%, mean underestimation total volume: -7.38%, mean underestimation peak velocity: -6.60%) (Table 1).

2. Application in aortic diseased patients to visualize and quantify pathologic flow patterns

CS and the conventional 4D Flow acquisitions were performed in 15 participants of the prospective "4D Flow in Aortic Disease (AD4D)" study. All participants had undergone aortic surgery for treatment of aortic dissection with supracoronary aortic replacement and "frozen elephant trunk" antegrade stent-graft implantation. 4D Flow imaging was performed within seven days of surgery. The mean total imaging time for CS and conventional acquisitions was 7:12 and 11:02 minutes respectively.

Overall, there are no statistically significant differences between conventional and CS measurements regarding total volume, mean pressure gradient, maximum mean velocity, and peak flow (e.g., Wilcoxon rank test for paired samples for conventional and CS 4D Flow total volume, $p = 0.715$; mean pressure gradient: $p = 0.255$; maximum mean velocity: $p = 0.255$; maximum flow: $p = 0.265$). Compared with conventional 4D Flow, CS 4D Flow tends to slightly underestimate maximum flow (-4.4%) and peak velocity (-5.9%). Peak systolic streamline visualization shows good agreement between conventional (Fig. 3A) and CS 4D Flow (Fig. 3B) acquisitions. The complicated flow pattern could be visualized by both techniques.

3. Application for novel imaging parameters, e.g., WSS analysis

Finally, we want to demonstrate that not only basic flow information but also novel imaging biomarkers such as WSS or vortex analysis can be derived in a comparable way from highly accelerated CS 4D Flow imaging. Figure 4 presents the case of a 54-year-old patient with bicuspid aortic valve and aneurysm in the ascending aorta. Systolic streamlines depict a complex helical flow pattern in the ascending aorta in both conventional and CS 4D Flow (Fig. 4A, B white arrows). CS 4D Flow is able to visualize areas of increased WSS in the same area as in the conventional 4D Flow (Fig. 4C, D red arrows).

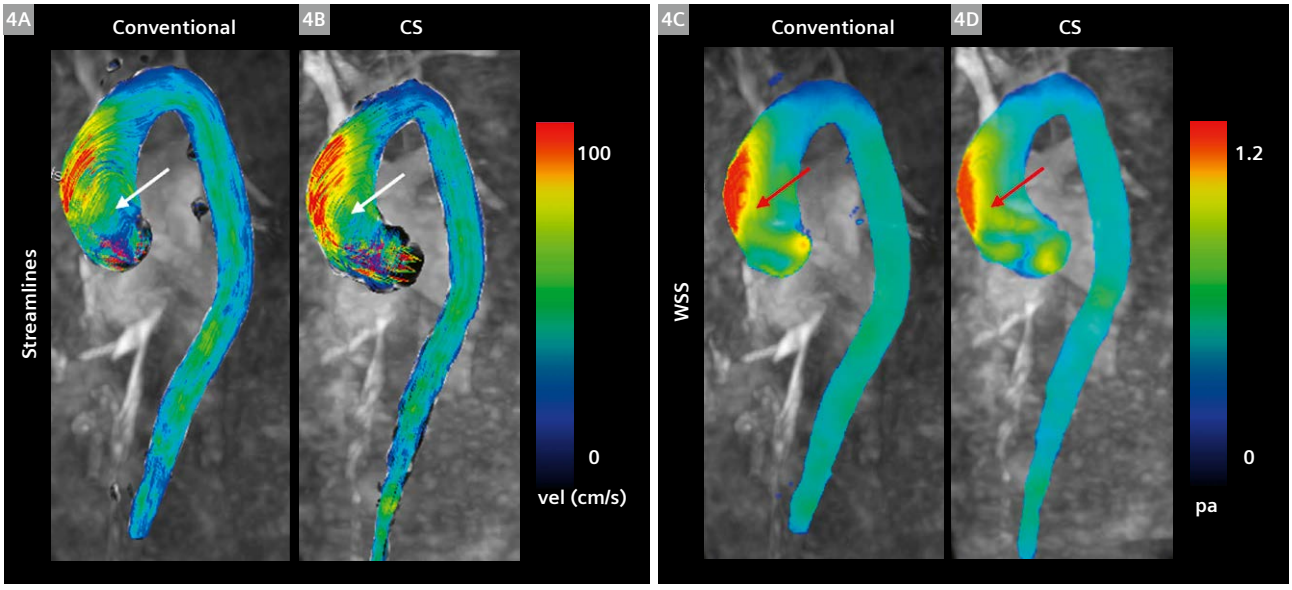

4 Peak systolic 3D streamlines and WSS from the conventional and CS 4D Flow in a 54-year-old patient with bicuspid aortic valve and aneurysm in the ascending aorta. Systolic streamlines depict complex helical flow pattern in the ascending aorta (**4A, B**, white arrows). Both techniques depict increased WSS in the same region (**4C, D**, red arrows).

Further studies are needed to quantitatively compare changes in advanced flow parameters from highly accelerated CS 4D Flow imaging to the conventional 4D Flow sequences.

Conclusion and outlook

In conclusion, CS and conventional 4D Flow acquisitions demonstrate the feasibility of visualizing blood flow pattern in healthy volunteers and patients with aortic diseases. Compared with conventional 4D Flow, CS 4D Flow significantly reduces the total acquisition time, making its integration into daily clinical routine feasible. However, highly accelerated CS 4D Flow acquisitions tend to slightly underestimate flow measurements. Future investigations will study CS 4D Flow in larger patient cohorts and validate classic and novel flow parameters against gold-standard measurements as well as determine prognostic implications of this method.

Contact

Tilman Emrich, M.D.
Department of Diagnostic and Interventional Radiology
University Medical Center Mainz
Langenbeckstr. 1
55131 Mainz
Germany
Tilman.Emrich@unimedizin-mainz.de

Acknowledgments

The authors wish to acknowledge the support of the team of technologists, doctoral candidates, and physicians of the "cardiovascular imaging" working group of the University Medical Center Mainz.

References

1 Dyverfeldt P et al. 4D flow cardiovascular magnetic resonance consensus statement. J Cardiovasc Magn Reson. 2015 Aug 10;17:72. doi: 10.1186/s12968-015-0174-5.
2 Ma LE et al. Aortic 4D flow MRI in 2 minutes using compressed sensing, respiratory controlled adaptive k-space reordering, and inline reconstruction. Magn Reson Med. 2019 Jun;81(6):3675-3690. doi: 10.1002/mrm.27684. Epub 2019 Feb 25

Cardiac PET/MR Delineates Extensive Subendocardial Infarction Leading to Acute Coronary Syndrome

Eun-Jung Kong, M.D. Ph.D[1]; Partha Gosh, M.D.[2]

[1] Division of Cardiology, Yeungnam University Medical Center, Daegu, South Korea
[2] Siemens Healthineers, Molecular Imaging, Hoffman Estates, IL, USA

History

A 57-year-old man with a 20-plus-year history of diabetes and hypertension presented with severe respiratory distress accompanied by eyeball deviation and swelling of lower limbs. Paramedics arrived and delivered cardio-pulmonary resuscitation (CPR) followed by defibrillation, necessitated by ventricular fibrillation. The CPR continued during the ambulance transport to the emergency room (ER) of the Yeungnam University Hospital. In the ER, the patient showed signs of hypoxic brain damage with stiffness of limbs and was successfully resuscitated. The patient's serum troponin level was significantly elevated (0.42 ng/ml) at the time of ER admission. An echocardiography, performed following resuscitation, showed mild regional-wall-motion abnormality in the anterior septum, with suspicion of hypertrophic cardiomyopathy due to asymmetric septal thickness.

Twelve years prior, the patient underwent a coronary angiography which demonstrated an absence of any luminal stenosis.

Findings

The patient underwent an adenosine stress ^{13}N NH_3 PET/CT myocardial perfusion study, which showed a reduction of blood flow to the anterior wall and upper septum (Fig. 1). In view of the suggestion of left anterior descending (LAD) territory ischemia and the history of sudden cardiac arrest, the patient was referred for a Fludeoxyglucose F 18 injection (^{18}F FDG) cardiac PET/MR to evaluate the cause of the acute coronary syndrome.

An ^{18}F FDG PET/MR study was performed on a Biograph mMR system five days after emergency admission. The patient received a low-carbohydrate diet the day prior to imaging, followed by a 12-hour fasting period in order to suppress physiological myocardial ^{18}F FDG uptake. Thirty minutes before the ^{18}F FDG injection, the patient received an intravenous dose of unfractionated heparin (50 UI/kg body weight) to further suppress physiological myocardial ^{18}F FDG uptake. Sixty minutes after the intravenous injection of 237.5 MBq of ^{18}F FDG, a 3D listmode PET scan in was started.

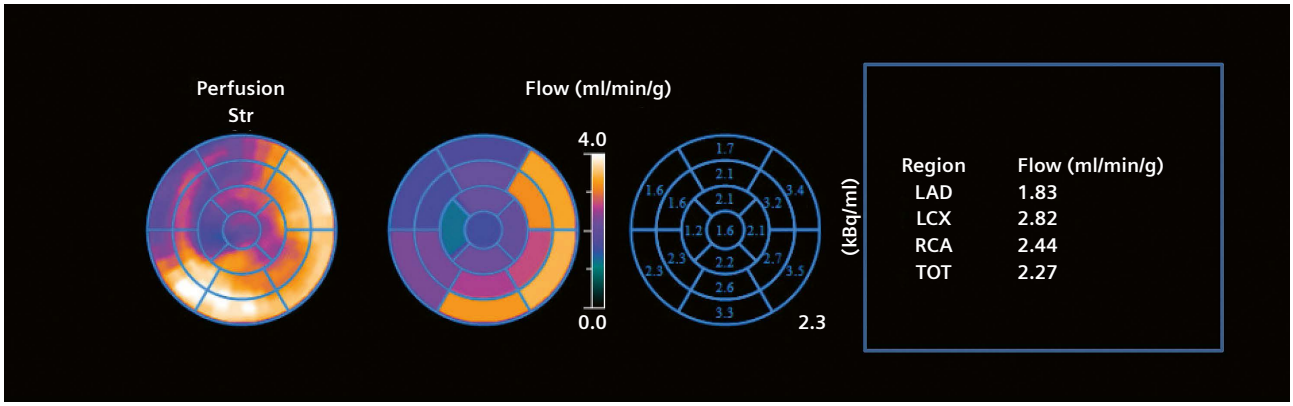

1 4DM (Invia, Ann Arbor, MI, USA) myocardial blood flow values at peak stress and stress perfusion bulls eye plot show decreased perfusion in the anterior wall, apex, and upper septum with significant reduction in myocardial blood flow values (1.83 ml/min/gm), as compared to the inferior and lateral walls, which is suggestive of the LAD territory ischemia during stress.

A two-point Dixon sequence was acquired for the purpose of PET attenuation correction. During the acquisition of listmode PET, multiple MR sequences were also acquired. Initial axial T2 HASTE, cine MRI using TrueFISP, and dark-blood T2 HASTE acquisitions were performed. Subsequently, intravenous Gadolinium (Gd) contrast was infused and a first-pass perfusion with turboFLASH sequence was performed, followed by late Gd enhancement with TrueFISP sequence in order to delineate myocardial contrast enhancement.

As depicted in Figures 2–4, the ^{18}F FDG PET/MR study shows late enhancement with Gd contrast seen with inversion recovery MR sequences limited to the subendocardium in the apex and adjacent septal and lateral walls, suggestive of subendocardial infarction. Simultaneously acquired ^{18}F FDG PET shows increased ^{18}F FDG uptake in the same subendocardial areas with the late Gd enhancement, which suggests the subendocardial hypermetabolism may be secondary to inflammation within the zone of acute myocardial infarction. The patient subsequently underwent coronary angiography.

Coronary angiography (Fig. 5) shows 80% stenosis in the proximal LAD and the origin of IM1. The stenotic lesions correlate with the distribution of the subendocardial infarct in the apex and septum, which correspond to the LAD territory.

The patient underwent balloon dilatation and stenting of the LAD and IM lesions. Six days following percutaneous coronary intervention, there was slight improvement of the regional wall-motion abnormality.

Comments

This study demonstrates the value of simultaneous ^{18}F FDG PET/MR in defining the extent of acute myocardial infarction, as well as the inflammatory process characteristic of such acute myocardial injury. The extent of post-Gd late enhancement, as seen on MRI, clearly delineates the subendocardial nature of the acute myocardial infarction. The exact co-registration of ^{18}F FDG uptake with the subendocardial post-contrast enhancement on MRI reflects the degree of inflammation caused by the acute myocardial injury, which is the hallmark of the immunological response immediately following acute myocardial infarction.

Myocardial infarction is often associated with adverse myocardial remodeling and development of heart failure in many patients. The immune system plays a key role in the repair and subsequent myocardial-scar formation. Shortly after acute myocardial infarction, neutrophils and monocytes invade the ischemic myocardium and cause the removal of dead cells as well as the breakdown of the extracellular matrix. Thereafter, anti-inflammatory cytokines are produced that stop the inflammatory processes and cause the transition to the proliferative phase. The final, so-called maturation, phase is thought to be responsible for a stable scar formation [1].

Exaggerated inflammatory response may result in the expansion of infarct and impaired infarct healing. Excessive cellular infiltration after myocardial infarction by neutrophils and monocytes may cause exaggerated degradation of the extracellular matrix and support infarct expansion, left ventricular dilatation, aneurysm formation,

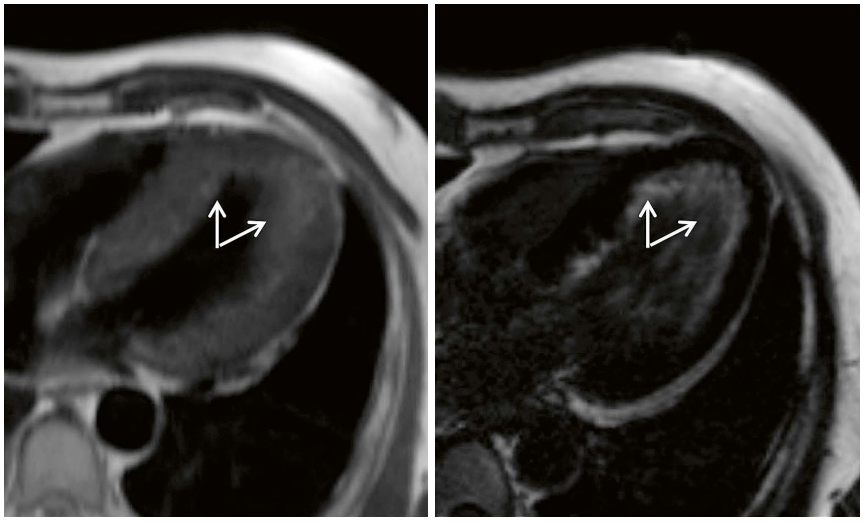

T2 HASTE Late Gd enhancement (TrueFISP)

2 Axial T2 HASTE and post-Gd TrueFISP show mild hyperintensity in the subendocardium in the apical region and the adjacent lateral wall and septum, which corresponds to the regions of contrast enhancement in the post-Gd sequence (arrows). These regions reflect patchy subendocardial infarction, which is illustrated by the Gadolinium enhancement. The myocardium appears slightly hypertrophied and the late Gd enhancent (TrueFISP) sequence clearly delineates the absence of myocardial signal characteristic of normal myocardium separate from the subendocardial contrast enhancement, which highlights the non-transmural nature of the infarction.

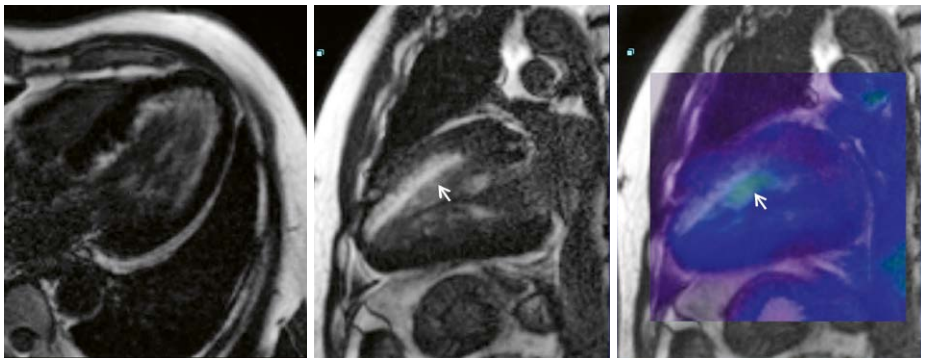

LGE TrueFISP Tra | LGE TrueFISP Sag | ^{18}F FDG PET/MR fusion

3 Two-chamber and four-chamber views through the left ventricle of the post-Gd TrueFISP sequence (late Gd enhancement also known as LGE) show the subendocardial contrast enhancement with increased ^{18}F FDG uptake in part of the subendocardium (arrows), reflecting inflammation induced by acute myocardial injury corresponding to the subendocardial infarction in the fused PET/MR images.

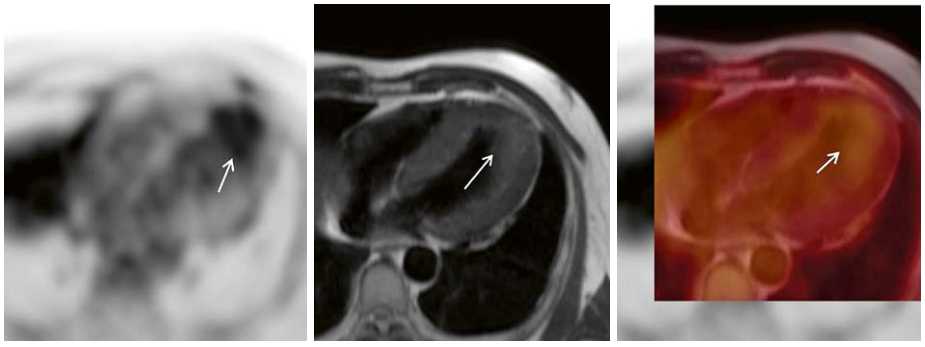

^{18}F FDG PET | T2 HASTE Tra | ^{18}F FDG PET/MR fusion

4 Four-chamber views of ^{18}F FDG PET, T2 HASTE, and fused PET/MR showing increased ^{18}F FDG uptake in the apical, septal, and adjacent lateral wall subendocardium (arrows), co-registering with the mild hyperintensity in the same myocardial region seen on the HASTE images, which reflects subendocardial inflammation secondary to acute myocardial infarction limited to the subendocardium.

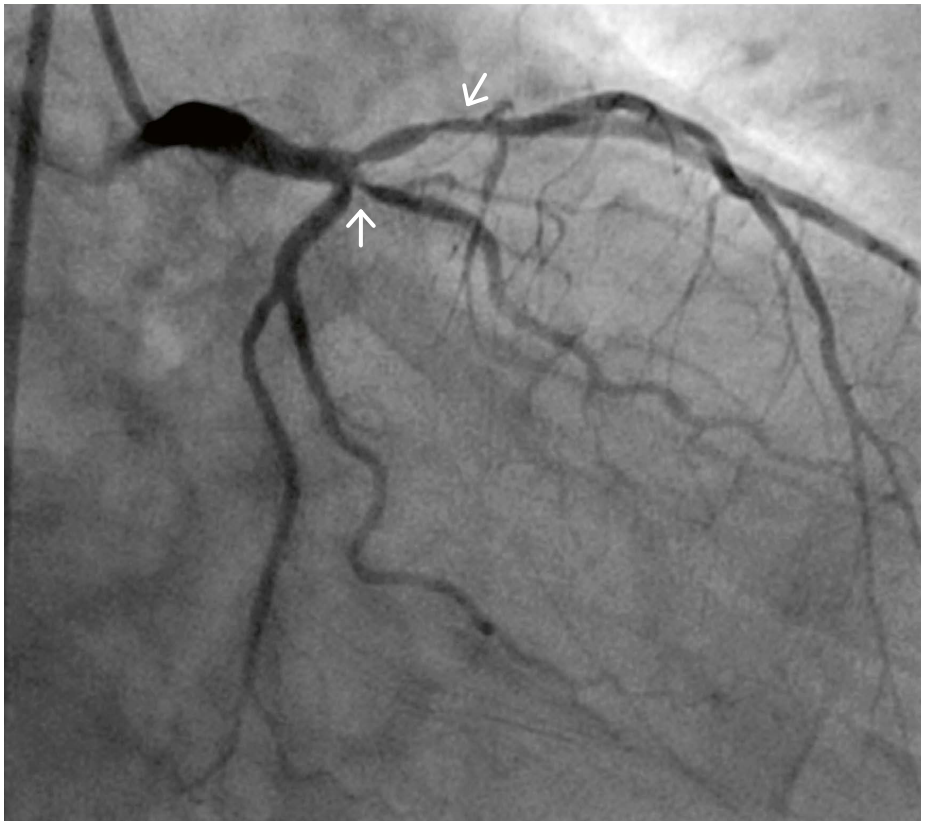

5 Coronary angiography shows 80% tubular eccentric stenosis in the proximal LAD as well as 80% discrete stenosis at the origin of the IM1 (arrows).

pLAD: Tubular eccentric stenosis 80% (arrow)
IM: Discrete eccentric stenosis 80% (arrow)
dRCA: Diffuse eccentric stenosis 30%

or even ventricular rupture [1]. This makes the immune system a potential therapeutic target for the prevention of heart failure after myocardial infarction.

Studies show that the intensity of ^{18}F FDG uptake in an infarcted myocardium – within a few days after acute injury – have significant correlation with the size of infarction, MRI measures of the left ventricular ejection fraction, and regional wall-motion abnormalities [2]. An increased accumulation of monocytes and macrophages within the infarcted myocardium leads to higher glucose metabolism reflected by a higher ^{18}F FDG uptake. This has led to the hypothesis that performing a ^{18}F FDG PET, soon after acute myocardial infarction, can be used to assess the extent of inflammation and act as a prognostic indicator. In order for ^{18}F FDG uptake to reflect myocardial inflammation, the normal uptake exhibited by a cardiac muscle must be suppressed by fasting, a high-fat diet, or injecting heparin prior to the PET scan. These measures help switch the nonischemically injured heart's metabolism from predominate glucose consumption towards fatty acid oxidation. Consequently, ^{18}F FDG is mainly absorbed by activated inflammatory cells in the post-ischemic myocardium after infarction. In this study fasting and intravenous heparin were used based on a protocol developed to image inflammation in coronary arteries and sarcoidosis.

Post-ischemic, viable cardiomyocytes upregulate the expression of glucose transporters on their surface and thus result in an increase in ^{18}F FDG uptake within viable myocytes during acute ischemia. However, the presence of post–Gd enhancement in the myocardium is strongly reflective of myocardial infarction and any ^{18}F FDG uptake within infarcted tissue is deemed to reflect post-injury inflammation, caused by leukocyte infiltration and edema [2]. In a simultaneous PET/MR study evaluating ^{18}F FDG uptake within the myocardium following acute infarction, SUV_{mean} in the infarct area was associated with deterioration of left-ventricular function, independent of the infarct size [3]. This suggests that the level of inflammatory response within infarcted myocardium has a direct correlation to a long-term outcome, including infarct-related remodeling and a resultant wall-motion impairment and ventricular dilatation. ^{18}F FDG PET, as a measure of inflammation extent and intensity, may serve as a biomarker for post-infarct inflammation and as a prognostic indicator for infarctrelated remodeling and ventricular functional outcome.

Conclusion

^{18}F FDG PET/MR shows increased uptake of ^{18}F FDG in subendocardial infarction, an observation that was also confirmed by the presence of late post-Gd contrast enhancement on MR. Both of these observations reflect inflammation within the myocardium after acute ischemic injury in a patient with aborted sudden cardiac death with evidence of LAD and IM1 stenosis.

Biograph mMR examination protocol

PET	
Injected dose	237.5 MBq ^{18}F FDG
Scan delay	60 minutes
Scan acquisition	Simulation listmode
MR	
Sequences	2-point Dixon
	T2 HASTE
	Dynamic Gd perfusion
	Late Gd enhancement

Contact

Eun-Jung Kong, M.D., Ph.D.
Division of Cardiology
Department of Internal Medicine
Yeungnam University Medical Center
317-1 Daemyeong 5(o)-dong, Nam-gu
Daegu
South Korea
kongej@yu.ac.kr

References

1 Rischpler C. Acute myocardial infarction. Q J Nucl Med Mol Imaging. 2016;60(3):236-251.
2 Wollenweber T, Roentgen P, Schafer A, et al. Characterizing the inflammatory tissue response to acute myocardial infarction by clinical multimodality noninvasive imaging. Circ Cardiovasc Imaging. 2014;7(5):811-818.
3 Rischpler C, Dirschinger RJ, Mekolla SG, et al. Prospective Evaluation of 18F-Fluorodeoxyglucose Uptake in Postischemic Myocardium by Simultaneous Positron Emission Tomography/Magnetic Resonance Imaging as a Prognostic Marker of Functional Outcome. Circ Cardiovasc Imaging. 2016;9(4):e004316. doi:10.1161/CIRCIMAGING.115.004316.

Motion-corrected Whole-heart Simultaneous Cardiac MR/PET Imaging: Initial Clinical Experience

Camila Munoz[1]; Karl P. Kunze[2]; Radhouene Neji[1,2]; Stephan G. Nekolla[3]; René M. Botnar[1]; Claudia Prieto[1]

[1] School of Biomedical Engineering and Imaging Sciences, King's College London, London, United Kingdom
[2] MR Research Collaborations, Siemens Healthcare Limited, Frimley, United Kingdom
[3] Technische Universität München, Nuklearmedizinische Klinik und Poliklinik, Munich, Germany

Abstract

Image degradation due to respiratory motion remains a challenge for cardiac MR/PET imaging. Although novel approaches for MR/PET motion compensation have been recently introduced, most of these schemes usually only acquire motion information from MRI data during the PET acquisition, and diagnostic MR data afterwards. This significantly increases total examination time and may lead to misaligned images between modali ties. We have recently proposed a simultaneous coronary MR angiography (CMRA) and cardiac PET acquisition and reconstruction framework[1] that enables MR visualization of the coronary anatomy and motion-corrected myocardial PET in a single efficient examination. Non-rigid respiratory motion is estimated from MR images and used to correct both the CMRA data and the simultaneously acquired PET data, resulting in intrinsically aligned motion-corrected images from both modalities. Initial validation of this approach has been performed in healthy subjects and patients with known or suspected cardiovascular disease. Results show that the motion correction approach improves quality in CMRA images, allowing for good depiction of the proximal and mid coronary arteries, while also improving PET image quality, resulting in sharper myocardial edges and allowing the observation of small anatomical features and pathologies. Overall, the proposed approach produces high quality images in both modalities, demonstrating the potential for enabling a comprehensive, non-invasive assessment of heart disease in a single and time-efficient MR/PET examination.

[1] *WIP, the product is currently under development and is not for sale in the U.S. and in other countries. Its future availability cannot be ensured.*

Introduction

Cardiovascular disease (CVD) is the leading cause of death worldwide, accounting for 31.5% of the total number of deaths in 2015 [1]. Amongst all cardiovascular diseases, coronary artery disease (CAD) has the highest mortality rate and overall is the most common cause of death globally. The recent development of hybrid MR/PET systems has opened new possibilities for a comprehensive non-invasive assessment of cardiovascular disease, by enabling the simultaneous acquisition of complementary anatomical and functional information in a single scan session [2–4]. In particular for CAD, MR-PET systems offer great potential for simultaneous assessment of myocardial integrity (perfusion or viability) and coronary plaque activity by PET [5], and coronary lumen integrity by CMRA in a single examination. However, respiratory motion is a major source of image quality degradation in both PET and MR cardiac imaging.

Respiratory motion can result in image blurring and ghosting artifacts in MRI, and in image blurring and artifacts due to mismatches between attenuation maps and emission maps in PET. Conventionally, the effect of respiratory motion in both PET and CMRA imaging has been mitigated by using techniques that sort the acquired data into near motion-free frames representing different positions within the respiratory cycle. These techniques, widely known as gating techniques, can be used to acquire data (or accept data for image reconstruction) only when the respiratory signal is within a predefined phase of the breathing cycle, typically end-expiration, rejecting all other data being acquired. The main drawback of gating approaches is that they lead to long acquisition times to acquire enough data, i.e. with high enough signal-to-noise ratio (SNR) for PET

and enough samples for a desired spatial resolution and coverage for MRI. Furthermore, as respiratory patterns vary greatly among subjects, gating usually results in unpredictable scan times, negatively impacting patient throughput.

Alternatively, the problem of respiratory motion can be addressed by obtaining information about the motion from the acquired data itself and then using it to produce motion-compensated images with improved image quality in a shorter acquisition time. Although several motion compensation approaches have been developed over the last decades separately for both PET and MR imaging, the introduction of hybrid MR/PET scanners has allowed the development of novel techniques to alleviate the problem of motion simultaneously for both modalities. In cardiac MR/PET imaging, most of the research efforts about motion compensation have focused on improving PET image quality by acquiring MR images with high spatial resolution and superior soft-tissue contrast simultaneously with PET, so that motion information obtained from such MR images can be used to correct the PET data [6, 7]. Although this approach has been shown to positively impact PET image quality and quantification, in general the simultaneously acquired MR data is being used only for motion estimation, limiting their use for diagnosis purposes.

Therefore, whereas clinical application of simultaneous cardiac MR/PET imaging for the diagnosis of CAD and other cardiovascular conditions would benefit from the complementarity between the functional and

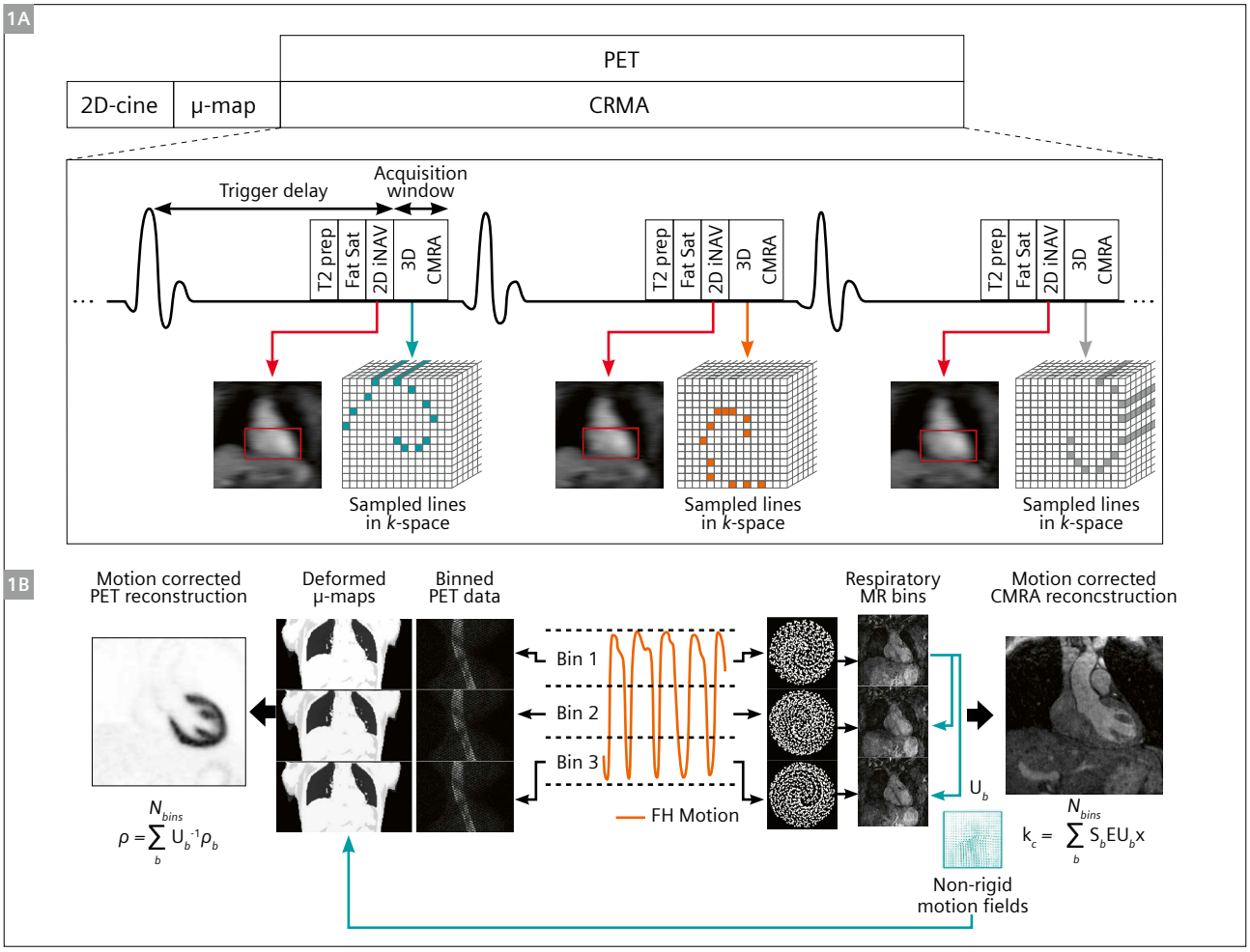

1 PET-CMRA acquisition and reconstruction method. **(1A)** PET-CMRA acquisition protocol, an image-navigator (2D iNAV) is acquired at each heartbeat before the CMRA acquisition for estimating respiratory motion. T2 preparation (T2 prep) and fat saturation (fatsat) pulses are used in order to improve contrast between blood and surrounding tissue. Before the PET-CMRA acquisition, a 2D cine image is acquired to define the trigger delay and acquisition window within the cardiac cycle for 3D CMRA, and a μ-map is acquired for attenuation correction of the PET data. **(1B)** Foot-head (FH) motion estimated from the 2D iNAVs is used to bin the PET and CMRA data in a number of respiratory bins. Non-rigid deformation fields (in teal) are estimated from MR images reconstructed at each respiratory position and used to transform the attenuation maps to each respiratory position, and in the proposed motion compensated PET and CMRA image reconstruction. *Figure adapted from [8].*

morphological diagnostic information provided by both modalities, in practice, state-of-the-art approaches acquire diagnostic information from each modality sequentially, leading to long acquisition times and misaligned diagnostic PET and MR images.

We have recently proposed a novel framework[1] for simultaneous non-rigid respiratory motion compensated cardiac MR/PET imaging, allowing for visualization of the coronary arteries by CMRA and assessment of myocardial integrity by PET from a single examination [8]. This framework enables respiratory motion tracking by including a 2D image navigator (iNAV) in the MR acquisition sequence, which allows for estimating the position of the heart within the respiratory cycle at each heartbeat. Then, by combining a beat-to-beat 2D translational motion correction with a bin-to-bin 3D non-rigid motion correction approach for CMRA, the MR-derived non-rigid motion information can be used to correct for both the CMRA and the simultaneously acquired PET data to the same respiratory position.

This approach is highly efficient since nearly all acquired data is used for image reconstruction (100% scan efficiency), resulting in predictable and shorter scan time compared to conventional gated acquisitions. Additionally, the framework enables the acquisition of diagnostic MR and PET images simultaneously, significantly reducing the total exam time compared to techniques that perform diagnostic MR acquisitions after the PET acquisition, without sacrificing image quality.

Here we present a brief summary of our technique, including some results from our initial clinical experience in patients with known or suspected cardiovascular disease [9], which demonstrate the benefits of the proposed motion-correction scheme for simultaneous CMRA and myocardial characterization by PET in different clinical contexts.

Methods

The whole-heart PET-CMRA acquisition consists of a free-breathing ECG-triggered CMRA sequence simultaneously acquired with list-mode cardiac PET data, as shown in Figure 1A. CMRA data is acquired using a 3D spoiled gradient echo sequence following a fully sampled golden-step Cartesian trajectory with spiral profile ordering, so that one spiral interleaf is acquired at each heartbeat [10]. A 2D iNAV [11] is acquired at the beginning of each spiral interleaf by spatially encoding low flip angle *k*-space lines, and fat saturation and T2 preparation [12] pulses are performed immediately prior to CMRA data acquisition to improve the contrast between arterial blood and the surrounding myocardium and epicardial fat.

As part of the cardiac PET-CMRA acquisition protocol, a standard Dixon-based attenuation map (μ-map hereafter) is acquired in breath-hold at end-expiration for MR-based attenuation correction of the PET data, with missing tissue due to the limited field of view of the MR (as compared to PET) estimated using the MLAA (maximum likelihood reconstruction of attenuation and activity) approach [13]. In order to define the trigger delay and length of the acquisition window of the 3D CMRA, a conventional 2D cine image is acquired before the PET-CMRA acquisition.

Motion-compensated PET-CMRA image reconstruction is performed in four steps, which are summarized in Figure 1B. In the first step, foot-head (FH) and right-left (RL) translational respiratory motion is estimated from the 2D iNAVs by using rigid image registration of a template covering the apex of the heart (as shown in Figure 1A, in red rectangles). In the second step, FH motion is used to bin the acquired PET and CMRA data in a number of respiratory windows or bins, ranging from end-expiration to end-inspiration, each containing approximately the same amount of data. In a third step, 3D MR images are reconstructed at each respiratory position using iterative SENSE with a soft-binning approach [14], and bin-to-bin respiratory deformation fields are estimated by non-rigid image registration, using the end-expiration bin as reference. Finally, the non-rigid deformation fields are used in a generalized matrix description formulation for motion-compensated CMRA reconstruction [15]. Moreover, the non-rigid motion fields are used to move the attenuation maps to each respiratory position and perform a motion-compensated PET reconstruction. Therefore, at the end of the image reconstruction process, co-registered respiratory motion-corrected CMRA and cardiac PET images are obtained.

Study design

The PET-CMRA acquisition protocol was implemented as a prototype on a 3T MR/PET scanner (Biograph mMR, Siemens Healthcare, Erlangen, Germany), and two preliminary studies were performed. In the first study, ten healthy subjects (age 30.0 ± 3.7 years, 4 males) were recruited for an MR-only examination with the proposed method, with the aim of validating the motion-corrected CMRA approach. For this purpose, an additional reference scan with 1D diaphragmatic navigator gating and tracking was performed for each subject, so the proposed motion-corrected CMRA could be validated against the current MR clinical standard.

[1] *WIP, the product is currently under development and is not for sale in the U.S. and in other countries. Its future availability cannot be ensured.*

Twenty patients referred to our institutions for a cardiac MR/PET examination were recruited for the second part of the study, whose aim was to evaluate the impact of the proposed motion-corrected PET-CMRA framework in a relevant patient population. 14 of the patients presented symptomatic CAD (angina or angina equivalent, excluding acute ST-elevation myocardial infarction patients) with chronic total occlusion (CTO) of a relevant coronary artery, and were referred for a hybrid ^{18}F-FDG MR/PET examination in order to improve risk stratification before elective percutaneous coronary intervention of the CTO. Four patients were referred for a hybrid ^{18}F-FDG MR/PET examination for differential diagnosis of cardiac sarcoidosis, and the remaining two were referred for a joint ^{13}N-Ammonia MR/PET myocardial perfusion examination. Relevant patient characteristics include: age 60.6 ± 12.4 years, 15 males. Written informed consent with respect to participation was obtained from all patients and healthy subjects, and the study was performed in concordance with the Declaration of Helsinki and approved by the institutional ethics committee.

For the CMRA acquisition, relevant imaging parameters included: coronal orientation, resolution = 1 × 1 × 2 mm^3 (interpolated to 1 mm^3 isotropic resolution during MR image reconstruction), field of view = 304 × 304 × 80–112 mm^3 covering the whole heart, TR/TE = 3.72/1.70 ms, flip angle = 15°. A subject-specific trigger delay was defined targeting mid-diastole, and an acquisition window of 89 to 119 ms (corresponding to 24 to 32 readouts per spiral interleaf)

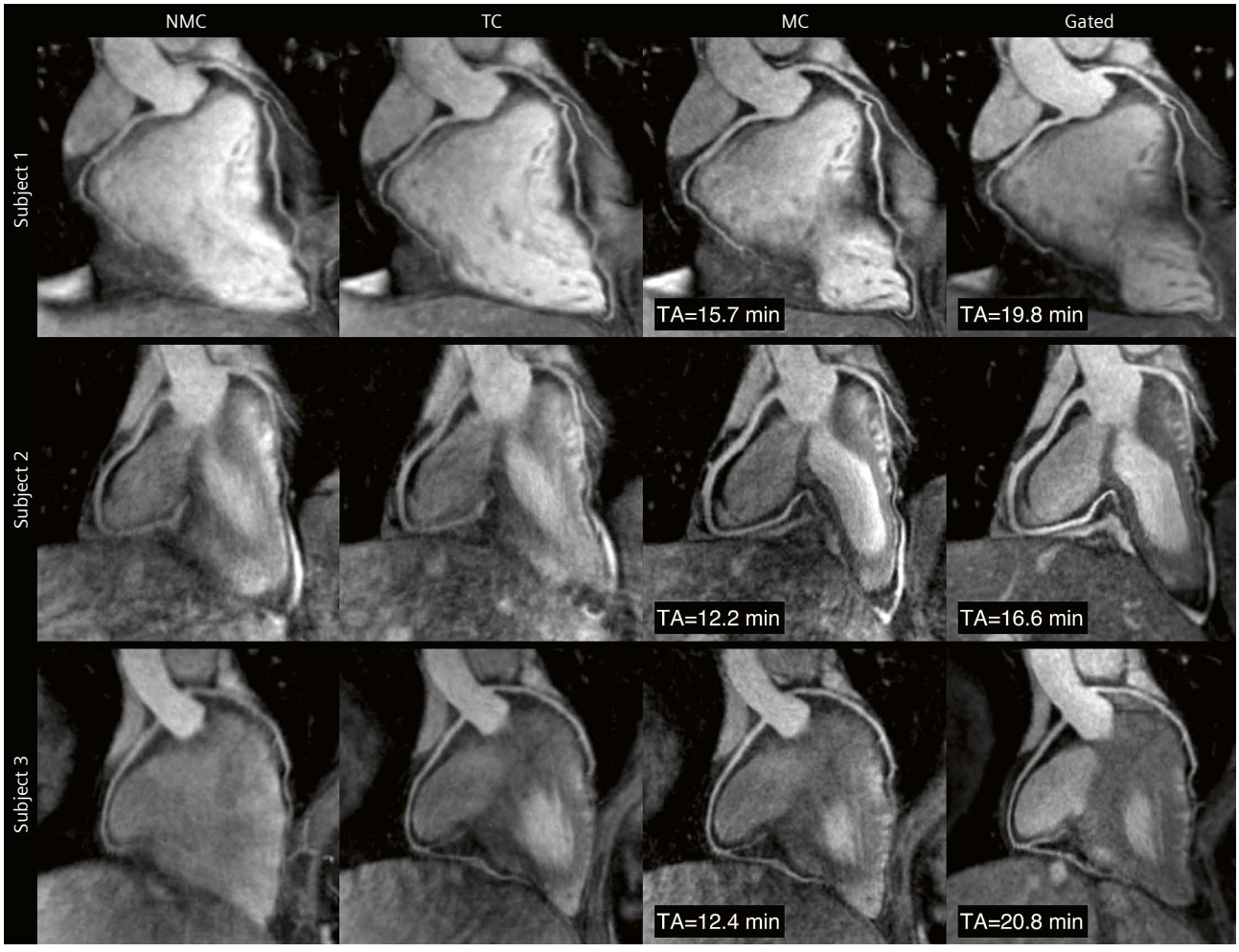

2 Multi-planar reformatting of CMRA images for three representative healthy subjects (rows) showing non-motion-corrected (NMC), translational motion-corrected (TC), non-rigid motion-corrected (MC) and diaphragmatic gated-and-tracked (Gated) images. The scan time for the MC (same for NMC and TC) and Gated approaches is indicated for each subject. Improvements in the visualization of the distal part of the RCA and LAD can be observed when applying TC and MC in comparison to NMC. Furthermore, the MC approach produces images of quality comparable to the Gated images, but in a shorter and predictable scan time.

was selected depending on the length of the mid-diastolic quiescent period of the cardiac cycle. The 2D iNAVs were acquired using the following imaging parameters: same field of view as the 3D CMRA acquisition, flip-angle = 3°, 14 readouts acquired with a high-low Cartesian trajectory, corresponding to a 1 × 21.7 mm^2 acquired resolution interpolated to 1 mm^2 before respiratory motion tracking. For PET attenuation correction, μ-maps were acquired for each of the twenty patients during a 19 s breath-hold at end-expiration using the Siemens' provided 2-point Dixon protocol (with acquisition parameters: coronal orientation, resolution = 2.6 × 2.6 × 3.1 mm^3, field of view = 328 × 500 × 399 mm^3, TR/TE1/TE2 = 3.60/1.23/2.46 ms).

CMRA and PET datasets were reconstructed offline with the described motion correction scheme (MC) and without motion correction (NMC) for comparison purposes. MR image reconstruction was performed in MATLAB (Mathworks, Natick, Massachusetts, USA) using custom developed software. PET image reconstruction was performed offline using RTA motion correction [16]. For this, the μ-map acquired at end-expiration was registered to each respiratory position in MATLAB using the deformation fields estimated from MR images. Each respiratory bin was independently reconstructed offline with Siemens Healthineers e7 Tools using the OSEM algorithm [17], with 3 iterations and 21 subsets, point spread function modelling, voxel size = 2.03 × 2.08 × 2.08 mm^3, matrix size = 127 × 344 × 344. Finally, images reconstructed at each respiratory position were combined in MATLAB to produce a motion-corrected PET image.

Results

Scans were successfully completed in all subjects. The average acquisition time for the proposed PET-CMRA framework was 12.3 ± 1.7 minutes for the healthy subjects and 11.9 ± 2.8 minutes for patients. Multi-planar reformatting of the 3D CMRA images for simultaneous visualization of the right coronary artery (RCA) and left anterior descending artery (LAD) are shown in Figure 2 for three representative healthy subjects. Reference 1D diaphragmatic gating and tracking (Gated) images, obtained with comparable acquisition parameters but with 2-fold acceleration, are displayed next to the motion corrected (MC) images for comparison purposes. Improvements in the visualization of the distal part of the LAD and RCA can be observed for all subjects when applying translational motion correction only (TC) in comparison with the uncorrected images (NMC), and further improvements can be observed with MC for the visualization of the vessels. Similar image quality can be seen for MC and Gated images for the depiction of both the LAD and RCA; however, the acquisition time for the motion-corrected approach was significantly shorter.

Similar results in terms of improvements in image quality were obtained for cardiac patients, despite more irregular breathing patterns. Reformatted CMRA images showing non-stented RCA and LAD for four of the cardiac patients are shown in Figure 3. As can be observed, MC enables the depiction of the proximal segment of all the vessels, even in cases where severe respiratory motion prevented the visualization of both the left and right coronary arteries in the NMC image, as observed for Patient 1 (green arrows). Furthermore, improvements in the depiction of the distal segment of the vessels were observed (blue arrows). Figure 4 shows example coronal slices of the reconstructed cardiac PET images for four representative patients. MC increased the sharpness of large structures such as the liver or the left ventricle myocardium, and enhanced the depiction of smaller structures such as the papillary muscles (blue arrows).

For the patients with CAD, the clinical MR/PET protocol included a conventional multi-slice 2D phase-sensitive inversion recovery (PSIR) LGE acquisition for assessment of myocardial viability (1.4–2.2 mm in-plane resolution, 8 mm slice thickness), and patients underwent interventional X-ray angiography the day after the MR/PET examination for elective CTO revascularization. Therefore, for this subset of patients, NMC and MC PET images were reoriented in short axis to visually compare them with the LGE images acquired in the same scan session, while MC CMRA images were reformatted following the anatomy observed in the X-ray angiography.

A visual comparison between the reformatted MC CMRA and the corresponding invasive X-ray angiogram is shown in Figure 5 for two of the CAD patients. Adequate spatial resolution and contrast in CMRA images allowed for a depiction of the proximal arteries comparable to the X-ray angiogram for both cases. In Patient 6, a stenosis observed in the mid segment of the RCA in CMRA was confirmed in the angiogram (Fig. 5, red arrows), while in Patient 7 an aneurysm in the proximal RCA was seen in both modalities (Fig. 5, green arrows).

Figure 6 shows a short axis view of the ^{18}F-FDG PET images both for NMC and MC reconstructions and corresponding slice of the 2D LGE scan for two CAD patients. It can be observed that MC PET images have an improved correspondence to the anatomy as observed in the LGE images and reduced noise compared to NMC images. In particular, improvements in delineation of viability defects are apparent: for Patient 6, the transmural viability defect observed in the infero-lateral wall was better depicted after motion correction (Fig. 6, blue arrows), while in Patient 8, motion correction allowed for the identification of viable myocardium in a defect that

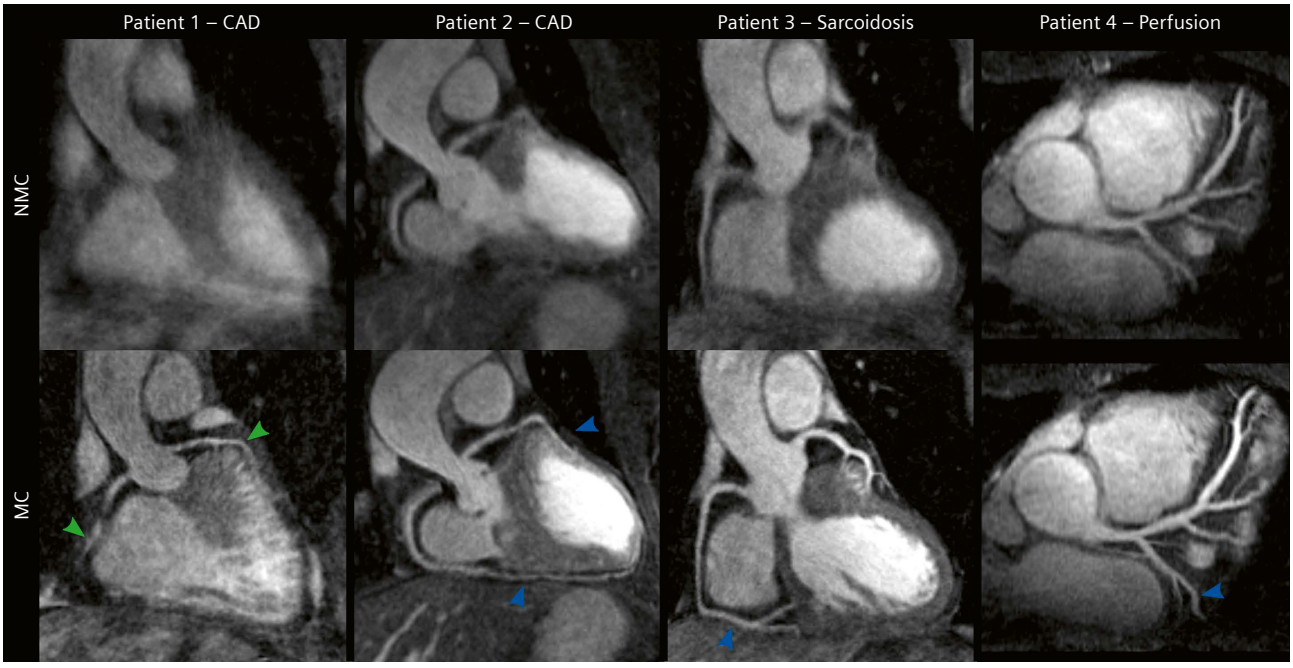

3 Multi-planar reformatting of CMRA images for four representative patients referred for CAD, sarcoidosis and myocardial perfusion examinations (columns) showing uncorrected (NMC) and motion-corrected (MC) CMRA images. Improvements in the visualization of the vessels are observed when applying MC for all cases, both in the proximal (green arrows) and in the distal segments of the arteries (blue arrows).

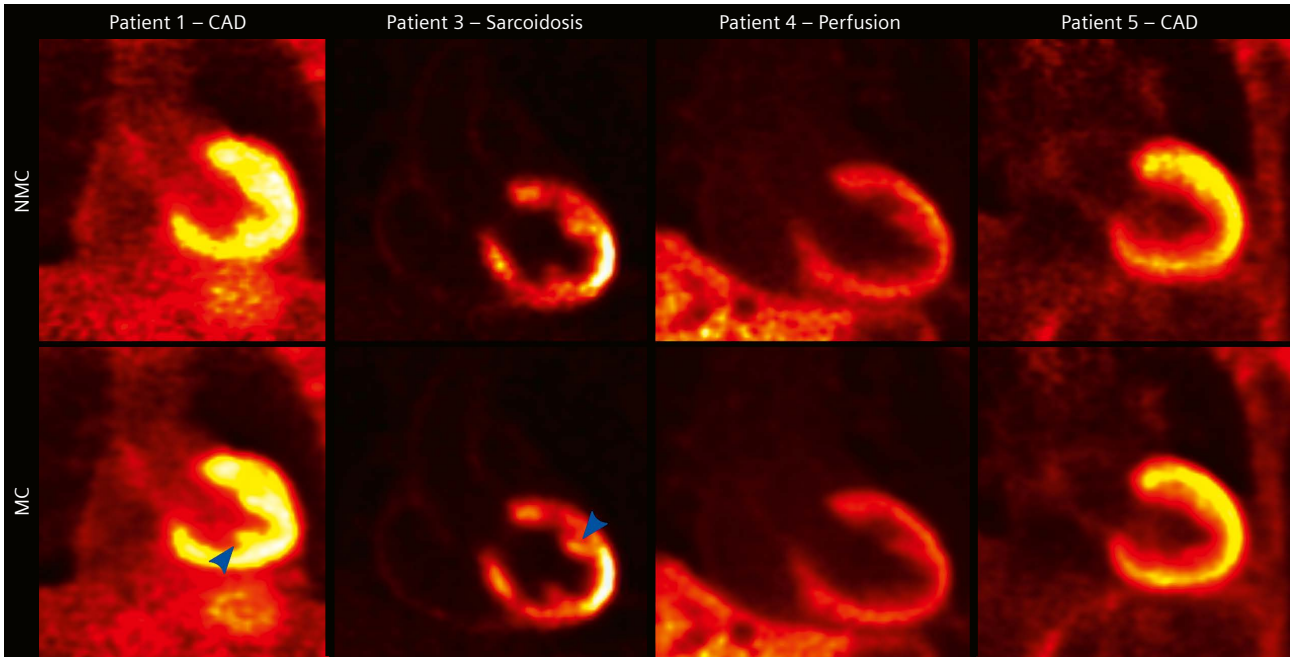

4 Coronal slice for four representative patients (columns) referred for CAD, sarcoidosis and myocardial perfusion examinations showing uncorrected (NMC) and motion-corrected (MC) viability ^{18}F-FDG (Patients 1, 3, 5) and perfusion ^{13}N-ammonia (Patient 4) PET images. Improvements in image quality can be observed when applying MC compared to NMC, particularly for small structures (blue arrows).

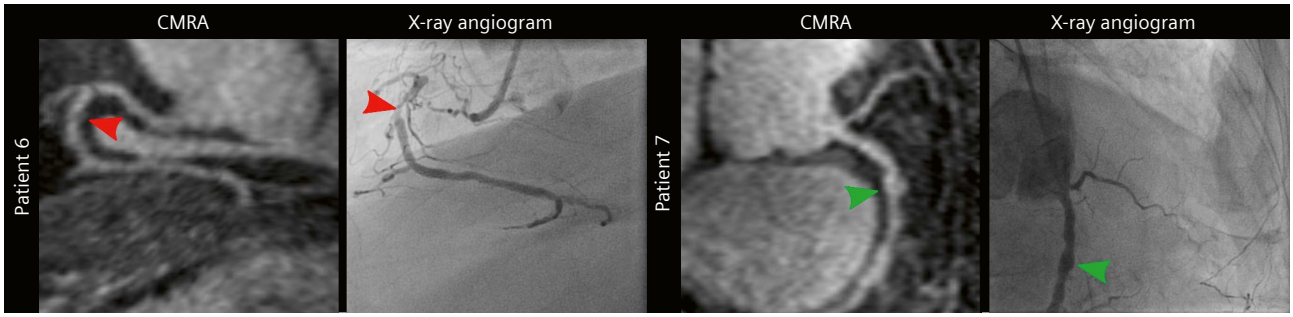

5 Reformatted CMRA and corresponding X-ray angiogram images for two CAD patients. In Patient 6, a stenosis in the mid segment of the right coronary artery (RCA) can be observed in both modalities (red arrows), while for Patient 7 an aneurysm can be observed in the proximal segment of the RCA (green arrows).
Figure adapted from [9].

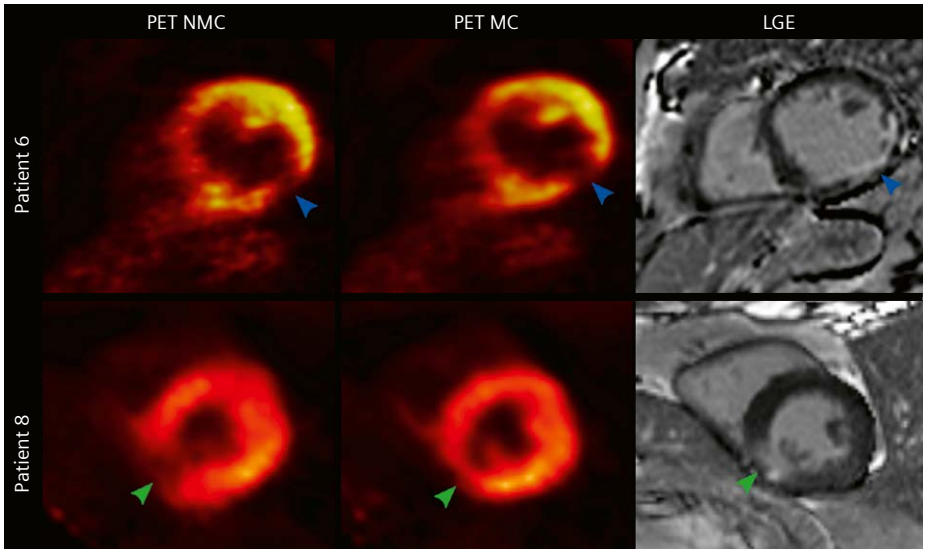

6 Short axis view for two CAD patients (rows) showing un-corrected (NMC) and motion-corrected (MC) viability ^{18}F-FDG PET images as well as corrspond-ing 2D LGE images. MC improves the correspondence of the PET images to the anatomy as observed in the LGE images, particularly in the delineation of viability defects (green and blue arrows).
Figure adapted from [9].

appeared misleadingly as transmural in the NMC image (Fig. 6, green arrows).

Finally, Figure 7 shows an example fused PET-CMRA dataset before and after motion correction. The framework produces co-registered diagnostic PET and CMRA images, improving the correspondence between modalities compared to uncorrected images.

Summary

In this article we have described a novel approach for respiratory motion-corrected cardiac MR/PET for the simultaneous visualization of coronary anatomy by CMRA and myocardial integrity (viability or perfusion) by PET. In contrast to many other MR-based motion correction approaches for cardiac PET data, that utilize MR images mainly for improving PET image quality, this approach produces diagnostic images with both modalities, potentially reducing total examination time. Furthermore, the proposed PET-CMRA acquisition and reconstruction scheme has a short and predictable scan time of approximately 12 minutes, which makes it suitable for clinical practice.

We performed a first clinical validation of the proposed approach, testing the benefit of the motion-correction scheme in a cohort of 20 patients with known or suspected cardiovascular disease. The reported results show that motion correction consistently improves image quality compared to the uncorrected images for both imaging modalities. A good agreement between coronary anatomy depicted by motion-corrected CMRA and X-ray angiography was observed in patients with coronary heart disease. In addition, motion-corrected ^{18}F-FDG images were in good agreement with LGE-MRI, showing more accurate depiction of both transmural and non-transmural viability defects than uncorrected images.

Results obtained from the cohort of patients with coronary artery disease and from additional preliminary tests in patients with a variety of cardiac conditions have shown that the PET-CMRA framework approach is robust

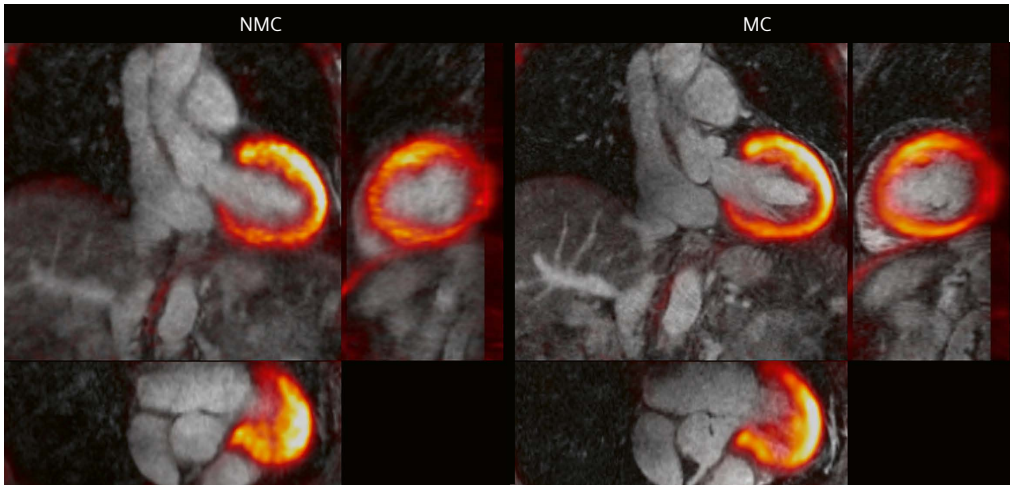

7 Example of fused PET-CMRA images showing uncorrected (NMC) and motion-corrected (MC) images for a representative patient. The motion correction framework produces co-registered diagnostic PET and MR images for which an improved correspondence between both modalities can be observed.
Figure adapted from [9].

and can be applied in combination with different PET radiotracers. Furthermore, the results suggest that the PET-CMRA framework allows the acquisition of diagnostic images with both modalities in a time-efficient and overall short examination, showing promise for its integration into clinical practice. Future work includes acceleration of the CMRA acquisition using variable density trajectories that allow undersampled acquisitions, such as the ones described in [18], in order to increase spatial resolution and volumetric coverage without increasing acquisition time.

References

1 Collaborators GBD (GBD) 2013 M and C of D. Global, regional, and national age–sex specific all-cause and cause-specific mortality for 240 causes of death, 1990–2013: a systematic analysis for the Global Burden of Disease Study 2013. Lancet 2014;385:117–71.
2 Nensa F, Bamberg F, Rischpler C, et al. Hybrid cardiac imaging using PET/MRI: a joint position statement by the European Society of Cardiovascular Radiology (ESCR) and the European Association of Nuclear Medicine (EANM). Eur Radiol 2018;2:14.
3 Robson PM, Dey D, Newby DE, et al. MR/PET Imaging of the Cardiovascular System. JACC Cardiovasc Imaging 2017;10:1165–1179.
4 Nazir MS, Ismail TF, Reyes E, Chiribiri A, Kaufmann PA, Plein S. Hybrid positron emission tomography–magnetic resonance of the heart: current state of the art and future applications. Eur Hear J – Cardiovasc Imaging 2018;19:962–974.
5 Robson PM, Dweck MR, Trivieri MG, et al. Coronary Artery PET/MR Imaging: Feasibility, Limitations, and Solutions. JACC Cardiovasc Imaging 2017;10:1103–1112.
6 Munoz C, Kolbitsch C, Reader AJ, Marsden P, Schaeffter T, Prieto C. MR-Based Cardiac and Respiratory Motion-Compensation Techniques for MR-PET Imaging. PET Clin 2016;11:179–191.
7 Catana C. Motion Correction Options in PET/MRI. Semin Nucl Med 2015;45:212–223.
8 Munoz C, Neji R, Cruz G, et al. Motion-corrected simultaneous cardiac positron emission tomography and coronary MR angiography with high acquisition efficiency. Magn Reson Med 2017;79:339–350.
9 Munoz C, Kunze KP, Neji R, et al. Motion-corrected whole-heart MR-PET for the simultaneous visualisation of coronary artery integrity and myocardial viability : an initial clinical validation. Eur J Nucl Med Mol Imaging 2018:1–12.
10 Prieto C, Doneva M, Usman M, et al. Highly efficient respiratory motion compensated free-breathing coronary MRA using golden-step Cartesian acquisition. J Magn Reson Imaging 2015;41:738–746.
11 Henningsson M, Koken P, Stehning C, Razavi R, Prieto C, Botnar RM. Whole-heart coronary MR angiography with 2D self-navigated image reconstruction. Magn Reson Med 2012;67:437–445.
12 Botnar RM, Stuber M, Danias PG, Kissinger K V., Manning WJ. Improved coronary artery definition with T2-weighted, free-breathing, three-dimensional coronary MRA. Circulation 1999;99:3139–3148.
13 Nuyts J, Bal G, Kehren F, Fenchel M, Michel C, Watson C. Completion of a truncated attenuation image from the attenuated PET emission data. IEEE Trans Med Imaging 2013;32:237–246.
14 Cruz G, Atkinson D, Henningsson M, Botnar RM, Prieto C. Highly efficient nonrigid motion-corrected 3D whole-heart coronary vessel wall imaging. Magn Reson Med 2017;77:1894–1908.
15 Batchelor PG, Atkinson D, Irarrazaval P, Hill DLG, Hajnal J, Larkman D. Matrix description of general motion correction applied to multishot images. Magn Reson Med 2005;54:1273–1280.
16 Picard Y, Thompson CJ. Motion correction of PET images using multiple acquisition frames. IEEE Trans Med Imaging 1997;16:137–44.
17 Hudson HM, Larkin RS. Accelerated image reconstruction using ordered subsets of projection data. IEEE Trans Med Imaging 1994;13:601–9.
18 Bustin A, Ginami G, Cruz G, et al. Five-minute whole-heart coronary MRA with sub-millimeter isotropic resolution, 100% respiratory scan efficiency, and 3D-PROST reconstruction. Magn Reson Med 2018 doi: 10.1002/mrm.27354.

Contact

Camila Munoz
School of Biomedical Engineering and Imaging Sciences
4th Floor, Lambeth Wing
St Thomas' Hospital
London, SE1 7EH
United Kingdom
camila.munoz@kcl.ac.uk

HIGHLIGHTS OF PRESCRIBING INFORMATION

These highlights do not include all the information needed to use Fludeoxyglucose F 18 Injection safely and effectively. See full prescribing information for Fludeoxyglucose F 18 Injection. Fludeoxyglucose F 18 Injection, USP For intravenous use Initial U.S. Approval: 2005

RECENT MAJOR CHANGES

Warnings and Precautions	
(5.1, 5.2)	7/2010
Adverse Reactions (6)	7/2010

INDICATIONS AND USAGE

Fludeoxyglucose F18 Injection is indicated for positron emission tomography (PET) imaging in the following settings:

- Oncology: For assessment of abnormal glucose metabolism to assist in the evaluation of malignancy in patients with known or suspected abnormalities found by other testing modalities, or in patients with an existing diagnosis of cancer.
- Cardiology: For the identification of left ventricular myocardium with residual glucose metabolism and reversible loss of systolic function in patients with coronary artery disease and left ventricular dysfunction, when used together with myocardial perfusion imaging.
- Neurology: For the identification of regions of abnormal glucose metabolism associated with foci of epileptic seizures (1).

DOSAGE AND ADMINISTRATION

Fludeoxyglucose F 18 Injection emits radiation. Use procedures to minimize radiation exposure. Screen for blood glucose abnormalities.

- In the oncology and neurology settings, instruct patients to fast for 4 to 6 hours prior to the drug's injection. Consider medical therapy and laboratory testing to assure at least two days of normoglycemia prior to the drug's administration (5.2).
- In the cardiology setting, administration of glucose-containing food or liquids (e.g., 50 to 75 grams) prior to the drug's injection facilitates localization of cardiac ischemia (2.3).

Aseptically withdraw Fludeoxyglucose F 18 Injection from its container and administer by intravenous injection (2).

The recommended dose:

- for adults is 5 to 10 mCi (185 to 370 MBq), in all indicated clinical settings (2.1).
- for pediatric patients is 2.6 mCi in the neurology setting (2.2).

Initiate imaging within 40 minutes following drug injection; acquire static emission images 30 to 100 minutes from time of injection (2).

DOSAGE FORMS AND STRENGTHS

Multi-dose 30mL and 50mL glass vial containing 0.74 to 7.40 GBq/mL (20 to 200 mCi/mL) Fludeoxyglucose F 18 Injection and 4.5mg of sodium chloride with 0.1 to 0.5% w/w ethanol as a stabilizer (approximately 15 to 50 mL volume) for intravenous administration (3).

CONTRAINDICATIONS

None

WARNINGS AND PRECAUTIONS

- Radiation risks: use smallest dose necessary for imaging (5.1).
- Blood glucose adnormalities: may cause suboptimal imaging (5.2).

ADVERSE REACTIONS

Hypersensitivity reactions have occurred; have emergency resuscitation equipment and personnel immediately available (6).

To report SUSPECTED ADVERSE REACTIONS, contact PETNET Solutions, Inc. at 877-473-8638 or FDA at 1-800-FDA-1088 or www.fda.gov/medwatch.

USE IN SPECIFIC POPULATIONS

Pregnancy Category C: No human or animal data. Consider alternative diagnostics; use only if clearly needed (8.1).

- Nursing mothers: Use alternatives to breast feeding (e.g., stored breast milk or infant formula) for at least 10 half-lives of radioactive decay, if Fludeoxyglucose F 18 Injection is administered to a woman who is breast-feeding (8.3).
- Pediatric Use: Safety and effectiveness in pediatric patients have not been established in the oncology and cardiology settings (8.4).

See 17 for PATIENT COUNSELING INFORMATION

Revised: 1/2011

FULL PRESCRIBING INFORMATION: CONTENTS*

*Sections or subsections omitted from the full prescribing information are not listed.

FULL PRESCRIBING INFORMATION

1 INDICATIONS AND USAGE

Fludeoxyglucose F 18 Injection is indicated for positron emission tomography (PET) imaging in the following settings:

1.1 Oncology

For assessment of abnormal glucose metabolism to assist in the evaluation of malignancy in patients with known or suspected abnormalities found by other testing modalities, or in patients with an existing diagnosis of cancer.

1.2 Cardiology

For the identification of left ventricular myocardium with residual glucose metabolism and reversible loss of systolic function in patients with coronary artery disease and left ventricular dysfunction, when used together with myocardial perfusion imaging.

1.3 Neurology

For the identification of regions of abnormal glucose metabolism associated with foci of epileptic seizures.

2 DOSAGE AND ADMINISTRATION

Fludeoxyglucose F 18 Injection emits radiation. Use procedures to minimize radiation exposure. Calculate the final dose from the end of synthesis (EOS) time using proper radioactive decay factors. Assay the final dose in a properly calibrated dose calibrator before administration to the patient [see Description (11.2)].

2.1 Recommended Dose for Adults

Within the oncology, cardiology and neurology settings, the recommended dose for adults is 5 to 10 mCi (185 to 370 MBq) as an intravenous injection.

2.2 Recommended Dose for Pediatric Patients

Within the neurology setting, the recommended dose for pediatric patients is 2.6 mCi, as an intravenous injection. The optimal dose adjustment on the basis of body size or weight has not been determined [see Use in Special Populations (8.4)].

2.3 Patient Preparation

- To minimize the radiation absorbed dose to the bladder, encourage adequate hydration. Encourage the patient to drink water or other fluids (as tolerated) in the 4 hours before their PET study.
- Encourage the patient to void as soon as the imaging study is completed and as often as possible thereafter for at least one hour.
- Screen patients for clinically significant blood glucose abnormalities by obtaining a history and/or laboratory tests [see Warnings and Precautions (5.2)]. Prior to Fludeoxyglucose F 18 PET imaging in the oncology and neurology settings, instruct patient to fast for 4 to 6 hours prior to the drug's injection.
- In the cardiology setting, administration of glucose-containing food or liquids (e.g., 50 to 75 grams) prior to Fludeoxyglucose F18 Injection facilitates localization of cardiac ischemia

2.4 Radiation Dosimetry

The estimated human absorbed radiation doses (rem/mCi) to a newborn (3.4 kg), 1-year-old (9.8 kg), 5-year-old (19 kg), 10-year-old (32 kg), 15-year-old (57 kg), and adult (70 kg) from intravenous administration of Fludeoxyglucose F 18 Injection are shown in Table 1. These estimates were calculated based on human[2] data and using the data published by the International Commission on Radiological Protection[4] for Fludeoxyglucose ^{18}F. The dosimetry data show that there are slight variations in absorbed radiation dose for various organs in each of the age groups. These dissimilarities in absorbed radiation dose are due to developmental age variations (e.g., organ size, location, and overall metabolic rate for each age group). The identified critical organs (in descending order) across all age groups evaluated are the urinary bladder, heart, pancreas, spleen, and lungs.

Table 1. Estimated Absorbed Radiation Doses (rem/mCi) After Intravenous Administration of Fludeoxyglucose F-18 Injection[a]

Organ	Newborn (3.4 kg)	1-year-old (9.8 kg)	5-year-old (19 kg)	10-year-old (32 kg)	15-year-old (57 kg)	Adult (70 kg)
Bladder wall[b]	4.3	1.7	0.93	0.60	0.40	0.32
Heart wall	2.4	1.2	0.70	0.44	0.29	0.22
Pancreas	2.2	0.68	0.33	0.25	0.13	0.096
Spleen	2.2	0.84	0.46	0.29	0.19	0.14
Lungs	0.96	0.38	0.20	0.13	0.092	0.064
Kidneys	0.81	0.34	0.19	0.13	0.089	0.074
Ovaries	0.80	0.8	0.19	0.11	0.058	0.053
Uterus	0.79	0.35	0.19	0.12	0.076	0.062
LLI wall *	0.69	0.28	0.15	0.097	0.060	0.051
Liver	0.69	0.31	0.17	0.11	0.076	0.058
Gallbladder wall	0.69	0.26	0.14	0.093	0.059	0.049
Small intestine	0.68	0.29	0.15	0.096	0.060	0.047
ULI wall **	0.67	0.27	0.15	0.090	0.057	0.046
Stomach wall	0.65	0.27	0.14	0.089	0.057	0.047
Adrenals	0.65	0.28	0.15	0.095	0.061	0.048
Testes	0.64	0.27	0.14	0.085	0.052	0.041
Red marrow	0.62	0.26	0.14	0.089	0.057	0.047
Thymus	0.61	0.26	0.14	0.086	0.056	0.044
Thyroid	0.61	0.26	0.13	0.080	0.049	0.039
Muscle	0.58	0.25	0.13	0.078	0.049	0.039
Bone surface	0.57	0.24	0.12	0.079	0.052	0.041
Breast	0.54	0.22	0.11	0.068	0.043	0.034
Skin	0.49	0.20	0.10	0.060	0.037	0.030
Brain	0.29	0.13	0.09	0.078	0.072	0.070
Other tissues	0.59	0.25	0.13	0.083	0.052	0.042

[a] MIRDOSE 2 software was used to calculate the radiation absorbed dose. Assumptions on the biodistribution based on data from Gallagher et al.1 and Jones et al.[2]

[b] The dynamic bladder model with a uniform voiding frequency of 1.5 hours was used.

*LLI = lower large intestine; **ULI = upper large intestine

2.5 Radiation Safety – Drug Handling

- Use waterproof gloves, effective radiation shielding, and appropriate safety measures when handling Fludeoxyglucose F 18 Injection to avoid unnecessary radiation exposure to the patient, occupational workers, clinical personnel and other persons.
- Radiopharmaceuticals should be used by or under the control of physicians who are qualified by specific training and experience in the safe use and handling of radionuclides, and whose experience and training have been approved by the appropriate governmental agency authorized to license the use of radionuclides.
- Calculate the final dose from the end of synthesis (EOS) time using proper radioactive decay factors. Assay the final dose in a properly calibrated dose calibrator before administration to the patient [see Description (11.2)].
- The dose of Fludeoxyglucose F 18 used in a given patient should be minimized consistent with the objectives of the procedure, and the nature of the radiation detection devices employed.

2.6 Drug Preparation and Administration

- Calculate the necessary volume to administer based on calibration time and dose.
- Aseptically withdraw Fludeoxyglucose F 18 Injection from its container.
- Inspect Fludeoxyglucose F 18 Injection visually for particulate matter and discoloration before administration, whenever solution and container permit.
- Do not administer the drug if it contains particulate matter or discoloration; dispose of these unacceptable or unused preparations in a safe manner, in compliance with applicable regulations. Use Fludeoxyglucose F 18 Injection within 12 hours from the EOS.

2.7 Imaging Guidelines

- Initiate imaging within 40 minutes following Fludeoxyglucose F 18 Injection administration.
- Acquire static emission images 30 to 100 minutes from the time of injection.

3 DOSAGE FORMS AND STRENGTHS

Multiple-dose 30 mL and 50 mL glass vial containing 0.74 to 7.40 GBq/mL (20 to 200 mCi/mL) of Fludeoxyglucose F 18 Injection and 4.5 mg of sodium chloride with 0.1 to 0.5% w/w ethanol as a stabilizer (approximately 15 to 50 mL volume) for intravenous administration.

4 CONTRAINDICATIONS

None

5 WARNINGS AND PRECAUTIONS

5.1 Radiation Risks

Radiation-emitting products, including Fludeoxyglucose F 18 Injection, may increase the risk for cancer, especially in pediatric patients. Use the smallest dose necessary for imaging and ensure safe handling to protect the patient and health care worker [see Dosage and Administration (2.5)].

5.2 Blood Glucose Abnormalities

In the oncology and neurology setting, suboptimal imaging may occur in patients with inadequately regulated blood glucose levels. In these patients, consider medical therapy and laboratory testing to assure at least two days of normoglycemia prior to Fludeoxyglucose F 18 Injection administration.

6 ADVERSE REACTIONS

Hypersensitivity reactions with pruritus, edema and rash have been reported in the post-marketing setting. Have emergency resuscitation equipment and personnel immediately available.

7 DRUG INTERACTIONS

The possibility of interactions of Fludeoxyglucose F 18 Injection with other drugs taken by patients undergoing PET imaging has not been studied.

8 USE IN SPECIFIC POPULATIONS

8.1 Pregnancy

Pregnancy Category C

Animal reproduction studies have not been conducted with Fludeoxyglucose F 18 Injection. It is also not known whether Fludeoxyglucose F 18 Injection can cause fetal harm when administered to a pregnant woman or can affect reproduction capacity. Consider alternative diagnostic tests in a pregnant woman; administer Fludeoxyglucose F 18 Injection only if clearly needed.

8.3 Nursing Mothers

It is not known whether Fludeoxyglucose F 18 Injection is excreted in human milk. Consider alternative diagnostic tests in women who are breast-feeding. Use alternatives to breast feeding (e.g., stored breast milk or infant formula) for at least 10 half-lives of radioactive decay, if Fludeoxyglucose F 18 Injection is administered to a woman who is breast-feeding.

8.4 Pediatric Use

The safety and effectiveness of Fludeoxyglucose F 18 Injection in pediatric patients with epilepsy is established on the basis of studies in adult and pediatric patients. In pediatric patients with epilepsy, the recommended dose is 2.6 mCi. The optimal dose adjustment on the basis of body size or weight has not been determined. In the oncology or cardiology settings, the safety and effectiveness of Fludeoxyglucose F 18 Injection have not been established in pediatric patients.

11 DESCRIPTION

11.1 Chemical Characteristics

Fludeoxyglucose F 18 Injection is a positron emitting radiopharmaceutical that is used for diagnostic purposes in conjunction with positron emission tomography (PET) imaging. The active ingredient 2-deoxy-2-[^{18}F]fluoro-D-glucose has the molecular formula of $C_6H_{11}{}^{18}FO_5$ with a molecular weight of 181.26, and has the following chemical structure:

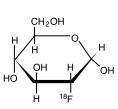

Fludeoxyglucose F 18 Injection is provided as a ready to use sterile, pyrogen free, clear, colorless solution. Each mL contains between 0.740 to 7.40GBq (20.0 to 200 mCi) of 2-deoxy-2-[^{18}F]fluoro-D-glucose at the EOS, 4.5 mg of sodium chloride and 0.1 to 0.5% w/w ethanol as a stabilizer. The pH of the solution is between 4.5 and 7.5. The solution is packaged in a multiple-dose glass vial and does not contain any preservative.

11.2 Physical Characteristics

Fluorine F 18 decays by emitting positron to Oxygen O 16 (stable) and has a physical half-life of 109.7 minutes. The principal photons useful for imaging are the dual 511 keV gamma photons, that are produced and emitted simultaneously in opposite direction when the positron interacts with an electron (Table 2).

Table 2. Pricipal Radiation Emission Data for Fluorine F18		
Radiation/Emission	% Per Disintegration	Mean Energy
Positron (b+)	96.73	249.8 keV
Gamma (±)*	193.46	511.0 keV

*Produced by positron annihilation

From: Kocher, D.C. Radioactive Decay Tables DOE/TIC-I 1026, 89 (1981)

The specific gamma ray constant (point source air kerma coefficient) for fluorine F 18 is 5.7 R/hr/mCi (1.35 x 10-6 Gy/hr/kBq) at 1 cm. The half-value layer (HVL) for the 511 keV photons is 4 mm lead (Pb). The range of attenuation coefficients for this radionuclide as a function of lead shield thickness is shown in Table 3. For example, the interposition of an 8 mm thickness of Pb, with a coefficient of attenuation of 0.25, will decrease the external radiation by 75%.

Table 3. Radiation Attenuation of 511 keV Photons by lead (Pb) shielding	
Shield thickness (Pb) mm	Coefficient of attenuation
0	0.00
4	0.50
8	0.25
13	0.10
26	0.01
39	0.001
52	0.0001

For use in correcting for physical decay of this radionuclide, the fractions remaining at selected intervals after calibration are shown in Table 4.

Table 4. Physical Decay Chart for Fluorine F18	
Minutes	Fraction Remaining
0*	1.000
15	0.909
30	0.826
60	0.683
110	0.500
220	0.250

*calibration time

12 CLINICAL PHARMACOLOGY

12.1 Mechanism of Action

Fludeoxyglucose F 18 is a glucose analog that concentrates in cells that rely upon glucose as an energy source, or in cells whose dependence on glucose increases under pathophysiological conditions. Fludeoxyglucose F 18 is transported through the cell membrane by facilitative glucose transporter proteins and is phosphorylated within the cell to [^{18}F] FDG-6-phosphate by the enzyme hexokinase. Once phosphorylated it cannot exit until it is dephosphorylated by glucose-6-phosphatase. Therefore, within a given tissue or pathophysiological process, the retention and clearance of Fludeoxyglucose F 18 reflect a balance involving glucose transporter, hexokinase and glucose-6-phosphatase activities. When allowance is made for the kinetic differences between glucose and Fludeoxyglucose F 18 transport and phosphorylation (expressed as the ‚lumped constant" ratio), Fludeoxyglucose F 18 is used to assess glucose metabolism. In comparison to background activity of the specific organ or tissue type, regions of decreased or absent uptake of Fludeoxyglucose F 18 reflect the decrease or absence of glucose metabolism. Regions of increased uptake of Fludeoxyglucose F 18 reflect greater than normal rates of glucose metabolism.

12.2 Pharmacodynamics

Fludeoxyglucose F 18 Injection is rapidly distributed to all organs of the body after intravenous administration. After background clearance of Fludeoxyglucose F 18 Injection, optimal PET imaging is generally achieved between 30 to 40 minutes after administration.

In cancer, the cells are generally characterized by enhanced glucose metabolism partially due to (1) an increase in activity of glucose transporters, (2) an increased rate of phosphorylation activity, (3) a reduction of phosphatase activity or, (4) a dynamic alteration in the balance among all these processes. However, glucose metabolism of cancer as reflected by Fludeoxyglucose F 18 accumulation shows considerable variability. Depending on tumor type, stage, and location, Fludeoxyglucose F 18 accumulation may be increased, normal, or decreased. Also, inflammatory cells can have the same variability of uptake of Fludeoxyglucose F 18.

In the heart, under normal aerobic conditions, the myocardium meets the bulk of its energy requirements by oxidizing free fatty acids. Most of the exogenous glucose taken up by the myocyte is converted into glycogen. However, under ischemic conditions, the oxidation of free fatty acids decreases, exogenous glucose becomes the preferred myocardial sub strate, glycolysis is stimulated, and glucose taken up by the myocyte is metabolized immediately instead of being converted into glycogen. Under these conditions, phosphorylated Fludeoxyglucose F 18 accumulates in the myocyte and can be detected with PET imaging.

In the brain, cells normally rely on aerobic metabolism. In epilepsy, the glucose metabolism varies. Generally, during a seizure, glucose metabolism increases. Interictally, the seizure focus tends to be hypometabolic.

12.3 Pharmacokinetics

Distribution: In four healthy male volunteers, receiving an intravenous administration of 30 seconds in duration, the arterial blood level profile for Fludeoxyglucose F 18 decayed triexponentially. The effective half-life ranges of the three phases were 0.2 to 0.3 minutes, 10 to 13 minutes with a mean and standard deviation (STD) of 11.6 (±) 1.1 min, and 80 to 95 minutes with a mean and STD of 88 (±) 4 min. Plasma protein binding of Fludeoxyglucose F 18 has not been studied.

Metabolism: Fludeoxyglucose F 18 is transported into cells and phosphorylated to [^{18}F]-FDG-6-phosphate at a rate proportional to the rate of glucose utilization within that tissue. [F18]-FDG-6-phosphate presumably is metabolized to 2-deoxy-2-[F18]fluoro-6-phospho-D-mannose([F 18]FDM-6-phosphate).

Fludeoxyglucose F 18 Injection may contain several impurities (e.g., 2-deoxy-2-chloro-D-glucose (ClDG)). Biodistribution and metabolism of ClDG are presumed to be similar to Fludeoxyglucose F 18 and would be expected to result in intracellular formation of 2-deoxy-2-chloro-6-phospho-D-glucose (ClDG-6-phosphate) and 2-deoxy-2-chloro-6-phospho-D-mannose (ClDM-6-phosphate). The phosphorylated deoxyglucose compounds are dephosphorylated and the resulting compounds (FDG, FDM, ClDG, and ClDM) presumably leave cells by passive diffusion. Fludeoxyglucose F 18 and related compounds are cleared from non-cardiac tissues within 3 to 24 hours after administration. Clearance from the cardiac tissue may require more than 96 hours. Fludeoxyglucose F 18 that is not involved in glucose metabolism in any tissue is then excreted in the urine.

Elimination: Fludeoxyglucose F 18 is cleared from most tissues within 24 hours and can be eliminated from the body unchanged in the urine. Three elimination phases have been identified in the reviewed literature. Within 33 minutes, a mean of 3.9% of the administrated radioactive dose was measured in the urine. The amount of radiation exposure of the urinary bladder at two hours post-administration suggests that 20.6% (mean) of the radioactive dose was present in the bladder.

Special Populations: The pharmacokinetics of Fludeoxyglucose F 18 Injection have not been studied in renally-impaired, hepatically impaired or pediatric patients. Fludeoxyglucose F 18 is eliminated through the renal system. Avoid excessive radiation exposure to this organ system and adjacent tissues. The effects of fasting, varying blood sugar levels, conditions of glucose intolerance, and diabetes mellitus on Fludeoxyglucose F 18 distribution in humans have not been ascertained [see Warnings and Precautions (5.2)].

13 NONCLINICAL TOXICOLOGY

13.1 Carcinogenesis, Mutagenesis, Impairment of Fertility

Animal studies have not been performed to evaluate the Fludeoxyglucose F 18 Injection carcinogenic potential, mutagenic potential or effects on fertility.

14 CLINICAL STUDIES

14.1 Oncology

The efficacy of Fludeoxyglucose F 18 Injection in positron emission tomography cancer imaging was demonstrated in 16 independent studies. These studies prospectively evaluated the use of Fludeoxyglucose F 18 in patients with suspected or known malignancies, including non-small cell lung cancer, colo-rectal, pancreatic, breast, thyroid, melanoma, Hodgkin's and non-Hodgkin's lymphoma, and various types of metastatic cancers to lung, liver, bone, and axillary nodes. All these studies had at least 50 patients and used pathology as a standard of truth. The Fludeoxyglucose F 18 Injection doses in the studies ranged from 200 MBq to 740 MBq with a median and mean dose of 370 MBq. In the studies, the diagnostic performance of Fludeoxyglucose F 18 Injection varied with the type of cancer, size of cancer, and other clinical conditions. False negative and false positive scans were observed. Negative Fludeoxyglucose F 18 Injection PET scans do not exclude the diagnosis of cancer. Positive Fludeoxyglucose F 18 Injection PET scans can not replace pathology to establish a diagnosis of cancer. Non-malignant conditions such as fungal infections, inflammatory processes and benign tumors have patterns of increased glucose metabolism that may give rise to false-positive scans. The efficacy of Fludeoxyglucose F 18 Injection PET imaging in cancer screening was not studied.

14.2 Cardiology

The efficacy of Fludeoxyglucose F 18 Injection for cardiac use was demonstrated in ten independent, prospective studies of patients with coronary artery disease and chronic left ventricular systolic dysfunction who were scheduled to undergo coronary revascularization. Before revascularization, patients underwent PET imaging with Fludeoxyglucose F 18 Injection (74 to 370 MBq, 2 to 10 mCi) and perfusion imaging with other diagnostic radiopharmaceuticals. Doses of Fludeoxyglucose F 18 Injection ranged from 74 to 370 MBq (2 to 10 mCi). Segmental, left ventricular, wall-motion assessments of asynergic areas made before revascularization were compared in a blinded manner to assessments made after successful revascularization to identify myocardial segments with functional recovery. Left ventricular myocardial segments were predicted to have reversible loss of systolic function if they showed Fludeoxyglucose F 18 accumulation and reduced perfusion (i.e., flow-metabolism mismatch). Conversely, myocardial segments were predicted to have irreversible loss of systolic function if they showed reductions in both Fludeoxyglucose F 18 accumulation and perfusion (i.e., matched defects). Findings of flow-metabolism mismatch in a myocardial segment may suggest that successful revascularization will restore myocardial function in that segment. However, false-positive tests occur regularly, and the decision to have a patient undergo revascularization should not be based on PET findings alone. Similarly, findings of a matched defect in a myocardial segment may suggest that myocardial function will not recover in that segment, even if it is successfully revascularized. However, false-negative tests occur regularly, and the decision to recommend against coronary revascularization, or to recommend a cardiac transplant, should not be based on PET findings alone. The reversibility of segmental dysfunction as predicted with Fludeoxyglucose F 18 PET imaging depends on successful coronary revascularization. Therefore, in patients with a low likelihood of successful revascularization, the diagnostic usefulness of PET imaging with Fludeoxyglucose F 18 Injection is more limited.

14.3 Neurology

In a prospective, open label trial, Fludeoxyglucose F 18 Injection was evaluated in 86 patients with epilepsy. Each patient received a dose of Fludeoxyglucose F 18 Injection in the range of 185 to 370 MBq (5 to 10 mCi). The mean age was 16.4 years (range: 4 months to 58 years; of these, 42 patients were less than 12 years and 16 patients were less than 2 years old). Patients had a known diagnosis of complex partial epilepsy and were under evaluation for surgical treatment of their seizure disorder. Seizure foci had been previously identified on ictal EEGs and sphenoidal EEGs. Fludeoxyglucose F 18 Injection PET imaging confirmed previous diagnostic findings in 16% (14/87) of the patients; in 34% (30/87) of the patients, Fludeoxyglucose F 18 Injection PET images provided new findings. In 32% (27/87), imaging with Fludeoxyglucose F 18 Injection was inconclusive. The impact of these imaging findings on clinical outcomes is not known. Several other studies comparing imaging with Fludeoxyglucose F 18 Injection results to subsphenoidal EEG, MRI and/or surgical findings supported the concept that the degree of hypometabolism corresponds to areas of confirmed epileptogenic foci. The safety and effectiveness of Fludeoxyglucose F 18 Injection to distinguish idiopathic epileptogenic foci from tumors or other brain lesions that may cause seizures have not been established.

15 REFERENCES

- 1. Gallagher B.M., Ansari A., Atkins H., Casella V., Christman D.R., Fowler J.S., Ido T., MacGregor R.R., Som P., Wan C.N., Wolf A.P., Kuhl D.E., and Reivich M. "Radiopharmaceuticals XXVII. ^{18}F-labeled 2-deoxy-2-fluoro-d-glucose as a radiopharmaceutical for measuring regional myocardial glucose metabolism in vivo: tissue distribution and imaging studies in animals," J Nucl Med, 1977; 18, 990-6.
- 2. Jones S.C., Alavi, A., Christman D., Montanez, I., Wolf, A.P., and Reivich M. "The radiation dosimetry of 2 [F-18] fluoro-2-deoxy-D-glucose in man," J Nucl Med, 1982; 23, 613-617.
- 3. Kocher, D.C. "Radioactive Decay Tables: A handbook of decay data for application to radiation dosimetry and radiological assessments," 1981, DOE/TIC-I 1026, 89.
- 4. ICRP Publication 53, Volume 18, No. I-4,1987, pages 75-76.

16 HOW SUPPLIED/STORAGE AND DRUG HANDLING

Fludeoxyglucose F 18 Injection is supplied in a multi-dose, capped 30 mL and 50 mL glass vial containing between 0.740 to 7.40 GBq/mL (20 to 200 mCi/mL), of no carrier added 2-deoxy-2-[F 18] fluoro-D-glucose, at end of synthesis, in approximately 15 to 50 mL. The contents of each vial are sterile, pyrogen-free and preservative-free.

NDC 40028-511-30; 40028-511-50

Receipt, transfer, handling, possession, or use of this product is subject to the radioactive material regulations and licensing requirements of the U.S. Nuclear Regulatory Commission, Agreement States or Licensing States as appropriate.

Store the Fludeoxyglucose F 18 Injection vial upright in a lead shielded container at 25°C (77°F); excursions permitted to 15-30°C (59-86°F).

Store and dispose of Fludeoxyglucose F 18 Injection in accordance with the regulations and a general license, or its equivalent, of an Agreement State or a Licensing State.

The expiration date and time are provided on the container label. Use Fludeoxyglucose F 18 Injection within 12 hours from the EOS time.

17 PATIENT COUNSELING INFORMATION

Instruct patients in procedures that increase renal clearance of radioactivity.

Encourage patients to:

- drink water or other fluids (as tolerated) in the 4 hours before their PET study.
- void as soon as the imaging study is completed and as often as possible thereafter for at least one hour.

Manufactured by: PETNET Solutions Inc. 810 Innovation Drive Knoxville, TN 37932

Distributed by: PETNET Solutions Inc.^ 810 Innovation Drive Knoxville, TN 37932^

PETNET Solutions

PN0002262 Rev. A

Marcg 1, 2011

Indications

Fludeoxyglucose F18 Injection is indicated for positron emission tomography (PET) imaging in the following settings:

Oncology: For assessment of abnormal glucose metabolism to assist in the evaluation of malignancy in patients with known or suspected abnormalities found by other testing modalities, or in patients with an existing diagnosis of cancer.

Cardiology: For the identification of left ventricular myocardium with residual glucose metabolism and reversible loss of systolic function in patients with coronary artery disease and left ventricular dysfunction, when used together with myocardial perfusion imaging.

Neurology: For the identification of regions of abnormal glucose metabolism associated with foci of epileptic seizures.

Important Safety Information

Radiation Risks: Radiationemitting products, including Fludeoxyglucose F18 Injection, may increase the risk for cancer, especially in pediatric patients. Use the smallest dose necessary for imaging and ensure safe handling to protect the patient and healthcare worker.

Blood Glucose Abnormalities: In the oncology and neurology setting, suboptimal imaging may occur in patients with inadequately regulated blood glucose levels. In these patients, consider medical therapy and laboratory testing to assure at least two days of normoglycemia prior to Fludeoxyglucose F18 Injection administration.

Adverse Reactions: Hypersensitivity reactions with pruritus, edema and rash have been reported; have emergency resuscitation equipment and personnel immediately available.

Dosage Forms and Strengths: Multiple-dose 30 mL and 50 mL glass vial containing 0.74 to 7.40 GBq/mL (20 to 200 mCi/mL) of Fludeoxyglucose F^{18} injection and 4.5 mg of sodium chloride with 0.1 to 0.5% w/w ethanolas a stabilizer (approximately 15 to 50 mL volume) for intravenous administration. Fludeoxyglucose F^{18} injection is manufactured by Siemens' PETNET Solutions, 810 Innovation Drive, Knoxville, TN 39732, USA.

Artificial Intelligence for MRI

Heinrich von Busch, Ph.D.

Siemens Healthineers, Erlangen, Germany

The developments of the last few years in computational hardware as well as algorithms, in particular the advent of methods suitable for training complex neural networks (Deep Learning), have opened up new possibilities for machine learning [1] and automation in many applications. Magnetic Resonance imaging, postprocessing and interpretation, in fact radiology in general, are no exception. In the following, we will attempt to provide a brief overview of the current state of development.

In 2016, computer expert Geoffrey Hinton suggested that "we should stop training radiologists now" [2], as the discipline would soon be made obsolete by intelligent new algorithms that outperform human readers. His statement attracted considerable attention and gave rise to countless passionate debates in the community. From a 2019 perspective, however, the idea that radiology could become extinct anytime soon appears less than plausible for a number of reasons, among them the appreciation that many aspects of radiology go way beyond well-defined, "sandbox" problem-solving. Put simply, in the absence of "general artificial intelligence", which could indeed replace humans in any complex cognitive task (and is as yet not even visible on the horizon), there is no algorithm that could *replace* a radiologist. That said, artificial intelligence (AI) promises to *augment* workflows in radiology in many ways, by providing supportive tools particularly for highly standardized and repetitive tasks, starting from the identification and delineation of anatomical structures and organs and the corresponding extraction of quantitative parameters. The concept, in fact, is not entirely new. Tools

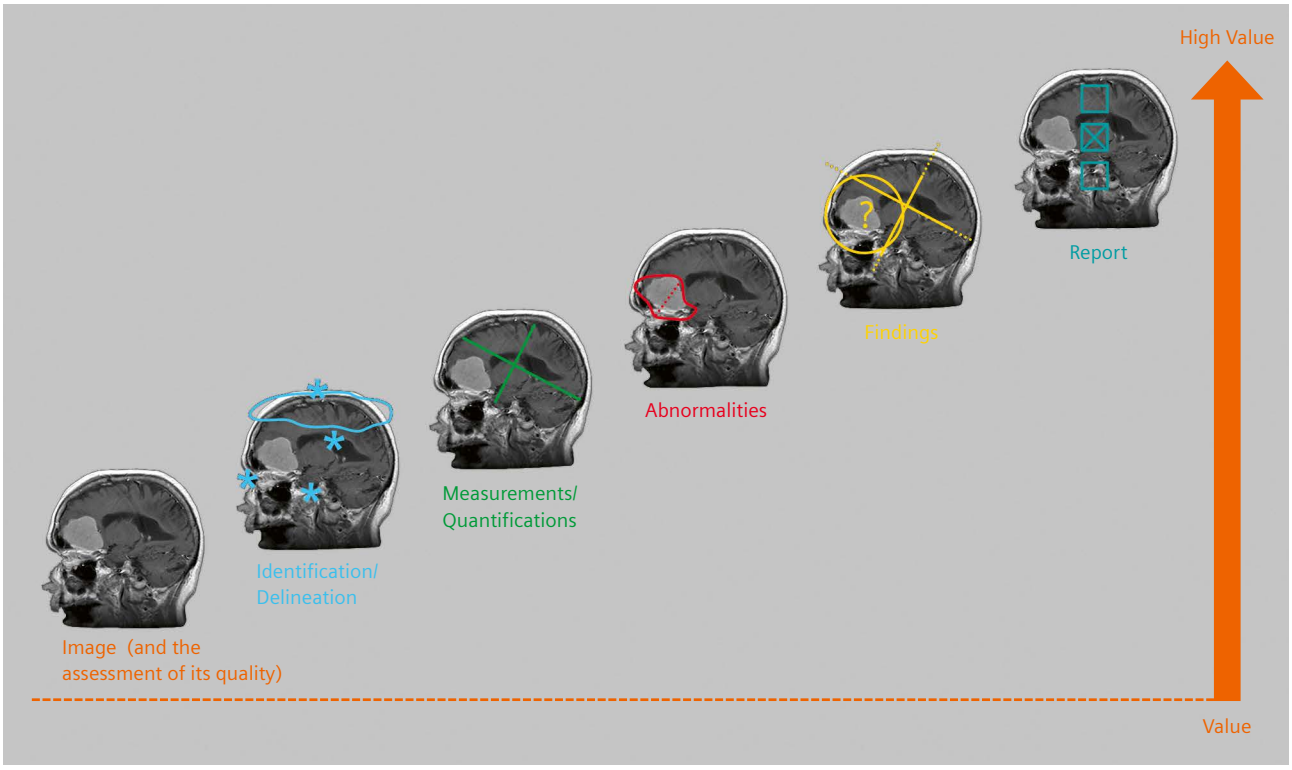

1 Steps in image analysis and interpretation

based on machine learning algorithms applied to medical images have been in wide clinical use for many years, as in MRI exam planning support provided by Siemens' Dot Engines. What is new is that the latest technical advances promise to improve the performance of such tools to a level that will extend their usefulness to many more use cases than could be covered previously.

Before addressing the state of the art in AI tools for radiology, let us review a case of machine problem-solving that exemplifies many of the characteristic traits that fuel the excitement about the latest level of AI – strategy games. Chess, in particular, has long been considered a touchstone of cognitive ability, so that the victory of IBM's Deep Blue over the reigning world chess champion Garri Kasparov in 1997 was seen as a milestone in machine intelligence. Fast forward to 2017 and the latest edition of Google DeepMind's software AlphaGo Zero [3] for the board game Go, and consider the leap forward. Not only does Go exhibit far more options per move than chess, but the inner workings of the machines involved could hardly be more different. Whereas Deep Blue relied on custom integrated circuits specifically designed for the ultrafast calculation of nothing but chess moves and was trained on a large library of matches played by human chess masters, AlphaGo Zero used general neural network hardware and learned Go starting from just the rules of the game by playing itself. With this approach, it took only a few days to surpass the level of the best human players.

While this was clearly an impressive achievement, it is important to place it in perspective in relation to "real-life" tasks and realize that games such as Chess and Go have a well-defined, limited set of input parameters, a clear figure of merit, and easily allow the generation of large volumes of data that an algorithm can be trained on. Image interpretation in radiology, by contrast, is characterized by very large sets of input parameters (such as high-resolution 3D image data), significant variability both in subjects and in the imaging process itself (particularly so in MRI), an often less-than-perfect reference standard, and, importantly, only limited access to training cases. Based on these observations, it is tempting to hypothesize that well-standardized, high-volume image interpretation tasks, such as those performed in screening, lend themselves most readily to AI support. Indeed, automated tools aiding the reading of chest CT scans and X-ray mammograms are among the first high-profile AI products for radiology on the market.

Among the many use cases of AI related to MR imaging, which range from exam planning to image reconstruction, to image interpretation, and to clinical decision support, let us now focus specifically on image analysis and interpretation and how AI tools may help in the process at different levels (Fig. 1). Going from an image series as the input to the radiology report as the result involves a number of steps. The first step is the assessment of the quality of the image. Next, there are the localization and delineation of anatomical structures in the image. Such results may already be highly useful in their own right because they relieve clinical caregivers of tedious work, e.g., in automated scan planning, or organ contouring for radiotherapy. Then the measurement and quantification of the morphological structures that were identified may follow, as in organ volumetry, which in fact is often only feasible in routine reading if supported by automation. Yet another step may identify abnormalities in the image, followed by an assessment of their clinical significance. It is here that we cross into the territory of computer-aided detection (CADe) and computer-aided diagnosis (CADx). Then there is the step of compiling the findings and results for a clinical report. Typically, this is the highest level of abstraction that is achievable based on information from images alone; in many cases the report, and certainly the recommendations for clinical follow-up, will require additional input beyond imaging, e.g., from patient anamnesis and laboratory exams.

Let us turn now to how AI tools will become available to the radiologist. It is our conviction at Siemens Healthineers that the success of AI in clinical practice will hinge not only on the stand-alone performance and robustness of the algorithms, but in equal measure on their seamless integration into the radiology workflow. One example of our vision is the AI-Rad Companion[1] as our platform for inserting AI into routine, PACS-based reading. The first application on this platform will be a comprehensive package of visualizations, evaluations, and quantifications for thorax CT[2]. Based on our teamplay infrastructure, results will be automatically generated as soon as the exam is complete, and added to the case as extra DICOM image series. In this way, they are readily accessible, along with the original images, in any viewer in which the reader may choose to open the case. In the chest CT example, the analyses cover the lung[2], the aorta[2], the heart[2], and the spine[3], so as to address not only the organ or organs that may have been the original focus for prescribing the exam, but other anatomies that are visible on the image as well. Figure 2 shows examples of the output. For the lung, evaluations comprise the detection of suspicious lung nodules including measurements of their size, as well as the visualization and quantification of volumes of low X-ray attenuation within the lung, both for the lung as a whole and for each lung lobe separately.

[1]The AI-Rad Companion Engine has 510(k) clearance.
[2]CT Chest, Heart, and Aorta are 510(k) pending.
[3]Work in progress: the application is currently under development and is not for sale in the U.S. and in other countries. Its future availability cannot be ensured.

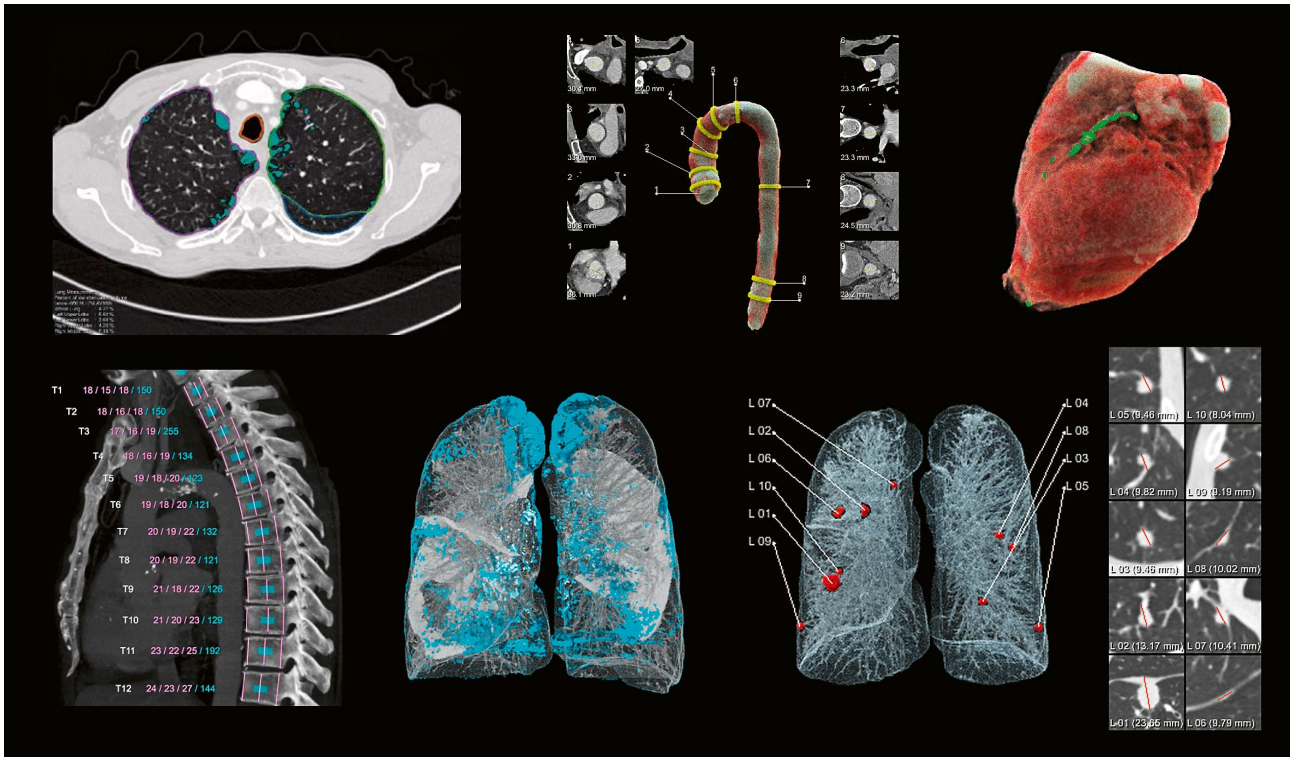

2 Chest CT[2] results from the AI-Rad Companion platform

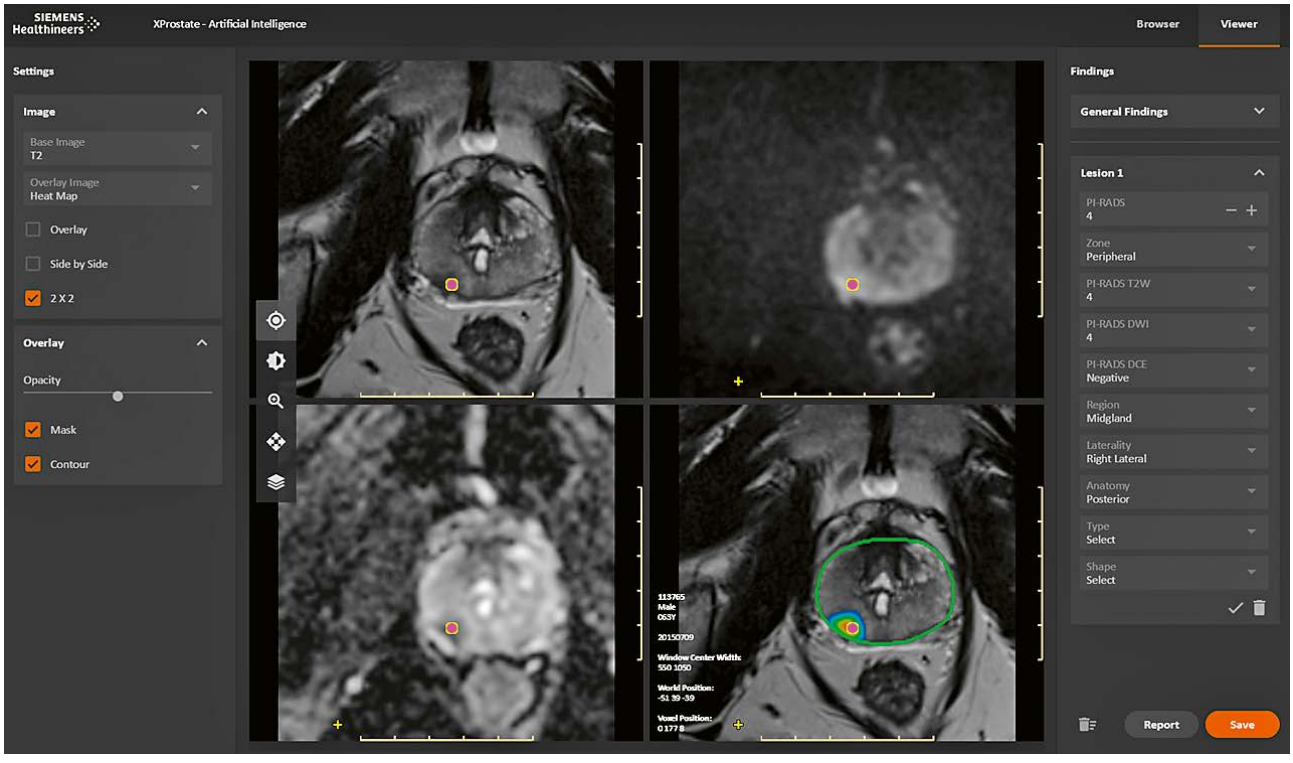

3 Prototype for AI evaluation of multiparametric prostate MRI[3]

For the heart, a visualization and quantification of the volume of the heart and in particular of coronary calcifications is prepared. For the aorta, a segmentation is performed and visualized, along with measurements of the diameters at different positions, and for the spine[3], the vertebral bodies are automatically segmented, visualized, labeled, and measured, both in height and in bone density. All of these evaluations are designed to be robust to the input variability presented by different CT scanners and acquisition protocols, and to work with and without the use of contrast agents.

It is worth noting that chest CT imaging is just the first area for which we plan to bring to the market AI functionalities that are designed to save time and support consistent quality in the reading process. For a glimpse of our vision of the future, let us discuss another application, currently work in progress, that targets the AI analysis of multiparametric prostate MRI and is intended to cover all the analysis steps described above for image reading up to the prepopulation of a structured report. Again, the aim is to save time and support consistent quality. Figure 3 shows a screenshot of a minimal user interface geared specifically to prostate MRI reading. In this prototype, AI algorithms provide an automatic segmentation of the overall prostate and of the peripheral zone of the prostate, a map of lesions identified as suspicious, and a proposal for their PI-RADS classification, for the reader to check and edit if necessary before the results are compiled in a structured report.

There are plenty of further application scenarios involving AI beyond those presented here, such as in more efficient image reconstruction, in patient triage, and in clinical decision support. What they all have in common is a supporting role, often in well-defined, repetitive tasks. Even though they will be powerful instruments in some rather well-standardized contexts, it is to be expected that these
applications will become just a new set of tools in the hands of the radiologist, assisting but not replacing the human reader. In fact, their use and usefulness may become so ubiquitous within a few years that, just as with chess programs, we will no longer even call them "AI".

References

1 Russell SJ, Norvig P. Artificial Intelligence: A Modern Approach. 3rd ed. Upper Saddle River: Prentice Hall; 2010.
2 Hinton G. On Radiology. [video file]. 2016 Nov 24. Available from: https://www.youtube.com/watch?v=2HMPRXstSvQ
3 Silver D, Schrittwieser J, Simonyan K et al. Mastering the game of Go without human knowledge. Nature [Internet]. 2017 Oct 19; 550: 354–359. Available from: https://www.nature.com/articles/nature24270

Contact

Heinrich von Busch, Ph.D.
Product Owner Artificial Intelligence for Oncology
Siemens Healthcare GmbH
SHS DS DAT AI
Hartmannstr. 17
91052 Erlangen, Germany
Mobile: +49 162 2883167
heinrich.von_busch@siemens-healthineers.com

We are looking forward to hearing from you

Founded in 1993 the MAGNETOM Flash magazine has been around almost as long as MAGNETOM MRI scanners.

In times of online media and digitalization we would value your feedback to ensure that the magazine continues to fit your interests and professional needs.

Please take a moment to complete a brief reader survey at
www.siemens.com/magnetom-world

syngo Virtual Cockpit – Your Software for Remote Scanning Assistance and More Flexible Workforce Management

Petra Kraft; Janis Dummet

Siemens Healthineers, Forchheim, Germany

Growing financial pressure and increasingly assertive patients are pushing imaging providers toward finding ways to deliver high-quality care while at the same time keeping costs low. As a relevant cost and quality factor, healthcare personnel have a considerable bearing on tackling these challenges. But as qualified staff is expensive and hard to come by in some markets, optimal deployment of human resources is key to success. New working methods are required that will enable hospitals to deal with the increasing workload and quality expectations despite having a smaller workforce at their disposal.

syngo Virtual Cockpit[1], our new software solution, allows medical staff to connect remotely to scanner workplaces to assist personnel at a different location, especially where more sophisticated examinations are required. *syngo* Virtual Cockpit can be used with CT, MR, and MR PET scanners from Siemens Healthineers. The ability to deploy experienced technologists across multiple locations allows healthcare providers to manage their workforce more flexibly and thus ease tight human resources.

Connecting clinical teams beyond physical boundaries

For radiological examinations, experienced colleagues can "tune in" quickly and in real time via headsets, conference speakers, chat or video functions. That means that the steering technologists[2] can remain at their own location and provide guidance to the modality technologist[3] operating the scanner at another location, e.g., to adjust protocol parameters.

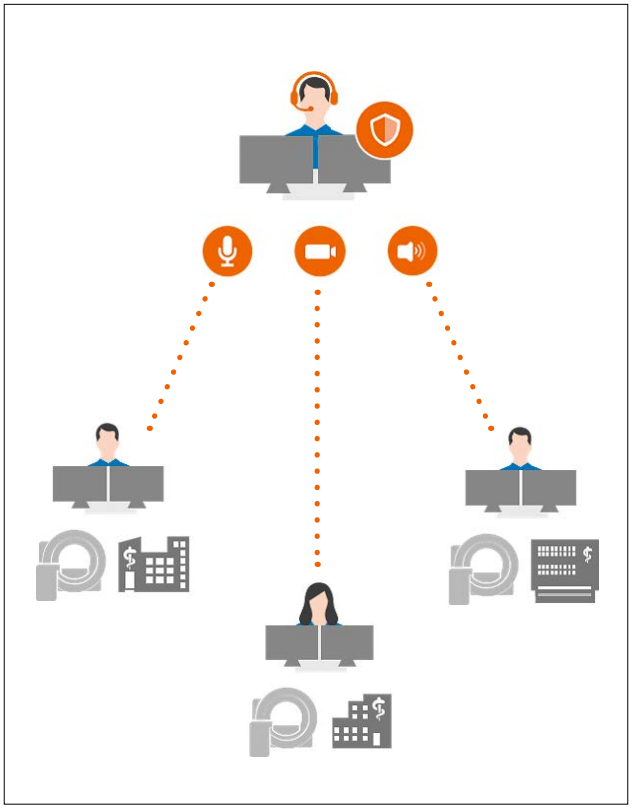

1 *syngo* Virtual Cockpit allows medical staff to provide comprehensive scanning assistance to imaging personnel via video, audio, and chat functions. Up to three scanners at different locations can be supported simultaneously by one steering technologist.

[1]*syngo Virtual Cockpit is not commercially available in all countries. For regulatory reasons, its future availability cannot be guaranteed. Precondition: Expert-i enabled modality from Siemens Healthineers.*
[2]*Steering technologist: An experienced technologist who works with syngo Virtual Cockpit and connects to modalities remotely.*
[3]*Modality technologist: A technologist who works locally at the modality site.*
[4]*The statements by Siemens Healthineers' customers presented here are based on results that were achieved in the customer's unique setting. Since there is no 'typical' hospital and many variables exist (e.g., hospital size, case mix, level of IT adoption), there can be no guarantee that other customers will achieve the same results.*

"We expect the use of syngo Virtual Cockpit to have a significant impact because we will save costs by not sending dedicated steering technologists from one site to the other. We will also be able to better utilize our scanner fleet. Our patients will also benefit, because they no longer have to go to a dedicated site in our network to get a special examination."[4]

Associate Professor Justus Roos, M.D., Head of Radiology and Nuclear Medicine
Lucerne Cantonal Hospital (LUKS), Switzerland

Improving workforce productivity

With this software tool, the steering technologist can perform scans at one location while offering remote support to up to three colleagues in parallel. This makes the best possible use of resources and can lead to an increase in the total number of scans performed. Having the support of a steering technologist on hand can also positively affect the efficiency of scan procedures. Experience from Alliar Médicos à Frente, a large radiology network in Brazil, showed that with *syngo* Virtual Cockpit, the scan time could be reduced by 33%. Furthermore, long commutes between different sites are no longer necessary as steering technologists can guide exams performed by on-site technologists with *syngo* Virtual Cockpit from anywhere, which in turn saves time and costs. Also, in this way it is easy to overcome bottlenecks due to vacation periods, sick leave, nightshifts or other reasons.

Achieving a higher level of standardization

Especially when it comes to complex examinations, expert knowledge is critical. With *syngo* Virtual Cockpit, less-experienced staff can always call on a colleague for live support. This remote collaboration helps reduce the number of unwarranted variations in reports, resulting in consistent image quality across the healthcare enterprise and more accurate diagnoses. With the introduction of *syngo* Virtual Cockpit Alliar Médicos à Frente in Brazil was able to reduce the number of rescans to less than 1% of cases.

Increasing patient satisfaction

Patient satisfaction is becoming an increasingly relevant factor in the reimbursement of healthcare services. *syngo* Virtual Cockpit can have a positive impact on the productivity of medical institutions. Furthermore, making

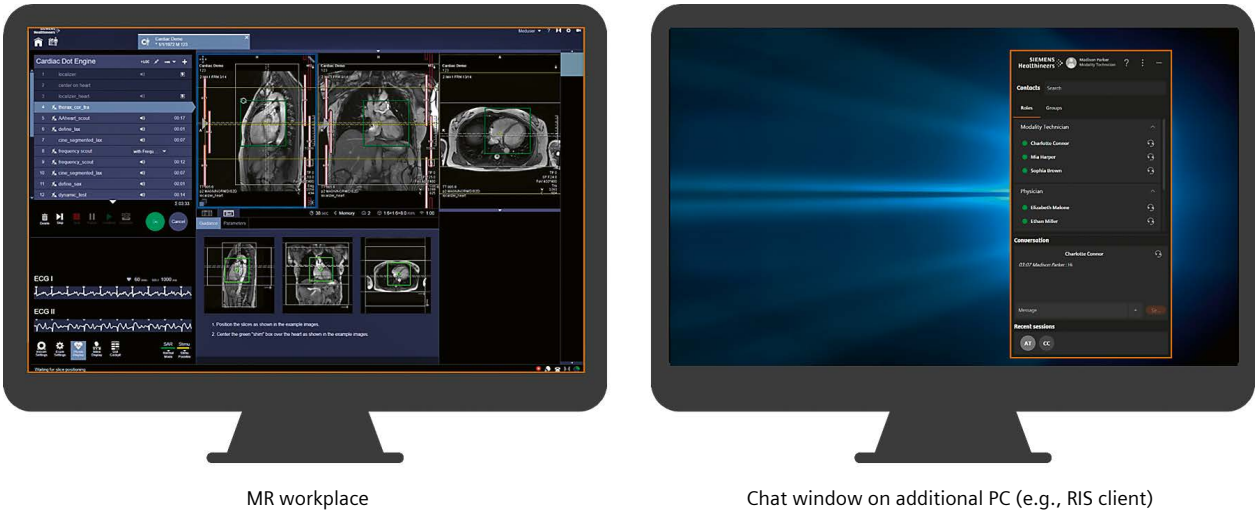

MR workplace

Chat window on additional PC (e.g., RIS client)

2 The modality technologist is sitting at the modality console. To start a supported session, the chat tool of *syngo* Virtual Cockpit can be opened on another Windows PC, for example, the PC used for the RIS.

expert knowledge available independent of location means that specialized examinations can be offered at any site in a healthcare network. As a result, patients receive appointments more quickly for examinations at their preferred location. In this way, *syngo* Virtual Cockpit improves patient convenience and provides access to healthcare to more patients, in particular those requiring complex examinations.

The *syngo* Virtual Cockpit workflow – easy and intuitive

Imagine a complex examination is planned at an MR scanner. Due to a lack of onsite knowledge, a decision is made to support the examination remotely.

Step 1: Establishing a connection between modality and steering technologist
The modality technologist is sitting at the MR workplace and logs onto the *syngo* Virtual Cockpit software at a Windows PC next to the modality console. In a chat window, the modality technologist can see a list of all available steering technologists. The modality technologist can now choose one of those colleagues and start a chat. Later the steering technologist can connect and assist remotely at the MR console.

Step 2: Logging on securely to the scanner workplace
To establish a connection via *syngo* Virtual Cockpit, the steering technologist needs to enter a one-time password provided by the modality technologist.

The modality technologist clicks the Expert-i icon on the modality workplace and a one-time password is displayed. The modality technologist types this password in the chat window of *syngo* Virtual Cockpit.

The steering technologist now has full access to the modality workplace. Two IP cameras can be set up at the modality to show e.g. the patient on the table and the monitor of the contrast injector.

Step 3: Performing the scan with remote assistance
The modality technologist positions the patient on the exam table. As soon as all workflow steps such as coil positioning have been completed, the modality technologist leaves the room.

Now the steering technologist assists in the scanning procedure. Both colleagues keep in constant contact by communicating via speakerphone, headset, or chat. If contrast media has to be injected, it is the task of the modality technologist to start injection on site. If a CT examination is being performed, it is also the modality technologist's task to start the radiation or move the table.

syngo Virtual Cockpit is compatible with most Siemens Healthineers scanners

syngo Virtual Cockpit software can be used with all MR systems equipped with software version MR VA or later that support Expert-i. For CT, *syngo* Virtual Cockpit is compatible with all Somaris 7-based scanners with software version VB20[5], all Somaris 5-based scanners with software version VC50, as well as all Somaris X-based scanners (.go platform) with software version VA30[5]. For details, please contact your local Siemens Healthineers organization.

3 Each modality is displayed in a dedicated segment of the screen on the steering technologist's workplace with its own chat window. The steering technologist can see all the necessary information on his or her workplace: Contact list, chat, modality camera and contrast monitor overview. Moreover, the user name of each technologist is always visible.

"If you really have a shortage of technicians and you have to decide every morning whether you have to close a machine, yes or no, that's not really convenient. I mean we totally reduced that down to zero."[4]

Professor Michael Forsting, M.D., Director, Institute of Diagnostic and Interventional Radiology and Neurology, University Hospital Essen, Germany

Technical requirements for *syngo* Virtual Cockpit

syngo Virtual Cockpit requires the following hardware and software equipment:

- The steering technologist workplace requires one PC (Windows 10), two monitors, and a communication device.
- The modality technologist workplace needs to be equipped with one PC (Windows 7/8/10) with one monitor, one to two IP cameras, and a communication device (with headset or speakerphone).
- For a stable connection, a minimum bandwidth of 60 Mbps[6] is needed between the steering client and the modality.[7]

Summary

Our new software solution *syngo* Virtual Cockpit has been designed to assist scan procedures remotely from any location. By making expert knowledge available across sites in real time, *syngo* Virtual cockpit addresses the challenge of the shortage of experienced technologists while at the same time ensuring high-quality care.

[5]Both software versions VB20 and VA30 are under development. Not available for sale. Future availability cannot be guaranteed.
[6]For connecting one scanner and no IP cameras.
[7]Server requirements can be stated only after the server has been implemented and after system testing results are known.

Janis Dummet

Petra Kraft

Contact

Petra Kraft
Siemens Healthineers
DI SY M&S M
Siemensstr. 3
91301 Forchheim
Germany
+49 (174) 3144075
petra.kraft@siemens-healthineers.com

Meet Siemens Healthineers

Siemens Healthineers: Our brand name embodies the pioneering spirit and engineering expertise that is unique in the healthcare industry. The people working for Siemens Healthineers are totally committed to the company they work for, and are passionate about their technology. In this section we introduce you to colleagues from all over the world – people who put their hearts into what they do.

Rebecca Ramb

Rebecca Ramb became Global Head of MR Collaboration Management at Siemens Healthineers after several years of active MRI research in academia. She completed her doctorate in Mathematics and MR Physics at the University of Freiburg, Germany, focusing on Parallel and Echo-Planar Imaging as part of Jürgen Hennig's group. In 2016, she won the Ferdinand-von-Lindemann prize for her work. Rebecca Ramb later worked as a postdoctoral fellow on Compressed Sensing Cardiac MRI together with Dan Sodickson and Ricardo Otazo at the New York University Langone Medical Center, USA. She has gained teaching experience of MR Physics, teaching MR techs as part of EduMed AG, Switzerland, and future MR techs as part of the University Medical Center Freiburg.
Rebecca is also a certified choir conductor and organ player. Since working for Siemens Healthineers, Rebecca has spent considerable time looking into how new technologies can better account for biovariabilities in MRI. She has also been part of the launch of two new 1.5T systems that address the daily challenges of clinical routine: 1.5T MAGNETOM Sola and MAGNETOM Altea. When she's not completely magnetized by MR, she enjoys running, yoga or playing the piano.

Erlangen, Germany

How did you first come into contact with MRI?
After studying mathematics, where I was convinced that only the most abstract and theoretical math was fun – I walked into the lab of Jürgen Hennig and was immediately captivated when I saw how theory can become reality – and how it can impact patients. I was incredibly impressed by this open, friendly, and smart interdisciplinary research group.

What is most fascinating about MRI?
There are so many things ... Please, don't laugh, but to me, it's still the very basic part that fascinates me: How we actually measure Fourier coefficients. For a mathematician like me, someone who always worked with theoretical concepts, when I first calculated how we actually really measure Fourier coefficients myself, I was thrilled. Fully understanding the basic signal excitation and processing, learning how encoding and reconstruction interplay, that's fun.

What is the most fascinating aspect of your job?
In my role as Collaboration Manger, I'm amazed every day at how much Siemens Healthineers invests (time and effort) into collaborating with its partners. We strongly believe that translation to clinical routine can only be achieved through a significant academic-industrial joint effort. This is what I work toward every day.

What do you think are the most important developments in MRI and in healthcare?
Gradient encoding and parallel imaging are certainly one of the milestones in MRI for me. I also believe that the clinical scientists nowadays who really put all their effort into creating and proofing the value of MR techniques by connecting the clinical questions and rigorous research are truly impressive.

What would you do, if you could spend a month doing whatever you wanted?
My bucket list is quite long! Whenever I can, I take three weeks off to travel to an exotic place. In August, I spent three weeks in Mongolia and last winter, I went hiking in Nepal. This gives me a chance to let my mind wander off so I can come back filled with creative ideas. I believe this is so helpful for my job and for me, personally.

The entire editorial staff at University Hospital Freiburg and at Siemens Healthineers extends their appreciation to all the radiologists, technologists, physicists, experts, and scholars who donate their time and energy – without payment – in order to share their expertise with the readers of MAGNETOM Flash.

MAGNETOM Flash – Imprint

Publisher:
Siemens Healthcare GmbH
Magnetic Resonance,
Karl-Schall-Str. 6, D-91052 Erlangen, Germany

Editor-in-chief:
Antje Hellwich
(antje.hellwich@siemens-healthineers.com)

Guest editor:
Prof. Dr. Dr. h. c. Jürgen Hennig
University Medical Center Freiburg
Dept. of Radiology, Medical Physics
Freiburg, Germany

Editorial Board:
Rebecca Ramb, Ph.D.; Sunil Kumar S. L., Ph.D.;
Wellesley Were; Gary R. McNeal, MS (BME)

Review Board:
Daniel Fischer; Christian Geppert, Ph.D.;
Berthold Kiefer, Ph.D.; Heiko Meyer, Ph.D.;
Efrén Ojeda; Christian Schuster, Ph.D.;
Gregor Thörmer, Ph.D.

Copy Editing:
Sheila Regan, Jen Metcalf, UNIWORKS,
www.uni-works.org
(with special thanks to Kylie Martin)

Layout:
Agentur Baumgärtner,
Friedrichstr. 4, D-90762 Fürth, Germany

Production:
Norbert Moser,
Siemens Healthcare GmbH

Printer:
G. Peschke Druckerei GmbH,
Taxetstr. 4, D-85599 Parsdorf b. Munich, Germany

MAGNETOM Flash is sent free of charge to Siemens Healthineers MR customers, qualified physicians, technologists, physicists and radiology departments throughout the world. It includes reports in the English language on magnetic resonance: diagnostic and therapeutic methods and their application as well as results and experience gained with corresponding systems and solutions. It introduces from case to case new principles and procedures and discusses their clinical potential. The statements and views of the authors in the individual contributions do not necessarily reflect the opinion of the publisher.

The information presented in these articles and case reports is for illustration only and is not intended to be relied upon by the reader for instruction as to the practice of medicine. Any health care practitioner reading this information is reminded that they must use their own learning, training and expertise in dealing with their individual patients. This material does not substitute for that duty and is not intended by Siemens Healthcare to be used for any purpose in that regard. The drugs and doses mentioned herein are consistent with the approval labeling for uses and/or indications of the drug. The treating physician bears the sole responsibility for the diagnosis and treatment of patients, including drugs and doses prescribed in connection with such use. The Operating Instructions must always be strictly followed when operating the MR system. The sources for the technical data are the corresponding data sheets. Results may vary.

We welcome your questions and comments about the editorial content of MAGNETOM Flash. Please contact us at
magnetomworld.team@siemens-healthineers.com

Manuscripts as well as suggestions, proposals and information are always welcome; they are carefully examined and submitted to the editorial board for attention. MAGNETOM Flash is not responsible for loss, damage, or any other injury to unsolicited manuscripts or other materials. We reserve the right to edit for clarity, accuracy, and space. Include your name, address, and phone number and send to the editors, address above.

MAGNETOM Flash is also available online:

www.siemens.com/magnetom-world

Not for distribution in the US

On account of certain regional limitations of sales rights and service availability, we cannot guarantee that all products included in this brochure are available through the Siemens sales organization worldwide. Availability and packaging may vary by country and is subject to change without prior notice. Some/All of the features and products described herein may not be available in the United States.

The information in this document contains general technical descriptions of specifications and options as well as standard and optional features which do not always have to be present in individual cases, and which may not be commercially available in all countries.

Due to regulatory reasons their future availability cannot be guaranteed. Please contact your local Siemens organization for further details.

Siemens reserves the right to modify the design, packaging, specifications, and options described herein without prior notice. Please contact your local Siemens sales representative for the most current information.

Note: Any technical data contained in this document may vary within defined tolerances. Original images always lose a certain amount of detail when reproduced.

Siemens Healthineers Headquarters
Siemens Healthcare GmbH
Henkestr. 127
91052 Erlangen, Germany
Phone: +49 9131 84-0
siemens-healthineers.com

Published by Siemens Healthcare GmbH · Order No. A91MR-1000-139M-7600 · Printed in Germany · 7172 041911. ·